



Joining of tungsten and steel for the first wall of a future fusion reactor

Vishnu Ganesh

Energie & Umwelt / Energy & Environment

Band / Volume 614

ISBN 978-3-95806-715-8

Forschungszentrum Jülich GmbH
Institut für Energie- und Klimaforschung (IEK)
Plasmaphysik (IEK-4)

Joining of tungsten and steel for the first wall of a future fusion reactor

Vishnu Ganesh

Schriften des Forschungszentrums Jülich
Reihe Energie & Umwelt / Energy & Environment

Band / Volume 614

ISSN 1866-1793

ISBN 978-3-95806-715-8

Bibliografische Information der Deutschen Nationalbibliothek.
Die Deutsche Nationalbibliothek verzeichnet diese Publikation in der
Deutschen Nationalbibliografie; detaillierte Bibliografische Daten
sind im Internet über <http://dnb.d-nb.de> abrufbar.

Herausgeber
und Vertrieb: Forschungszentrum Jülich GmbH
 Zentralbibliothek, Verlag
 52425 Jülich
 Tel.: +49 2461 61-5368
 Fax: +49 2461 61-6103
 zb-publikation@fz-juelich.de
 www.fz-juelich.de/zb

Umschlaggestaltung: Grafische Medien, Forschungszentrum Jülich GmbH

Druck: Grafische Medien, Forschungszentrum Jülich GmbH

Copyright: Forschungszentrum Jülich 2023

Schriften des Forschungszentrums Jülich
Reihe Energie & Umwelt / Energy & Environment, Band / Volume 614

D 294 (Diss. Bochum, Univ., 2023)

ISSN 1866-1793
ISBN 978-3-95806-715-8

Vollständig frei verfügbar über das Publikationsportal des Forschungszentrums Jülich (JuSER)
unter www.fz-juelich.de/zb/openaccess.



This is an Open Access publication distributed under the terms of the [Creative Commons Attribution License 4.0](https://creativecommons.org/licenses/by/4.0/),
which permits unrestricted use, distribution, and reproduction in any medium, provided the original work is properly cited.

List of publications

Part of this thesis has already been published in the following articles:

- V. Ganesh et al., Manufacturing of W-steel joint using plasma sprayed graded W/steel-interlayer with current assisted diffusion bonding; *Fusion Engineering and Design*, 172, 112896, 2021.
DOI: 10.1016/j.fusengdes.2021.112896
- V. Ganesh, et al., Manufacturing of W/steel composites using electro-discharge sintering process, *Nuclear Materials and Energy*, 30, 101089, 2022.
DOI: 10.1016/j.nme.2021.101089
- V. Ganesh, et al., Processing and properties of sintered W/steel composites for the first wall of future fusion reactor, *Journal of Nuclear Engineering*, 4, 177–192, 2023.
DOI: 10.3390/jne4010014
- V. Ganesh, et al., High heat flux testing of graded W-steel joining concepts for the first wall, *Energies*, 16, 3664, 2023.
DOI: 10.3390/en16093664

Abstract

Nuclear fusion energy has the potential to be the future source of CO₂-free clean energy. However, harnessing it needs overcoming significant engineering and scientific challenges. One major challenge is manufacturing a first wall (FW) that can withstand extreme thermal, particle, and neutron loading. As per the current understanding, it would consist of protective tungsten (W) armour joined to the underlying structure. This structure is made of reduced activation ferritic/martensitic steel, like Eurofer 97. Presently, several literatures presume that the direct joining of W and Eurofer 97 cannot be foreseen, as the coefficient of thermal expansion (CTE) of Eurofer 97 is more than twice of W. This leads to macroscopic thermal stress at the bonding seam that might cause early failure of the joint during the operation of the reactor. One solution is redistributing the stresses by introducing a graded interlayer between them that can gradually change the CTE. This graded interlayer is known as functionally graded material (FGM), which is itself a mixture of W and steel with several layers, each with a gradually varying W/steel ratio; each layer is a W/steel-composite of a certain volume content of W. Thus, the goal was to investigate the feasibility of this concept. Three different manufacturing techniques have been explored: spark plasma sintering (SPS), electro discharge, and atmospheric plasma spraying (APS); their feasibility was investigated. First, the processing parameters of the manufacturing techniques were optimized to produce individual composites—consisting of three volume concentrations of W: 25 %, 50 %, and 75 %—with low porosity while minimizing the formation of brittle intermetallic compounds. It was found that the EDS was not the most unsuitable technique. Second, using the optimized parameters, composites were prepared. These were then characterized for their microstructure, mechanical, and thermophysical behaviour. The elastic modulus and flexural deformation behaviour were determined by resonant ultrasound spectroscopy and a miniature 4-point bending test. The thermophysical characterization was carried out by dilatometry, dynamic differential scanning calorimetry and laser flash analysis method. The composites produced by the SPS had the most promising and superior properties compared with that of APS. Third, post characterization, graded joint, directly bonded W-steel joint, and joint featuring a V interlayer were manufactured. Fourth, these joints were benchmarked by high heat flux (HHF) test at an electron beam facility to investigate their thermal fatigue response. This revealed an important finding; the most critical factor responsible for the lifetime of a graded joint is the bonding between the W and FGM, and not the properties of FGM itself. The thesis also concluded that none of the FGM concepts improved the lifetime of the joint. Finally, a thorough discussion led to recommendations for future work towards successfully realising the joining of W and steel.

Table of contents

| | |
|---|-------------|
| List of publications | iii |
| Abstract | v |
| Table of contents | vii |
| Abbreviations, formula symbols, and nomenclatures | xi |
| List of Figures | xix |
| List of Tables | xxix |
| 1 Introduction | 1 |
| 1.1 Nuclear fusion..... | 1 |
| 1.2 Future fusion reactor..... | 2 |
| 1.3 First wall | 2 |
| 1.4 Materials for first wall | 3 |
| 1.4.1 Tungsten | 3 |
| 1.4.2 Reduced activation ferritic/martensitic steel | 5 |
| 1.5 Joining W and steel..... | 6 |
| 1.5.1 Boundary conditions and challenges..... | 6 |
| 1.5.2 Direct joining..... | 7 |
| 1.5.3 Joining using interlayer | 9 |
| 1.5.4 Joining using a functionally graded material | 11 |
| 1.6 Realization of functionally graded first wall components..... | 12 |
| 1.6.1 Plasma spraying of tungsten on steel with/without FGM | 12 |
| 1.6.2 Plasma sprayed FGM with bulk-W armour | 14 |
| 1.6.3 Electric current activated/assisted sintering | 15 |
| 1.7 High heat flux testing of W-steel joints..... | 16 |
| 1.8 Goal and outline of the work | 17 |
| 2 Manufacturing of individual W/steel-composite | 19 |
| 2.1 Atmospheric plasma spraying..... | 19 |
| 2.1.1 Working principle of APS process..... | 19 |
| 2.1.2 Methodology for plasma spraying..... | 20 |
| 2.1.3 Optimized plasma sprayed composites | 22 |
| 2.2 Electro discharge sintering | 24 |
| 2.2.1 Working principle of EDS process..... | 24 |

| | | |
|----------|--|-----------|
| 2.2.2 | Methodology for sintering..... | 24 |
| 2.2.3 | Optimization of sintering parameters for 25W | 27 |
| 2.2.4 | Optimization of sintering parameters for 50W | 29 |
| 2.2.5 | Optimization of sintering parameters for 75W | 30 |
| 2.2.6 | Non-homogenous discharge of current | 32 |
| 2.3 | Spark plasma sintering..... | 33 |
| 2.3.1 | Working principle of SPS process | 33 |
| 2.3.2 | Methodology for sintering..... | 34 |
| 2.3.3 | Optimization of sintering parameter for 25W | 35 |
| 2.3.4 | Optimization of sintering parameters for 50W | 37 |
| 2.3.5 | Optimization of co-sintering of 75W with bulk-W | 38 |
| 2.4 | Summary of manufacturing of individual composites..... | 41 |
| 3 | Characterization of W/steel-composites | 43 |
| 3.1 | Comprehensive microstructural characterization | 43 |
| 3.1.1 | As-sprayed plasma sprayed composites..... | 43 |
| 3.1.2 | Plasma sprayed composites after heat treatment..... | 44 |
| 3.1.3 | As-sintered composites | 49 |
| 3.1.4 | Sintered composites after heat treatment | 51 |
| 3.2 | Mechanical characterization | 52 |
| 3.2.1 | Resonant ultrasound spectroscopy | 52 |
| 3.2.2 | Four-point bending test | 53 |
| 3.3 | Physical property | 57 |
| 3.3.1 | Archimedes' density..... | 57 |
| 3.4 | Thermophysical characterization..... | 58 |
| 3.4.1 | Dilatometer analysis | 58 |
| 3.4.2 | Differential scanning calorimetry analysis..... | 60 |
| 3.4.3 | Laser flash analysis | 62 |
| 3.5 | Summary of characterization of composites..... | 65 |
| 4 | Manufacturing of joints | 67 |
| 4.1 | Joint featuring sintered graded interlayer | 67 |
| 4.1.1 | Co-sintering of 75W and bulk-W..... | 67 |
| 4.1.2 | Joining of W and steel with 3-layer FGM..... | 71 |
| 4.1.3 | Joining of W and steel with 2-layer FGM..... | 72 |
| 4.2 | Joint featuring plasma sprayed graded interlayer | 74 |
| 4.2.1 | Joining trials for bonding 75W and bulk-W..... | 75 |
| 4.2.2 | Joining trials for bonding 75W and bulk-W with thin V-foil | 76 |
| 4.2.3 | Joining 75W, 50W, and 25W together..... | 78 |
| 4.2.4 | Joining 25W and bulk-steel..... | 81 |

| | | |
|----------|--|------------|
| 4.2.5 | Joining W and steel with 3-layer FGM | 82 |
| 4.2.6 | Joining W and steel with 2-layer FGM | 83 |
| 4.3 | Joining with V interlayer | 83 |
| 4.4 | Joining W and steel directly | 84 |
| 4.5 | Summary..... | 86 |
| 5 | High heat flux testing of W-steel joints | 87 |
| 5.1 | Methodology of benchmark test | 87 |
| 5.1.1 | Testing setup | 87 |
| 5.1.2 | Overview of joints tested..... | 88 |
| 5.1.3 | Testing protocol..... | 90 |
| 5.2 | Performance of the joints..... | 91 |
| 5.3 | Summary and lifetime of the joints | 95 |
| 6 | Post mortem analysis of tested joints | 97 |
| 6.1 | V-3.FG-APS joint..... | 97 |
| 6.1.1 | Investigation of the cross-sectional cut | 97 |
| 6.1.2 | Summarized failure mechanism | 101 |
| 6.2 | 2.FG-SPS joint..... | 102 |
| 6.2.1 | Investigation of the cross-sectional cut | 102 |
| 6.2.2 | Investigation of the delaminated W-tile and 50W surface..... | 105 |
| 6.2.3 | Summarized failure mechanism | 108 |
| 6.3 | 3.FG-SPS joint..... | 108 |
| 6.3.1 | Investigation of the cross-sectional cut | 108 |
| 6.3.2 | Investigation of the delaminated W-tile and 75W surface..... | 111 |
| 6.3.3 | Summarized failure mechanism | 113 |
| 6.4 | W-steel direct joint | 113 |
| 6.4.1 | Investigation of the cross-sectional cut | 113 |
| 6.4.2 | Investigation of delaminated W-tile and steel surfaces..... | 116 |
| 6.4.3 | Summarized failure mechanism | 120 |
| 7 | Concluding discussion | 121 |
| 7.1 | Evaluation of FGM/individual composites..... | 121 |
| 7.2 | Evaluation of graded W-steel joints | 123 |
| 7.3 | Realization of an actual FW for future fusion reactor | 126 |
| 7.4 | Closure | 128 |
| 8 | Summary and outlook | 131 |
| 8.1 | Summary..... | 131 |
| 8.2 | Outlook | 132 |
| 9 | References | 135 |

| | |
|--|----------|
| Appendix A: Metallographic preparation | a |
| Appendix B: SEM micrographs of starting powders | b |
| Appendix C: Shrouding chamber and process control of APS | d |
| Appendix D: Resistance and efficiency of EDS sintering trials | f |
| Appendix E: Instruments for measuring thermophysical properties | h |
| Appendix F: Metallurgical bonding of W-W interface | n |
| Lebenslauf | t |
| Acknowledgement | u |

Abbreviations, formula symbols, and nomenclatures

List of abbreviations:

Elements

| | |
|----|------------|
| Ar | Argon |
| Be | Beryllium |
| D | Deuterium |
| C | Carbon |
| Co | Cobalt |
| Cu | Copper |
| Cr | Chromium |
| Fe | Iron |
| Ge | Germanium |
| H | Hydrogen |
| He | Helium |
| Li | Lithium |
| Mn | Manganese |
| Mo | Molybdenum |
| N | Nitrogen |
| Nb | Niobium |
| Ni | Nickel |
| O | Oxygen |
| P | Phosphorus |
| S | Sulfur |
| T | Tritium |
| Ta | Tantalum |
| Ti | Titanium |
| V | Vanadium |

Materials

| | |
|------------|--|
| W | Tungsten |
| RAFM | Reduced activation ferritic/martensitic steel |
| TZM | Titanium-Zirconium-Molybdenum alloy |
| WC | Tungsten carbide |
| C-foil | Graphite foil |
| Mo-foil | Molybdenum foil |
| Eurofer 97 | A Reduced activation ferritic/martensitic steel developed at the EU side |

Fusion Technology

| | |
|---------|--|
| D-T | Deuterium-Tritium fusion reaction |
| DEMO | Demonstration fusion reactor, aimed after ITER |
| EU DEMO | Demonstration fusion reactor proposed at the EU side, aimed after ITER |
| fpv | Full power year |
| FW | First wall |
| HCPB | Helium cooled pebble bed breeding blanket |
| HHF | Heat high flux |
| n | Neutron |
| PFC | Plasma-facing component |
| WCLL | Water cooled lithium lead breeding blanket |

Acronyms specific to this thesis

| | |
|-----------------|--|
| at% | Atomic percentage |
| bulk-steel | refers to a bulk Eurofer 97 steel |
| bulk-W | refers to the forged W-bar manufactured by Plansee SE, Austria |
| CTE | Coefficient of thermal expansion |
| D ₅₀ | Particle size at 50 % in cumulative particle size distribution |
| DBTT | Ductile-to-brittle transition temperature |

| | |
|----------------|--|
| MPH | Materials property handbook is a structured handbook which provides concise materials properties by compiling the data from several literatures for designers/engineers to determine the design limit of in-vessel components of future fusion reactor |
| EUROfusion MPH | Handbook documenting and summarizing the material data of Eurofer 97 steel for the designer. This internal project document is distributed to EUROfusion participants |
| FE | Finite element |
| FG | Functionally graded |
| FGM | Functionally graded material |
| IMC | Intermetallic compound |
| ITER MPH | Handbook documenting and summarizing the material data of relevant materials used in fusion reactor for the designer. This internal project document is distributed to ITER participants |
| mea. | Measured values |
| PBHT | Post bonding heat treatment |
| ppm | Part per million |
| PSD | Particle size distribution |
| PSF | Particle size fraction |
| PS-W | Plasma sprayed pure W |
| th. | Theoretical expected values |
| vol% | Volume percentage |
| wt% | Weight percentage |

Manufacturing processes

| | |
|-------|---|
| APS | Atmospheric plasma spraying |
| CA-DB | Current assisted diffusion bonding |
| DB | Diffusion bonding |
| ECAS | Electric current activated/assisted sintering |
| EDM | Electric discharge machining |
| EDS | Electro discharge sintering |
| Exp-W | Underwater explosive welding |

| | |
|----------|--|
| FAST | Field assisted sintering technology |
| HIP | Hot isostatic pressing |
| HIP-DB | Diffusion bonding using hot isostatic pressing |
| PS | Plasma spraying |
| PVD | Physical vapour deposition |
| SPS | Spark plasma sintering |
| VPS | Vacuum plasma spraying |
| wire-EDM | Wire electric discharge machining |

Analysis techniques

| | |
|---------|--|
| BSE | Back scattered electron |
| DSC | Differential scanning calorimetry |
| EDX | Energy dispersive X-ray spectroscopy |
| FIB | Focused ion beam |
| ICP-OES | Inductively coupled plasma emission spectroscopy |
| LFA | Laser flash analysis |
| RUS | Resonant ultrasound spectroscopy |
| SE | Secondary electron |
| SEM | Scanning electron microscopy |
| WD | Working distance in scanning electron microscopy |
| XRD | X-ray diffraction |

Relevant research organizations

| | |
|--------------|--|
| FZJ | Forschungszentrum Jülich GmbH, Germany |
| IPP-CAS | Institute of Plasma Physics of the Czech Academy of Sciences, Czech Republic |
| LWT-RUB | Lehrstuhl Werkstofftechnik, Ruhr-Universität Bochum, Germany |
| KIT | Karlsruher Institut für Technologie, Germany |
| IPP Garching | Max-Planck-Institut für Plasmaphysik, Garching, Germany |

List of symbols:

| | |
|--------------------|---|
| A_{steel} | Adhesion strength to steel |
| E | Young's modulus/ elastic modulus |
| R_m | Ultimate tensile strength/ ultimate flexural strength |
| a | Thermal diffusivity |
| λ | Thermal conductivity |
| σ_{yield} | Yield strength |
| Ra | Roughness average of a surface |
| h | Height of the bending test specimen |
| E_W | Elastic modulus of bulk-W taken from ITER MPH |
| E_{sec} | Total electrical energy delivered to the secondary circuit of electro discharge sintering |
| E_{steel} | Elastic modulus of Eurofer 97 taken from EUROfusion MPH |
| E_{th} | Theoretical expected elastic modulus of the composite |
| F | Force in bending test |
| I | Discharge current in the secondary circuit of electro discharge sintering |
| I_{max} | Maximum discharge current in the secondary circuit of electro discharge sintering |
| L | Support span in bending test |
| R | Electrical resistance of the secondary circuit of electro discharge sintering calculated at maximum discharge current |
| T | Testing temperature |
| V | Electrical potential at the secondary circuit of electro discharge sintering |
| V_W | Volume concentration of tungsten |
| b | Width of the bending specimen |
| δ | Mid span deflection of bending specimen during bending test |
| ε_f | Flexural strain at the outermost fibre of the bending specimen |
| η_{eff} | Efficiency of electro discharge sintering |
| $\sigma_{f,steel}$ | Yield strength of Eurofer 97 taken from EUROfusion MPH |
| $\sigma_{f,W}$ | Yield strength of bulk-W taken from ITER MPH |

| | |
|-------------------|---|
| $\sigma_{f,th}$ | Theoretical yield strength of composite |
| σ_f | Flexural stress at the outermost fibre of the bending specimen |
| α_{th-APS} | Theoretical secant coefficient of thermal expansion of plasma sprayed composite |
| α_{th-SPS} | Theoretical secant coefficient of thermal expansion of sintered composite |
| α_W | Secant coefficient of thermal expansion of bulk-W taken from ITER MPH |
| α_{steel} | Secant coefficient of thermal expansion of Eurofer 97 taken from EUROfusion MPH |
| $c_{p,W}$ | Specific heat capacity of bulk-W taken from ITER MPH |
| $c_{p,steel}$ | Specific heat capacity of Eurofer 97 taken from EUROfusion MPH |
| $c_{p,th}$ | Theoretical specific heat capacity of composite |
| ρ_W | Density of tungsten |
| ρ_{steel} | Density of steel |
| λ_W | Thermal conductivity of bulk-W taken from ITER MPH |
| λ_{steel} | Thermal conductivity of Eurofer 97 taken from EUROfusion MPH |
| λ_{th} | Theoretical thermal conductivity of the composite |

List of nomenclatures specific to this thesis:

| | |
|---------------|--|
| Splats | Flattened solidified molten droplets in thermal sprayed materials |
| 25W | Tungsten steel composition with 25 vol% W |
| 50W | Tungsten steel composition with 50 vol% W |
| 75W | Tungsten steel composition with 75 vol% W |
| JUDITH 2 | Jülich Divertor Test Facility in the Hot cells, an electron beam facility at Forschungszentrum Jülich GmbH |
| Layers of FGM | refers to the individual composites that constitute a functionally graded material |
| APS-FGM | Functionally graded material composed of atmospheric plasma sprayed composites |

| | |
|-------------|---|
| SPS-FGM | Functionally graded material composed of spark plasma sintered composites |
| 3-layer FGM | Functionally graded material composed of 25W, 50W and 75W composites |
| 2-layer FGM | Functionally graded material composite of 25W, and 50W composites |

List of Figures

Figure 1.1 Schematic representation of a tokamak machine [5] 1

Figure 1.2 Schematic representation of a future fusion reactor showing: A) vacuum vessel, B) plasma, C) heat fluxes to breeding blanket, D) breeding blanket, and E) electricity generation [6] 2

Figure 1.3 Cross-sectional cut of an EU DEMO reactor showing two conceptual breeding blanket concepts: a) Helium Cooled Pebble Bed (HCPB) and b) Water Cooled Lead Lithium (WCLL); along with a rudimentary representation of a FW (adapted from [7,10,11])..... 3

Figure 1.4 a) Photograph of forged W-bar manufactured by Plansee SE, Austria, b) Transversal grain orientation, and c) Longitudinal grain orientation 4

Figure 1.5 Microstructure of etched Eurofer 97; a) Light microscopy micrograph [23] and b) Scanning electron microscopy (SEM) micrograph showing precipitates [24]..... 5

Figure 1.6 Concept of joining W and steel using FGM interlayer to produce a graded FW 11

Figure 2.1 a) Photograph of the APS setup, and b) its schematic representation 20

Figure 2.2 a) Porosity and oxide content and b) W and steel content of the APS composites (*Note: image analysis was not able to capture Fe_xCr_yO content in 75W composite*) 22

Figure 2.3 Microstructure of the produced APS composites of composition: a), b) 25W, c), d) 50W, e), f) 75W 23

Figure 2.4 a) Photograph of EDS setup and b) schematic representation of EDS setup..... 24

Figure 2.5 a) An exemplary discharge current and voltage profile for one sintering trial and b) corresponding punch load and its displacement..... 26

Figure 2.6 a) Effect of discharge energy when sintered at 388 MPa, and b) Effect of sintering pressure when sintered at 80 kJ on the residual porosity and discharge current for two 25W combinations 28

Figure 2.7 Microstructure of the composites sintered at 388 MPa, 80 kJ: a), b) 25W₁₀₋₃₀+75S₄₀₋₁₀₀, and c), d) 25W₃₀₋₆₀+75S₄₀₋₁₀₀ 28

Figure 2.8 a) Effect of discharge energy when sintered at 388 MPa and b) Effect of sintering pressure when sintered at 80 kJ on the residual porosity and discharge current for two 50W combinations 29

Figure 2.9 Microstructure of composites sintered at 388 MPa, 80 kJ: a), b) 50W₃₀₋₆₀+50S₄₀₋₁₀₀ and c), d) 50W₆₀₋₉₀+50S₄₀₋₁₀₀ 30

| | |
|--|----|
| Figure 2.10 Effect of various combinations of PSF for 75W composite on the obtained residual porosity and maximum discharge current..... | 31 |
| Figure 2.11 Microstructure of poorly consolidated 75W composites sintered at 388 MPa, 80 kJ: a) 75W ₈₀₋₉₀ +25S ₄₀₋₁₀₀ , b) 75W ₆₀₋₉₀ +25S ₄₀₋₁₀₀ , c) 75W ₃₀₋₆₀ +25S ₄₀₋₁₀₀ and d)75W ₁₀₋₃₀ +25S ₄₀₋₁₀₀ | 31 |
| Figure 2.12 Cross-sectional micrographs taken at three different locations for: a) 25W and b) 75W composite sintered at 388 MPa, 80 kJ showing the effect of local inhomogeneity | 32 |
| Figure 2.13 a) Photograph and b) schematic representation of the lab scale SPS setup | 33 |
| Figure 2.14 a) An exemplary current and voltage profile and b) the corresponding temperature and punch displacement for a typical sintering trial (<i>Note: data taken from an experiment of 25W₁₀₋₃₀+75S₁₀₋₂₀ sintered at 900 °C, 5 min, 50 MPa; pyrometer can only measure >400 °C</i>)..... | 33 |
| Figure 2.15 a) Effect of sintering temperature and b) Effect of sintering pressure on the residual porosity of 25W composites sintered at two different thicknesses..... | 35 |
| Figure 2.16 Microstructure of a 3 mm thick 25W composite sintered at 50 MPa, 5 min with three sintering temperatures: a), b) 900 °C, c) 1000 °C, and d) 1100 °C..... | 36 |
| Figure 2.17 a) Microstructure of optimized 25W composite, and b) Submicron-scale pores inside its steel matrix | 36 |
| Figure 2.18 Microstructure of a 3 mm thick 50W ₁₀₋₃₀ +50S ₁₀₋₂₀ composite sintered at 50 MPa, 5 min with three sintering temperatures: a), b) 900 °C, c) 1000 °C, and d) 1100 °C..... | 37 |
| Figure 2.19 a) Effect of sintering temperature on the residual porosity, when sintered at 50 MPa, 5 min, for two combinations 50W ₁₀₋₃₀ +50S ₁₀₋₂₀ and 50W ₁₀₋₃₀ +50S ₃₋₁₃ , b) Effect of sintering time and pressure on the residual porosity and IMC for a 0.75 mm thick 50W ₁₀₋₃₀ +50S ₃₋₁₃ composite sintered at 1000 °C..... | 38 |
| Figure 2.20 Microstructure of 50W ₁₀₋₃₀ +50S ₃₋₁₃ composite sintered at 1000 °C, 5 min with pressure: a) 50 MPa and b) 125 MPa | 38 |
| Figure 2.21 a) Residual porosity and b) IMC for a 75W ₁₀₋₃₀ +S ₃₋₁₃ combination co-sintered at different temperatures for four sintering time | 39 |
| Figure 2.22 a) Residual porosity and b) IMC for a 75W ₃₀₋₆₀ +S ₁₀₋₂₀ combination co-sintered at different temperatures for three sintering time | 40 |
| Figure 2.23 Microstructure of two 75W combinations sintered at 1000 °C, 5 min: a), b) 75W ₁₀₋₃₀ +25S ₃₋₁₃ and c), d) 75W ₃₀₋₆₀ +25S ₁₀₋₂₀ | 40 |
| Figure 3.1 Microstructure of heat-treated plasma sprayed 25W composite..... | 45 |
| Figure 3.2 EDX elemental map of an oxide film present in heat-treated 25W composite (<i>spatial location of Region-A is marked in Figure 3.1</i>) | 45 |

| | |
|--|----|
| Figure 3.3 EDX elemental map of an area consisting of IMC and steel, enclosed inside an oxide film present in heat-treated 25W composite (<i>spatial location of Region-B is marked in Figure 3.1</i>)..... | 46 |
| Figure 3.4 EDX analysis map of steel in between a W-splat and an oxide film in heat-treated 25W composite (<i>spatial location of Region-C is marked in Figure 3.1</i>)..... | 47 |
| Figure 3.5 EDX elemental map at an interface between a W-splat and a steel-splat in heat-treated 25W composite (<i>spatial location of Region-D is marked in Figure 3.1</i>)..... | 48 |
| Figure 3.6 Microstructure of 75W after heat treatment with some steel-splats containing IMC | 49 |
| Figure 3.7 Microstructures attained through FIB cuts showing different phases in steel: a) 25W, b) 50W, and c) 75W composite. The micrograph also indicates EDX spectral points marked in red, see Table 3.3 | 50 |
| Figure 3.8 Microstructure of sintered composites after heat treatment: a) 25W, b) 50W, and c) 75W | 51 |
| Figure 3.9 Elastic modulus: a) plasma sprayed [50], and b) sintered composites | 52 |
| Figure 3.10 Flexural stress-strain profile of plasma sprayed composites: a) 25W, b) 50W and c) 75W (<i>Note: the testing was not performed at 550 °C, and the tests on the 75W at 20 °C and 100 °C were not possible due to its extremely brittle behaviour</i>)..... | 55 |
| Figure 3.11 Flexural stress-strain profile of sintered composites: a) 25W, b) 50W and c) 75W (<i>Note: the tests on the sintered 25W composite above 300 °C had to be stopped at 8 % flexural strain, as it was the maximum limit of the testing machine</i>) | 56 |
| Figure 3.12 Flexural yield stress: a) plasma sprayed composites [11], and b) sintered composites (<i>Note: mea. refers to measured value and th. refers to theoretical expected value</i>)..... | 56 |
| Figure 3.13 Density measured by Archimedes' principle and theoretical expected density, along with the calculated relative density for: a) plasma sprayed composite, and b) sintered composites..... | 57 |
| Figure 3.14 a) Relative change in length for plasma sprayed composites, b) Secant CTE for as-sprayed composites and their respective theoretical expected values (<i>Note: mea. refers to measured value and th. refers to theoretical expected value</i>)..... | 59 |
| Figure 3.15 a) Relative change in length for sintered composites, b) Secant CTE for as-sintered composites and their respective theoretical expected values (<i>Note: mea. refers to measured value and th. refers to theoretical expected value</i>) | 60 |

| | |
|---|----|
| Figure 3.16 Temperature dependent specific heat capacity response of: a) plasma sprayed composites in their as-sprayed state, b) sintered composites in their as-sintered state (<i>Note: mea. refers to measured value and th. refers to theoretical expected value</i>)..... | 61 |
| Figure 3.17 Temperature dependent thermal conductivity of: a) plasma sprayed composites in their as-sprayed state, b) sintered composites in their as-sintered state | 63 |
| Figure 3.18 Temperature dependent thermal conductivity of: a) plasma sprayed composites, b) sintered composites after heat treatment..... | 64 |
| Figure 4.1 Results of co-sintering of 75W powder and bulk-W for: a) 75W ₃₀₋₆₀ +25S ₁₀₋₂₀ , and b) 75W ₁₀₋₃₀ +25S ₃₋₁₃ (<i>Nomenclature: ✓ represents the trial where the 75W and bulk-W remain attached after removing the stack out of the die and even after cutting it for metallographic investigation, ✕ represents the trial where the 75W and bulk-W fall apart/delaminate</i>)..... | 67 |
| Figure 4.2 Bonding seam between the sintered 75W ₃₀₋₆₀ +25S ₁₀₋₂₀ and bulk-W for the co-sintering performed at 1000 °C, 125 MPa, 5 min | 68 |
| Figure 4.3 Bonding seam between 75W ₃₀₋₆₀ +25S ₁₀₋₂₀ and bulk-W at different regions; co-sintering performed at 1000 °C, 125 MPa, 5 min | 68 |
| Figure 4.4 Delaminated surface of bulk-W for the co-sintering trial of 75W ₃₀₋₆₀ +25S ₁₀₋₂₀ performed at 1300 °C for 5 min..... | 69 |
| Figure 4.5 Cross-sectional micrographs of co-sintering of bulk-W and 75W ₁₀₋₃₀ +25S ₃₋₁₃ ; a) Bonding seam showing macrocracks for the co-sintering performed at 1400 °C, 0 min, b) Microstructure of bulk-W after the co-sintering at 1400 °C, 0 min, c) and d) Co-sintering performed at 1400 °C, 5 min showing microcracks inside IMC. e) Microstructure of the completely recrystallized bulk-W, f) Macrocracks in bulk-W as well as in 75W for a co-sintering performed at 1400 °C, 10 min..... | 70 |
| Figure 4.6 Delaminated surface of bulk-W for the trial of 75W ₁₀₋₃₀ +25S ₃₋₁₃ performed at 1200 °C, 5 min..... | 71 |
| Figure 4.7 a) Cross-section of the W-steel graded joint featuring a 3-layer sintered FGM interlayer; b) Bonding seam between bulk-W and 75W, c) Transition between 75W and 50W, d) Transition between 50W and 25W, and e) Bonding seam between 25W and bulk-steel | 72 |
| Figure 4.8 a) Cross-section of the W-steel graded joint featuring a 2-layer sintered FGM interlayer; Interface of b) bulk-W and 50W showing two regions of interest | 73 |
| Figure 4.9 Schematic representation of the produce; a) Setup for current-assisted diffusion bonding, b) Temperature, pressure vs time profile for joining | 74 |

| | |
|---|----|
| Figure 4.10 Cross-sectional micrographs after joining 75W and bulk-W at 1000 °C, 30 min, showing two random locations with insufficient bonding | 75 |
| Figure 4.11 Cross-sectional micrographs after joining 75W and bulk-W with the following joining parameters: a), b) 1100 °C, 30 min and c), d) 1200 °C, 30 min..... | 76 |
| Figure 4.12 a) Cross-sectional micrograph of 75W bonded to bulk-W with a V-filler; joining performed at 900 °C, 30 min, b) Bonding seam between V-filler and 75W showing the formation of vanadium carbide with steel-splat of 75W..... | 77 |
| Figure 4.13 Interface of W-V for the joining performed at: a) 800 °C, 60 min and b) 900 °C, 30 min | 77 |
| Figure 4.14 Bonding seam between 75W and 50W; joining performed at 900 °C, 30 min..... | 79 |
| Figure 4.15 Bonding seam between 75W and 50W; joining performed at 900 °C, 30 min..... | 79 |
| Figure 4.16 Bonding seam between 75W and 50W; joining performed at 1000 °C, 30 min..... | 80 |
| Figure 4.17 Bonding seam between 50W and 25W; joining performed at 1000 °C, 30 min..... | 80 |
| Figure 4.18 Bonding seam between 25W and bulk-steel; a) edge of the joint, performed at 800 °C, 60 min, b) near the edge of a joint, performed at 900 °C, 30 min, c) centre of the joint, performed at 1000 °C, 30 min, d) near the edge of the joint performed at 1000 °C, 30 min..... | 82 |
| Figure 4.19 Cross-section of the W-steel joint featuring a 3-layer plasma sprayed FGM interlayer..... | 82 |
| Figure 4.20 a) Cross-section of a W and steel joint with 0.3 mm thick V interlayer, b) W-V bonding interface, c) V-steel bonding seam (<i>Note: the darker marks on V are not pores/defects, but scratch marks coming from the inappropriate grinding steps used during the metallographic sample preparation</i>)..... | 83 |
| Figure 4.21 a) Cross-sectional micrograph of a directly bonded W-steel joint b) W-steel bonding seam c) W-steel bonding interface showing IMC and a ferrite region d) Grain structure of bulk-W after joining e) Martensitic structure in bulk-steel after joining..... | 85 |
| Figure 5.1 Photograph of the prepared samples (joints); top polished surface is W-tile | 87 |
| Figure 5.2 Schematic illustration of the testing procedure of HHF benchmark test, along with respective photographs | 88 |
| Figure 5.3 Two sets of Cu-modules mounted inside the HHF facility (<i>Note: The experimental campaign also included other W-steel joining concepts which are not relevant to this thesis; V(0.8) joint, Ti(0.3, 0.8, 1.5) was W-Ti-steel joint of different thicknesses of Ti, W(wire)-steel was a conceptual joint</i>) | |

| | | |
|--------------------|--|-----|
| | <i>consisting of W-wires bonded to steel, W(additive)-steel was an additive manufactured W bonded directly to steel)</i> | 90 |
| Figure 5.4 | a) Schematic of electron beam pattern hitting the actively cooled component, b) Schematic representation of cyclic steady state thermal loading..... | 90 |
| Figure 5.5 | An exemplary IR image showing the surface temperature of W-tiles for a screening@1.5MW..... | 91 |
| Figure 5.6 | Macroscopic image of all the joints before and after the HHF testing (<i>Note: for the sample labelling please refer to Table 5.1</i>) | 92 |
| Figure 5.7 | Steady-state surface temperature of W-tile over cumulative number of cycles for different samples of a) V-3.FG-APS, b) V(0.3), and c) V(1.5) joints. (<i>Note: A, B, C represents sample label</i>)..... | 93 |
| Figure 5.8 | Steady state surface temperature of W over cumulative number of cycles for different samples of a) Direct, b) 2.FG-SPS, and c) 3.FG-SPS joints. (<i>Note: A, B, C ... represents sample label</i>) | 94 |
| Figure 5.9 | Lifetime of various W-steel joints (<i>Note: ✖ represents the lifetime of each sample and ▨ represents the scatter band</i>) | 95 |
| Figure 6.1 | Macroscopic examination of V-3.FG-APS joints (before and after HHF testing)..... | 97 |
| Figure 6.2 | Cross-section of the failed V-3.FG-APS joint (sample-A) with five marked regions (Region-1 to -5), which were further analysed (see Figure 6.3 to Figure 6.5) | 97 |
| Figure 6.3 | a) Micrograph of Region-1, b) Micrograph of Region-2 (their spatial locations are marked in Figure 6.2), c) Close-up of the W-V bond seam, d) Three modes of failure at the W-V bond seam | 98 |
| Figure 6.4 | a) Micrograph of Region-3, b) Micrograph of Region-4 showing failure inside 75W layer (their spatial locations are marked in Figure 6.2) | 99 |
| Figure 6.5 | a) Micrograph of Region-5 (its spatial location is marked in Figure 6.2), b) Close-up of the W-V bond seam | 99 |
| Figure 6.6 | Cross-section of the failed V-3.FG-APS joint (sample-C) | 99 |
| Figure 6.7 | Microstructure of individual FGM layers of the failed V-3.FG-APS joint; a) 25W, b) 50W, c) 75W | 100 |
| Figure 6.8 | a) Cross-section of the failed V-3.FG-APS joint (sample-B) with two marked regions (Region-1 and -2), b) Region-1 showing cracks inside the 75W, c) Region-2 showing macroscale vacancy in V-filler | 101 |
| Figure 6.9 | Macroscopic examination of 2.FG-SPS joints (before and after the HHF testing)..... | 102 |
| Figure 6.10 | Cross-section of the failed 2.FG-SPS joint (sample-H) with two marked regions (Region-1 and -2); these regions were closely analysed as shown in Figure 6.11 and Figure 6.12 (<i>Note: it is a stitched image and thus the stitching lines must be ignored</i>)..... | 103 |

| | |
|---|-----|
| Figure 6.11 a) Micrograph of Region-1 (its spatial location in marked in Figure 6.2); close-up of the fracture surface of: b) delaminated W-tile side, c) delaminated 50W side | 103 |
| Figure 6.12 a) Micrograph of Region-2 (its spatial location in marked in Figure 6.10); close-up micrograph showing the failure pattern near the W-50W bond line at four sites: b) [A], c) [B], d) [C], e) [D] (<i>Note: during the metallographic preparation (grinding step), some materials might get trapped inside the gaps, termed as smeared material, as can be seen in b) and c). In reality, this gap must be vacant and therefore, these must be ignored</i>) | 104 |
| Figure 6.13 a) Delaminated surface of W-tile, b) its close up BSE micrograph showing the topography of W and IMC in purple and pink magnified snippet box; the yellow box is the EDX scan area marked as “EDX-map” along with locations of four EDX point analyses marked as “Spectrum-1 to -4”, c) W spectrum map, d) Fe spectrum map, e) Cr spectrum map | 106 |
| Figure 6.14 a) Micrograph of the delaminated W-tile positioned at 45° tilt, b) its close-up | 106 |
| Figure 6.15 a) Micrograph of the delaminated 50W surface, b) The close-up SEM micrograph marked with yellow box showing the EDX scan area marked as “EDX-map” along with the spatial locations of three EDX point analyses marked as “Spectrum-1 to -3”, whose elemental compositions are provided in Table 6.2, c) W spectrum map, d) Fe spectrum map, e) Cr spectrum map..... | 107 |
| Figure 6.16 Macroscopic examination of 3.FG-SPS joints (before and after the HHF testing) | 108 |
| Figure 6.17 Cross-section of the failed 3.FG-SPS joint (sample C) showing four regions of interest (region-1 to region-4) for further examination..... | 109 |
| Figure 6.18 Micrograph showing the delamination occurring at the edge of the joint for two regions: a) Region-1 and b) Region-2 (<i>their spatial locations are marked in Figure 6.17</i>)..... | 109 |
| Figure 6.19 a) Micrograph of Region-3, b) SEM micrograph of Region-4 (<i>their spatial locations are marked in Figure 6.17</i>); Close-up showing the failure pattern near the W-75W bond line at four sites: b) [A] showing fracture inside steel, c) [B] showing fracture inside steel and W-particle, d) [C] showing fracture at IMC-steel interface, e) [D] showing fracture at W-IMC interface (<i>Note: as seen in d), some smeared material gets trapped inside the gap and these must be ignored</i>)..... | 110 |
| Figure 6.20 a) SE micrograph of the delaminated W-tile, b) BSE micrograph, c) SE micrograph of a location showing EDX-spectrum mapping and marked points for individual elemental composition analyses, d) its BSE micrograph, e) W spectrum map, f) Fe spectrum map, g) Cr spectrum map (<i>Note: the dark black spots in b) are just dust particles</i>). | 111 |

| | |
|--|-----|
| Figure 6.21 a) SE micrograph of delaminated 75W side, b) BSE micrograph of the same..... | 112 |
| Figure 6.22 Macroscopic examination of Direct joints (before and after the HHF testing)..... | 113 |
| Figure 6.23 a) Region-1 representing the SEM micrograph of location at the edge of the direct joint. b) Delamination of the W-tile at the edge of the joint, c) Close-up of the location showing the delamination pattern (<i>Note: the dark spots and patches in the SEM micrograph are just external dust and contamination</i>)..... | 114 |
| Figure 6.24 Cross-section of the failed direct joint (sample A) with four regions of interest for further analysis..... | 114 |
| Figure 6.25 a) Region-2 represents the micrograph of a location at the centre of the direct joint. b) Close-up micrograph showing IMC, c) Close-up micrograph of the reaction layer showing a mixture of IMC inside the ferritic phase..... | 115 |
| Figure 6.26 a) Region-3 representing the micrograph of location just below the reaction layer showing ferritic phase, b) Region-4 further below showing the martensitic phase | 116 |
| Figure 6.27 Delaminated surface of W-tile with four marked regions (Region-1 to -4) for further investigation..... | 116 |
| Figure 6.28 a) Micrograph of Region-1 (<i>its location is marked in Figure 6.27</i>), b) Close-up of the pyramidal pattern sticking on to the W-tile and the corresponding EDX spectrum map area, c) W spectrum map, d) Fe spectrum map, e) Cr spectrum map, f) O spectrum map, g) C spectrum map..... | 117 |
| Figure 6.29 a) SE micrograph of Region-2 (<i>its location is marked in Figure 6.30</i>) and the corresponding EDX spectrum map area, b) It's BSE micrograph for better visualization , c) W spectrum map, d) Fe spectrum map, e) Cr spectrum map (<i>Note: the O and C spectrum maps were not relevant and not shown</i>) | 118 |
| Figure 6.30 a) Micrograph of Region-3 (corner of the delaminated W-tile) showing contamination, b) Micrograph of Region-4 showing microcracks in W-tile (<i>their locations are marked in Figure 6.27</i>)..... | 118 |
| Figure 6.31 Micrograph of the surface of delaminated steel side with a marked Region-1 for further investigation..... | 119 |
| Figure 6.32 a) SE micrograph of Region-1 (<i>its spatial location is marked in Figure 6.31</i>), b) Close-up micrograph of one site and the corresponding EDX spectrum area map marked with yellow box, c) W spectrum map, d) Fe spectrum map, e) Cr spectrum map, f) O spectrum map, g) C spectrum map | 120 |
| Figure 7.1 CTE distribution for a V-3.FG-APS joint..... | 123 |

Figure 7.2 Geometry and temperature distribution of a conceptual FW panel considering a V-3.FG-APS joint with a 3 mm thick W-tile and coolant flowing at 300 °C through steel..... 126

List of Tables

| | |
|---|----|
| Table 1.1 Advantageous and disadvantageous properties of W | 4 |
| Table 1.2 Chemical composition of main alloying elements of Eurofer 97 in wt% | 5 |
| Table 1.3 Direct joining of W and steel performed as of now | 8 |
| Table 1.4 Joining of W and steel using V interlayer performed as of now | 9 |
| Table 1.5 Joining of W and steel using Ti interlayer performed as of now | 10 |
| Table 1.6 Plasma spraying of W on steel substrate performed as of now | 12 |
| Table 1.7 W/steel-composites manufactured via advanced powder metallurgy techniques | 15 |
| Table 1.8 Overview of various HHF on W-steel small-scale mock-ups; T_{surf} represents the approximate surface temperature of W | 16 |
| Table 2.1 PSF and manufacturer information of powders used for the APS process | 20 |
| Table 2.2 Chemical composition of the feedstocks used for the APS process..... | 21 |
| Table 2.3 Optimized feed rate and spraying distance for the APS process..... | 22 |
| Table 2.4 PSF and manufacturer's information of powders used for the EDS process | 25 |
| Table 2.5 Chemical composition of the powders used for the EDS process..... | 25 |
| Table 2.6 Sintering parameters of the experimental trials for sintering 25W composite..... | 27 |
| Table 2.7 Sintering parameters of the experimental trials for sintering 50W composite..... | 29 |
| Table 2.8 Sintering parameters of the experimental trials for sintering 75W composite..... | 30 |
| Table 2.9 PSF and manufacturer's information of the powders used for the SPS process | 34 |
| Table 3.1 Element composition at various points of interest corresponding to Figure 3.3 | 46 |
| Table 3.2 Element composition at various points of interest corresponding to Figure 3.4 | 48 |
| Table 3.3 Elemental composition at points corresponding to the red markings in Figure 3.7..... | 50 |
| Table 3.4 Inferences on the elastic modulus of plasma sprayed and sintered composites | 53 |
| Table 3.5 Inferences on the flexural properties of plasma sprayed and sintered composites | 54 |
| Table 3.6 Summarized overview of the properties of plasma sprayed and sintered composites | 65 |
| Table 4.1 Joining trials for bonding bulk-W with plasma sprayed 75W | 75 |
| Table 4.2 Joining trials for bonding bulk-W and 75W with V-foil and observations | 76 |
| Table 4.3 Joining trials for bonding 75W, 50W and 25W together and their observations | 78 |
| Table 4.4 Joining trials for bonding 25W and bulk-steel and their observations | 81 |
| Table 5.1 Nomenclature and thickness of various W-steel joints tested | 89 |

| | |
|--|-----|
| Table 5.2 Testing protocol for cyclic steady-state thermal loading | 91 |
| Table 5.3 Summary of the HHF testing of various joints..... | 96 |
| Table 6.1 Element composition at various locations corresponding to Figure 6.13 | 106 |
| Table 6.2 Element composition at various locations corresponding to Figure 6.15 | 107 |
| Table 6.3 Element composition at various locations corresponding to Figure 6.20 | 112 |
| Table 6.4 Element composition at various points of interest corresponding to Figure 6.25 | 115 |
| Table 7.1 Assessment of FGM/individual sublayers based on important criteria..... | 121 |
| Table 7.2 Correlation of HHF testing (see Figure 5.7 to 5.9) and conceptual FW loaded with 1 MW/m ² , representing the maximum expected heat load scenario for a future fusion reactor (T _{surf-HHF} is the average surface temperature of all samples in the HHF testing) | 127 |
| Table 7.3 Closing remark considering all available existing approaches..... | 129 |

1 Introduction

The world's electricity demand is increasing rapidly and is projected to reach ~10 TW in the second half of the 21st century [1]. Therefore, clean energy sources must be considered to meet future demand and limit CO₂ emissions. Presently, 62 % of global electricity generation comes from fossil fuels, while only 38 % comes from clean energy sources, such as wind, solar, nuclear fission, and hydro energy [2]. Despite wind and solar being attractive options, they do not provide stable electricity to the electrical grid, and fossil fuels currently fill these fluctuations. Nuclear fission energy is also viable, but public acceptance and safe disposal of nuclear waste are the two significant challenges. Nuclear fusion energy, if commercially available in the near future, could fill this gap and strengthen global energy security [3].

1.1 Nuclear fusion

The deuterium-tritium (D-T) reaction is the most efficient fusion reaction that releases 17.58 MeV energy, which is carried away by a helium (⁴He) nucleus and a neutron (n) in the form of particle energy [4].



For fusion to occur, D and T nuclei must overcome Coulomb repulsion, which requires them to be in a plasma state, typically at a temperature of 10⁸–10⁹ K. Furthermore, this plasma must be confined to ensure a sufficient reaction rate. Tokamak is the most promising device for a commercial fusion power plant that can confine the plasma, as schematically represented in Figure 1.1 [4]. It confines the plasma (charged particles) using twisted magnetic fields in a doughnut shape called a torus.

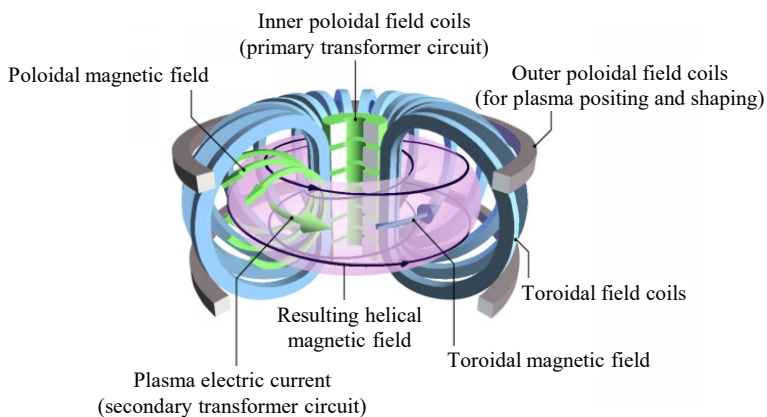


Figure 1.1 Schematic representation of a tokamak machine [5]

1.2 Future fusion reactor

A breakthrough in fusion research would be the operation of the largest experimental tokamak called ITER; it will not produce electricity but will pave the way for future fusion reactors. The EUROfusion consortium aims to commission a future fusion reactor in the second half of the 21st century, known as the DEMONstration fusion power plant (DEMO), designed to generate 300–500 MW electricity [1]. The working principle of such a reactor is schematically described in Figure 1.2. The D and T are injected into the torus for the subsequent D-T reaction. The heat generated is then absorbed by coolant flowing through the breeding blankets, which drives the steam turbine to generate electricity.

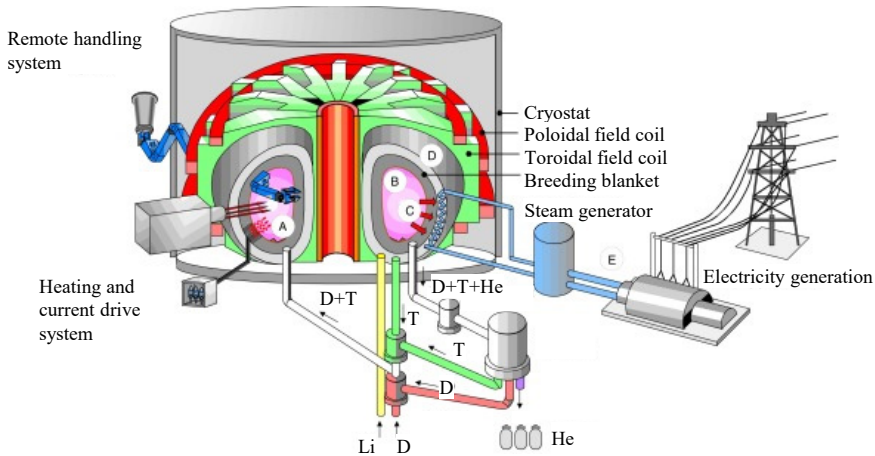
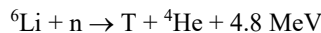


Figure 1.2 Schematic representation of a future fusion reactor showing: A) vacuum vessel, B) plasma, C) heat fluxes to breeding blanket, D) breeding blanket, and E) electricity generation [6]

Apart from generating electricity, the reactor must also breed T to make it self-sufficient. This is because D is abundant in Earth's oceans, but T is not naturally occurring. The breeding can be done by using breeding blankets containing Lithium-6 (${}^6\text{Li}$), as mentioned below:



1.3 First wall

Plasma-facing components (PFCs) are the essential components that are in the direct vicinity of the hot plasma; they must withstand high particle and heat loads. The two PFCs are the first wall (FW), covering most of the inside of the torus, and the divertor, covering the bottom of the torus, as shown in Figure 1.3. The FW is assembled in modules to cover the entire area. The complete module assembly—consisting of complex cooling channels, shield block, support structures, T breeding unit, and other auxiliary systems—is called a breeding blanket or a breeding blanket module. A recent assessment study has emphasized focusing on two conceptual breeding blanket designs for EU DEMO, schematically depicted in Figure 1.3 [7,8].

In principle, the FW is basically the blanket's plasma-facing side (highlighted in orange), which can be represented in a simple rudimentary sketch, as shown at the bottom in Figure 1.3 [7].

The heat fluxes at the FW come from the radiative heat load and particle flux load. It is expected that the peak heat flux on the FW during normal steady-state operation of the reactor will not exceed 1 MW/m^2 [7,9]. These heat fluxes would hit the FW in a thermocycling fashion due to the cyclic nature of plasma pulses.

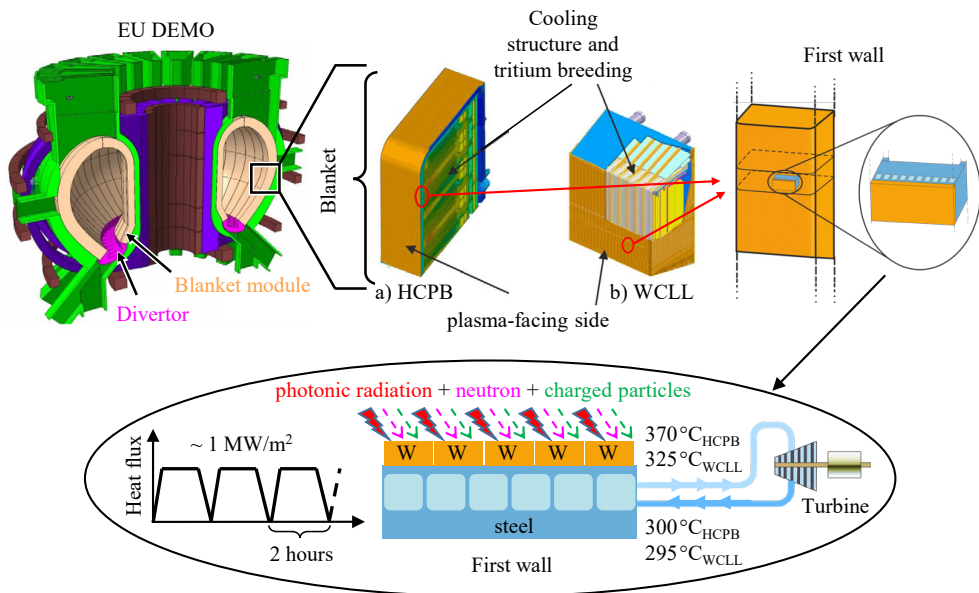


Figure 1.3 Cross-sectional cut of an EU DEMO reactor showing two conceptual breeding blanket concepts: a) Helium Cooled Pebble Bed (HCPB) and b) Water Cooled Lead Lithium (WCLL); along with a rudimentary representation of a FW (adapted from [7,10,11])

1.4 Materials for first wall

The material directly facing the plasma is called armour material, and the inner structure is made of structural material. Currently, 2 mm thick tungsten is considered a suitable armour [10], and reduced activation ferritic/martensitic steel is considered a suitable structural material [12], as depicted in Figure 1.3.

1.4.1 Tungsten

Tungsten (W) is a metal that has the highest melting point ($\sim 3400^\circ\text{C}$), meaning it can withstand high heat load and has a high creep resistance. Its industrial application dates back to the 19th century: the 1850s, when W was used in Mushet steel [13]. Its conventional industrial production is explained briefly: First, the W oxides are extracted from the W ores, which are then reduced under H_2 atmosphere to get W powder. The powder is then compacted under 200–400 MPa pressure to achieve 55–65 % green density. This is then sintered under flowing H_2 atmosphere at 2000–2500 $^\circ\text{C}$ to achieve a relative density of 92–98 %. To get a dense W of

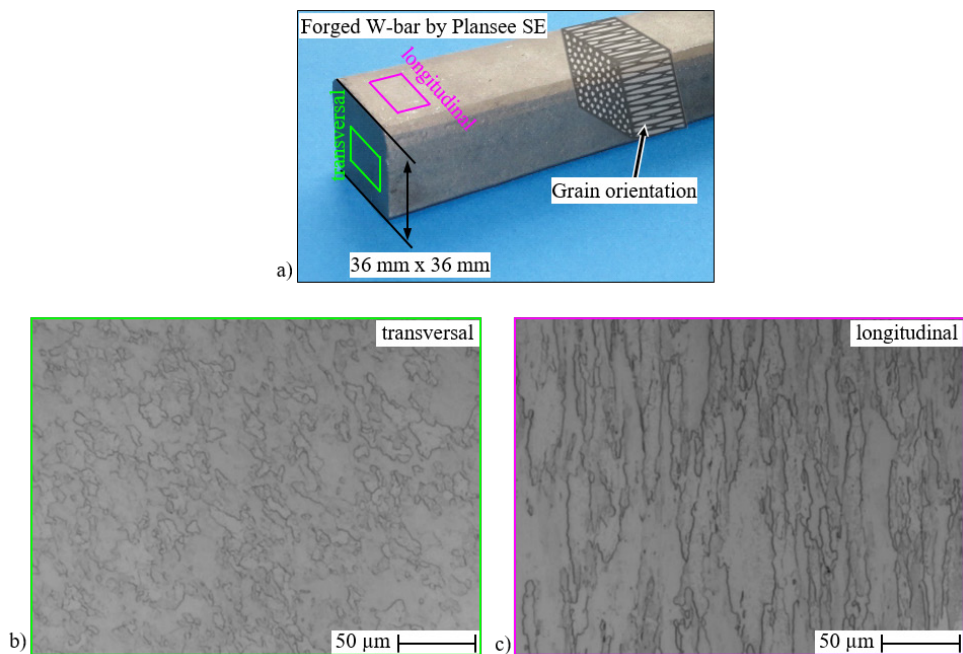


Figure 1.4 a) Photograph of forged W-bar manufactured by Plansee SE, Austria, b) Transversal grain orientation, and c) Longitudinal grain orientation

desired properties, the sintered compact undergoes multiple stages of hot forming, above its recrystallization temperature, at 1500–1700 °C with intermediate recovery (stress relief annealing) and recrystallization (annealing) steps. Then it undergoes cold forming at still high temperature, but below its recrystallization temperature, to induce the necessary strain hardening. Finally, it undergoes one last recovery step to obtain the final forged product [13,14]. A forged W-bar, manufactured by Plansee SE, Austria, was used in this thesis. For simplicity, it is referred to as bulk-W. Its microstructure is shown in Figure 1.4 [15]. The advantageous and disadvantageous properties of W are summarized in Table 1.1.

Table 1.1 Advantageous and disadvantageous properties of W

| Advantages | Disadvantages |
|--|---|
| - high elastic modulus (~400 GPa) | - high ductile-to-brittle transition temperature (depending on mechanical, structural and chemical conditions) [13] |
| - high tensile strength (~1400 MPa depending on manufacturing method [16]) | - recrystallization embrittlement [18] |
| - high thermal conductivity (~170 W/m·K) | |
| - low erosion under plasma loads [17] | |
| - short activation decay time after exposure to neutron irradiation (n flux coming from D-T reaction) [17] | |

1.4.2 Reduced activation ferritic/martensitic steel

The research on ferritic/martensitic steels, consisting of 9–12 wt% Cr, 1–2 wt% Mo with appropriate amounts of C, V, W, Ni, Nb, etc., dates back to 1970s for their application in fast breeder fission reactors. Later on, they were investigated for fusion reactors [19]. The research started in the 1980s in the USA, Japan and EU to develop steel with a low activation level. This steel is termed reduced activation ferritic/martensitic (RAFM) steel. Finally, in 1997, a modified DIN X10CrWMoVNb9-2 steel called Eurofer 97 was developed in the EU by replacing/removing high activation elements, such as Mo, Nb, Ni, etc. [20]. The chemical composition of the latest developed Eurofer 97 is provided in Table 1.2 [21]. Eurofer 97 has many beneficial properties: resistance to neutron irradiation damage, creep resistance, high temperature strength, high toughness, and its activation dose rate (neutron activation) to less than the recycling limit after 100 years of storage [21].

Table 1.2 Chemical composition of main alloying elements of Eurofer 97 in wt%

| | C | Cr | Mn | W | Ta | V | N ₂ |
|-----|------|------|------|------|------|------|----------------|
| min | 0.09 | 8.50 | 0.20 | 1.00 | 0.10 | 0.15 | 0.015 |
| max | 0.12 | 9.50 | 0.60 | 1.20 | 0.14 | 0.25 | 0.045 |

In principle, Eurofer 97 is martensitic steel produced by following a specific heat treatment procedure. First, the steel undergoes austenitization annealing at 980 °C\ 30 min followed by immediate quenching, producing quenched martensite having a hardness of ~400 HV30. Second, it is tempered by heating at 760 °C\ 90 min and allowing it to cool down, producing tempered martensite [20]. The tempering step decreases its hardness to 200–240 HV30, resulting in better toughness [21]. The tempering forms precipitate, predominantly M₂₃C₆ carbide and MX carbonitride. The M₂₃C₆ is rich in Cr, Fe, and W, and is found in a size range 30–300 μm. The MX feature rich TaC and VN phases with size <50 nm [22]. The microstructure of Eurofer 97 and its precipitates are shown in Figure 1.5 a) and b).

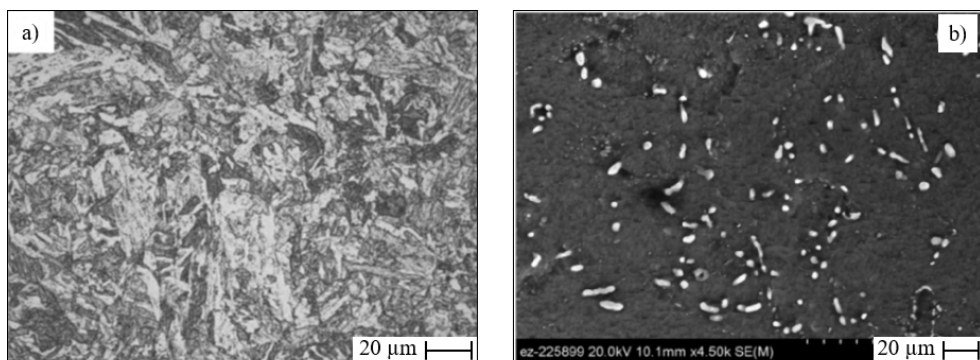


Figure 1.5 Microstructure of etched Eurofer 97; a) Light microscopy micrograph [23] and b) Scanning electron microscopy (SEM) micrograph showing precipitates [24]

This thesis used a rolled Eurofer 97 plate of thickness 4 mm, provided by Karlsruher Institut für Technologie, Germany (KIT). For simplicity, it is referred to as bulk-steel. It is also worth mentioning that as Eurofer 97 is not commercially available, so many studies have used other similar martensitic steels, such as DIN X10CrMoVNb9-1 (Grade P91), DIN X10CrWMoVNb9-2 (Grade P92), DIN X12Cr13 (AISI 410) and F82H (Japanese RAFM).

1.5 Joining W and steel

1.5.1 Boundary conditions and challenges

There are several key aspects and requirements for the successful operation of the FW, as listed below:

- Various loads: During the operation of the reactor, the FW is exposed to several loads, as seen in Figure 1.3. These include charged particle loading resulting in surface erosion of W; neutron flux resulting in irradiation damage; electromagnetic load; neutron wall load resulting in volumetric heating; and cyclic surface heat fluxes resulting in thermomechanical fatigue. The FW must withstand these combined loads for at least 5 full power years (fpy) before replacement [25].
- Service temperature: The above-mentioned surface heat fluxes of $\sim 1 \text{ MW/m}^2$ affect the operating temperature of the materials. This hits the W, while the coolant flows at $\sim 300 \text{ }^\circ\text{C}$ through steel, as shown in Figure 1.3. This means the temperature of steel and W must be within their maximum service temperature. For Eurofer 97, it is $550 \text{ }^\circ\text{C}$ (limited by creep temperature). For bulk-W, it is $\sim 1300 \text{ }^\circ\text{C}$ (limited by recrystallization temperature [14]).
- Bonding: The joints must have good interfacial bonding and defect free continuous contact over the entire bonding surface for optimal heat removal from the W into the coolant.
- Difference in CTE: Thermal stress might be the most relevant criterion for the failure of the FW. This stress arises due to the different properties: thermal conductivity ($170 \text{ W/m}\cdot\text{K}$ for W and $28 \text{ W/m}\cdot\text{K}$ for steel), CTE ($4.5 \times 10^{-6}/\text{K}$ for W and $10.3 \times 10^{-6}/\text{K}$ for steel), elastic modulus (397 GPa for W and 210 GPa for steel). This results in a strong temperature gradient from the W surface to the coolant, resulting in thermal stress at the bonding seam between W and steel, mainly because of their different CTE.
- Insolubility of W and Fe: Apart from their different properties, W and iron (Fe) are located far apart in the periodic table. According to the Fe-W phase diagram, W and Fe have limited solubility and primarily form two brittle compounds (Fe_2W and Fe_7W_6). [26,27]. They are called intermetallic compounds (IMC). Thus, when W and steel are joined directly, such IMC is formed at the bonding seam, and could be detrimental to the lifetime of the FW.

- Miscellaneous: In terms of manufacturing, another consideration is the mass production of large FW components. The FW cover a surface area of 1200 m². Thus, the technology must be capable of producing large components with high throughput with fewer production defects [7].

So, the following sections discuss important studies conducted to date.

1.5.2 Direct joining

Only a handful of researchers have performed the direct joining of W and steel, as listed in Table 1.3. The joining was performed using the following techniques: diffusion bonding using uniaxial press (DB) [28], diffusion bonding using hot isostatic pressing (HIP-DB) [29], and current-assisted diffusion bonding (CA-DB) using spark plasma sintering (SPS) setup [30]. In general, diffusion bonding is a solid-state joining process that involves keeping the components to be joined under close contact at moderate pressure, elevated temperature, and for a certain duration. The mating surfaces undergo creep deformation to cover the micro-asperities leading to complete contact, and the bonding occurs through the diffusion of atoms.

So far, only three studies have reported W and steel diffusion bonding, as summarized in Table 1.3. In the as-joined state, the resulting bonding seam was defect free and formed the following layers starting from the W-side to the steel-side:

- A thin IMC layer of composition: 37.6 at% Fe, 37.3 at% W, 5.8 at% Cr and 19.2 at% C. This layer also contained brittle metallic carbides [28]. In the case of DB, the thickness of this IMC was found to be 2.5 μm and 4 μm for a bonding time of 1 h and 4 h, respectively [28]. In the case of CA-DB, its thickness was 2.5 μm [30].
- Below this IMC, a thick fully ferritic steel layer was formed of composition: 81.5 wt% Fe, 11.0 wt% W and 7.4 wt% Cr [28]. The hardness of this layer was 285 HV. In the case of DB, the thickness of this layer was 13 μm and 25 μm for the bonding time of 1 h and 4 h, respectively [28]. In the case of CA-DB, its thickness was 60 μm [30].
- Below this layer, the rest of the steel retained its original chemical composition as that of Eurofer 97.

As seen in Table 1.3, the diffusion bonding was performed above the austenite transformation temperature of Eurofer 97 (820–890 °C [20]). This means that the joints should undergo a post bonding heat treatment (PBHT) to return the original mechanical properties of Eurofer 97. Thus, to get back the tempered martensite microstructure, the joint underwent tempering at 760 °C\90 min. However, the obtained observations were vague. In one of the studies, the diffusion bonded joint failed at the bonding seam, and the W delaminated entirely due to some internal residual stress [28]. Contrarily, in the second study (case of HIP-DB), after the PBHT— included in the HIP process itself—, the bonding seam remained intact without any delamination, but surface cracks were observed in the W; it was mentioned that it is due to the CTE mismatch of W and steel [29]. In the third study (case of CA-DB), the PBHT was successful, but no additional information was provided [30].

Table 1.3 Direct joining of W and steel performed as of now

| Type | Geometry (mm) | Joining parameter | PBHT | Remarks |
|--------|---------------------------------------|------------------------|------|---|
| DB | W: Ø18×16 steel: Ø18×20 | 1050 °C, 1 h, 20 MPa | - | Bonding surfaces were polished to a surface finish Ra of 0.02 µm. |
| | | 1050 °C, 3 h, 15 MPa | | Successful bonding with the formation of thin IMC and ferrite layer. |
| | | 1050 °C, 4 h, 13 MPa | | Tensile joint strength of 440 MPa when tested at 650 °C [28] |
| | | 1050 °C, 4 h, 13 MPa | Yes | Joint failed [28] |
| CA-DB | W: 3×5×10 steel: Ø20×32 | 960 °C, 0.5 h, 20 MPa | - | F82H steel used. |
| | | | | Bonding surfaces ground to a grit size of P180. |
| | | | | Successful bonding with the formation of thin IMC and thick ferrite layer [30] |
| | | | Yes | Successful [30] |
| HIP-DB | W: 50×50×2 steel: 50×50×30 | 900 °C, 1.5 h, 100 MPa | - | P91 steel used. |
| | | | | Successful bonding [29] |
| | | | Yes | Edge delaminated after PBHT, and cracks observed in W with one part sticking to steel and other part sticking to canning material [29] |
| Exp-W | W: 50×50×0.2 steel: 50×50×3 | - | - | Underwater explosive welding |
| | | | | Not so common technique |
| | | | | F82H steel used. |
| | | | | Successful defect free bonding without the formation of IMC, nanoindentation and microstructural investigation showed the formation of inter-mixed W-Fe layer [31] |
| DB | W: 1.5 mm thick steel: 10 mm thick | 1240 °C, 0.5 h, 10 MPa | - | Oxide dispersion strengthened* (ODS) ferritic steel, which is not similar to Eurofer 97. However, for the sake of completeness, the result is mentioned. Successful bonding with the formation of a hard 5 µm thick reaction layer consisting of W, Fe, Cr and C [32] |

1.5.3 Joining using interlayer

W and steel have also been joined using a stress-relieving interlayer. There are specific requirements for the selection of the interlayer material: it must have CTE in between that of W and steel, it should also have a low melting point as the DB occurs with the phenomenon of creep mechanism—creep starts at 0.5 times its melting point (in Kelvin)—, it should preferably make solid solution with W without forming any detrimental brittle compound, and it must possess reduced activation after neutron irradiation. Considering this, the most promising interlayers are vanadium (V) and titanium (Ti). Some rare interlayers, such as Fe, FeTi, and Zr, have also been studied but not discussed here [7,33].

V has a CTE of $8.4 \times 10^{-6}/\text{K}$ [34], forms a solid solution with W and has a low melting point of 1910 °C. As of now, there are only three studies about using V interlayer, as listed in Table 1.4. Basuki and Aktaa [35] successfully bonded W and Eurofer 97 using a 1 mm thick V. The V-steel bonding seam showed a proper diffusion of V into the steel for depth 290 μm . Three distinct reaction layers were observed starting from the V-side towards the steel-side: first, a thin (6 μm) hard brittle V_2C layer, then a thin (8 μm) hard σ phase (Fe-V), and then a thick (280 μm) fully ferritic steel phase. In another study, the joining parameter was optimized, which was found to be 700 °C, 4 h, 97 MPa [36]. It is worth mentioning that joining performed below the austenite transformation temperature does not require a PBHT step.

Table 1.4 Joining of W and steel using V interlayer performed as of now

| Type | Geometry (mm) | Joining parameter | PBHT | Remarks |
|------|--|--|------|---|
| | | | | Bonding surfaces ground and polished to a surface finish of $R_a = 0.02 \mu\text{m}$ |
| | | 1050 °C, 1 h, 17 MPa | Yes | Successful bonding, defect-free bonding seam Joint tensile strength of 172 MPa at 550 °C, fracture occurred at V_2C layer [35] |
| DB | W: $\text{Ø}18 \times 16$ V: $\text{Ø}18 \times 1$ steel: $\text{Ø}18 \times 22$ | 700 °C, 1 h 700 °C, 2 h 700 °C, 4 h, 97 MPa 800 °C, 1 h | - | Optimized parameter: 700 °C, 4 h, 97 MPa Joint tensile strength: 300 MPa at 550 °C Tensile test: W-V and V-steel bonding seam remained intact; ductile fracture inside V [36] |
| | | 700 °C, 4 h, 97 MPa | - | Survived thermocycling testing between 350 °C and 500 °C for 100 cycles [37] |

Ti has a CTE of $8.6 \times 10^{-6}/\text{K}$, a limited solubility with W and a low melting point of 1668 °C. Another advantage of Ti is its transformation from α -phase (HCP) to β -phase (BCC) at 882 °C; First, the β -phase is relatively soft and ductile, meaning the joints manufactured above 882 °C would have relatively lower residual stresses. Second, the β -phase shows a complete solubility with W. There are numerous studies on using Ti, compiled in Table 1.5.

Table 1.5 Joining of W and steel using Ti interlayer performed as of now

| Type | Geometry (mm) | Joining parameter | PBHT | Remarks |
|--------|--|------------------------|------|--|
| DB | W: 10×5×2 Ti: 10×5×0.6 steel: 10×5×2 | 800 °C, 1 h, 10 MPa | - | F82H steel used |
| | | 850 °C, 1 h, 10 MPa | - | Defect free bonding for all parameters. The highest shear strength for bonding performed at 900 °C with fracture occurring at Ti-steel bonding seam [38] |
| | | 900 °C, 1 h, 10 MPa | - | |
| | | 950 °C, 1 h, 10 MPa | - | |
| | | 1000 °C, 1 h, 10 MPa | - | |
| HIP-DB | W: 63×12×2 Ti: 63×12×0.5 steel: 63×12×30 | 760 °C, 4 h, 150 MPa | - | P91 steel used Shear test of the joint resulted in fracture of W-Ti interface suggesting a weak W-Ti bonding [39] |
| | | 900 °C, 1.5 h, 100 MPa | Yes | P91 steel used Defect free bonding Interdiffusion at Ti-steel interface, forming intermetallic phases (FeTi and Fe ₂ Ti) |
| | | | Yes | Formation of 200 µm thick ferritic steel phase [29,40], |
| CA-DB | W: Ø20×5 Ti: Ø20×0.040 steel: Ø20×5 | 850 °C, 0.17 h, 10 MPa | - | AISI 316L steel used Optimum thickness of Ti: 0.5 mm Diffused 15 µm thick W-Ti solid solution and complex reaction phases at Ti-steel interface. Sufficient shear strength and Charpy impact energy. [41] |
| | | 900 °C, 0.17 h, 10 MPa | - | ODS ferritic steel used, which is not similar to Eurofer 97. However, for the sake of completeness, the result is mentioned. Joint bonded at 900 °C showed highest shear strength [42] |
| | W: - Ti: - 0.1 mm thick Pure Fe: - | 950 °C, 0.08 h, 57 MPa | - | Successful bonding Joint survived 12 thermal cycles between 750 °C and 20 °C; Interface remained intact [43] |

At low temperature (760 °C), although the joining results in a defect free bonding seam, the diffusion of W into Ti is limited, resulting in a weak W-Ti interface [39]. Increasing the temperature to 800 °C does not improve the interdiffusion at the W-Ti interface. Therefore, it was found that the temperature must be at least above 850 °C for sufficient diffusion of W into Ti [38]. Above 850 °C, it was observed that the W-Ti interface showed appropriate diffusion, forming a solid-solution layer with a needle-like microstructure. The thickness of this diffused layer increased from 2 μm to 12 μm as the bonding temperature increased from 850 °C to 950 °C. Above 850 °C, the Ti-steel interface produced complex, brittle intermetallic phases containing FeTi, Fe₂Ti and Cr₂Ti. It was observed that increasing the joining temperature from 800 °C to 900 °C led to an increase in the shear strength of the joint; this is attributed to the significant interdiffusion between W and Ti. But above 900 °C, a decrease in the shear strength was observed; this is attributed to the severe formation of the above-mentioned brittle intermetallic phases [38]. Thus, in most studies, ~900 °C is considered the optimum bonding temperature.

1.5.4 Joining using a functionally graded material

Instead of joining W and steel using a single interlayer, a functionally graded material (FGM) can be introduced as an interlayer. FGM is itself made of W and steel with variation in composition. The schematic representation of this conceptual approach is shown in Figure 1.6. Introducing an FGM interlayer gradually macroscopically changes the CTE from the W-side to the steel-side, redistributing the thermal stresses [44,45]. Previous finite element (FE) numerical studies have shown that a 3-layer FGM, as shown in Figure 1.6, is an appropriate choice to redistribute the thermal stresses without increasing the manufacturing complexity [44]. This 3-layer FGM changes the CTE in a stepwise gradation and consists of three distinct W/steel-composites of composition: 25 vol% W, 50 vol% W and 75 vol% W. For ease of reading, these are termed 25W, 50W and 75W, respectively.

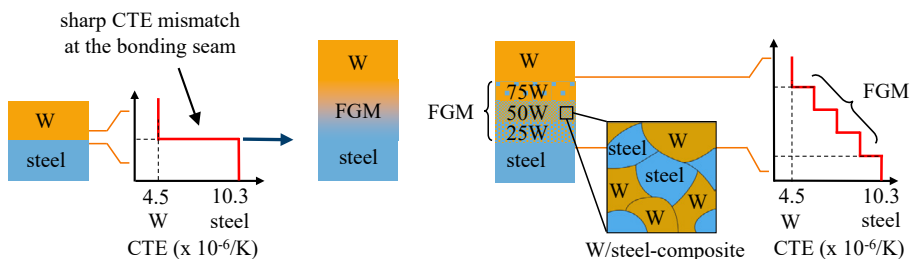


Figure 1.6 Concept of joining W and steel using FGM interlayer to produce a graded FW

1.6 Realization of functionally graded first wall components

Research in manufacturing W/steel-composites and FGM started almost a decade ago, and since then, several manufacturing routes have been applied. Two notable routes investigated are plasma spraying and electric current-activated/assisted sintering (ECAS). In the case of plasma spraying, the approach for the fabrication of graded FW can be divided into two categories:

- One-step process with plasma sprayed W as armour: The first approach is to spray coat the steel with or without FGM, and end the spraying with a plasma sprayed 100 vol% W (PS-W) at the top.
- Two-step process with bulk-W as armour: The second approach is to fabricate the FGM separately by plasma spraying and join it with bulk-W and steel or plasma spray FGM on bulk-W and join it with steel.

1.6.1 Plasma spraying of tungsten on steel with/without FGM

Most studies incorporating this approach come from a handful of research institutions. That is why, for ease of understanding, the current progress and significant findings are clustered in terms of research institutions, as summarized in Table 1.6. The first FGM was processed by plasma spraying in 2009 [46]. However, the FGM had 6–10 % porosity and had low thermal conductivity (λ) of 10–15 W/m·K. It must be noted that the properties of the plasma sprayed materials depend significantly on the processing parameters like: plasma gun power, relative speed of plasma gun relative speed to the substrate, feeding rate of powder, feeding distance, pressure of carrier gas, spraying distance, substrate temperature, pressure, chemical composition of the spraying chamber atmosphere, etc. Thus, after years of development, the porosity had been significantly reduced to less than 2 % for the FGM and less than 5 % for the PS-W [47]. The technology has recently been transferred to the industry to fabricate a large-scale FW component. Although spraying W on steel seems attractive, it has one major disadvantage; the inferior mechanical and thermophysical properties of PS-W compared to bulk-W. As can be seen in Table 1.6, the PS-W have low tensile/bending strength (R_m), low elastic modulus (E), low fracture toughness, low thermal conductivity (λ), and low adhesion strength to steel (A_{steel}) [7].

Table 1.6 Plasma spraying of W on steel substrate performed as of now

| Research institution | Configuration | Properties/ Remarks |
|--|---|---|
| Greuner et al. [48] (2005, IPP Garching) | At first, 0.5 mm thick mixed (50 vol%) W/steel layer sprayed on steel substrate and on top of this, a 2 mm thick pure W was sprayed Steel dimension: 60 mm × 190 mm Steel material: Eurofer 97, F82H, AISI 316L | Porosity of PS-W: ~25 % λ of PS-W: 20 W/m·K E of PS-W: 120 GPa R_m of PS-W: 60 MPa A_{steel} : 20 MPa |

| Research institution | Configuration | Properties/ Remarks |
|--|--|---|
| Matejcek and Boldyryeva [46], Matejcek et al. [49], Heuer et al. [50] (2009-2021, IPP-CAS) | - 1 mm thick PS-W on 25 mm × 100 mm steel substrate - 1.5 mm thick coating on 25 mm × 100 mm steel substrate consisting of approximately 0.2 mm thick PS-W at the top with 1 mm thick 3-layer graded W/steel mixed layer and 0.3 mm thick pure steel as bond coat | Porosity of PS-W: ~10 % λ of PS-W: 16 W/m·K E of PS-W: 74 GPa |
| Gareth [51] (2009, University of Oxford, UK) | - 0.1 mm thick PS-W on top of 0.25 mm thick 50 vol% mixed W/Diamalloy layer on mild steel substrate - 0.08 mm thick PS-W on top of a 0.4 mm thick 5-layer graded mixed W/Diamalloy layer on mild steel substrate - 0.1 mm thick PS-W on top of a 0.55 mm thick 11-layer graded mixed W/Diamalloy layer on mild steel substrate - 2 mm thick PS-W on sculptured mild steel substrate to enhance adhesion | Porosity of PS-W: ~9 % E of PS-W: 194 GPa Cracks in PS-W |
| Nagasaka et al. [52] (2009, Kyoto university, Japan) | 0.7 mm thick W coating on F82H steel substrate | Porosity of PS-W: 11 % λ of PS-W: 50 W/m·K E of PS-W: 20–50 % that of bulk-W |
| Yahiro et al. [53] (2009, Kyushu university, Japan) | - 1 mm thick PS-W sprayed on 20 mm × 20 mm × 2.5 mm F82H steel substrate - Additional heat treatment | Porosity of PS-W: 0.6 % λ of PS-W: ~100 W/m·K Good metallurgical bonding between PS-W and steel |
| Tokunaga et al. [54] (2013, Kyushu university, Japan) | - 1 mm thick PS-W on F82H steel substrate of dimensions: 50 mm × 50 mm × 5 mm, 40 mm × 40 mm × 5 mm, 30 mm × 30 mm × 5 mm - 1 mm thick PS-W also on W substrate of dimension Ø30 mm × 5 mm | Porosity of PS-W: ~9 % λ of PS-W: 97 W/m·K Low adhesion between W-splats reported |

| Research institution | Configuration | Properties/ Remarks |
|---|--|---|
| Tokunaga et al. [55], Tokunaga et al. [56] (2013-2018, Kyushu university, Japan) | <ul style="list-style-type: none"> - 1 mm thick PS-W on F82H steel substrate of dimension 20 mm × 20 mm × 2.6 mm - 0.6 mm thick PS-W on F82H steel of dimension: 50 mm × 350 mm × 7 mm | Porosity of PS-W: 11 % λ of PS-W: 70 W/m·K E of PS-W: 145 GPa |
| Qu [47], Emmerich et al. [57], Emmerich et al. [58], Weber [23] (2013-2020 KIT, Germany) | Lab scale coating: <ul style="list-style-type: none"> - 1.2 mm thick coating on steel substrate of dimension 100 mm × 100 mm consisting of 0.5 mm thick PS-W at the top and 0.7 mm thick 5-layer graded mixed W/steel interlayer - 2 mm thick coating on steel substrate of dimension 50 mm × 50 mm consisting of 0.8 mm thick PS-W and 1.2 mm thick 5-layer graded mixed W/steel interlayer - Optimized large scale coating on several steel substrates of dimension 300 mm × 200 mm with actual coating area of 270 mm × 115 mm; the coating consisted of 0.8 mm thick PS-W with 1.2 mm thick 5-layer graded mixed W/steel interlayer | Porosity of PS-W: 5 % λ of PS-W: 113 W/m·K <ul style="list-style-type: none"> - Good adhesion of plasma sprayed coating and the steel substrate - For the coating on 300 mm × 100 mm steel substrate, 0.6 mm thick PS-W spalled off from the planned 0.8 mm thick PS-W resulting in only 0.2 mm thick PS-W at the top - The coating also survived 5000 thermal fatigue cycles between 300–550 °C |
| Grammes et al. [59] (2021 KIT, Germany) | Industrial scale coating: <ul style="list-style-type: none"> - Plasma spraying on large steel substrate of dimension: 500 mm × 250 mm × 20 mm - 2 mm thick coating consisting of 0.8 mm thick PS-W and 1.2 mm thick 5-layer graded mixed W/steel-interlayer | Porosity of PS-W: 0.5 % <ul style="list-style-type: none"> - No delamination or defects analyzed by ultrasonic investigations - Good bonding with steel substrate |

1.6.2 Plasma sprayed FGM with bulk-W armour

As mentioned above, bulk-W is superior compared with PS-W. So, a bulk-W as armour would be a better alternative. However, this approach is challenging; so far, only two studies have been reported. In one study, a 3-layer FGM was first sprayed on Eurofer 97, and then it was diffusion bonded to a bulk-W using a 20 μm thick V-foil at 800 °C, 60 MPa, 2 h. This joint underwent a thermocycling test between 20–650 °C for 10 cycles. However, microcracks were observed along the bonding seam [60]. In another study, FGM was sprayed on bulk-W substrate. Various laser textured bulk-W substrates were tested to enhance the adhesion of

plasma sprayed FGM onto bulk-W substrate. The laser texturing increases the substrate's roughness and surface area, improving the mechanical interlocking between sprayed material and the substrate. As a result, 3-layer FGM was sprayed on bulk-W containing "sloped hole" patterns. However, the adhesion strength was low (7 MPa) due to inevitable residual stress [61].

1.6.3 Electric current activated/assisted sintering

A conventional powder metallurgical sintering technique is challenging to manufacture W/steel-composites and/or FGM as the melting points of W (~3400 °C) and steel (~1450 °C) are wide apart. ECAS is a promising method, as the powders can be heated up and sintered quickly by exploiting the Joule heating effect. Electro discharge sintering (EDS) and spark plasma sintering (SPS) are two such techniques. SPS is also called field-assisted sintering technology (FAST). EDS is still a lab scale technique, while SPS is an emerging industrial technique. Only few studies have been reported about the processing of W/steel-composites, as summarized in Table 1.7.

Table 1.7 W/steel-composites manufactured via advanced powder metallurgy techniques

| Technique | Processing | Pros | Cons |
|-----------|--|---|--|
| SPS [62] | <ul style="list-style-type: none"> - Mechanical milling of W and AISI 316L steel powders - Sintered at 1050 °C, 5 min - 20W, 50W and 80W | <ul style="list-style-type: none"> - Dense composites - Produced 3-layer FGM | <ul style="list-style-type: none"> - High amount of detrimental brittle phases (IMC and Fe₃W₃C) formed at the W-steel boundaries - This high amount was due to the formation of such phases in mechanical milling step itself |
| SPS [63] | <ul style="list-style-type: none"> - Manual mixing of irregularly shaped W and P91 steel powders by omitting mechanical milling - Sintered at 1100 °C, 2 min | <ul style="list-style-type: none"> - Dense 20W and 43W composites | <ul style="list-style-type: none"> - Composites still had significant amount of IMC; 20W, 43W, and 69W contained around 21 %, 12 %, and 13 %, respectively - 69W composite: only 82 % dense - Low elastic modulus of composites than expected, especially for the 43W and 69W composites |
| EDS [64] | <ul style="list-style-type: none"> - Preliminary study - Mechanically milling W and Fe powders - 25W, 50W, and 75W | <ul style="list-style-type: none"> - Ultra-fast sintering technique (within milliseconds) - Hindering the formation of IMC - Composites 98 % dense | <ul style="list-style-type: none"> - Due to mechanical milling, the produced composites had fine microscale lamellar W/Fe structures, which act as local stress concentration regions, reducing the overall ductility of the composites - Unsuccessful attempt to bond bulk-W and FGM using the sintering process itself |

As listed above, the produced composites still have some drawbacks. One of the disadvantages is the high amount of brittle IMC, whose presence inside the composite could reduce the structural integrity and performance of FW. It should be noted that it is inevitable to avoid IMC altogether because W and Fe have limited solubility, and they form metallurgical bonding by forming two IMC phases (Fe_2W , Fe_7W_6) [27,65]. Moreover, the bonding of sintered FGM and bulk-W has not yet been thoroughly investigated.

1.7 High heat flux testing of W-steel joints

High heat flux (HHF) testing is the final qualification technique to investigate the performance of components by simulating similar thermocycling loading as in fusion reactors. A handful of HHF studies on small-scale mock-ups have been reported, as listed in Table 1.8.

Table 1.8 Overview of various HHF on W-steel small-scale mock-ups; T_{surf} represents the approximate surface temperature of W

| Configuration | Joint specification | | | HHF condition | | | Results/ Remarks |
|-------------------------------|---------------------|------------|----------|----------------------------|------------------------|--------|--|
| | Armour | Interlayer | Geometry | Load | T_{surf} | Cycles | |
| | (mm) | (mm) | (mm) | (MW/m^2) | ($^{\circ}\text{C}$) | (No.) | |
| VPS of W [48] | PS-W: 2 | 50W: 0.5 | 190×60 | 2.0 | 900 | 720 | No damage |
| | | | | 2.5 | 1100 | 10 | No damage |
| | | | | 4.8 | 817 | 100 | No damage |
| VPS of W [54] | PS-W: 1 | None | 50×50 | 5.5 | 877 | 16 | Cracks in PS-W No delamination of PS-W from steel |
| | | | | | | | No damage |
| VPS of W [55] | PS-W: 1 | None | 20×20 | 3.2 | 600 | 200 | No crack No delamination of PS-W from steel |
| VPS of W+FGM [57,66] | PS-W: 0.2 | FGM: 1.2 | 270×62 | 0.7 | 800 | 1000 | No signs of deterioration |
| HIP-DB W and steel [67] | bulk-W: 2 | Ti: 0.032 | 45×45 | 1.5 | 570 | 469 | 1 st mock-up lead to delamination of W from Ti at 469 th cycle |
| | | | | | | 1000 | 2 nd mock-up survived 1000 cycles |

Most HHF studies have investigated the vacuum plasma sprayed (VPS) tungsten on steel (Eurofer 97 or F82H). Only one HHF test has been conducted on a mock-up containing 5-layer FGM interlayer with a 0.2 mm thin PS-W armour. However, the thickness of PS-W armour was lower than the required thickness for FW (2–3 mm). Also, only one study has reported the testing of HIP-DB bonded bulk-W and steel using a thin Ti interlayer.

1.8 Goal and outline of the work

As discussed, there has been noteworthy progress. However, a successful realization of a FW has not been achieved, and all the concepts are still in the primary research stage. The concept of using FGM is promising. But, its deeper investigation and its processing techniques are needed. Therefore, this thesis aims to produce and test W-steel graded joints consisting of bulk-W as the armour featuring FGM interlayer. In the course of achieving this goal, this thesis will address the following objectives/questions:

- Explore three different manufacturing routes to produce W/steel-composites: EDS, SPS and plasma spraying; as their diverse microstructures facilitate a comprehensive assessment.
- Characterization of individual W/steel-composites
Instead of characterising the FGM as a whole, it is essential to characterize the individual composites separately for better understanding and to support the FE numerical modelling of the FGM. So, three prime characterizations would be performed: microstructural, mechanical and thermophysical.
- How to manufacture a graded FW with a plasma sprayed FGM?
A hybrid technique consisting of plasma spraying and CA-DB would be investigated to produce such a graded joint.
- How to manufacture a FW with sintered FGM as an interlayer?
- Manufacture a simple directly bonded W-steel joint using CA-DB.
- Final qualification of produced joints through HHF testing with directly bonded joint as a reference; estimating their limits and assessing graded joints.

In accordance with the aforementioned objectives, the thesis is structured as follows: The second chapter discusses manufacturing individual W/steel-composites by exploiting three processing routes and optimizing the processing parameters. The third chapter discusses the microstructural, thermophysical and mechanical characterization of the optimized composites produced in the previous chapter. The fourth chapter focuses on manufacturing various graded joints and a directly bonded joint. The fifth chapter evaluates the lifetime of joints produced in the previous chapter via benchmarking HHF test. The sixth chapter presents the post-mortem analysis of the joints tested in the HHF testing. The seventh chapter provides a general concluding discussion. The last, eighth chapter offers a summary and outlook for future work.

2 Manufacturing of individual W/steel-composite

This chapter discusses manufacturing individual W/steel-composites with varying W volume contents (25W, 50W, and 75W) using two powder metallurgy processes and one plasma spraying process. The primary objective is to optimize the processing parameters to minimize residual porosity and IMC. So, this chapter first outlines the working principles of the manufacturing processes, then investigates the effects of processing parameters, and finally determines the optimized parameters. An image analysis technique was used to estimate the amount of individual constituents, such as residual porosity, IMC, W contents, etc. The produced composites were cross-sectioned and prepared for SEM analysis to obtain secondary electron (SE) and backscattered electron (BSE) micrographs using DSM 982 and CROSSBEAM 540 from Carl Zeiss AG, Germany. The acceleration voltage (3 kV/ 5 kV/ 10 kV) and working distance (WD) were adjusted as needed. Appendix A contains further details regarding the methodology for metallographic preparation and includes photographs of the produced composites. Multiple micrographs were taken at different magnifications at different cross-sectional locations to capture mesoscale and microscale features for subsequent image analysis. The mean of the measurements obtained from image analyses on these several micrographs was considered as the residual porosity of the composite, while the corresponding standard deviation was considered as the error band. Similar procedures were used to estimate the amounts of other constituents. It is important to note that these area-based quantities are assumed to be representative of the entire volume.

2.1 Atmospheric plasma spraying

2.1.1 Working principle of APS process

The first manufacturing process was an argon (Ar) shrouded atmospheric plasma spraying (APS). The setup is at the Institute of Plasma Physics of the Czech Academy of Sciences (IPP-CAS) in Prague, Czech Republic. The system comprises a hybrid water/argon-stabilised plasma torch capable of generating 25000 K hot plasma at its nozzle tip, with a maximum electrical input power of 150 kW [11,68]. The torch is held by a 6-axis robotic manipulator, as shown in Figure 2.1. The steel and W powders are fed separately through their respective injectors from the side. The W powder is fed through two injectors located near the nozzle exit, while the steel powder is fed through a single injector located farther away from the nozzle exit, as shown in Figure 2.1 a) and b). This is because the temperature inside the plasma jet is highest near the nozzle exit, which helps to melt the W powder efficiently, as W's melting point is higher than steel's. The angle between the injector and the plasma stream is optimized and set to 110°. The powders are fed using a dual hopper volumetric powder feeder from Sulzer Metco (now

2.1 Atmospheric plasma spraying

Oerlikon Metco), which uses Ar carrier gas. During the spraying process, the powders melt as they enter the plasma jet and deposit on the hot substrate inside a shrouding chamber. These deposited molten droplets cool down rapidly and solidify, producing a plasma sprayed composite with a pancake-type microstructure.

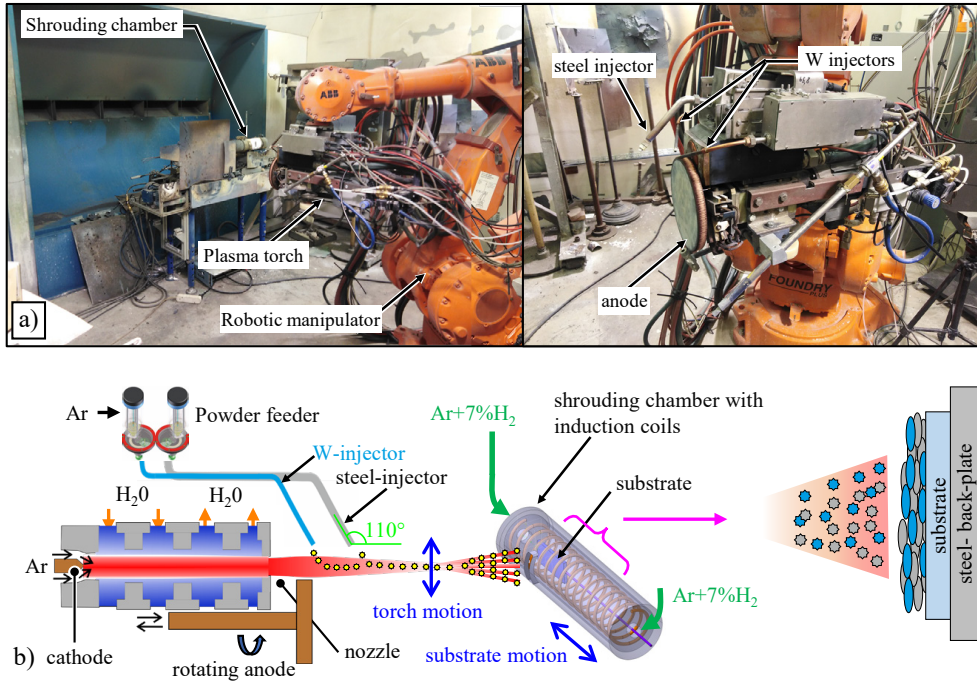


Figure 2.1 a) Photograph of the APS setup, and b) its schematic representation

2.1.2 Methodology for plasma spraying

2.1.2.1 Powders used

The first feedstock was a commercially available AISI 410 (DIN X12Cr13) steel powder with similar Cr content (12 wt%) to Eurofer 97. For the second feedstock, W powder was mixed with tungsten carbide (WC) powder in a 5:1 wt ratio to reduce the in-flight oxidation of molten W, because WC serves as a reducing agent. The particle size fraction (PSF) of the powders was already adjusted in previous studies, which are listed in Table 2.1 [11,49,50]. The elemental composition of the feedstocks is provided in Table 2.2 [11,50], and their SEM micrographs are provided in Appendix B [11].

Table 2.1 PSF and manufacturer information of powders used for the APS process

| Powder | PSF (μm) | Manufacturer |
|------------------|-----------------------|---------------------------------------|
| W | 63–80 | Alldyne powder technologies, USA |
| WC (Grade BC75H) | 40–80 | Osram, Czech Republic |
| AISI 410 | 90–140 | Flame spray technologies, Netherlands |

Table 2.2 Chemical composition of the feedstocks used for the APS process

| Feedstock powder | Chemical composition (wt%) | | | | | |
|------------------|----------------------------|------|------|------|------|------|
| | Fe | Cr | W | O | C | Rest |
| AISI 410 | 83.6 | 12.0 | - | 0.03 | 0.01 | Bal. |
| W+WC | 0.03 | - | 96.3 | 0.02 | 0.72 | Bal. |

2.1.2.2 Substrate

As shown in Figure 2.1 b), the composite was sprayed on AISI 316L steel substrate of geometry 27 mm × 70 mm × 2 mm. Before spraying, the substrate was grit blasted with Al₂O₃ particles for 5 min, then cleaned in an ultrasonic acetone bath at room temperature. This resulted in mean surface roughness Ra of 5.5 μm, which enhanced the adhesion of the sprayed composite to the substrate. The substrate was then mounted on a steel back-plate that was connected to a bar coupled to a scotch-yoke type mechanism, as shown in Figure 2.1 b). This resulted in the substrate reciprocating horizontally, facing the plasma torch, while the plasma torch reciprocated vertically. Thermocouples were attached to the front and back of the substrate to monitor and control its temperature. The substrate was inside a shrouding chamber during the spraying to limit oxide formation, as shown in Figure 2.1 b).

2.1.2.3 Shrouding chamber

The photograph and schematic representation of the shrouding chamber are shown in Figure 2.1 a) and b), respectively. It is made of graphite and has a vertical slit through which the composite is sprayed. It comprises induction coils embedded inside it, resulting in the quick preheating of the substrate to 450–500 °C before the spraying. This quick heating helps in reducing the oxidation of the substrate's surface, resulting in better adhesion of the sprayed composite to it. Shrouding gas (Ar + 7 % H₂) was flushed inside the chamber at 140 NI/min flow rate. This gas also functions as a cooling medium to cool the substrate between spraying passes. This combination of induction heating and gas cooling maintains the temperature of the substrate during the spraying to 450–550 °C. Moreover, N₂ gas was blown at 50 NI/min on the outer of the shrouding chamber to cool the graphite and increase its lifetime. The effectiveness of the shrouding chamber in limiting oxidation can be seen in Appendix C.

2.1.2.4 Process parameters

The process parameters were already optimized in previous studies [11,49,50,69]. These are listed as follows:

- Feeding distance: It is the distance between the injector and the plasma nozzle. The feeding distance for the steel injector was 105 mm, while that for W+WC was 30 mm.
- Feeding rate: It is the powder feeding rate, which is listed in Table 2.3.
- Spraying distance: It is the distance between the plasma nozzle and the substrate, which is listed in Table 2.3.

- Substrate temperature: It refers to the temperature of the substrate during the spraying process. The temperature was maintained at 450–500 °C. Appendix C shows one exemplary progression of the temperature for one spraying trial.
- Spraying passes: It refers to the total number of spraying passes performed by the robotic manipulator, which controls the thickness of the coating (composite) on the substrate. 15–17 passes were performed to achieve a coating thickness of 2 mm.

Table 2.3 Optimized feed rate and spraying distance for the APS process

| Configuration | Feed rate | | Spraying distance (mm) | Theoretical expected content | |
|---------------|----------------|-------|---------------------------|------------------------------|-----------------|
| | W+WC (kg/h) | steel | | W (vol%) | steel (vol%) |
| 25W* | 10.5 | 8.7 | 300 | 25 | 75 |
| 50W | 18 | 5 | 260 | 50 | 50 |
| 75W | 24 | 2.2 | 230 | 75 | 25 |

(Note: 25W* refers to W/steel-composite with nominal expected W content of 25 vol% and steel content of 75 vol%. Similar for 50W and 75W)

2.1.3 Optimized plasma sprayed composites

2.1.3.1 Porosity and W content

The residual porosity and oxide content (Fe_xCr_yO) are presented in Figure 2.2 a), and the W and steel contents are presented in Figure 2.2 b). The W content in the 50W and 75W composites was slightly higher than expected. Similarly, the steel content in 25W, 50W and 75W was lower than expected. Notably, the amount of Fe_xCr_yO oxides (Figure 2.2 a) represents the volumetric quantity measured by image analysis. The actual weight percentage of overall oxide content may differ. In fact, it was measured using ICP-OES for the same composites by Heuer [11], and found to be 0.95 wt%, 0.6 wt%, and 0.25 wt% in the 25W, 50W, and 75W composites, respectively.

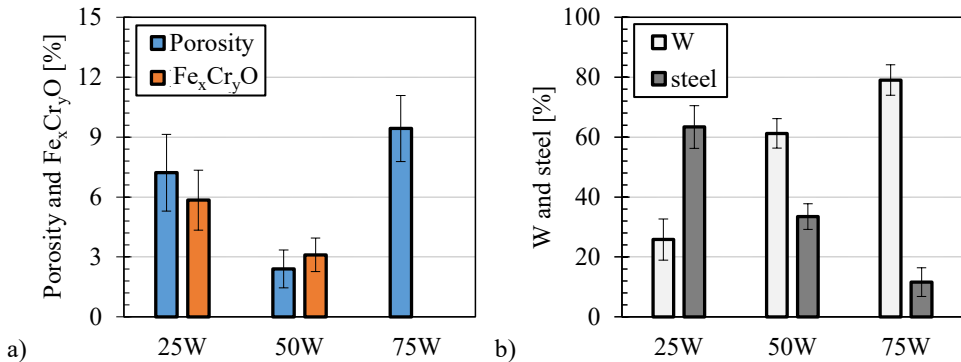


Figure 2.2 a) Porosity and oxide content and b) W and steel content of the APS composites (Note: image analysis was not able to capture Fe_xCr_yO content in 75W composite)

2.1.3.2 Microstructure

The produced plasma sprayed composites showcase lamellar type (pancake-type) microstructure, as shown in Figure 2.3. Heuer et al. [50] reported that four distinct constituents were found in the composites: layered W- and steel-splats, layered oxide films ($\text{Fe}_x\text{Cr}_y\text{O}$), irregularly shaped pores, and interdiffused phase ($\text{Fe}_x\text{W}_y\text{Cr}_z$). Occasionally some cracks were also detected. “Splats” is the terminology in plasma spraying for flattened solidified molten droplets, forming a layered type pattern [70]. These four constituents were also detected in this thesis. The W and steel constituents were homogeneously distributed, with voids spreading over the entire area. Figure 2.3 b) shows that, in most cases, no metallurgical bonding was

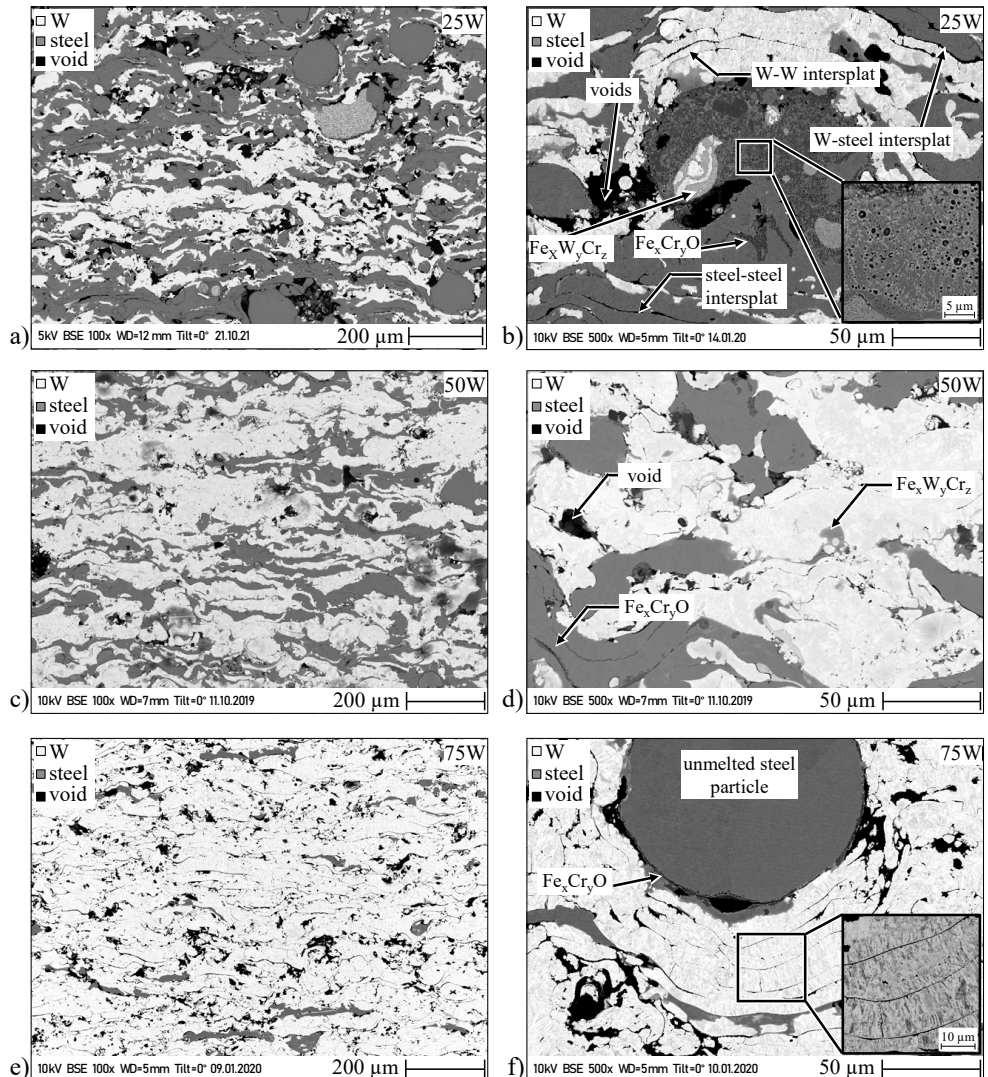


Figure 2.3 Microstructure of the produced APS composites of composition: a), b) 25W, c), d) 50W, e), f) 75W

established in most W-W, W-steel and steel-steel splats. These non-bonded splats were observed not only in 25W but also in 50W and 75W composites. In certain locations, $\text{Fe}_x\text{Cr}_y\text{O}$ oxide film was observed between two interconnected steel-splats, as shown in Figure 2.3 b) and d). In certain locations, marked in Figure 2.3 b) and d), an interdiffused phase ($\text{Fe}_x\text{W}_y\text{Cr}_z$) was observed. These are not IMC but a blend of Fe, W and Cr. In certain locations, some complex mixture of $\text{Fe}_x\text{Cr}_y\text{O}$, $\text{Fe}_x\text{W}_y\text{Cr}_z$ and voids was observed, as seen in the magnified snippet of the micrograph in Figure 2.3 b). The W-splats showcased a grain orientation along the spraying direction, which is evident in Figure 2.3 f). Rarely a non-melted steel particle enclosed by a thin $\text{Fe}_x\text{Cr}_y\text{O}$ oxide film was also observed.

2.2 Electro discharge sintering

2.2.1 Working principle of EDS process

EDS is a state-of-the-art ultra-fast sintering method for metallic powders. The setup is at Lehrstuhl Werkstofftechnik, Ruhr-Universität Bochum (LWT-RUB). It consists of two CuCo2Be punches/electrodes of diameter 19 mm, connected to a capacitor bank through a step-down transformer, as shown in Figure 2.4 [71]. The capacitor can store a maximum of 80 kJ electrical energy. The powder to be sintered is fed into the steel die, which has an insulating Si_3N_4 liner. The powder is then mechanically compacted by the punches connected to a hydraulic pressing system. After this, the electrical energy stored in the capacitor bank is discharged, resulting in a single pulse high DC (200–300 kA) at a lower electrical potential (~11 V) flowing entirely through the powder within milliseconds (5–10 ms) [64,71]. The electrical resistance caused by the powder's particle-particle contact generates Joule heating, resulting in metallurgical bonding between the particles.

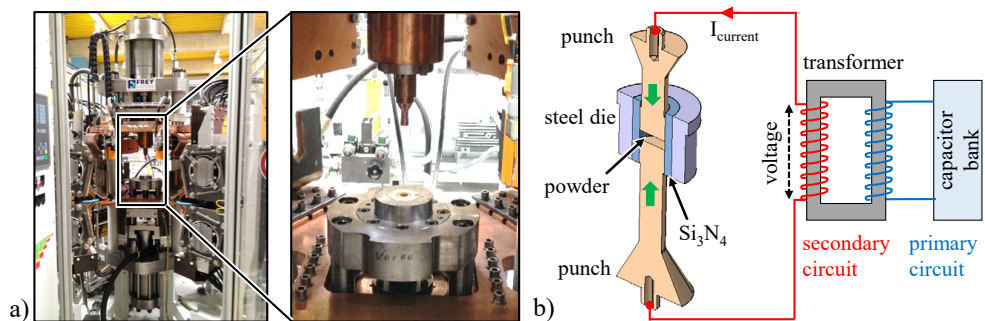


Figure 2.4 a) Photograph of EDS setup and b) schematic representation of EDS setup

2.2.2 Methodology for sintering

2.2.2.1 Powders used

Spherical W and steel powders were used as the starting material. Two batches of powders were purchased for W and steel, respectively. Their particle sizes and elemental compositions,

provided by the manufacturer, are listed in Table 2.4 and Table 2.5, respectively. The elemental composition of steel is almost the same as that of Eurofer 97 (see Table 1.2). The SEM micrographs of these starting materials are provided in Appendix B.

Table 2.4 PSF and manufacturer's information of powders used for the EDS process

| Powder | PSF | D ₅₀ | Sieved to PSF | | Production | Manufacturer |
|--------|--------|-----------------|------------------------------------|--|--|---|
| | | | (μm) | | | |
| W | 10–30 | 17 | - | | Radio frequency plasma spheroidization | China Tungsten Online (Xiamen) Manu. & Sales Corp., China |
| | 30–90 | 71 | 30–60; 60–90; 80–90 | | Plasma atomized | Tekna Advanced Materials Inc., Canada |
| steel | 10–100 | 32 | 10–20; 10–40; 30–80; 40–63; 40–100 | | Gas atomization | Nanoval GmbH & Co. KG., Germany |
| | 10–20 | 13 | - | | | |

Table 2.5 Chemical composition of the powders used for the EDS process

| Powder | Chemical composition | | | | | | | |
|-----------------|----------------------|----|---------|----------------------|-----|------|----------------------|--------------------|
| | Fe | Cr | W | Mn | V | Ta | C | O |
| | (wt%) | | | | | | | |
| W (China) | < 0.003 [#] | - | > 99.50 | < 0.002 [#] | - | - | < 0.002 [#] | 0.013* |
| W (Tekna) | - | - | > 99.90 | - | - | - | - | < 250 [#] |
| steel (Nanoval) | 89.07 | 9 | 1.1 | 0.4 | 0.2 | 0.12 | 0.11 | - |

(Note: [#]concentration in ppm, *measured by helium gas hot extraction)

2.2.2.2 Sintering procedure

The EDS setup has a measurement system to record the discharge current (I), and voltage (V) in the secondary circuit, as well as the pressing load and punch displacement during sintering. An exemplary measurement is shown in Figure 2.5 with the following output measurement nomenclatures: I_{max} (maximum discharge current) and R (resistance of the secondary circuit at I_{max}). The current discharges within 12 ms, and the powder consolidates within this time. The Joule heating delivered at the secondary circuit can be calculated using the formula $E_{sec} = \int V \cdot I \cdot dt$ [72]. Assuming all this Joule heating is utilized for sintering, the consolidation efficiency (η_{eff}) can be calculated by dividing it with the input discharge energy of the capacitor bank (energy stored at capacitor). The R and η_{eff} obtained for various sintering trials are provided in Appendix D.

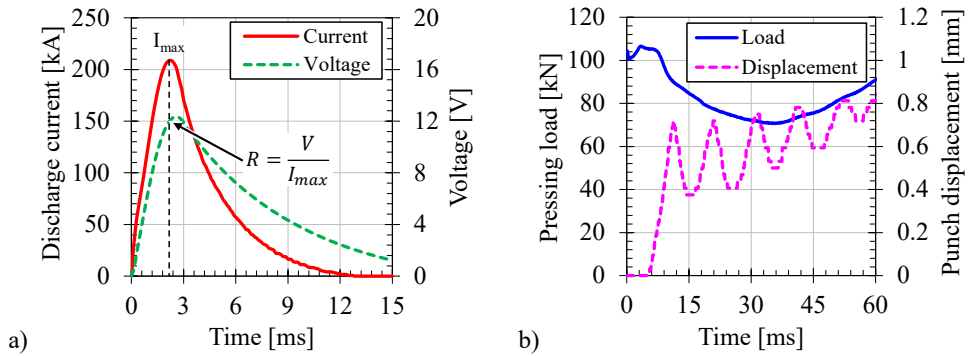


Figure 2.5 a) An exemplary discharge current and voltage profile for one sintering trial and b) corresponding punch load and its displacement

W and steel powders were sieved using a vibratory sieve shaker from Retsch GmbH, Germany, to get powders over a wide range of PSF, as specified in Table 2.4. This was done to study the effect of PSF of the powder on its consolidation behaviour. Thus, various W and steel powders were mixed, ranging from coarser to finer powder. For the mixing, the powders were weighed appropriately, considering the desired volume concentration of W. Then, these were put inside a gastight plastic jar. The entire powder handling and weighing was done inside an Ar atmosphere glove box to inhibit the formation of any surface oxide on the powder particles. Then this jar was sealed with parafilm under Ar atmosphere—jar still inside the glove box—and mixed for 48 h using a tumble mixer. The resulting mixed powder was then weighed corresponding to a volume of geometry $\varnothing 19 \text{ mm} \times 3 \text{ mm}$, assuming 100 % density and poured into the steel die for sintering.

2.2.2.3 Process parameters

The following process parameters were studied:

- PSF of W and steel powders
- Sintering pressure
- Discharge energy

The primary aim was to study the effect of process parameters on the composites' densification (residual porosity) and to find the optimized parameters. The secondary aim was to study the effect of process parameters on the directly measured quantity like maximum discharge current (I_{max}).

2.2.3 Optimization of sintering parameters for 25W

Table 2.6 lists the sintering trials for the manufacturing of 25W composite. Only the powder combination with coarser steel powder of PSF 40–100 μm sintered properly, whereas others welded to the electrode.

Table 2.6 Sintering parameters of the experimental trials for sintering 25W composite

| Combination | W PSF | steel PSF | Pressure (MPa) | Energy (kJ) | Remark |
|---|-------------------|-----------|--------------------|----------------|------------------------|
| | (μm) | | | | |
| 25W ₁₀₋₃₀ +75S ₁₀₋₂₀ | | 10–20 | 388 | 80 | welded with electrode |
| 25W ₁₀₋₃₀ +75S ₁₀₋₄₀ | 10–30 | 10–40 | 388 | 80 | |
| 25W ₁₀₋₃₀ +75S ₄₀₋₁₀₀ | | 40–100 | 388; 317; 247; 176 | 40; 60; 80 | sintered |
| 25W ₃₀₋₆₀ +75S ₁₀₋₂₀ | | 10–20 | 388 | 80 | welded with electrode |
| 25W ₃₀₋₆₀ +75S ₃₀₋₈₀ | 30–60 | 30–80 | 388 | 40; 60; 80 | |
| 25W ₃₀₋₆₀ +75S ₄₀₋₆₃ | | 40–63 | 388 | 40; 60; 80 | only sintered at 80 kJ |
| 25W ₃₀₋₆₀ +75S ₄₀₋₁₀₀ | | 40–100 | 388; 317; 247; 176 | 40; 60; 80 | sintered |

As anticipated and can be seen in Figure 2.6 a), an increase in discharge energy results in higher discharge current and a significant improvement in densification. The combination with coarser W powder (30–60 μm) showed better densification than the finer W powder (10–30 μm). This is because finer powder has a higher number of particle-particle contacts, increasing the overall resistance of the powder. Since the electrical potential remains the same, a lower discharge current flows through the finer powder, resulting in lower Joule heating. As a result, 25W₃₀₋₆₀+75S₄₀₋₁₀₀ consolidated slightly better compared to 25W₁₀₋₃₀+75S₄₀₋₁₀₀, as shown in Figure 2.6 a) and b).

Similarly, it was observed that the pressure also improved the consolidation, as shown in Figure 2.6 b). This suggests that sintering the powder at the highest pressure and discharge energy is better. Figure 2.7 shows that in both composites, sintered at 388 MPa, 80 kJ, most pores were inside the steel matrix. In the case of 25W₁₀₋₃₀+75S₄₀₋₁₀₀, the W particles were clustered together. In 25W₃₀₋₆₀+75S₄₀₋₁₀₀, the W particles were somewhat more homogeneously distributed in the steel matrix. Thus, it can be stated that the 25W₃₀₋₆₀+75S₄₀₋₁₀₀ combination sintered at 388 MPa, 80 kJ, resulting in 5 % porosity, could be considered as the optimized 25W composite.

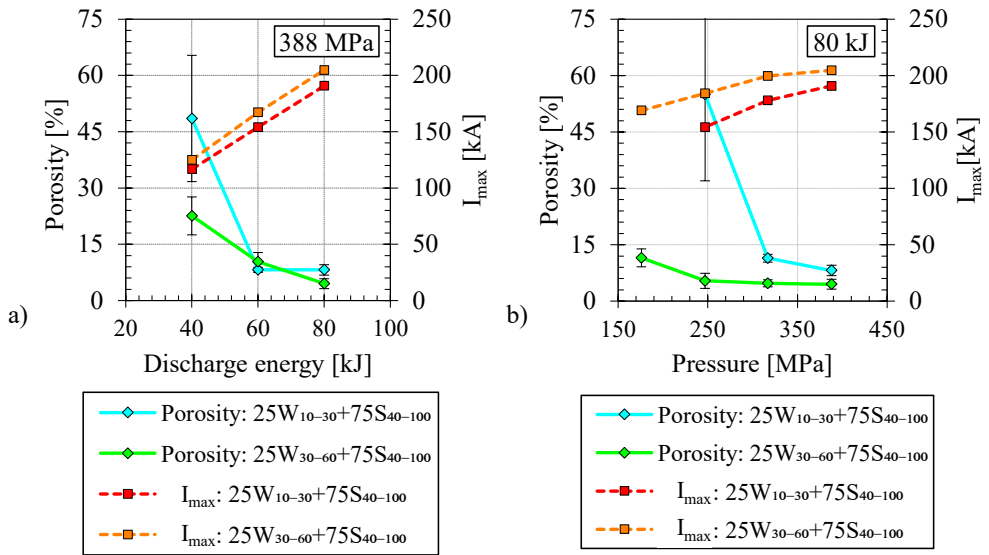


Figure 2.6 a) Effect of discharge energy when sintered at 388 MPa, and b) Effect of sintering pressure when sintered at 80 kJ on the residual porosity and discharge current for two 25W combinations

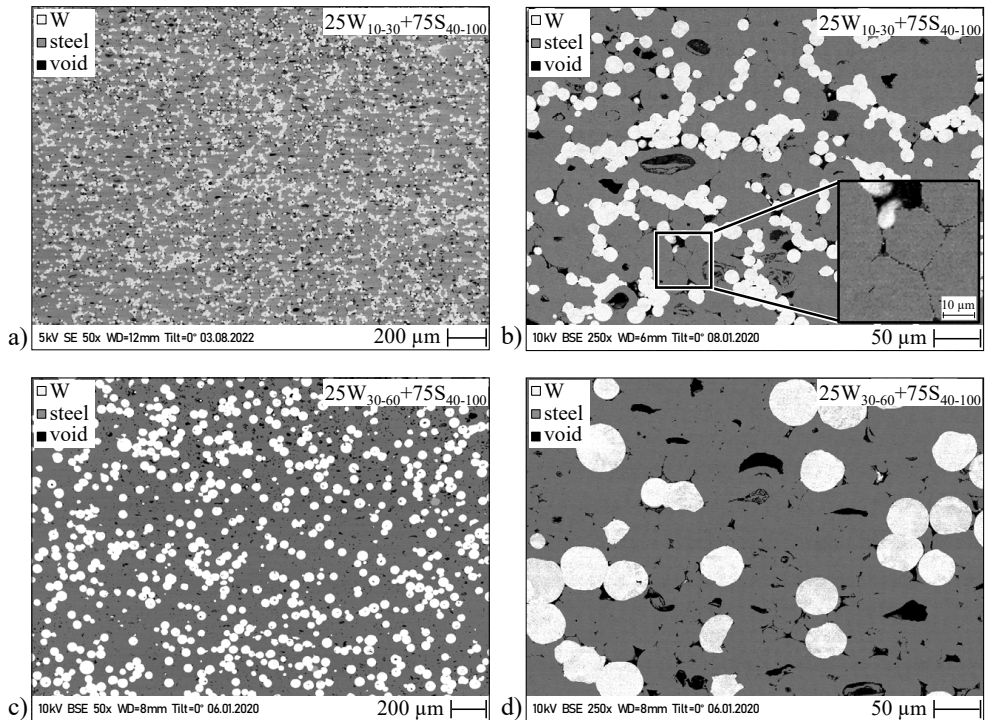


Figure 2.7 Microstructure of the composites sintered at 388 MPa, 80 kJ: a), b) 25W₁₀₋₃₀+75S₄₀₋₁₀₀, and c), d) 25W₃₀₋₆₀+75S₄₀₋₁₀₀

2.2.4 Optimization of sintering parameters for 50W

Here as well, only the combination with coarser steel powder (40–100 μm) resulted in proper sintering, as reported in Table 2.7. Similar to 25W, higher discharge energy and pressure resulted in better consolidation, as can be seen in Figure 2.8 a) and b). The resulting residual porosity and discharge current was almost identical for both combinations (50W₃₀₋₆₀+50S₄₀₋₁₀₀ and 50W₆₀₋₉₀+50S₄₀₋₁₀₀). The SEM micrographs of both the 50W combinations sintered at 388 MPa, 80 kJ are shown in Figure 2.9. It was observed that most W-W interfaces did not form sufficient metallurgical bonding, as seen in the magnified snippet of Figure 2.9 b). As both combinations have the same residual porosity, it can be stated that both the combinations sintered at 388 MPa, 80 kJ could be considered the optimized 50W composite.

Table 2.7 Sintering parameters of the experimental trials for sintering 50W composite

| Combination | W PSF | steel PSF | Pressure | Energy | Remark |
|---|-------------------|-----------|--------------------|------------|----------------------------------|
| | (μm) | (MPa) | | | |
| 50W ₁₀₋₃₀ +50S ₁₀₋₂₀ | 10–30 | 10–20 | 388 | 80 | welded with electrode |
| 50W ₃₀₋₆₀ +50S ₁₀₋₂₀ | 30–60 | 10–20 | 388 | 80 | welded with electrode |
| 50W ₃₀₋₆₀ +50S ₄₀₋₁₀₀ | | 40–100 | 388; 317; 247; 176 | 40; 60; 80 | sintered only at 60 kJ and 80 kJ |
| 50W ₆₀₋₉₀ +50S ₃₀₋₈₀ | | 30–80 | 388 | 80 | welded with electrode |
| 50W ₆₀₋₉₀ +50S ₄₀₋₆₃ | 60–90 | 40–63 | 388 | 40; 60; 80 | not sintered properly |
| 50W ₆₀₋₉₀ +50S ₄₀₋₁₀₀ | | 40–100 | 388 | 40; 60; 80 | sintered |

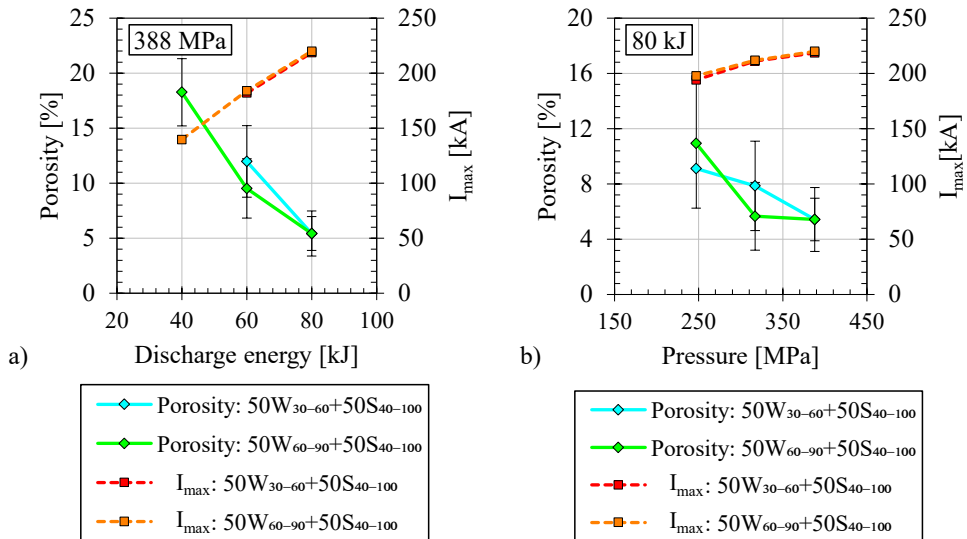


Figure 2.8 a) Effect of discharge energy when sintered at 388 MPa and b) Effect of sintering pressure when sintered at 80 kJ on the residual porosity and discharge current for two 50W combinations

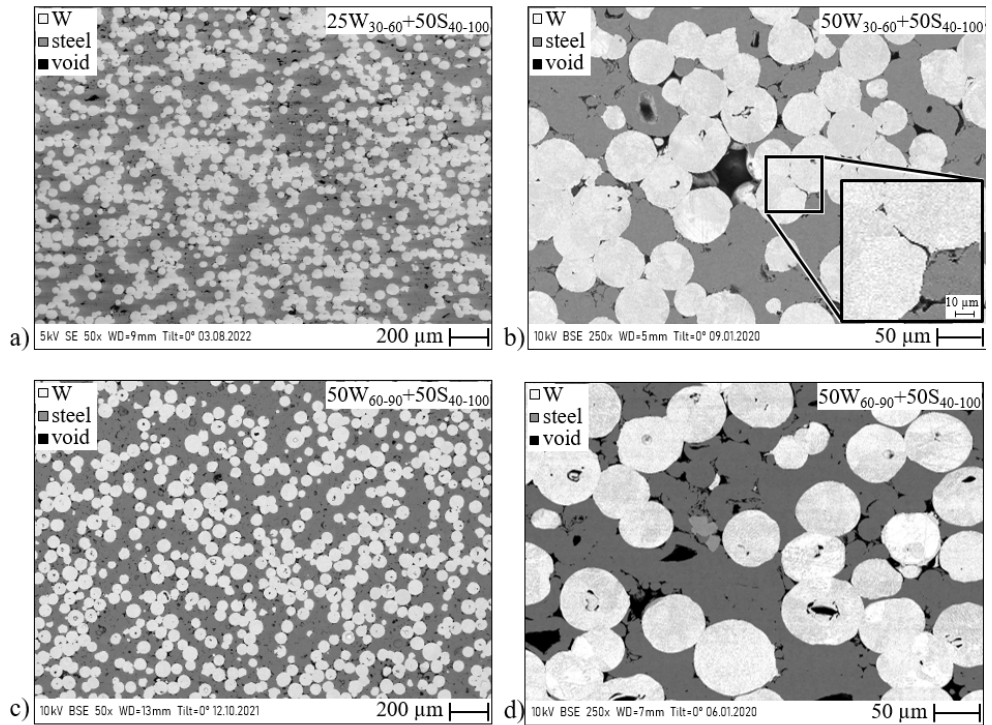


Figure 2.9 Microstructure of composites sintered at 388 MPa, 80 kJ: a), b) $50W_{30-60}+50S_{40-100}$ and c), d) $50W_{60-90}+50S_{40-100}$

2.2.5 Optimization of sintering parameters for 75W

The consolidation of 75W powders was not successful; first, it resulted in high porosity (>20 %), and second, it resulted in only localized sintering (see Table 2.8, Figure 2.10 and Figure 2.11). The discharge energy was insufficient to initiate the diffusion between particles for forming metallurgical bonds. This is because of W's high conductivity and melting point. The SEM micrographs taken at some locations with poor consolidation are shown in Figure 2.11.

Table 2.8 Sintering parameters of the experimental trials for sintering 75W composite

| Combination | W PSF (μm) | steel PSF (MPa) | Pressure (kJ) | Energy | Remark |
|----------------------------|----------------------------|-------------------------------|-----------------------------|------------|--|
| $75W_{10-30}+25S_{40-100}$ | 10–30 | | | | |
| $75W_{30-60}+75S_{40-100}$ | 30–60 | 40–100 | 388 | 40; 60; 80 | only sintered at 80 kJ and only at some locations |
| $75W_{60-90}+25S_{40-100}$ | 60–90 | | | | |
| $75W_{80-90}+25S_{40-100}$ | 80–90 | | | | |

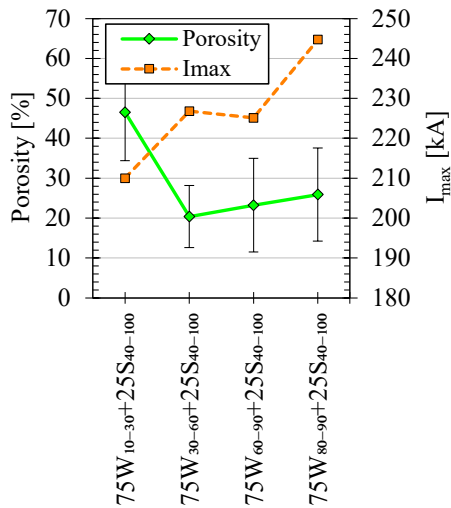


Figure 2.10 Effect of various combinations of PSF for 75W composite on the obtained residual porosity and maximum discharge current

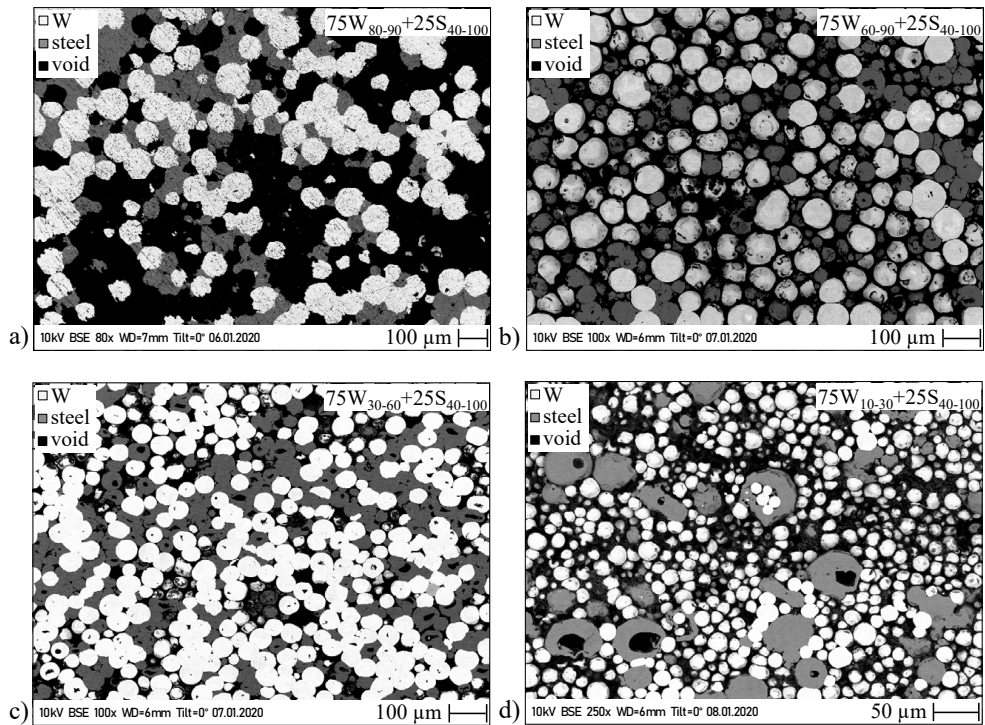


Figure 2.11 Microstructure of poorly consolidated 75W composites sintered at 388 MPa, 80 kJ: a) 75W₈₀₋₉₀+25S₄₀₋₁₀₀, b) 75W₆₀₋₉₀+25S₄₀₋₁₀₀, c) 75W₃₀₋₆₀+25S₄₀₋₁₀₀ and d) 75W₁₀₋₃₀+25S₄₀₋₁₀₀

2.2.6 Non-homogenous discharge of current

Another critical drawback of the EDS process is the inhomogeneous consolidation. This inhomogeneity was also observed in the sintering of NdFeB magnets by Leich et al. [72]. Therefore, two composites ($25W_{30-60}+75W_{40-100}$ and $75W_{60-90}+25W_{40-100}$) sintered at 388 MPa, 80 kJ were studied closely by investigating the microstructure captured at three random locations in the cross-section, as shown in Figure 2.12. In case of $25W_{30-60}+75W_{40-100}$ composite, as shown in Figure 2.12 a), although the average residual porosity was 5 %, there were areas in the same sintered specimen where the powder was fully densified (location-1 with 0.5 % residual porosity) and other areas, where it was only semi-densified (location-2 and location-3 with 9 % residual porosity). In case of $75W_{60-90}+25W_{40-100}$ composite, as shown in Figure 2.12 b), location-1 and location-2 were only densified with 5 % residual porosity. However, location-3 remained completely porous with over 40 % residual porosity. It can be assumed that electrical current mostly flowed through location-1 and location-2.

Although this phenomenon is not fully understood, some probable causes can be mentioned: First, the presence of two materials (W and steel) of different conductivity. Second, the particle size distribution broadens due to mixing W and steel powders. Third, Leich et al. [72] explained that the uniaxial pressing results in inhomogeneous initial electrical resistance of the pressed powder, which causes inhomogeneous Joule heating.

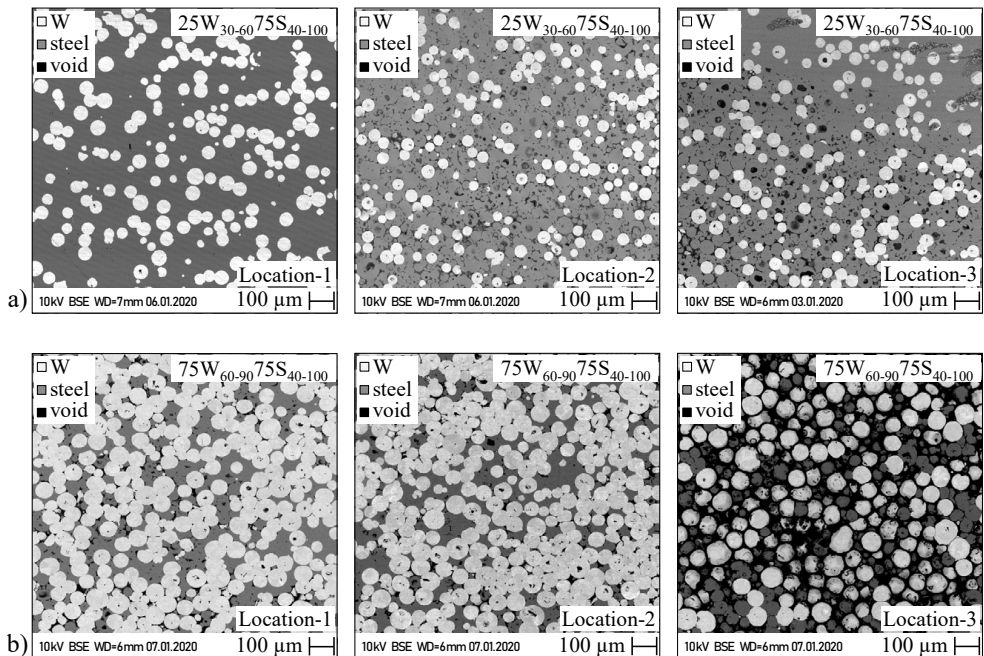


Figure 2.12 Cross-sectional micrographs taken at three different locations for: a) 25W and b) 75W composite sintered at 388 MPa, 80 kJ showing the effect of local inhomogeneity

2.3 Spark plasma sintering

2.3.1 Working principle of SPS process

A lab scale sintering facility, HP D-5 from FCT Systeme GmbH, Germany, capable of sintering the powder under 0.1 mbar vacuum, was used. The setup is at Forschungszentrum Jülich GmbH, Germany (FZJ), as shown in Figure 2.13.

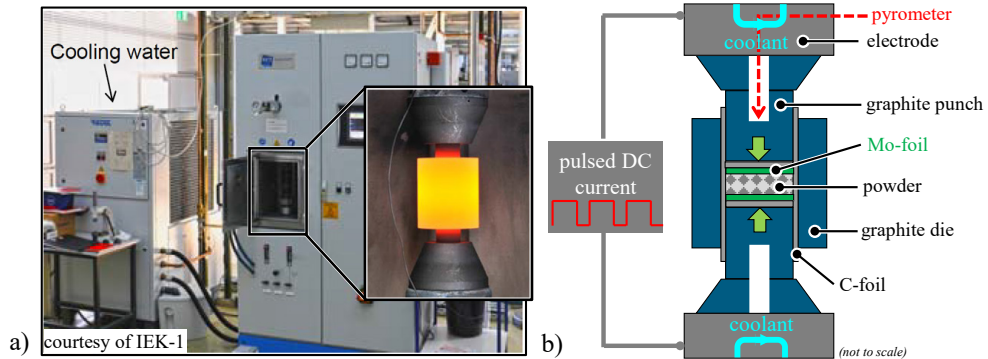


Figure 2.13 a) Photograph and b) schematic representation of the lab scale SPS setup

In the SPS process, a pulsed DC flows through the powder and the graphite die, resulting in Joule heating and consolidation. The pulse ON and OFF times were 25 ms and 5 ms during the heating cycle, respectively. The temperature was controlled by a vertical pyrometer pointed at the bore of the punch. A PID controller controls the amplitude of the DC/voltage to achieve the specified temperature. The heating rate was kept constant at 100 K/min, and after reaching the specified sintering temperature, the temperature was held for the specified sintering time before the cooling step. An exemplary current and temperature profile for a sintering trial is depicted in Figure 2.14. During the cooling step, the current stops flowing, and the die is actively cooled by the coolant flowing through the electrodes, allowing the material to cool down rapidly.

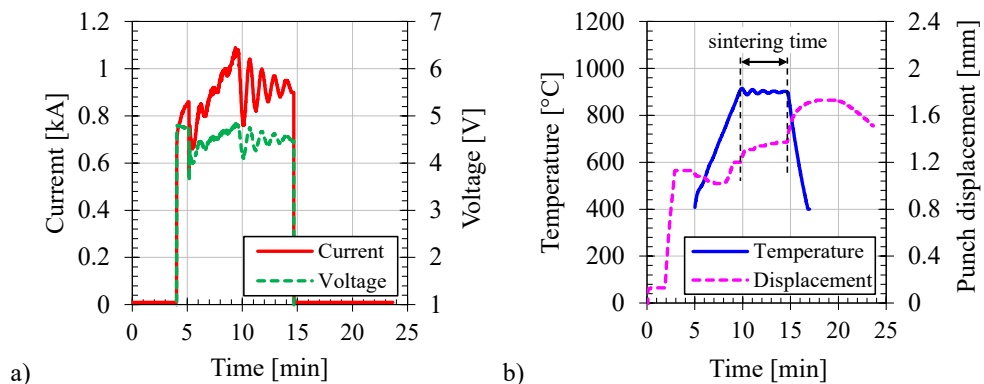


Figure 2.14 a) An exemplary current and voltage profile and b) the corresponding temperature and punch displacement for a typical sintering trial (*Note: data taken from an experiment of 25W₁₀₋₃₀+75S₁₀₋₂₀ sintered at 900 °C, 5 min, 50 MPa; pyrometer can only measure >400 °C*)

The necessary tools (punches and die) were made out of isostatically pressed graphite material of grade 2334 (compressive strength of 230 MPa) from Mersen Group, France. The tool geometry was optimized using FE numerical simulation to withstand a maximum pressure of 125 MPa. The diameter of the punch was 20 mm, resulting in a sintered disc of identical diameter. The powder to be sintered is poured inside this die, which is covered by a circular graphite foil (C-foil) of thickness 0.38 mm to prevent the powder from welding to the die. This is done to reuse the die after the sintering. At the top and bottom of the powder, thin molybdenum (Mo) foils of thickness 0.025 mm were placed between the powder and the punch. This was done to suppress the diffusion of carbon from the graphite punch into the powder. Although, as stated by Kwak et al. [73], tantalum (Ta) is a better carbon barrier than Mo, considering the higher cost of Ta, Mo-foil was used. A circular Mo-foil (carbon barrier) around the side covering the powder was avoided as most of the carbon diffusion comes from the top and bottom, as the electric current flows along the punch into the powder. This powder-filled die stack was hand-pressed with the punches and then pre-pressed to 125 MPa using a manually operated hydraulic press before sintering in the SPS setup.

2.3.2 Methodology for sintering

2.3.2.1 Powders used

Here as well, spherical W and steel powders were used as the starting material, as listed in Table 2.9. The appropriate mixing of the powders was done similarly to what was explained in Section 2.2.2.2.

Table 2.9 PSF and manufacturer's information of the powders used for the SPS process

| Powder | PSF | D ₅₀ | Sieved to | Manufacturer |
|--------|-------|-----------------|-----------|--|
| | | | PSF | |
| | | (μm) | | |
| W | 10–30 | 17 | - | China Tungsten Online (Xiamen) Manu & Sales Corp., China |
| | 30–90 | 71 | 30–60 | Tekna Advanced Materials Inc., Canada |
| steel | 3–13 | 7 | - | Nanoval GmbH & Co. KG., Germany |
| | 10–20 | 13 | - | |

2.3.2.2 Process parameters

The sintered composite had geometry of disc with a diameter 20 mm. Two thicknesses (3 mm and 0.75 mm) were studied. Following process parameters were investigated and optimized:

- PSF of W and steel powders
- Sintering temperature
- Sintering time
- Sintering pressure

2.3.3 Optimization of sintering parameter for 25W

Only one powder combination (25W₁₀₋₃₀+75S₁₀₋₂₀) was sufficient to optimize the sintering parameters to produce a dense composite. This combination was first sintered at three different sintering temperatures for the same sintering time (5 min). The thickness of the consolidated composite was kept at 3 mm and 0.75 mm. As expected, an increase in sintering temperature resulted in better densification, as can be seen in Figure 2.15 a). As can be seen in Figure 2.16 a) and b), most pores in the composite sintered at 900 °C were present inside the steel matrix itself, indicating that the temperature was too low for the complete densification of steel. As the temperature was raised to 1000 °C, the pores began to close up, leading to significantly improved consolidation, as can be seen in Figure 2.16 b) and c). This resulted in a reduction of residual porosity from approximately 4.5 % to 2 %. A further increase in the temperature to 1100 °C produced a dense composite with 1 % porosity, but at the expense of a high amount of IMC (~6 %). These IMCs were identified by energy dispersive X-ray spectroscopy (EDX) analysis (see Section 3.1.3 for a more detailed investigation). These IMCs were not only present at the W-steel boundaries but also in a few regions along the grain boundary of the steel, as can be seen in the magnified snippet in Figure 2.16 d). This investigation suggested that the sintering temperature must be kept below 1100 °C to limit the amount of IMC; ideally, the sintering temperature should not exceed 1000 °C.

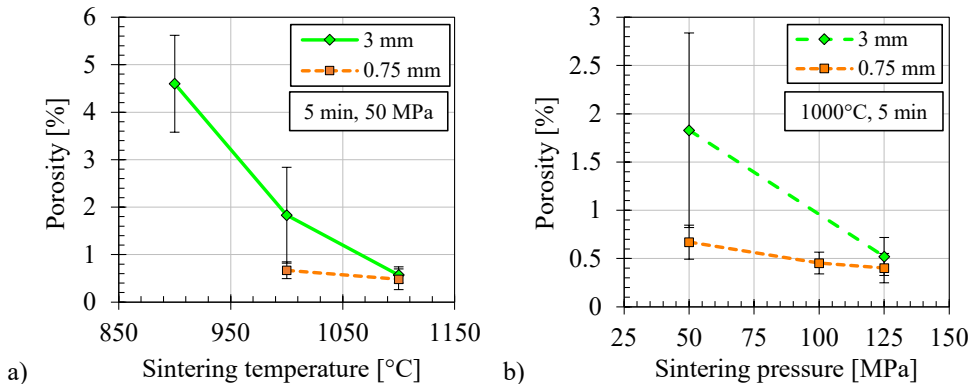


Figure 2.15 a) Effect of sintering temperature and b) Effect of sintering pressure on the residual porosity of 25W composites sintered at two different thicknesses

Figure 2.15 a) shows an interesting phenomenon in which the thinner composite (0.75 mm) showed lower porosity than the thicker one (3 mm) when sintered at 1000 °C, 5 min, 50 MPa. This can be attributed to the phenomenon of wall friction effect in powder metallurgy. Thus, in the second set of experiments, the pressure was varied to investigate its effect on densification. As shown in Figure 2.15 b), a higher pressure overpowers the wall friction effect in thicker composite (3 mm), improving densification and reducing the porosity to only 0.5 %.

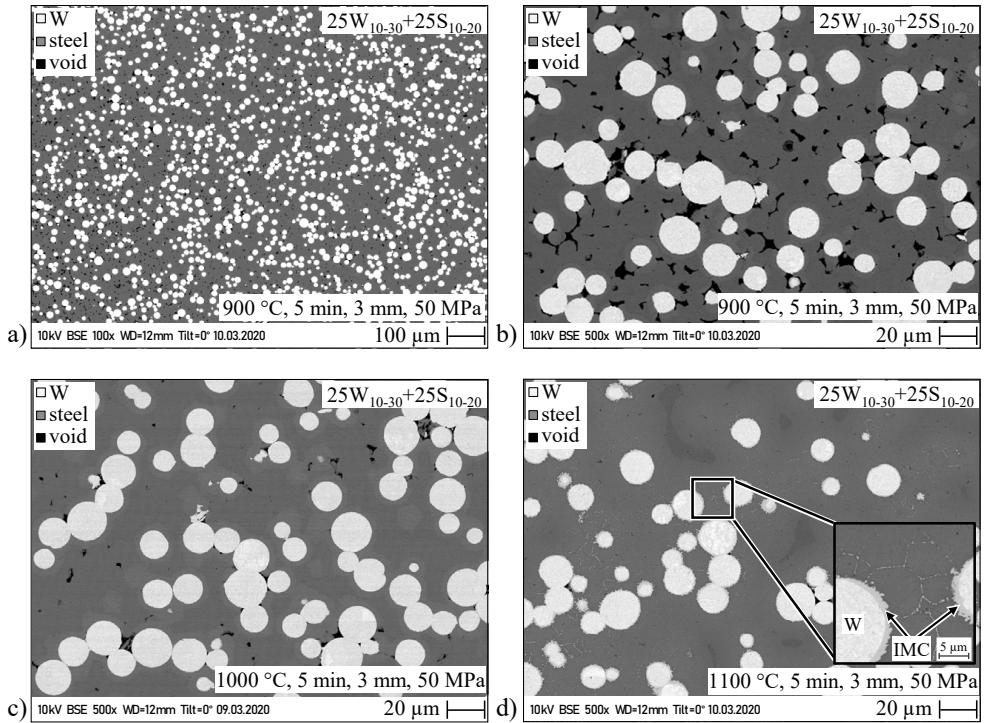


Figure 2.16 Microstructure of a 3 mm thick 25W composite sintered at 50 MPa, 5 min with three sintering temperatures: a), b) 900 °C, c) 1000 °C, and d) 1100 °C

So, the optimum sintering parameters for the 25W composite were found to be 1000 °C, 5 min, 125 MPa using the powder combination $25W_{10-30}+75S_{10-20}$. The resulting microstructure of this optimized 25W composite is depicted in Figure 2.17 a). The composite had 0.5 % porosity, which comes from submicron-scale pores randomly distributed inside the steel, as marked by arrows in Figure 2.17 b).

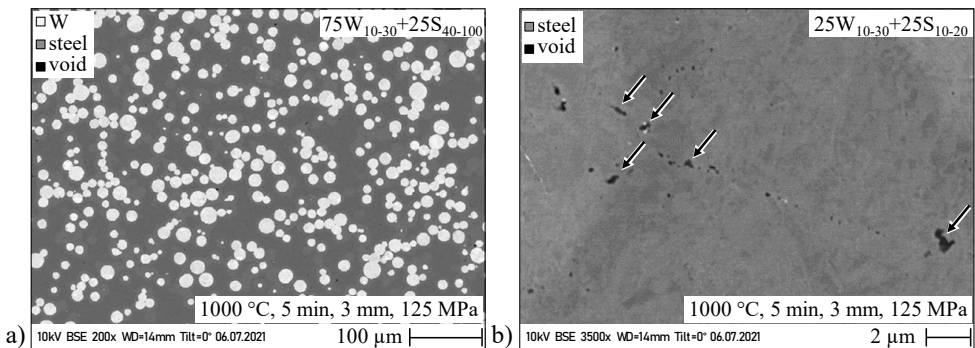


Figure 2.17 a) Microstructure of optimized 25W composite, and b) Submicron-scale pores inside its steel matrix

2.3.4 Optimization of sintering parameters for 50W

Two powder combinations were investigated: $50W_{10-30}+50S_{10-20}$ and $50W_{10-30}+50S_{3-13}$. At first, the combination $50W_{10-30}+50S_{10-20}$ was sintered between 900 °C and 1100 °C for 5 min at 50 MPa, whose resulting micrographs are shown in Figure 2.18. Again, higher sintering temperatures resulted in lower residual porosity, as illustrated in Figure 2.19 a). However, when sintered at 1000 °C, the porosity was still relatively high (~7 %). Even reducing the thickness from 3 mm to 0.75 mm did not improve the densification, suggesting that increasing the pressure would be ineffective. Although increasing the sintering temperature to 1100 °C reduced the porosity, this temperature was still higher than the optimized sintering temperature for 25W composite. Moreover, the amount of IMC in $50W_{10-30}+50S_{10-20}$ composite when sintered at 1100 °C was still relatively high (15 %), as can be seen in Figure 2.18 d).

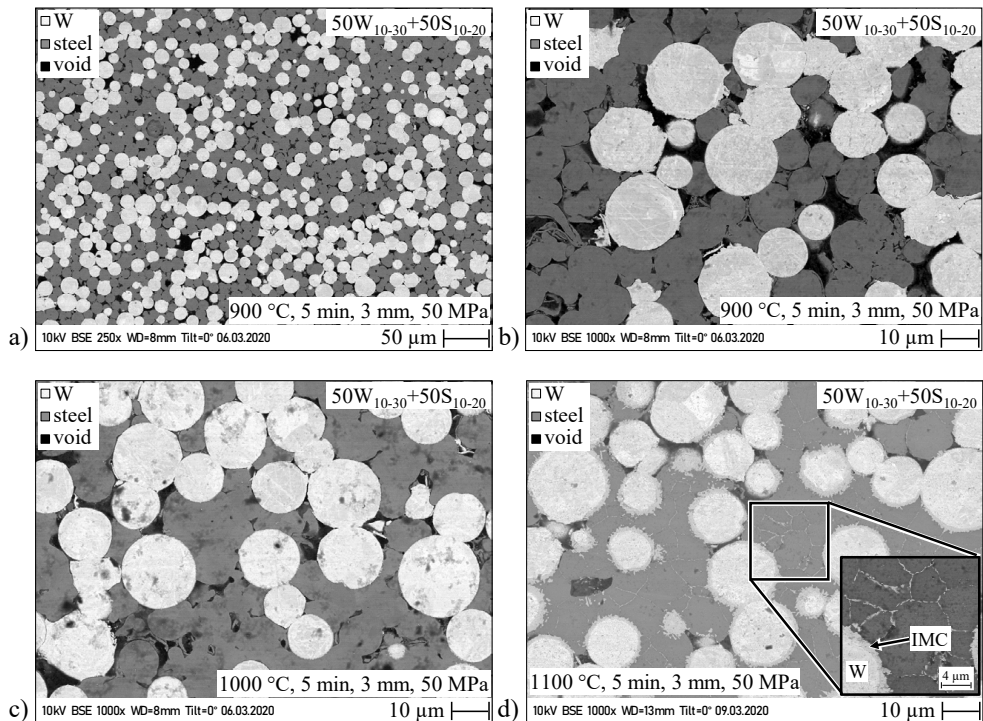


Figure 2.18 Microstructure of a 3 mm thick $50W_{10-30}+50S_{10-20}$ composite sintered at 50 MPa, 5 min with three sintering temperatures: a), b) 900 °C, c) 1000 °C, and d) 1100 °C

To limit the sintering temperature to 1000 °C, another combination ($50W_{10-30}+50S_{3-13}$) with comparatively much finer steel particles was investigated. This mixture allows the steel particles to cover the spherical W particles, forming a thin steel layer around them. When this combination was sintered at 1000 °C, 5 min, 50 MPa, the porosity dropped to less than 2 % for the thinner composite, as can be seen in Figure 2.19 a) and b). It can be seen from its micrograph in Figure 2.20 a) that the majority of pores were present only inside steel. To reduce the porosity even further, the sintering time was increased from 5 min to 10 min, keeping the other sintering

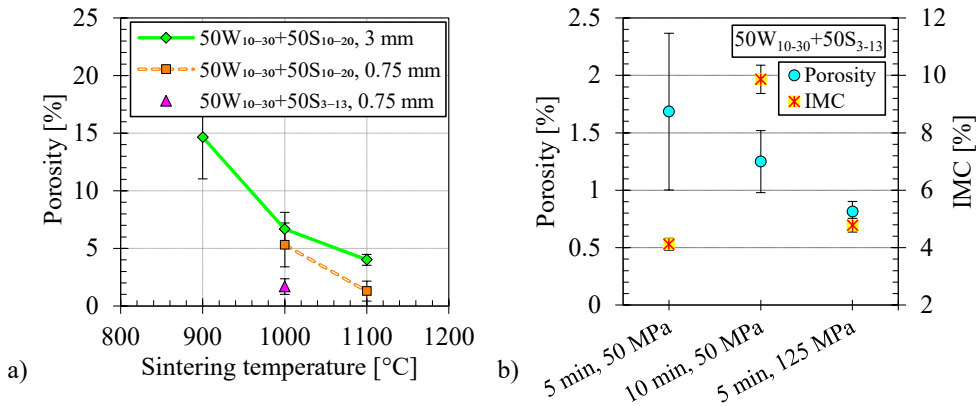


Figure 2.19 a) Effect of sintering temperature on the residual porosity, when sintered at 50 MPa, 5 min, for two combinations 50W₁₀₋₃₀+50S₁₀₋₂₀ and 50W₁₀₋₃₀+50S₃₋₁₃, b) Effect of sintering time and pressure on the residual porosity and IMC for a 0.75 mm thick 50W₁₀₋₃₀+50S₃₋₁₃ composite sintered at 1000 °C

parameters the same (1000 °C, 50 MPa), but it doubled the amount of IMC, as can be seen in Figure 2.19 b). Therefore, in another sintering trial, the pressure was increased to 125 MPa, keeping the other parameters the same (1000 °C, 5 min). The porosity reduced to less than 1 %, as can be seen in Figure 2.19 b). Here also, this residual porosity comes from the submicron-scale pores, marked with red arrow in Figure 2.20 b). Furthermore, the IMC content was also limited to 5 %. Therefore, for the 50W composite, the optimum sintering parameters were found to be 1000 °C, 5 min, 125 MPa using the combination 50W₁₀₋₃₀+50S₃₋₁₃.

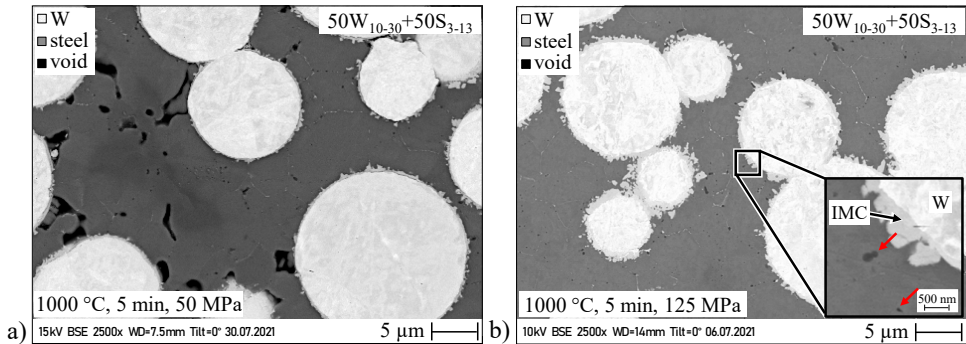


Figure 2.20 Microstructure of 50W₁₀₋₃₀+50S₃₋₁₃ composite sintered at 1000 °C, 5 min with pressure: a) 50 MPa and b) 125 MPa

2.3.5 Optimization of co-sintering of 75W with bulk-W

The 75W powder was co-sintered with bulk-W instead of sintering alone for two reasons: First, to realise a complete graded joint featuring a sintered FGM interlayer, the topmost layer of the FGM (75W) must be bonded with bulk-W. Second, co-sintering reduces the number of required experimental trials as the weldability of 75W and bulk-W and the residual

porosity/microstructure of the 75W can be investigated from the same experimental trial. The procedure for co-sintering was the following: At first, a bulk-W disc was cut into a geometry of $\text{Ø } 20 \text{ mm} \times 3 \text{ mm}$ using wire electric discharge machining (EDM), then ground and cleaned in an ultrasonic acetone bath for 20 min. It was then placed inside the graphite die with the ground side facing up. The already mixed 75W powder was weighed corresponding to a volume of geometry $\text{Ø } 20 \text{ mm} \times 0.75 \text{ mm}$, and poured on top of the bulk-W disc. Mo-foils were placed at the top and bottom of the stack and pre-pressed using graphite punches. Some preliminary experimental trials showed that pre-pressing this stack to 125 MPa resulted in the crack formation in bulk-W. This could be due to the brittle nature of bulk-W below its Ductile-to-Brittle Transition Temperature (DBTT), which is around 400 °C [74]. So, for later experimental trials, the pre-pressing force was limited to 3 kN (corresponding to $\sim 10 \text{ MPa}$), which is the minimum pressing force required in the heating step of sintering process. Then during the heating step, when temperature reached 450 °C , the pressure was increased rapidly to 125 MPa. Then the stack was sintered at different sintering temperatures ($1000\text{--}1400 \text{ °C}$) for various sintering times (0–15 min). Two 75W combinations were investigated: $75\text{W}_{10-30}+25\text{S}_{3-13}$ and $75\text{W}_{30-60}+25\text{S}_{10-20}$. In this Section, only the result regarding the porosity and IMC content is presented, as shown in Figure 2.21 and Figure 2.22. The result regarding the weldability is presented in Section 4.1.1. To reduce the number of experimental trials, only a few sintering times were tested to understand the general trend. The sintering time only slightly influenced the densification; the sintering temperature played a significant role. Both the combinations resulted in similar porosity, but the amount of IMC in $75\text{W}_{30-60}+25\text{S}_{10-20}$ was slightly less than in $75\text{W}_{10-30}+25\text{S}_{3-13}$.

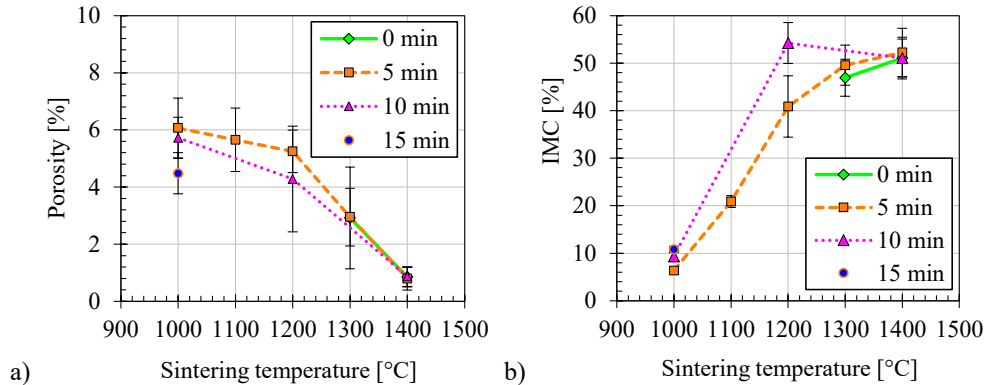


Figure 2.21 a) Residual porosity and b) IMC for a $75\text{W}_{10-30}+\text{S}_{3-13}$ combination co-sintered at different temperatures for four sintering time

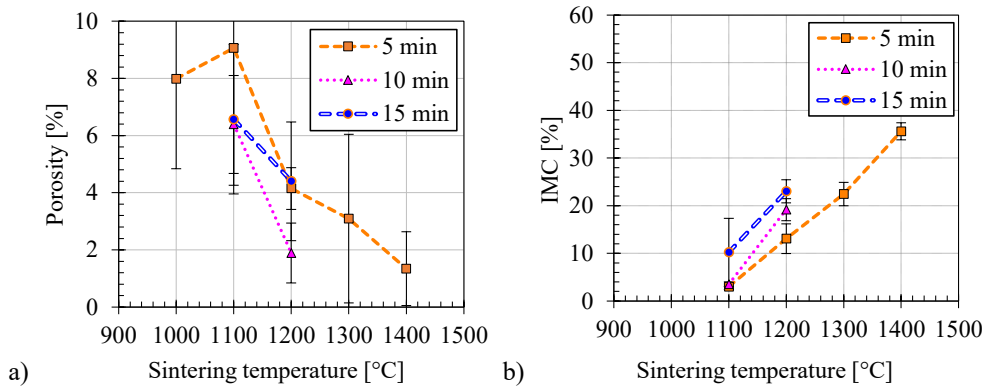


Figure 2.22 a) Residual porosity and b) IMC for a $75W_{30-60}+S_{10-20}$ combination co-sintered at different temperatures for three sintering time

Defining the optimal sintering parameter for the 75W composite is not trivial. First, on the one hand, low sintering temperature led to high porosity (5–8 %), but on the other hand, high sintering temperature led to a high amount of IMC. Second, the sintering parameter for producing 75W should be the same as that of 25W and 50W (1000 °C, 5 min, 125 MPa); it is needed to produce a complete graded joint in a one step process. Thus, only the microstructures of the 75W composites sintered at this parameter are shown in Figure 2.23 a) and b).

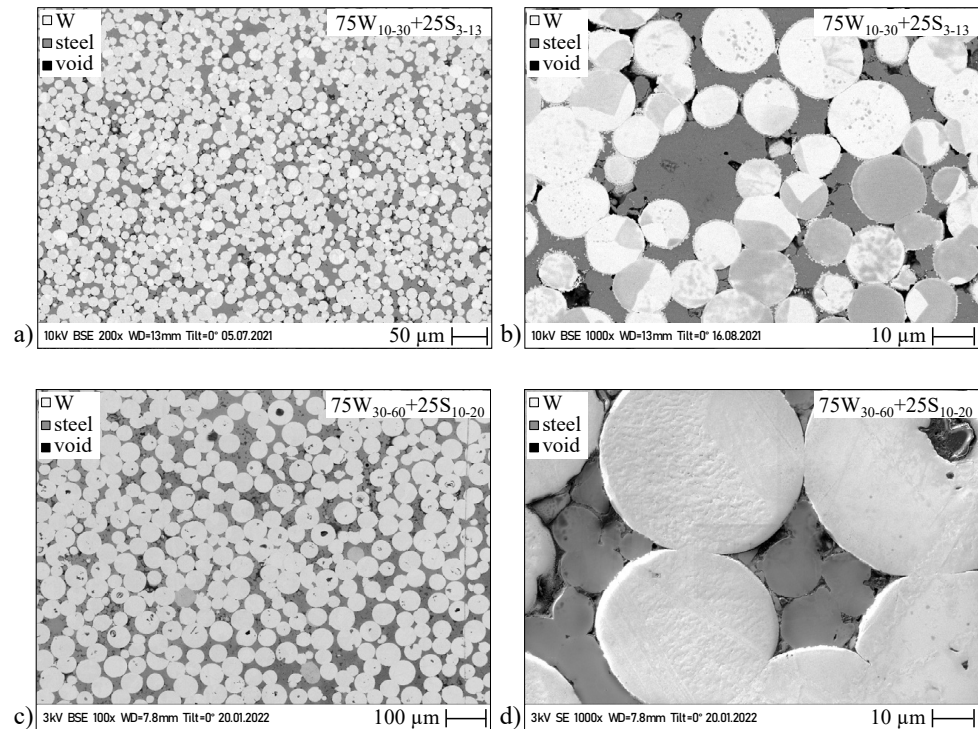


Figure 2.23 Microstructure of two 75W combinations sintered at 1000 °C, 5 min: a), b) $75W_{10-30}+25S_{3-13}$ and c), d) $75W_{30-60}+25S_{10-20}$

This co-sintering feasibility study revealed that only the $75W_{30-60}+25S_{10-20}$ composite resulted in bonding with the bulk-W. The other $75W_{10-30}+25S_{3-13}$ composite did not bond with bulk-W. Therefore, the $75W_{30-60}+25S_{10-20}$ was considered the optimal 75W combination, which should be sintered at the optimized sintering parameter 1000 °C, 5 min, 125 MPa.

2.4 Summary of manufacturing of individual composites

Three processes were investigated to manufacture W/steel-composites of three compositions: 25W, 50W and 75W. The composites were produced by the APS process using the parameters that were already optimized in previous studies. Following highlights and key insights have been found:

- Residual porosities of around 7 %, 3 %, and 10 % for 25W, 50W, and 75W, respectively were achieved. The composites have higher W content and lower steel content than their theoretical expected values. The shrouding chamber limited the formation of oxides resulting in about 6 % and 3 % for 25W and 50W composite, respectively.
- The preliminary microstructural investigations revealed that most W-W, W-steel, and steel-steel splats showed no metallurgical bonding.
- Plasma spraying is still a well established industrial process capable of producing larger composites. Thus, despite the drawbacks mentioned above, the composites were considered for further characterization and would be used as the layers of FGM in the graded joint.

The process parameters for the EDS process were extensively studied: the particle size fraction of the powders, discharge energy and compaction pressure. Following key insights have been found:

- Despite a comprehensive experimental analysis, the EDS process could not produce a 75W composite. Even the 25W and 50W composites produced had around 5 % residual porosity.
- Considering the microstructure of the 50W composite, there was a high number of non-sintered and weakly bonded W-W interfaces. This could deteriorate the structural integrity of the composite and would result in low thermal conductivity. This shall have a negative implication on their application as FGM.
- The consolidation efficiency of the process was found to be 9–11 %. This means only this much percentage of the input electrical energy stored in the capacitor bank goes for the Joule heating (consolidation). In the future, developments must be made to improve the electrical circuit of the setup to improve its efficiency.
- Till now, EDS is only used on a laboratory scale, and if the necessary upscaling of this process can be done is still questionable.

- Another major disadvantage is the non-homogenous sintering which results in insufficiently densified locations.
- Thus, despite the advantage of the EDS process being able to sinter the powder within milliseconds and limiting the formation of IMC, its disadvantages are more serious.
- Therefore, considering all these significant disadvantages, the composites sintered by EDS were discarded at this stage.

The composites produced by SPS process have, so far, the best density. The optimized process parameters resulted in the following key highlights:

- The spark plasma sintered composites contain no oxides, as the entire powder processing and sintering were performed under a controlled environment. Additionally, the composites were uniform and homogenous.
- The SPS process produced dense 25W, 50W and 75W composites. For the 25W composition, 25W₁₀₋₃₀+75S₁₀₋₂₀ combination; for 50W, a 50W₁₀₋₃₀+50S₃₋₁₃ combination; for 75W, 75W₃₀₋₆₀+25S₁₀₋₂₀ combination was found to be the optimum.
- The optimum sintering parameter was found to be 1000 °C, 5 min, 125 MPa. The optimized 25W, 50W, and 75W composites resulted in 0.5 %, 0.7 %, and 8 % residual porosity with a low amount of IMC.
- Considering this, the composites were considered for further characterization and used as the layers of FGM in the graded joint.

3 Characterization of W/steel-composites

The concept of introducing the FGM as a stress-relieving interlayer is supported by several rudimentary FE numerical simulation studies [11,23,44,45,75]. These simulations need temperature dependent material properties to model the FGM; to be precise, data for individual layers of the FGM with fixed compositions. However, all the studies have modelled it by assuming their properties to follow the rudimentary rule of mixtures—some standard empirical equations—. These assume their properties as linear interpolations of pure W and pure steel, depending on the volume content of W. The properties of pure W and pure steel are the properties of bulk-W and bulk-steel (Eurofer 97), respectively, available in the ITER materials property handbook (MPH) and EUROfusion MPH, respectively [16,21]. Therefore, it is essential to measure the temperature dependent properties and compare them with theoretical expected values following these standard empirical equations mentioned in Weber [23] and Heuer [11]. Considering this, the optimized individual W/steel-composites prepared by APS and SPS (in Chapter 2) were characterized via microstructural, mechanical and thermophysical characterizations.

3.1 Comprehensive microstructural characterization

3.1.1 As-sprayed plasma sprayed composites

As-sprayed refers to a plasma sprayed material without undergoing any further/additional processing. In-depth microstructural investigation of as-sprayed plasma sprayed composites has already been conducted in many studies [11,46,49,50]. Thus, just a summary is provided here:

- *Intersplat bonding*: It refers to the adhesion between two adjacent splats. Matejicek and Boldryeva [46] mentioned that properties, such as thermal conductivity and elastic modulus, were influenced by voids, oxides ($\text{Fe}_x\text{Cr}_y\text{O}$ and WO_x^*), and primarily the degree of bonding between splats. As discussed in Section 2.1.3.1, the degree of bonding between splats was relatively poor, and this was also observed in previous studies by Matejicek et al. [70] and Heuer [11].
- *Oxide films*: Although the plasma spraying was performed in a shrouding chamber, the molten steel particles do get oxidized during their in-flight motion. According to Volenik et al. [76], the molten steel particles form an oxidized outer shell during their in-flight motion, which was believed to be FeCr_2O_4 . Similarly, Matejicek et al. [49] found that oxide films in plasma sprayed steel coatings had M_3O_4 structure, as detected by X-ray diffraction (XRD) analysis. Heuer et al. [50] suggested that these oxide films mainly contain Cr and Fe, based on the EDX analysis.

* WO_x was not detected in microstructural investigations, but its presence cannot be ruled out

- *IMC*: Heuer et al. [50] investigated the effect of preheating temperatures of the substrates: 500 °C, 700 °C and 900 °C. The composites sprayed at 700 °C and 900 °C preheating temperatures showed the presence of IMC at the W-steel boundaries, forming voids/pores. The formation of these voids/pores could be understood based on two phenomena, as postulated by Tan et al. [77]. These are: Kirkendall effect and volume expansion. The Kirkendall effect occurs because of the difference in the diffusivity between W and steel, as W has a higher activation energy for self-diffusion than Fe. Kirkendall effect results in microscale voids, often called Kirkendall voids. The second phenomenon is volume expansion. This is because the density of IMC (Fe_7W_6 , Fe_2W) is lower than that of W; this results in the overall expansion of the composite, which is then relaxed by the formation of voids.

The composites sprayed at 500 °C showed discrete W-steel interfaces without forming IMC; the XRD analysis showed no presence of IMC [11]. Another study also mentioned that the steel and W constituents do not result in any mutual reaction and do not form IMC, even though both the W and steel constituents come into contact in molten state [70]. The reason for this is the following: rapid solidification, lower temperature of the substrate, and imperfect contact between the phases. Since the plasma spraying in this thesis was performed at a substrate temperature of 450–500 °C, no IMC was observed.

- *Interdiffused $\text{Fe}_x\text{W}_y\text{Cr}_z$ phase*: In the case of 25W and 50W (see Figure 2.3 b) and d)), a phase rich in Fe, W and Cr was observed in some locations. This phase may have formed due to the rapid solidification of mixed molten W and steel droplets without allowing sufficient diffusion to form IMC.
- *Martensite phase of steel*: As mentioned above, the absence of any mutual interaction between W- and steel-splats at a substrate preheating temperature of 500 °C suggests that the martensitic steel retains its original elemental composition. Furthermore, the rapid cooling in the plasma sprayed composite facilitates the formation of martensite phase.

3.1.2 Plasma sprayed composites after heat treatment

To investigate the effect of heat treatment, the composites underwent heat treatment as per the requirement of Eurofer 97: austenitizing (1000 °C\ 30 min) and quick cooling, followed by tempering (760 °C\ 90 min) [20]. After the heat treatment, 25W and 50W composites showed identical behaviour. Thus, only the investigation performed on heat-treated 25W composite is presented here. Figure 3.1 illustrates a representative microstructure with four regions of interest, which were studied in detail.

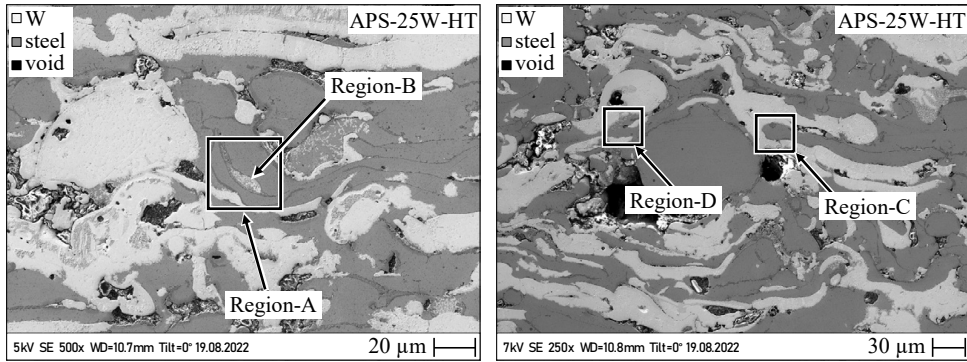


Figure 3.1 Microstructure of heat-treated plasma sprayed 25W composite

- *Region-A (Oxide-film)*: To analyse the oxide film, EDX elemental map was generated, as shown in Figure 3.2. The analysis showed that the oxide film was primarily composed of Cr rather than Fe. This suggests that Cr segregates into the oxide film after the heat treatment.

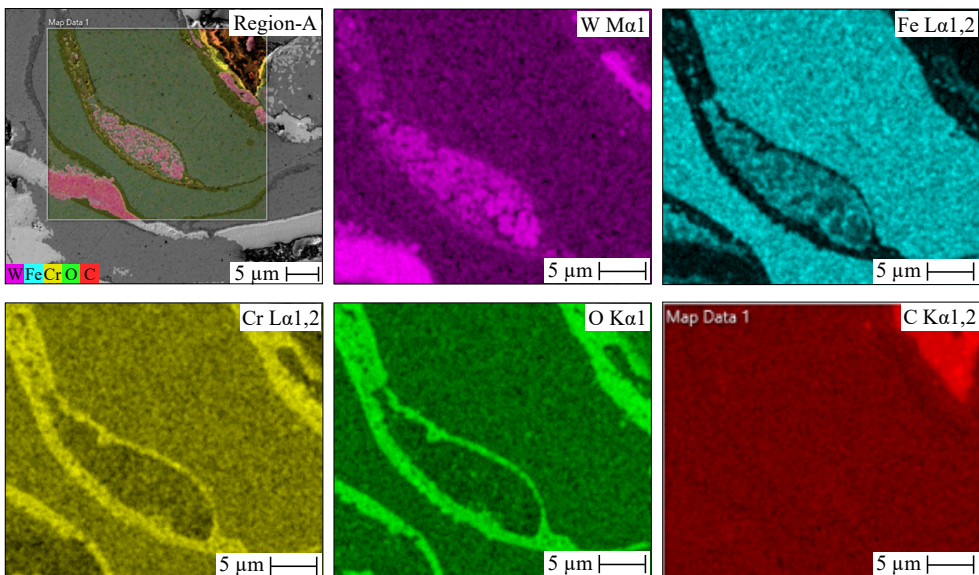


Figure 3.2 EDX elemental map of an oxide film present in heat-treated 25W composite (*spatial location of Region-A is marked in Figure 3.1*)

- *Region-B (mixture of IMC and steel)*: The area enclosed inside the oxide film was investigated further by analyzing both EDX elemental map and elemental concentration at several points. As shown in Figure 3.3, the steel present next to the oxide film (spectrum-1 in Table 3.1) has an elemental composition almost identical to the original martensitic AISI 410 steel. But, it has slightly lower Cr content (~10 wt%) compared with AISI 410 (12 wt%), possibly due to minor diffusion of Cr into the nearby oxide film. The

area encapsulated inside the oxide film consisted of a mixture of steel and IMC. The EDX analysis (spectrum-2 and spectrum-3 in Table 3.1) suggested that these should be IMC, based on the atomic ratio of Fe:W, which was approximately 3:2. According to the Fe-W phase diagram proposed by Goldbeck [26] in 1982, this IMC could be a μ -phase (Fe_3W_2). This μ -phase is now termed Fe_7W_6 in more recent literature [11,27].

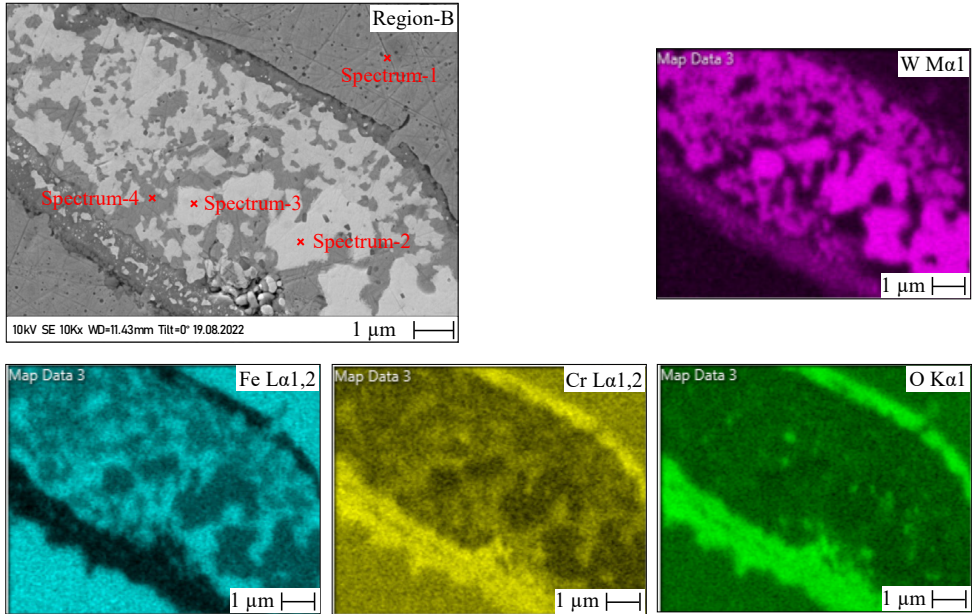


Figure 3.3 EDX elemental map of an area consisting of IMC and steel, enclosed inside an oxide film present in heat-treated 25W composite (*spatial location of Region-B is marked in Figure 3.1*)

Table 3.1 Element composition at various points of interest corresponding to Figure 3.3

| EDX-spectrum | Chemical composition | | | |
|---------------------------|----------------------|------|------|-----|
| | Fe | Cr | W | Si |
| Spectrum-1 (<i>wt%</i>) | 88.3 | 9.8 | 1.7 | 0.2 |
| Spectrum-2 (<i>wt%</i>) | 30.3 | 3.1 | 37.6 | - |
| Spectrum-2 (<i>at%</i>) | 56.3 | 6.1 | 37.6 | - |
| Spectrum-3 (<i>wt%</i>) | 30.3 | 3.2 | 66.5 | - |
| Spectrum-3 (<i>at%</i>) | 56.2 | 6.3 | 37.5 | - |
| Spectrum-4 (<i>wt%</i>) | 85.6 | 10.1 | 4.3 | - |

- *Region-C (W-steel boundary)*: The EDX elemental map in Figure 3.4 shows a steel-splat close to a W-splat. The steel at the upper part, denoted by spectrum-1, formed through metallurgical bonding with the W-splat by forming a thin (~1 μm) wavy IMC layer of

elemental composition: 60.5 at% Fe, 27.9 at% W, and 11.7 at% Cr. This elemental composition was similar to what was observed in previous studies by Matejicek et al. [49] and Weber [23]. The steel at the upper part had a high amount of W (~6 wt%) and 12 wt% Cr, as represented by spectrum-1 in Table 3.2. This high W amount resulted from significant W diffusion from the W-splat into the steel constituent. The high amount of W and Cr in the steel transformed it into a fully ferritic steel. This is because both W and Cr are known to be ferrite stabilizers; based on the ternary Cr-W-Fe phase diagram proposed by Gustafson [78], the elemental composition plotted on it indicated a ferrite phase. The steel at the lower part, represented by spectrum-2 in Table 3.2, did not show any significant W diffusion from the adjacent W-splat into it and retained almost the same elemental composition as that of the original martensitic AISI 410 steel. The reason behind this less diffusion is the presence of the oxide film between the W and the steel constituent, which acts as a barrier.

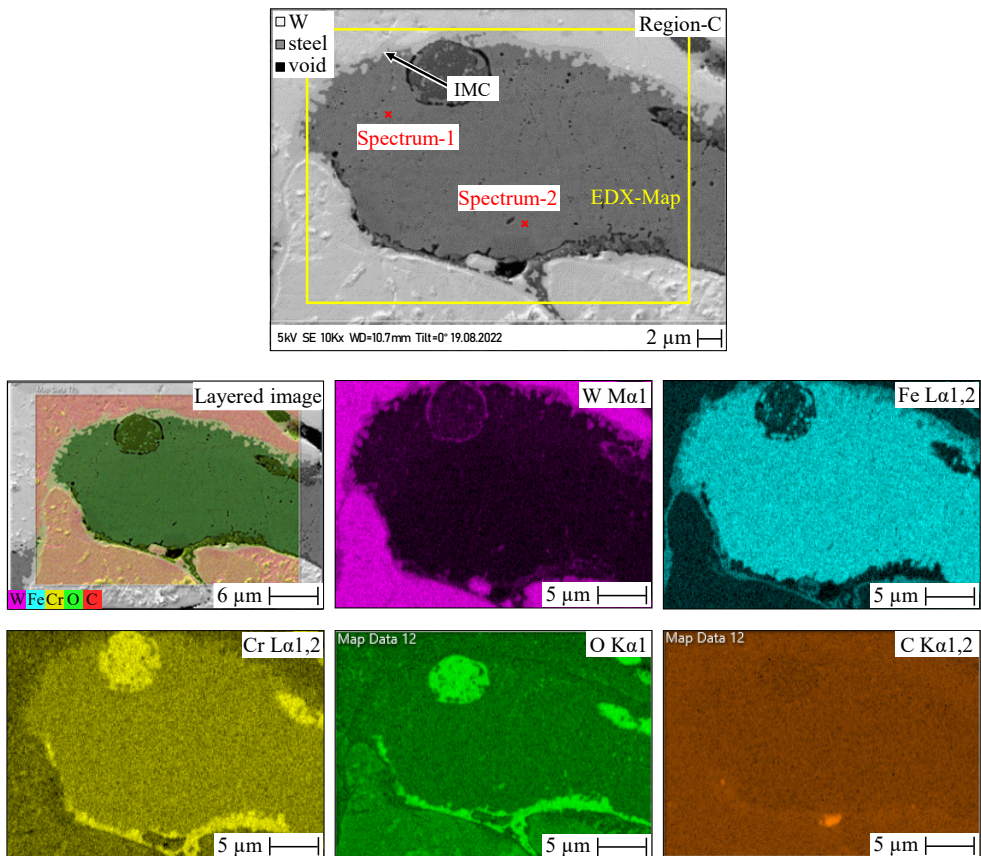
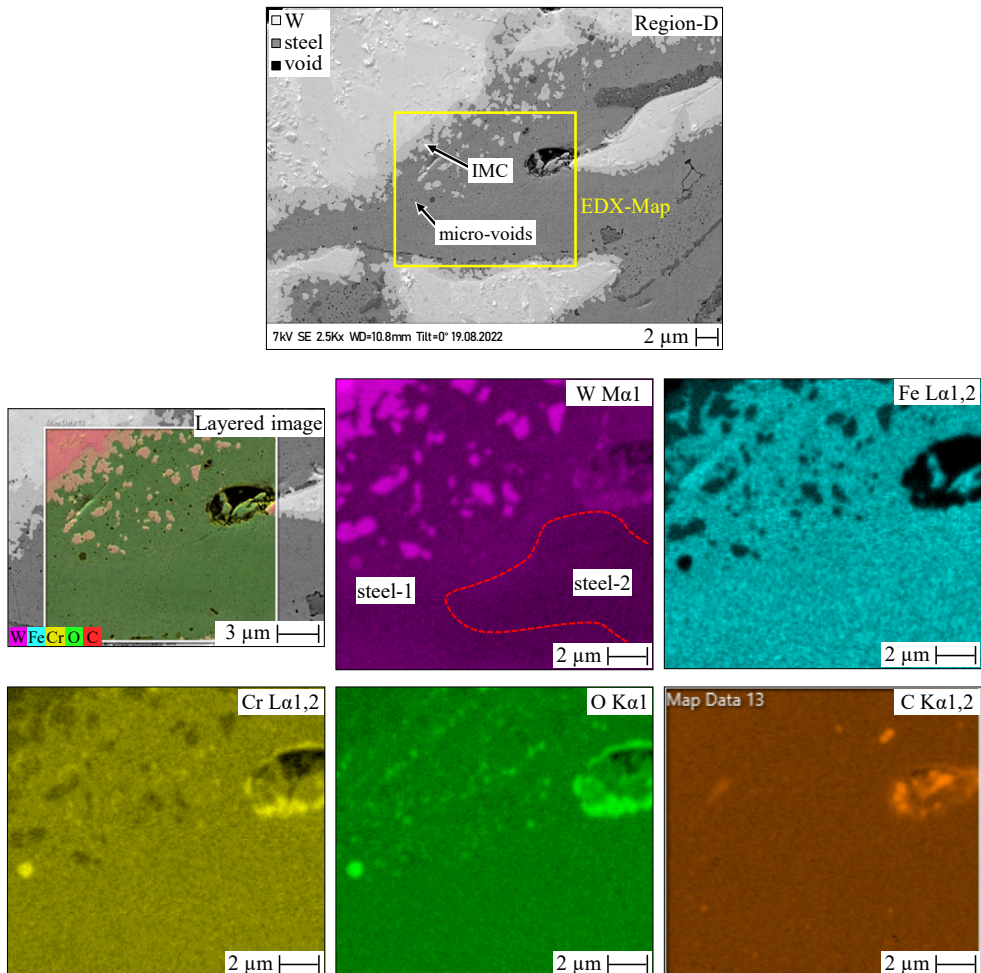


Figure 3.4 EDX analysis map of steel in between a W-splat and an oxide film in heat-treated 25W composite (*spatial location of Region-C is marked in Figure 3.1*)

Table 3.2 Element composition at various points of interest corresponding to Figure 3.4

| EDX-spectrum | Chemical composition (wt%) | | | |
|--------------|----------------------------|------|-----|-----|
| | Fe | Cr | W | Si |
| Spectrum-1 | 81.8 | 11.8 | 5.8 | 0.6 |
| Spectrum-2 | 85.9 | 12.7 | 0.8 | 0.6 |

- *Region-D (IMC)*: Figure 3.5 shows the EDX elemental map at the W-steel boundary, forming a thin IMC layer. The IMC was present at the W-steel boundary as well as inside the steel matrix (steel-1). As per the W-map, it was found that the steel present next to these IMCs (steel-1) had higher W content than the steel present farther away from it (steel-2).

**Figure 3.5** EDX elemental map at an interface between a W-splat and a steel-splat in heat-treated 25W composite (*spatial location of Region-D is marked in Figure 3.1*)

The 75W composite showed no significant change after the heat treatment, as it contained no significant oxide film and only showed the formation of some IMC, as shown in Figure 3.6.

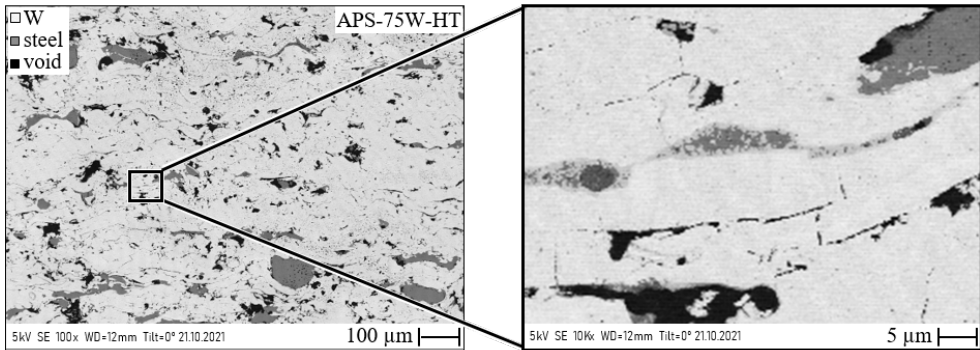


Figure 3.6 Microstructure of 75W after heat treatment with some steel-splats containing IMC

3.1.3 As-sintered composites

The microstructural analysis of the spark plasma sintered composites was also conducted. The conventional chemical-mechanical polishing could not achieve a well-polished surface for interpreting individual phases. Thus, polished surfaces were obtained by cutting the samples using a focussed ion beam (FIB) at CROSSBEAM 540 system, as illustrated in Figure 3.7. Based on this analysis, following observations were drawn:

- First, a thin IMC layer formed at the W-steel boundary. In the case of 25W, the IMC had a uniform thickness of approximately 100 nm. In 50W, its thickness was approximately 200 nm and in 75W, its thickness was approximately 300–900 nm. As can be seen in Figure 3.7 b) and c), the IMC had a wavy shape. The elemental composition of the IMC, represented by spectrum-5 in Table 3.3, was similar to the elemental composition observed in plasma sprayed composites. The atomic ratio of Fe:W was once again approximately 3:2, suggesting a μ -phase (Fe_7W_6). A similar study by Koller et al. [63] also indicated that the IMC could be Fe_7W_6 .
- Second, although the composites were dense (except 75W), nanoscale pores were observed in the steel matrix. These pores were mainly observed along the grain boundaries, as can be seen in Figure 3.7 a) and b). Also, spherical pores were observed inside the steel grain close to the IMC (Figure 3.7 b) and c)), which were formed due to the phenomenon of Kirkendall effect.
- Third, the steel phase close to the W particles transformed into a fully ferritic steel (α), marked in 25W of Figure 3.7 a). This fully ferrite steel phase was also suggested by the EDX analysis, as represented by spectrum-3 in Table 3.3. This steel phase contained almost the same amount of Cr (~8 wt%) as that of Eurofer 97 but had a higher W content (~8 wt%) than Eurofer 97. As mentioned in Section 3.1.2, this high amount of W and Cr transforms the steel into fully ferritic steel.

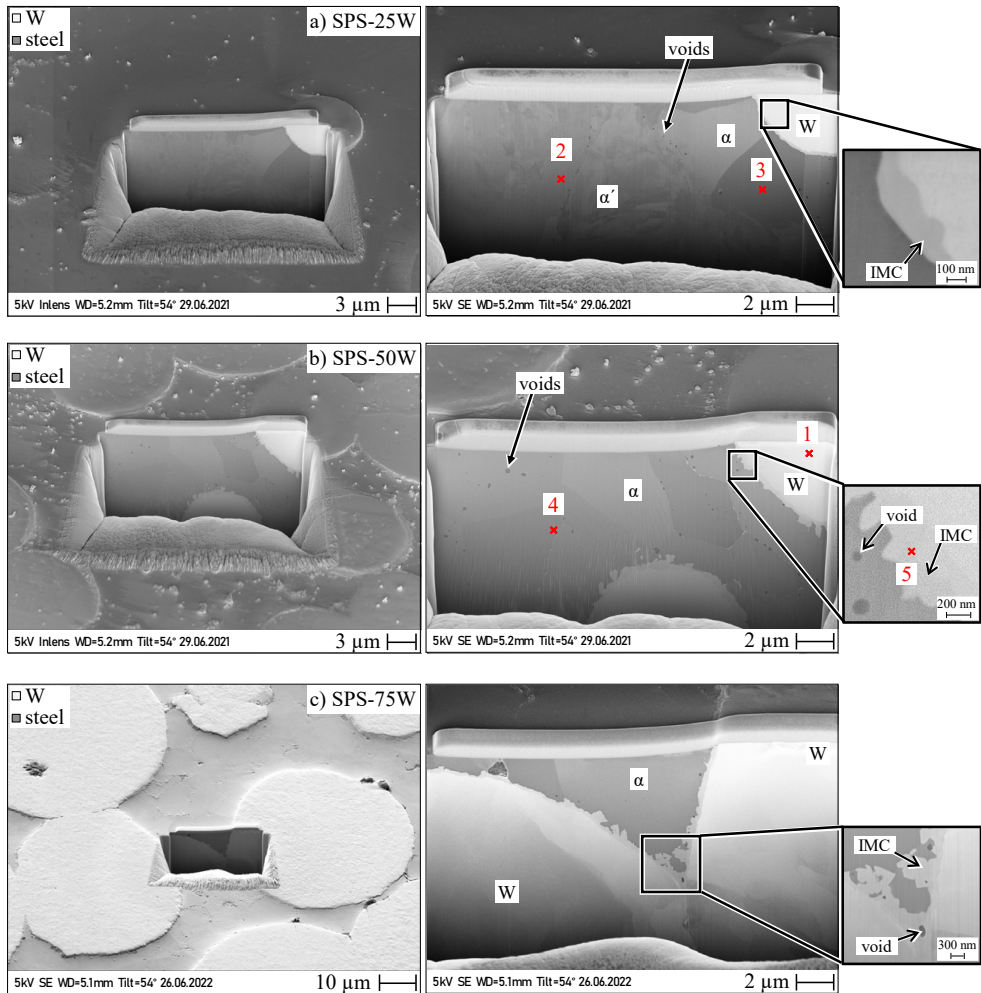


Figure 3.7 Microstructures attained through FIB cuts showing different phases in steel: a) 25W, b) 50W, and c) 75W composite. The micrograph also indicates EDX spectral points marked in red, see Table 3.3

Table 3.3 Elemental composition at points corresponding to the red markings in Figure 3.7

| Spectrum | Fe | Cr | W | V | Mn | Ta |
|------------------|-------|-----|------|-----|-----|-----|
| | (wt%) | | | | | |
| Spectrum-1 | 0.5 | - | 99.5 | - | - | - |
| Spectrum-2 | 88.8 | 8.9 | 1.6 | 0.3 | 0.3 | 0.1 |
| Spectrum-3 | 82.8 | 8.3 | 8.3 | 0.2 | 0.4 | - |
| Spectrum-4 | 82.3 | 7.9 | 9.4 | 0.2 | 0.2 | - |
| Spectrum-5 | 31.9 | 4.3 | 63.6 | 0.1 | 0.1 | - |
| Spectrum-5 (at%) | 57.1 | 8.3 | 34.6 | - | - | - |

- Fourth, the steel present farther away from the W particle formed martensite (α'), as confirmed by the needle like pattern in Figure 3.7 a). Besides, its elemental composition, represented by spectrum-2 in Table 3.3, was almost similar to that of the Eurofer 97. The cooling rate during the sintering process also confirmed the presence of this martensitic structure. The cooling rate was found to be 210 K/min, which is significantly higher than the critical cooling rate (~ 5 K/min) to accomplish martensitic transformation without undergoing any ferrite+carbide ($\alpha + M_{23}C_6$) transformation [20,79]. In the case of 50W and 75W, no such martensite phase was detected, as seen in Figure 3.7 b) and c).

3.1.4 Sintered composites after heat treatment

Similar to plasma sprayed composites, the sintered composites also underwent heat treatment, and their corresponding microstructures are shown in Figure 3.8. Following inferences were drawn:

- First, as the temperature of the composite increases, the W diffuses from the W particles into the nearby steel matrix, transforming the steel into a fully ferritic (α) steel phase. Hence, after the heat treatment, no martensite was detected in 50W and 75W. In the case of 25W, it was observed that the steel, far away from the W particles, retained its martensitic structure.

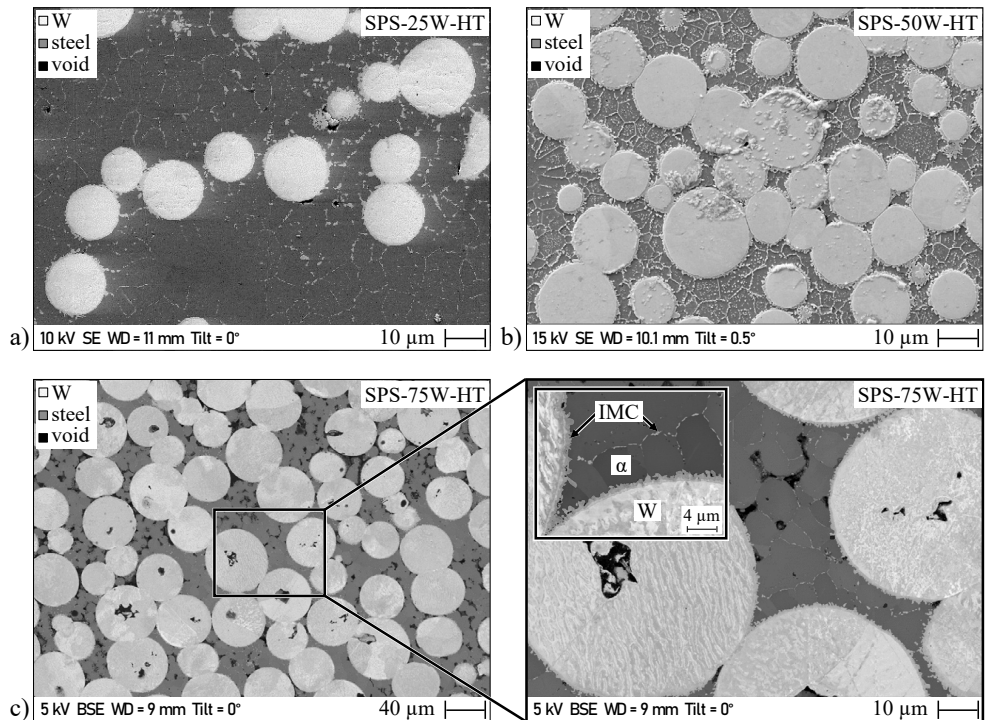


Figure 3.8 Microstructure of sintered composites after heat treatment: a) 25W, b) 50W, and c) 75W

- Second, the heat treatment increased the thickness of the IMC at the W-steel boundaries. The thickness was approximately 0.3–1.5 μm in 25W, 0.5–2 μm in 50W and 0.5–2 μm in 75W. Also, the heat treatment increased the amount of IMC. In the as-sintered state, the 25W and 75W composites had a negligible amount of IMC, and 50W contained around 5 % IMC. After the heat treatment, the amount of IMC in 25W, 50W, and 75W increased to approximately 7 %, 13 %, and 3 %, respectively. Also, it can be seen from Figure 3.8 that the 50W showed severe formation of IMC as compared to other compositions.
- Third, the heat treatment resulted in the creation of a network of IMC forming along the grain boundaries of the steel, as can be seen in Figure 3.8 a) and b). In some sites, IMC was also found inside the steel grain.

3.2 Mechanical characterization

3.2.1 Resonant ultrasound spectroscopy

Resonant ultrasound spectroscopy (RUS) technique was used to determine the elastic modulus at room temperature. This method works on the principle of examining the mechanical resonance of a solid object to extract its elastic modulus [80]. Figure 3.9 shows the elastic modulus (E_1 and E_2) measured along two directions. For the plasma sprayed composites, E_1 represents the modulus along the coating plane. For the sintered composites, E_1 represents the modulus along the direction perpendicular to the direction of applied consolidation force. These are schematically represented in Figure 3.9 a) and b). E_2 represents the modulus along the direction perpendicular to that of E_1 . The measured value was then compared with the theoretical (th.) expected elastic modulus (E_{th}) following the Equation (3.1). V_W represents the volume concentration of W. E_W and E_{steel} represents the elastic modulus of bulk-W and bulk-steel, respectively. E_W and E_{steel} were taken from MPH [16,21]. The measurements for the plasma sprayed composites were performed by Heuer et al. [50], and these results are presented here. The inferences drawn are summarized in Table 3.4.

$$E_{th}(V_W) = E_W V_W + E_{steel}(1 - V_W) \quad (3.1)$$

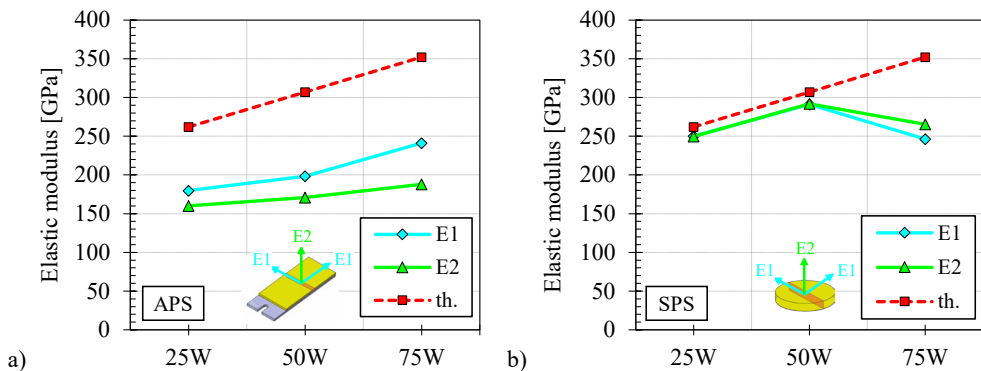


Figure 3.9 Elastic modulus: a) plasma sprayed [50], and b) sintered composites

Table 3.4 Inferences on the elastic modulus of plasma sprayed and sintered composites

| Plasma sprayed composites | Sintered composites |
|---|---|
| - Anisotropic nature | - Isotropic nature |
| - Elastic modulus along the lamellar direction (E1) is higher than that of the direction perpendicular (E2) to it | - Measured elastic modulus of 25W and 50W agree with theoretical expected value |
| - Overall the measured values (E1 and E2) were 40 % lower compared to theoretical expected value | - Elastic modulus of 75W lower than theoretical expected value. This could be due to two factors: first, high porosity of 75W and second, 75W has high number of W particles and it could be expected that the metallurgical bonding between W particles is weak/insufficient |
| - Low elastic modulus due to: high porosity, poor intersplat bonding, presence of oxides, and presence of microcracks | |

3.2.2 Four-point bending test

Due to the limited size of the composites, a quasi-static miniature 4-point bending test was considered to determine the yield strength and investigate the ductile/brittle behaviour. The geometry of the test was 1 mm × 1 mm × 12 mm. The specimens were cut using wire EDM. The test was performed at 20 °C, 100 °C, 300 °C and 550 °C (under vacuum). The cross-head speed was 0.033 mm/min. The load span was 5 mm, the support span was 10 mm, and the diameter of the support spans was 1 mm. The bending tests on the plasma sprayed composites were performed by Heuer [11], and the results are presented here. The plasma sprayed specimens had a 150 µm deep notch of width 120 µm in the middle of the specimen. This notch was created to allow the failure to occur in the middle of the specimen, considering the brittle nature of the composite. The sintered composites had no such notch. The flexural stress (σ_f) and flexural strain (ε_f) at the outermost surface were calculated based on the formula provided in ASTM D7262/D7264M [81]. The σ_f for the sintered composites were calculated following Equation (3.2). F is the applied force, L is the support span (10 mm), b is the width of the specimen (1 mm), and h is the height of the specimen (1 mm).

$$\sigma_f = \frac{3FL}{4bh^2} \quad (3.2)$$

Heuer [11] calculated σ_f for the plasma sprayed composites by multiplying Equation (3.2) by a stress exaggeration factor of 2.5 due to the presence of notch. However, the use of such stress exaggeration factor is incorrect and overestimates the actual yield strength of the composites. This can be understood based on the following reasons: First, the stress at the surface of this notch must be calculated just by subtracting the height of the specimen (1 mm) by the depth of this notch (0.15 mm). Second, even the experimental results contradict the calculation. For instance, a bending specimen made out of plasma sprayed 100 vol% steel

(AISI 410) was also tested alongside by Heuer [11]. Using this stress exaggeration factor, the yield stress was found to be 800 MPa, which is almost double the yield strength of a bulk-AISI 410 (450 MPa). In reality, the yield strength of that plasma sprayed 100 vol% steel must be even lower than 450 MPa. Therefore, in this thesis σ_f of the plasma sprayed composites were recalculated by ignoring the stress exaggeration factor.

The ε_f was calculated following Equation (3.3) [82], where δ is the cross-head displacement of the machine, which corresponds to the deflection at the load span. It must be noted that both Equations (3.2) and (3.3) are only valid in the elastic regime, and therefore, the results must be read with care.

$$\varepsilon_f = \frac{4.36 \cdot (1.375\delta) \cdot h}{L^2} \quad (3.3)$$

Figure 3.10 and Figure 3.11 shows the flexural stress vs strain profile of the plasma sprayed and sintered composites, respectively. The inferences drawn from their results are listed in Table 3.5.

Table 3.5 Inferences on the flexural properties of plasma sprayed and sintered composites

| Plasma sprayed composites [11] | Sintered composites |
|--|---|
| - All the compositions showed no signs of ductility and exhibited brittle fracture | - 25W displayed ductile behaviour even at 20 °C, showing a clear elastic-plastic regime and fractured at 5 % strain |
| - Fracture strain was approximately 0.5 % | - 50W showed ductile behaviour starting from 300 °C and fractured at 3 % strain |
| - Poor properties due to poor intersplat bonding, high porosity and presence of oxides | - 75W showed ductile behaviour starting from 500 °C and fractured at 5 % strain |

The flexural yield stress of the composites, illustrated in Figure 3.12, was determined from their flexural stress-strain response (Figure 3.10 and Figure 3.11). As can be seen in Figure 3.10, the plasma sprayed composites showed no signs of ductility/yielding. To be precise, the yield stress of any material is defined as the stress at which the material starts to deform plastically; it is fundamentally defined only for ductile materials, as brittle materials do not exhibit any yield point. However, for ease of comparison, the maximum flexural stress is considered the yield stress for plasma sprayed composites. This also applies to sintered 50W—up to 100 °C—and sintered 75W—up to 300 °C—.

This temperature (T) dependent measured yield stress (mea.) of the composites was compared to their theoretical (th.) expected values ($\sigma_{f,th}$). Similar to Section 3.2.1, $\sigma_{f,th}$ is the

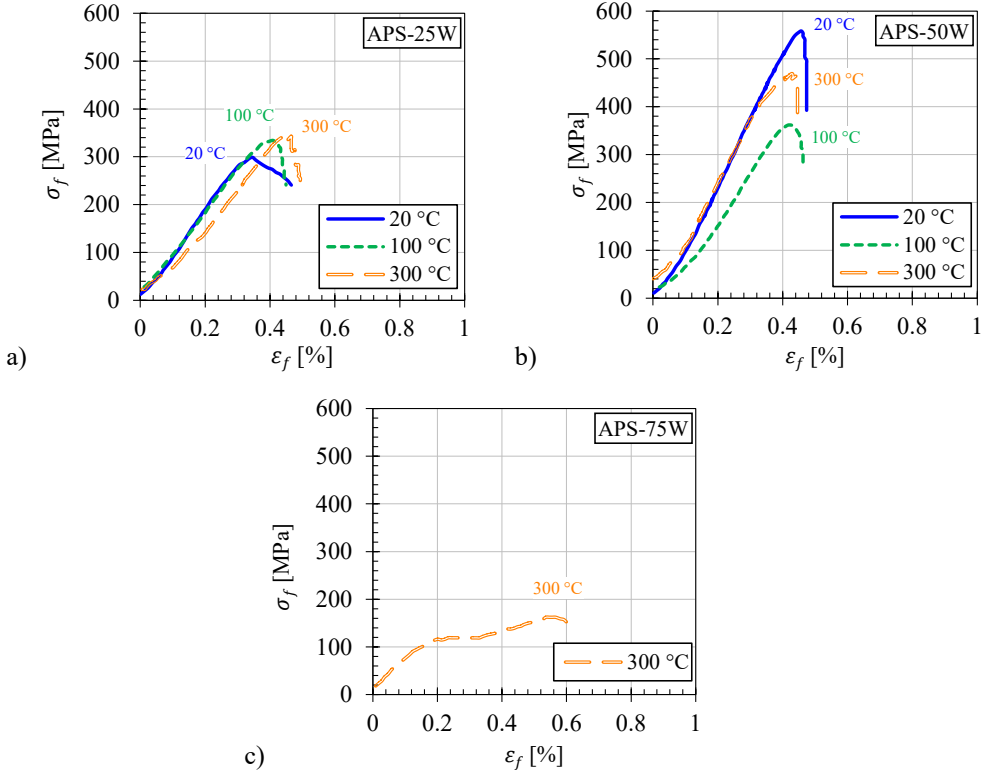


Figure 3.10 Flexural stress-strain profile of plasma sprayed composites: a) 25W, b) 50W and c) 75W (Note: the testing was not performed at 550 °C, and the tests on the 75W at 20 °C and 100 °C were not possible due to its extremely brittle behaviour)

linear interpolation of the yield stress of bulk-steel ($\sigma_{f,W}$) and bulk-W ($\sigma_{f,steel}$), following the Equation (3.4), whose values were taken from MPH [16,21].

$$\sigma_{f,th}(V_W, T) = \sigma_{f,W}(T)V_W + \sigma_{f,steel}(T)(1 - V_W) \quad (3.4)$$

The results led to the following inferences:

- First, the yield stresses of both plasma sprayed and sintered composites were much lower than their theoretical expected values. The plasma sprayed composites have lower yield stress than sintered composites, except for 50W composition.
- Second, the low yield stress of the sintered composites could be explained by the following: The W particles result in localized plastic deformation of the nearby steel matrix, thus reducing the overall yield strength of the composite. Only the yield stress of sintered 25W was somewhat close to its theoretical expected value, but for the sintered 50W and 75W, the yield stresses were even less than that of 25W. This could be due to the higher W volume content in 50W and 75W, which results in a higher number of W-W interfaces, and most of these interfaces could be weak and partially bonded.

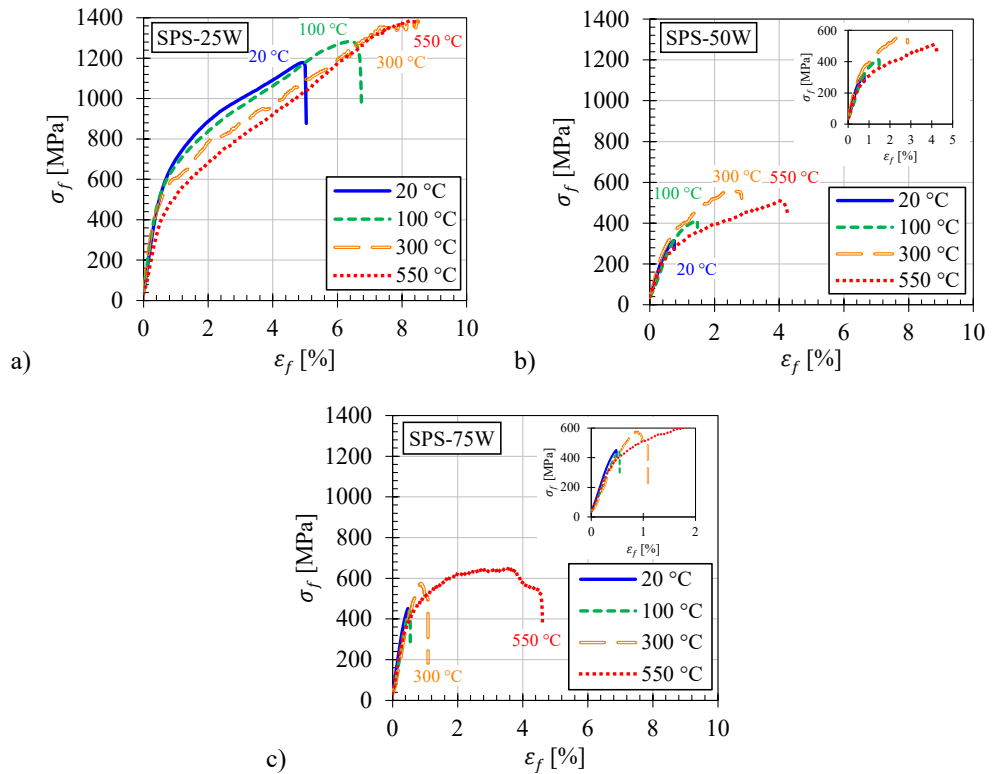


Figure 3.11 Flexural stress-strain profile of sintered composites: a) 25W, b) 50W and c) 75W (Note: the tests on the sintered 25W composite above 300 °C had to be stopped at 8 % flexural strain, as it was the maximum limit of the testing machine)

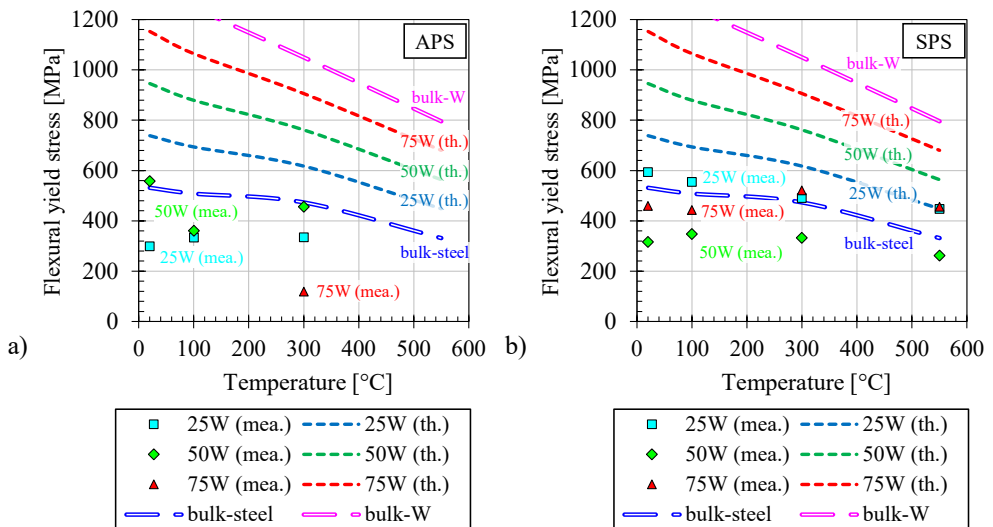


Figure 3.12 Flexural yield stress: a) plasma sprayed composites [11], and b) sintered composites (Note: mea. refers to measured value and th. refers to theoretical expected value)

- Second, the low yield stress of the sintered composites could be explained by the following: The W particles result in localized plastic deformation of the nearby steel matrix, thus reducing the overall yield strength of the composite. Only the yield stress of sintered 25W was somewhat close to its theoretical expected value, but for the sintered 50W and 75W, the yield stresses were even less than that of 25W. This could be due to the higher W volume content in 50W and 75W, which results in a higher number of W-W interfaces, and most of these interfaces could be weak and partially bonded.

3.3 Physical property

3.3.1 Archimedes' density

In addition to the porosity measured via image analysis in Chapter 2, the density of the optimized composites was also measured by Archimedes' principle using 99.9 % pure ethanol fluid at room temperature. Figure 3.13 shows the measured and theoretical (th.) expected density. The theoretical expected density refers to the density assuming no pores. The theoretical expected density for the plasma sprayed composite was calculated based on the actual W volume content, as it contained slightly higher W content than expected (see Figure 2.2 b)). The relative density refers to the ratio of Archimedes' density to that of the theoretical expected density.

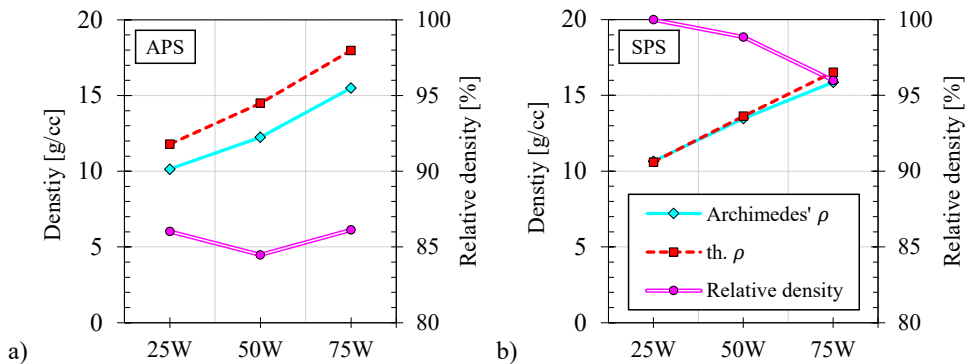


Figure 3.13 Density measured by Archimedes' principle and theoretical expected density, along with the calculated relative density for: a) plasma sprayed composite, and b) sintered composites

The density measured via Archimedes' principle was lower than the theoretical expected density for the plasma sprayed composites; corresponding to $\sim 15\%$ porosity for all three compositions. This shows that the porosity measured by Archimedes' principle is higher than the porosity measured by image analysis (see Figure 2.2 a)). Such behaviour was also observed in previous studies concerning the plasma sprayed composites [11,46,83]. Two reasons can explain this behaviour: First, Archimedes' principle can detect fine pores which cannot be detected by image analysis [83]. Second, the image analysis is performed on micrographs

captured on mechanically polished metallographic samples. The mechanical polishing could close down fine pores/cracks and alter the surface. After the heat treatment, there was a slight increase in Archimedes' density. The density increased by 1.9 %, 2.0 %, and 2.6 % for 25W, 50W, and 75W composite, respectively, to their original density.

For the sintered composites, the density measured from Archimedes' principle and theoretical expected density was almost the same, as can be seen in Figure 3.13 b). The 25W and 50W composites were 99+ % dense, and the 75W resulted in 96 % relative density (corresponding to 4 % porosity). After the heat treatment, 25W and 75W showed no significant change in the density. Only in 50W, the density reduced by 0.4 % to its original density after the heat treatment; this could be due to the formation of severe IMC, resulting in the volume expansion, as mentioned earlier.

3.4 Thermophysical characterization

The thermophysical characterizations were performed on as-sintered/as-sprayed as well as on heat-treated composites.

3.4.1 Dilatometer analysis

The dilatation behaviour was investigated with the help of a vertical double specimen dilatometer DIL L75 V from Linseis Messgeräte GmbH, Germany. The measurement was performed under Ar atmosphere between 20–1000 °C at 3 K/min heating rate. The specimen geometry for the plasma sprayed composites and sintered composites was 25 mm × 3 mm × 2 mm and 15 mm × 4 mm × 2 mm, respectively. The dilatation measurement for the plasma sprayed composites was performed along the coating plane. The same for the sintered composites was measured along the direction perpendicular to the direction of applied consolidation force. The measured secant CTE was also compared with the theoretical expected value. The precise prediction of the theoretical CTE of the composite is complex and highly influenced by the spatial placement of its constituents and their elastic-plastic behaviour [84]. So, two simple models have been used for the estimation. The temperature dependent theoretical expected secant CTE ($\alpha_{th-APS}(V_W, T)$) for the plasma sprayed composite was calculated following Equation (3.5) [50]. This model was chosen because of the lamellar structure of W and steel constituents. The same for sintered composites ($\alpha_{th-SP}(V_W, T)$) was calculated following a simple linear interpolation model, as per Equation (3.6). This model was chosen because of the homogenous and random distribution of spherical W particles inside the steel matrix. $\alpha_W(T)$ and $\alpha_{steel}(T)$ are the temperature dependent secant CTE of bulk-W and bulk-steel, respectively. $E_W(T)$ and $E_{steel}(T)$ are the temperature dependent elastic modulus of bulk-W and bulk-steel, respectively. These temperature dependent values for bulk-W and bulk-steel were taken from MPH [16,21].

$$\alpha_{th-APS}(V_W, T) = \frac{\alpha_W(T) \cdot V_W \cdot E_W(T) + \alpha_{steel}(T) \cdot (1 - V_W) \cdot E_{steel}(T)}{V_W E_W(T) + (1 - V_W) E_{steel}(T)} \quad (3.5)$$

$$\alpha_{th-SPS}(V_W, T) = \alpha_W(T) \cdot V_W + \alpha_{steel}(T) \cdot (1 - V_W) \quad (3.6)$$

3.4.1.1 Dilatation behaviour of plasma sprayed composites

The relative change in length ($\Delta L/L_0$) is presented in Figure 3.14 a). A kink at around 600 °C was observed during the first measurement cycle (heating step) for the as-sprayed 25W and 50W composites, which was not present during the second measurement cycle. Upon further heating above 600 °C, all three compositions underwent austenitic transformation (γ_{trans}) in their as-sprayed state. The austenite start temperature (Ac_1) and finish temperature (Ac_3) were 820 °C and 850 °C, respectively. Upon cooling (~ 0.133 K/s), the austenite fully transformed into ferrite+carbide ($\alpha+M_{23}C_6$) without showing any martensitic transformation—martensitic transformation would theoretically occur at 300–400 °C—. The start (Ar_4) and finish (Ar_1) temperatures of this $\alpha+M_{23}C_6$ transformation were 770 °C and 710 °C, respectively. The heat-treated composites showed no austenitic transformation, as shown in Figure 3.14, where a heat-treated 25W is also plotted. Similar behaviour was observed for heat-treated 50W and 75W composites (see Appendix E).

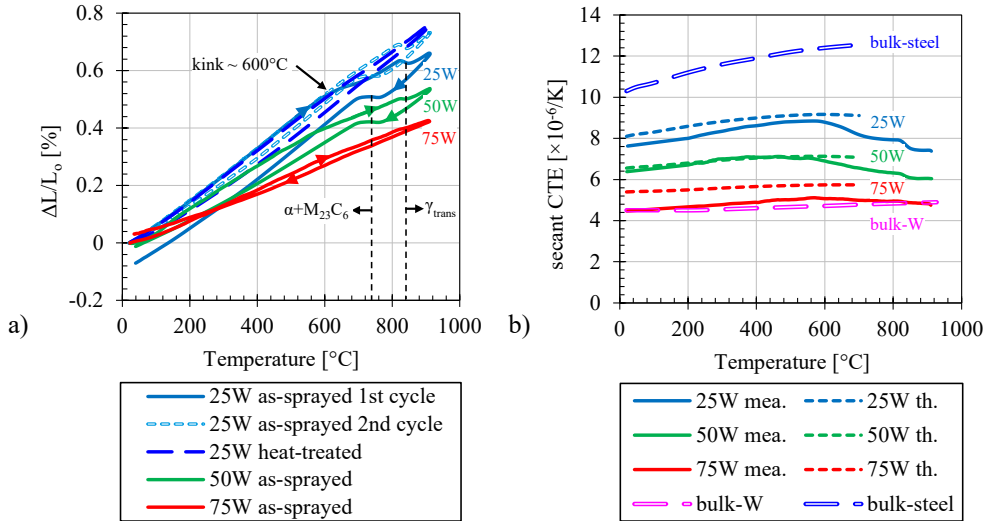


Figure 3.14 a) Relative change in length for plasma sprayed composites, b) Secant CTE for as-sprayed composites and their respective theoretical expected values (*Note: mea. refers to measured value and th. refers to theoretical expected value*)

The secant CTE calculated for 25W and 50W as-sprayed composites agree well with the theoretical expected value up to 600 °C, as shown in Figure 3.14 b), along with that of bulk-W and bulk-steel taken from MPH [16,21]. Beyond 600 °C, there is a decrease in the CTE due to the kink mentioned above at 600 °C. This decrease was absent in the heat-treated composites,

and the CTE matched well with theoretical value, even beyond 600 °C. The CTE of the 75W composite was significantly lower than its theoretical counterpart; the reason for this is not fully understood. Supplementary information comprising individual measurement data is provided in Appendix E.

3.4.1.2 Dilatation behaviour of sintered composites

Figure 3.15 a) illustrates the percentage relative change in length for sintered composites in their as-sintered and heat-treated states. The 25W and 75W composites did not show any change in their length after the complete measurement (heating+cooling) cycle. However, the 50W composite showed a 0.32 % increase in length after each measurement cycle, indicating an increase in volume. It is because of the steep increase in the length in the range 900–1000 °C; this could be attributed to the formation of severe IMC, as mentioned earlier.

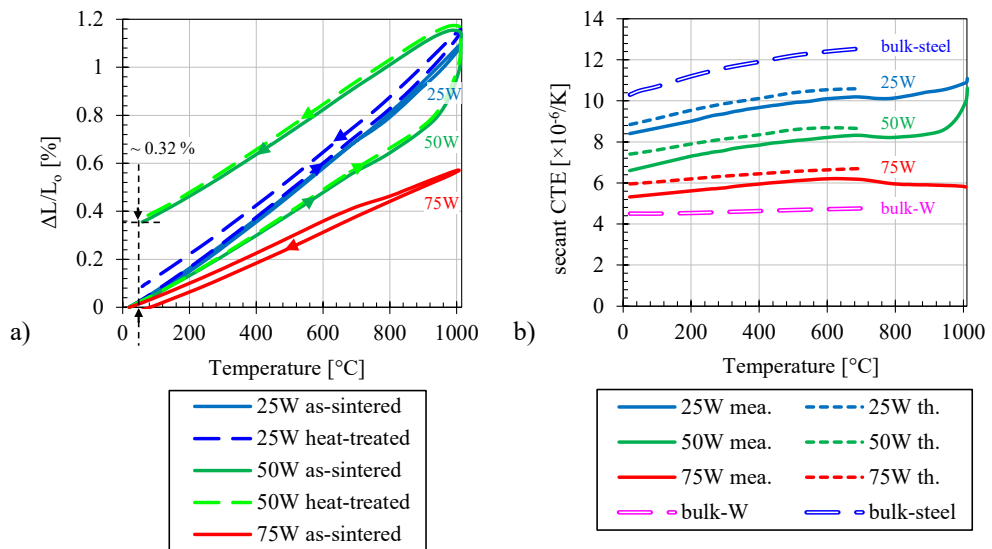


Figure 3.15 a) Relative change in length for sintered composites, b) Secant CTE for as-sintered composites and their respective theoretical expected values (*Note: mea. refers to measured value and th. refers to theoretical expected value*)

The secant CTEs calculated for the as-sintered state agree reasonably well with their theoretical expected values, as illustrated in Figure 3.15 b). Likewise, the CTEs for the heat-treated state also agreed well with the theoretical expected values (see Appendix E).

3.4.2 Differential scanning calorimetry analysis

The specific heat capacity was determined by differential scanning calorimetry (DSC) technique with the help of equipment DSC 404 F3 from Netzsch-Gerätebau GmbH, Germany. The specimens had a geometry of $\varnothing 5 \text{ mm} \times 1.5 \text{ mm}$. The measurements were performed under Ar atmosphere at a heating rate of 20 K/min between 20–1000 °C. The measured values were compared with the theoretical expected values ($c_{p,h}(V_{W,T})$) following Equation (3.7). $c_{p,W}(T)$

and $c_{p,steel}(T)$ are the temperature dependent specific heat capacity of bulk-W and bulk-steel, whereas ρ_W and ρ_{steel} are the density of W and steel. These values are taken from the MPH [16,85].

$$c_{p,th}(V_W, T) = \frac{c_{p,W}(T)\rho_W V_W + c_{p,steel}(T)\rho_{steel}(1 - V_W)}{\rho_W V_W + \rho_{steel}(1 - V_W)} \quad (3.7)$$

All the composites showed Curie transformation at around 735 °C, as can be seen in Figure 3.16. The plasma sprayed composites showed austenitic transformation for all three compositions in both their as-sprayed and heat-treated states. The Ac_1 and Ac_3 in their as-sprayed state were found to be 820 °C and 855 °C, respectively. This was almost the same as what was observed in Section 3.4.1. After the heat treatment, Ac_1 and Ac_3 increased slightly to 835 °C and 890 °C, respectively. This increase is due to the diffusion of W from W-splats into the steel-splats; the increase in W content in steel increases the eutectoid temperature (austenite transformation temperature) [86]. As can be seen from Figure 3.16 a), the specific heat capacity of the plasma sprayed composites in their as-sprayed state is slightly lower than the theoretical expected values. However, after the heat treatment, the response became closer to the expected value, as shown in Appendix E.

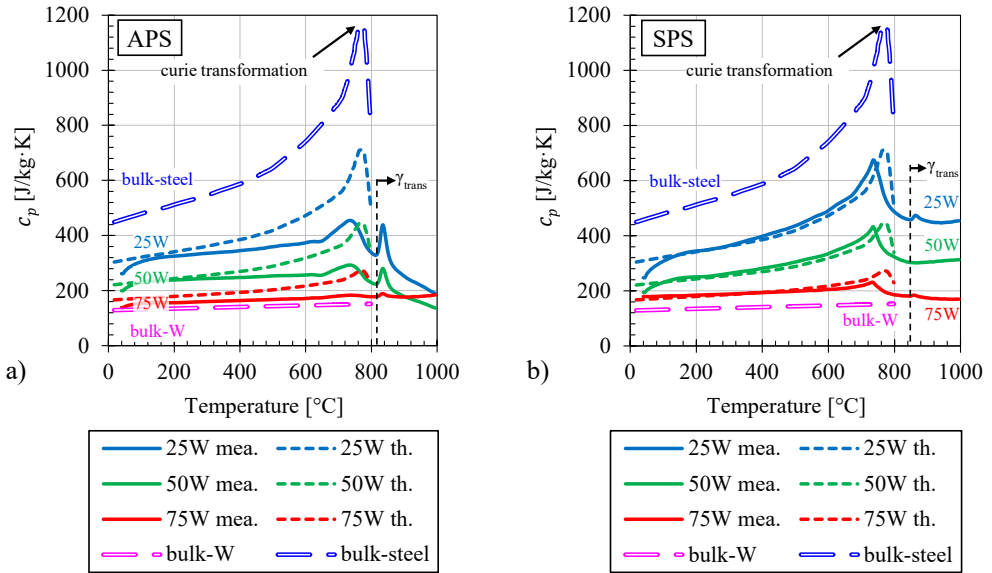


Figure 3.16 Temperature dependent specific heat capacity response of: a) plasma sprayed composites in their as-sprayed state, b) sintered composites in their as-sintered state (*Note: mea. refers to measured value and th. refers to theoretical expected value*)

The specific heat capacity of the sintered composites agrees well with the theoretical expected values, as seen in Figure 3.16 b). The as-sintered composites displayed austenitic transformation with Ac_1 and Ac_3 of 850 °C and 890 °C respectively, which is close to that of the literature value of Eurofer 97 ($Ac_1 = 830$ °C and $Ac_3 = 890$ °C) [22]. The heat treatment did

not affect the specific heat capacity, except that none of the compositions showed any austenitic transformation after the heat treatment. The measurement data for the heat-treated state can be found in Appendix E.

3.4.3 Laser flash analysis

The thermal conductivity was determined with the help of laser flash analysis (LFA) technique, using an equipment LFA 427 from Netzsch-Gerätebau GmbH, Germany. The specimen geometry was 10 mm × 10 mm × 1.5 mm. The measurement was performed under Ar atmosphere, and the laser shots were fired between 20 °C and 1000 °C at an interval of 200 °C. The measured temperature dependent thermal conductivity was compared with the theoretical expected value ($\lambda_{th}(V_W, T)$) following the Equation (3.8). The temperature dependent thermal conductivity of bulk-steel ($\lambda_{steel}(V_W, T)$) and bulk-W ($\lambda_W(V_W, T)$) were taken from MPH [16,21]. This empirical relation was previously used for the FE numerical modelling of FGM by Heuer et al. [44] and Heuer [11]. Also, this empirical relation fits very well, considering the microstructure of the composites. The plasma sprayed composites have a W and steel lamellar type structure, meaning the heat must flow through one after another. In the case of sintered composites, the steel phase acts as a matrix and as explained by Heuer et al. [44], the heat must also flow through each constituent (W and steel) one after the other.

$$\lambda_{th}(V_W, T) = \left(\frac{1 - V_W}{\lambda_{steel}(T)} + \frac{V_W}{\lambda_W(T)} \right)^{-1} \quad (3.8)$$

The temperature dependent thermal conductivity of the plasma sprayed and sintered composites in their as-sprayed and as-sintered states are shown in Figure 3.17 a) and b), respectively. The sintered composites, in their as-sintered state, showed better thermal conductivity. This is expected due to the dense nature of the composites. But the thermal conductivities of plasma sprayed conditions were found to be significantly low and were independent of the volume content of W. This behaviour was also observed by Matejicek et al. [49]. This can be explained based on the following hypothesis:

- Thermal conductivity depends on the quality of intersplat bonding, oxides, porosity and IMC. As explained in Section 3.1.1, the plasma sprayed composites in their as-sprayed state do not contain any IMC, indicating that the other three factors are critical.
- Presence of porosity: Porosity significantly reduces thermal conductivity, and the composites have 15 % porosity, as measured by Archimedes' principle.
- Presence of oxides: Oxides typically have low thermal conductivity; for instance, Fe₃O₄ and Cr₃O₄ have a thermal conductivity of approximately 3.8 W/m·K [87] and 2 W/m·K [88], respectively. The 25W and 50W contain only a low amount of Fe_xCr_yO oxides, approximately 6 % and 3 %, respectively. However, even considering the presence of these oxides, it is unlikely that they are the leading cause of the low thermal conductivity

of the composites. Furthermore, 75W composite contains almost no oxides yet exhibits low thermal conductivity.

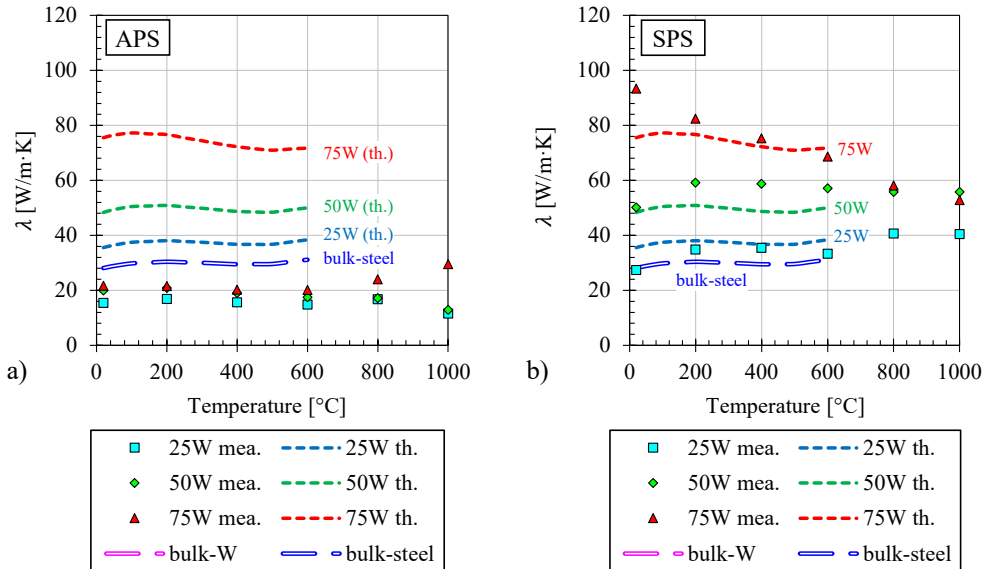


Figure 3.17 Temperature dependent thermal conductivity of: a) plasma sprayed composites in their as-sprayed state, b) sintered composites in their as-sintered state

- Intersplat bonding: As discussed in Sections 2.1.3.1 and 3.1.1, the adhesion between splats is weak. This poor bonding is the significant contributing factor to the low thermal conductivity, as also stated in the literature [50,89].

After the heat treatment, the thermal conductivity of plasma sprayed composites remained almost unchanged, as can be seen in Figure 3.18 a). However, the thermal conductivities of the sintered 50W and 75W composites decreased significantly, as can be seen in Figure 3.18 b). The underlying cause is unclear, but some observations can be made. Heat treatment leads to the formation of IMC, which generally have lower thermal conductivity. The exact thermal conductivity of IMC has not been experimentally determined in any study, but Matejicek et al. [90] have postulated it to be 14–26 W/m·K. The amount of IMC in the sintered 50W composition increased from 5 % to 13 % after heat treatment, which may explain the decrease in its thermal conductivity. However, for the sintered 75W composition, the amount of IMC was only 3 % after heat treatment, which cannot account for the significant reduction in its thermal conductivity.

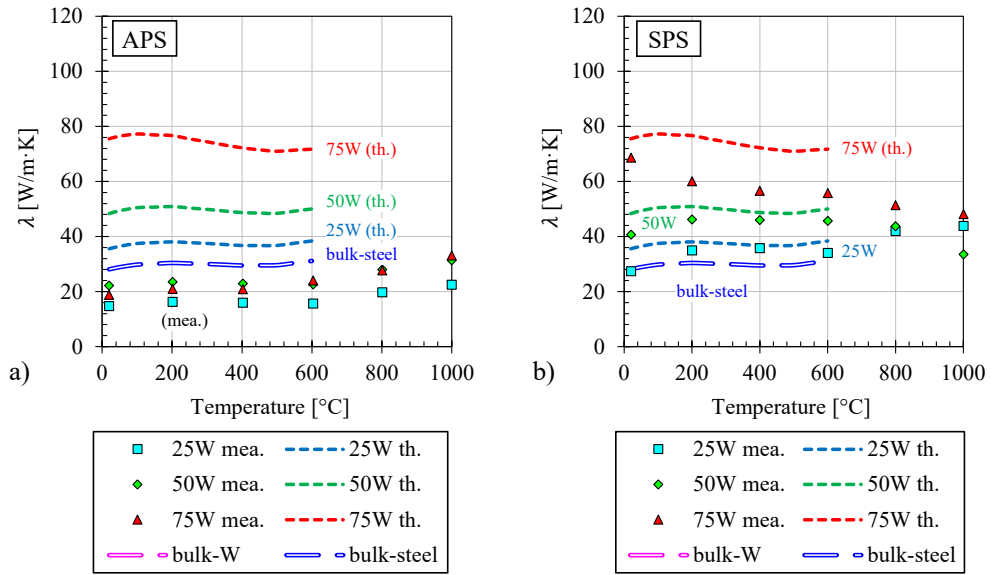


Figure 3.18 Temperature dependent thermal conductivity of: a) plasma sprayed composites, b) sintered composites after heat treatment

3.5 Summary of characterization of composites

The optimized composites manufactured in Chapter 2 were characterized by investigating their microstructure, temperature dependent mechanical, and thermophysical properties. The highlights and essential aspects are summarized in Table 3.6.

Table 3.6 Summarized overview of the properties of plasma sprayed and sintered composites

| Aspect | Plasma sprayed composites | Spark plasma sintered composites |
|----------------|---|---|
| Porosity | <ul style="list-style-type: none"> - Porosity determined via Archimedes' principle was significantly higher than that measured via image analysis. - All three composites were only 85 % dense, corresponding to 15 % porosity | <ul style="list-style-type: none"> - Porosity determined via Archimedes' principle was almost the same as that of what was measured via image analysis - 25W and 50W: 99+ % dense - 75W: 96 % dense, corresponding to 4 % porosity |
| Heat treatment | <ul style="list-style-type: none"> - No significant impact - Only a slight amount of IMC formed (its quantity not detected by image analysis) - This is due to the poor adhesion between W- and steel-splats that hinders the diffusion of W and Fe - Evident austenitic transformation even after heat treatment | <ul style="list-style-type: none"> - Significant impact - Composites showed a substantial amount of IMC, which was not only formed at the W-steel boundaries but also along the grain boundaries of the steel matrix. - This IMC formation is due to the diffusion of W and Fe because of good bonding between W and steel. - Interestingly, IMC does not significantly affect the CTE, specific heat capacity or thermal conductivity. - Steel near the W particles transformed into fully ferritic steel because of the higher W content, which is due to the diffusion of W |
| CTE | <ul style="list-style-type: none"> - Agree well with theoretical model, except for 75W composition - CTE of 75W composite was lower than expected and was close to that of pure W - Heat treatment has no significant effect on CTE | <ul style="list-style-type: none"> - Agree well with theoretical model - Suggests severe formation of IMC in 50W composite between 900–1000 °C |

| Aspect | Plasma sprayed composites | Spark plasma sintered composites |
|---|--|---|
| Specific heat capacity | - Somewhat lower than expected but agreed well with the theoretical model after the heat treatment | - Agree with the theoretical model. |
| <p><i>The FGM must possess suitable mechanical properties, such as elastic modulus, yield strength and ductility, to deform plastically without fracture.</i></p> <p><i>The composites' yield stress/mechanical properties cannot be predicted from simple empirical relations, as they significantly depend on the microstructure.</i></p> | | |
| Mechanical properties | <ul style="list-style-type: none"> - All three compositions showed brittle nature - Low elastic modulus - No ductility - Low flexural strength | <ul style="list-style-type: none"> - 25W: ductile behaviour even at 20 °C - 50W: ductile nature at 300 °C - 75W: ductile nature at 500 °C - Better elastic modulus - Better toughness - Stress response for 50W and 75W is substantially lower than that of 25W, even though 50W and 75W have higher W volume content. - Low yield stress of 50W and 75W |
| <p><i>Generally, the FGM should have high thermal conductivity to quickly remove the heat generated inside the reactor and reduce the W armour's temperature.</i></p> | | |
| Thermal conductivity | <ul style="list-style-type: none"> - Low thermal conductivity - Lower than steel | <ul style="list-style-type: none"> - Higher than that of plasma sprayed composites - Higher than steel - Agree with theoretical expected models - However, the heat treatment reduced the thermal conductivity of composites. This reduction in thermal conductivity is probably not because of the formation of IMC |
| Major learnings | Poor properties are due to the following reasons: poor intersplat bonding, higher porosity and the presence of oxides. | The dense nature of the sintered composites also reflects their better properties, but the poor bonding of W-W interface in 50W and 75W lowers their mechanical properties. |

4 Manufacturing of joints

After characterizing individual layers of the FGM, W-steel graded joints featuring FGM interlayer were manufactured. The bulk-W, at the top of the joint, and bulk-steel (Eurofer 97), at the bottom of the joint, both had a thickness of 3 mm. This thickness was chosen considering the previous FE numerical study of a graded FW by Heuer et al. [44]. The intended thickness of each layer of the FGM (25W, 50W, and 75W) was 0.5 mm. So, this chapter aims to meet the following objectives:

- To manufacture joints that can be benchmarked via cyclic HHF thermal loading.
- To join bulk-W with 75W composite, which is the most challenging part.
- To optimize the processing parameters with the help of microstructural investigation.

4.1 Joint featuring sintered graded interlayer

4.1.1 Co-sintering of 75W and bulk-W

As explained in Section 2.3.5, a feasibility study was conducted to bond bulk-W and 75W together using a co-sintering method. The methodology was discussed in the same section, and two 75W powder combinations were tested: $75W_{10-30}+25S_{3-13}$ and $75W_{30-60}+25S_{10-20}$. The outcomes of this study are shown in Figure 4.1.

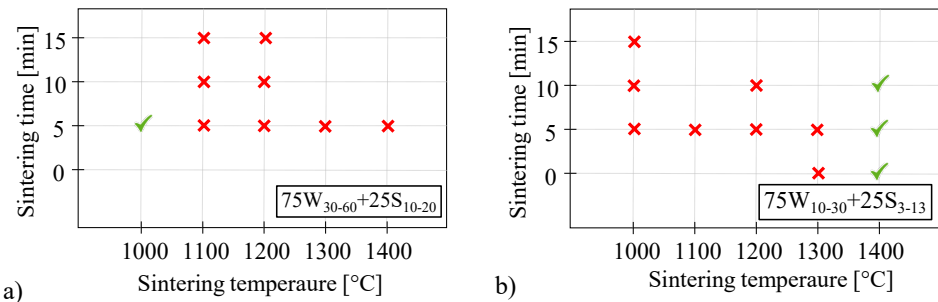


Figure 4.1 Results of co-sintering of 75W powder and bulk-W for: a) $75W_{30-60}+25S_{10-20}$, and b) $75W_{10-30}+25S_{3-13}$ (Nomenclature: ✓ represents the trial where the 75W and bulk-W remain attached after removing the stack out of the die and even after cutting it for metallographic investigation, ✗ represents the trial where the 75W and bulk-W fall apart/delaminate)

For $75W_{30-60}+25S_{10-20}$, only the co-sintering performed at 1000 °C resulted in a successful bonding, as can be seen in Figure 4.1 a). The low temperature (1000 °C) and short time (5 min) retained the original elongated grain structure of the bulk-W, as can be seen in Figure 4.2. The

co-sintering performed at 1100 °C, 5 min resulted in an inconclusive result; in one trial, sintered 75W and bulk-W remained attached, while in the other trial, they fell apart during the cutting for its metallographic investigation. For all other trials, sintered 75W and bulk-W fell apart just after being removed from the graphite die.

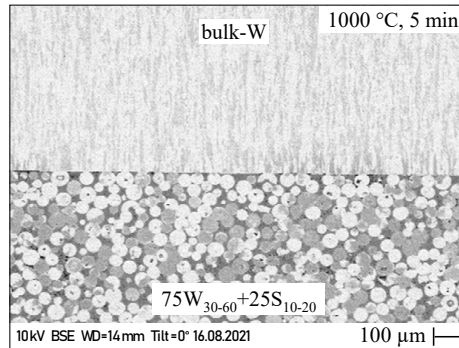


Figure 4.2 Bonding seam between the sintered 75W₃₀₋₆₀+25S₁₀₋₂₀ and bulk-W for the co-sintering performed at 1000 °C, 125 MPa, 5 min

As only the co-sintering performed at 1000 °C was successful, a comprehensive microstructural investigation of its 75W-W bonding seam was performed, as shown in Figure 4.3. Some random regions were investigated, and it was found that the bonding was not satisfactory, which was based on the following observations:

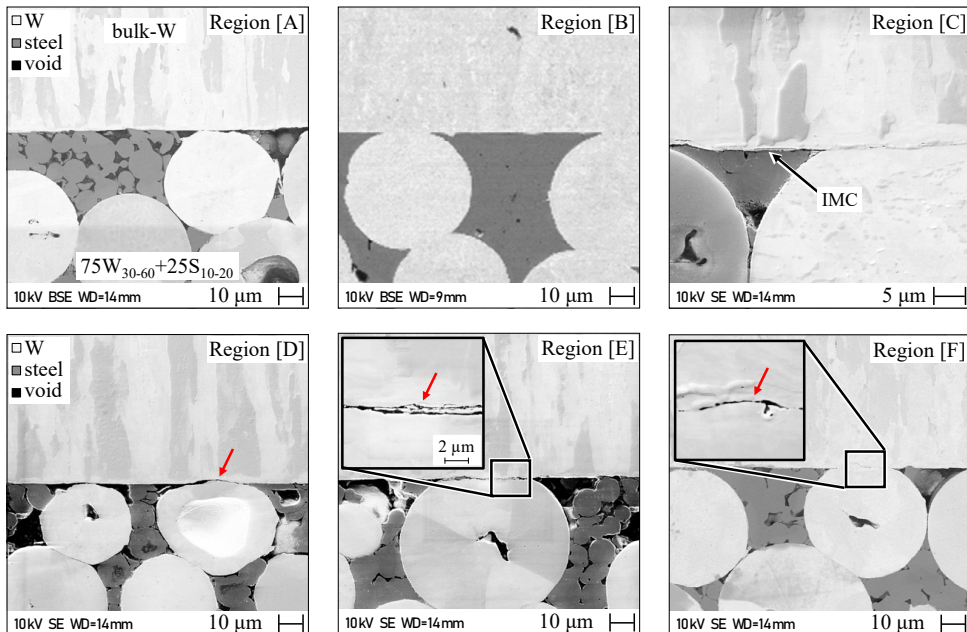


Figure 4.3 Bonding seam between 75W₃₀₋₆₀+25S₁₀₋₂₀ and bulk-W at different regions; co-sintering performed at 1000 °C, 125 MPa, 5 min

- In certain regions, such as Region A in Figure 4.3, the steel particles adjacent to the bonding seam did not sinter. As a consequence, there were vacancies near the bonding seam, leading to poor bonding between the steel and bulk-W. This was due to insufficient steel particles near the bonding seam to fill the vacancies created by the W particles.
- In certain regions, such as Region B and C, the steel particles filled the gap created by the packed W particles, resulting in ideal metallurgical bonding with bulk-W. Additionally, W particles also formed proper metallurgical bonding with bulk-W.
- In other regions, such as Region D to F, W particles did get pressed onto the bulk-W. However, they did not initiate metallurgical bonding, as marked by the red arrow.
- While it is beyond the scope of this thesis to quantitatively determine the number of W particles that form perfect bonding with bulk-W, it can be qualitatively assumed that only a partial number of W particles make metallurgical bonding.

Strangely, co-sintering at temperatures higher than 1000 °C did not bond 75W₃₀₋₆₀+25S₁₀₋₂₀ with bulk-W, despite higher temperatures typically resulting in better diffusion and metallurgical bonding. For one failed trial, the delaminated surface of bulk-W was examined, revealing a large portion of IMC and circular marks where W particles were in contact with the bulk-W, as shown in Figure 4.4. Unfortunately, this investigation did not provide a definitive explanation for this unexpected behaviour. It is currently assumed that internal residual stress

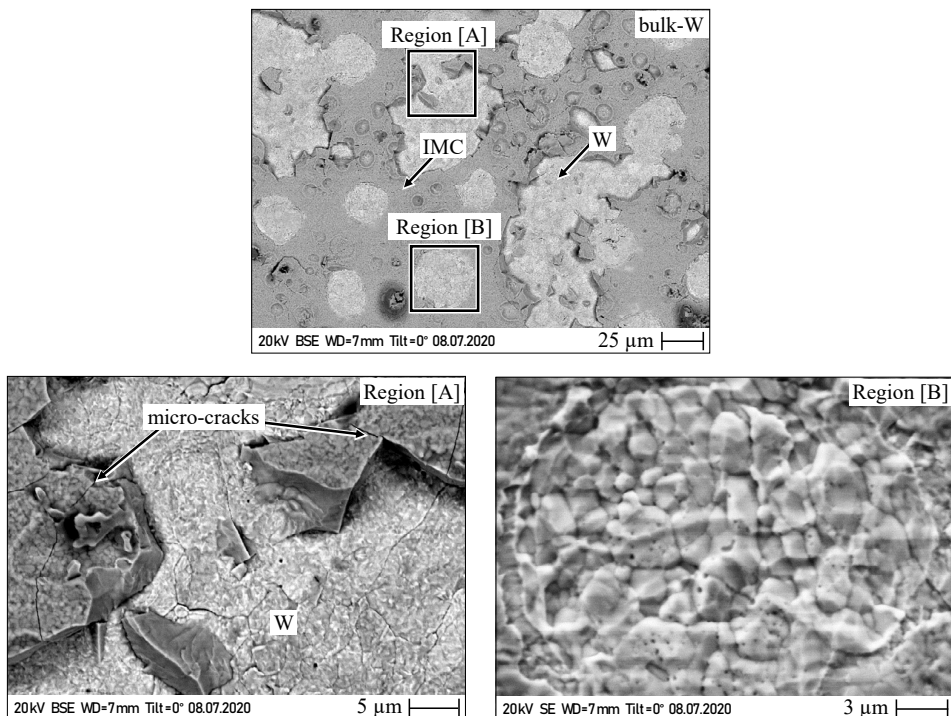


Figure 4.4 Delaminated surface of bulk-W for the co-sintering trial of 75W₃₀₋₆₀+25S₁₀₋₂₀ performed at 1300 °C for 5 min

arising after the co-sintering is the likely cause. One might contemplate that this might be due to the rapid cooling during co-sintering, but few trials were also performed with slow cooling, yet detachment still occurred.

For another combination with finer W particles ($75W_{10-30}+25S_{3-13}$), only the co-sintering performed at 1400 °C resulted in the bonding, as can be seen in Figure 4.1 b). The sintered

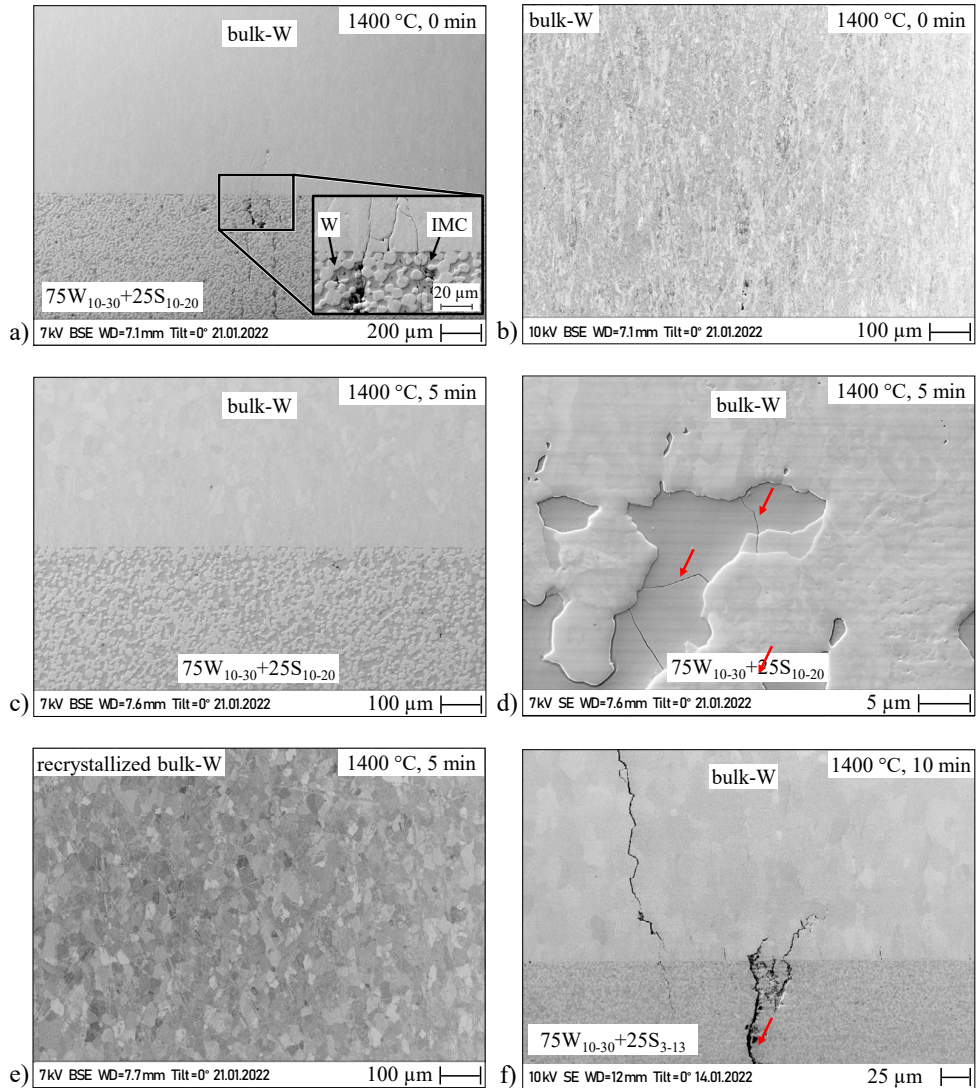


Figure 4.5 Cross-sectional micrographs of co-sintering of bulk-W and $75W_{10-30}+25S_{3-13}$; a) Bonding seam showing macrocracks for the co-sintering performed at 1400 °C, 0 min, b) Microstructure of bulk-W after the co-sintering at 1400 °C, 0 min, c) and d) Co-sintering performed at 1400 °C, 5 min showing microcracks inside IMC. e) Microstructure of the completely recrystallized bulk-W, f) Macrocracks in bulk-W as well as in $75W$ for a co-sintering performed at 1400 °C, 10 min

75W₁₀₋₃₀+25S₃₋₁₃ formed good metallurgical bonding with bulk-W, as can be seen in Figure 4.5. Even the W-particles formed an ideal metallurgical bonding with bulk-W over the entire bonding seam. Despite successful bonding, several significant disadvantages make it undesirable for further application: First, the entire steel constituent of the 75W transformed into brittle IMC, resulting in macrocracks throughout the 75W composite, as seen in Figure 4.5 a) and f). Second, the high sintering temperature (1400 °C) caused the recrystallization of bulk-W. The bulk-W, however, retained some of its original long grain structure to a certain extent for the sintering time of 0 min*, as can be seen in Figure 4.5 b). An increase in the sintering time to 5 min or 10 min completely recrystallized the bulk-W, as can be seen in Figure 4.5 e) and f). The recrystallisation is not desired as it weakens the bulk-W, makes it prone to cracking (Figure 4.5 f), and makes it less suitable for the application as FW armour [91]. Third, microcracks were also observed in IMC, marked by red arrow in Figure 4.5 d).

At a lower co-sintering temperature of 1000 °C, the sintered 75W₁₀₋₃₀+25S₃₋₁₃ detached from bulk-W, unlike 75W₃₀₋₆₀+25S₁₀₋₂₀. Again, the reason behind this strange behaviour is not fully understood. The residual stress within the 75W composite likely caused it to detach from bulk-W. Likewise, the delaminated surface of W-tile for a co-sintering trial of 75W₁₀₋₃₀+25S₃₋₁₃ and bulk-W performed at 1200 °C showed some IMC sticking onto it, as can be seen in Figure 4.6. But, no further explanation could be given for this strange behaviour.

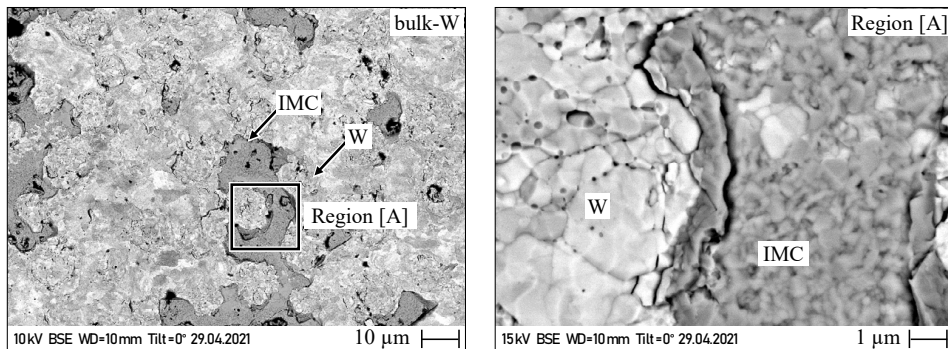


Figure 4.6 Delaminated surface of bulk-W for the trial of 75W₁₀₋₃₀+25S₃₋₁₃ performed at 1200 °C, 5 min

4.1.2 Joining of W and steel with 3-layer FGM

The co-sintering feasibility study revealed that only one combination (75W₃₀₋₆₀+25S₁₀₋₂₀) could bond with bulk-W when co-sintered at 1000 °C, 5 min, 125 MPa without severe disadvantages. Although the bonding is not perfect, it still holds both parts together. So from now on, for ease of reading, 75W refers to this particular combination 75W₃₀₋₆₀+25S₁₀₋₂₀. It must also be remembered that the 25W and 50W sintered composites also have the same optimum sintering parameter, i.e. 1000 °C, 5 min, 125 MPa. Therefore, a graded joint featuring 3-layer FGM interlayer was manufactured. For this, bulk-steel and bulk-W were cut in the form of disc (Ø 20 mm × 3 mm). The bonding surfaces were ground and then cleaned in an ultrasonic bath

*0 min means heating to the desired sintering temperature, and then cooling down, without any dwell time

using acetone. The bulk-steel disc was placed inside the graphite die. Then 25W powder of volume corresponding to a geometry $\text{Ø } 20 \text{ mm} \times 0.5 \text{ mm}$ was poured onto it. This was then pre-pressed to 125 MPa pressure. Afterwards, 50W powder of the same volume was poured and pre-pressed to 125 MPa, followed by 75W powder following the same procedure. Finally, the bulk-W disc was placed at the top, and this complete stack was pre-pressed only to 3 kN ($\sim 10 \text{ MPa}$). This complete stack was sintered at the optimum sintering parameter ($1000 \text{ }^\circ\text{C}$, 5 min, 125 MPa), followed by rapid cooling to produce quenched martensite. The cross-section of this manufactured joint is shown in Figure 4.7.

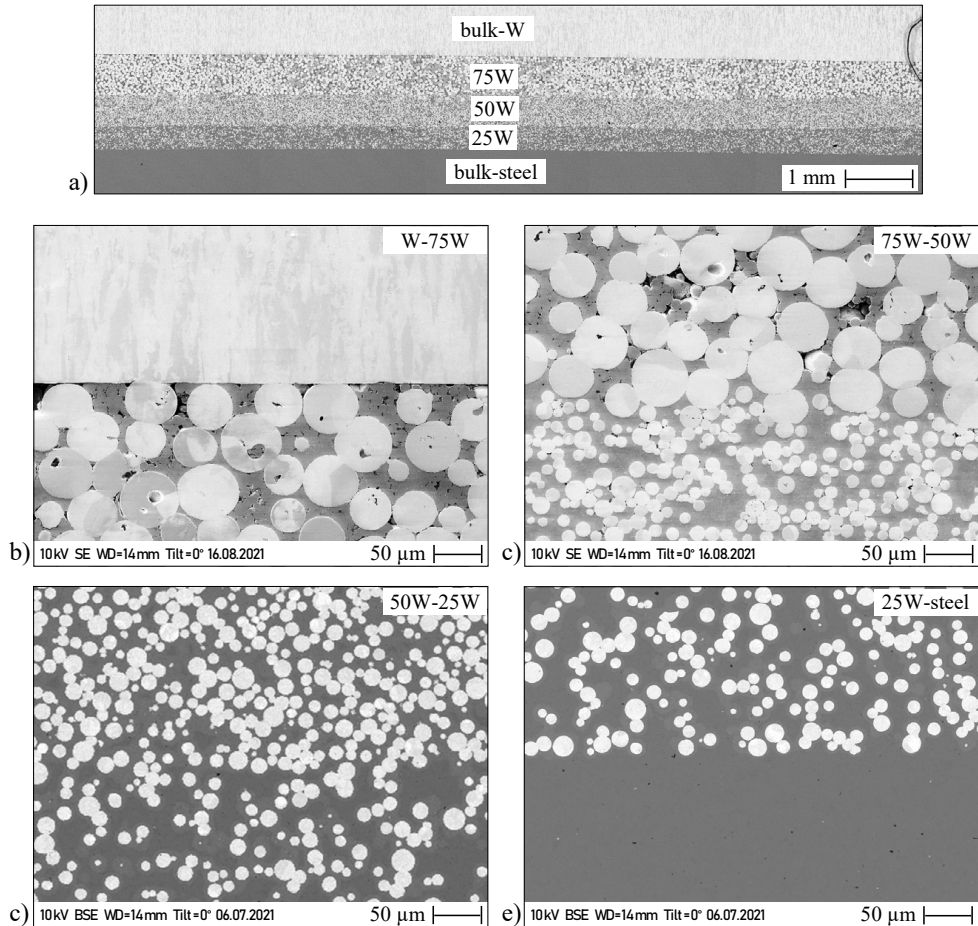


Figure 4.7 a) Cross-section of the W-steel graded joint featuring a 3-layer sintered FGM interlayer; b) Bonding seam between bulk-W and 75W, c) Transition between 75W and 50W, d) Transition between 50W and 25W, and e) Bonding seam between 25W and bulk-steel

4.1.3 Joining of W and steel with 2-layer FGM

As mentioned in Section 4.1.1, the bonding between 75W and bulk-W was not perfect. Therefore, one more graded joint was manufactured by omitting the topmost 75W layer, which means a 2-layer FGM interlayer consisting of 25W and 50W. The manufacturing procedure

was the same as explained above. The stack was sintered at the same optimum sintering parameters (1000 °C, 5 min, 125 MPa). The cross-section of this manufactured joint is shown in Figure 4.8. The bonding seam between bulk-W and 50W revealed a perfect bonding; the steel constituent formed a thin layer of IMC with bulk-W, and the W particles also formed sufficient metallurgical bonding with bulk-W, as seen in Region A and B of Figure 4.8 b).

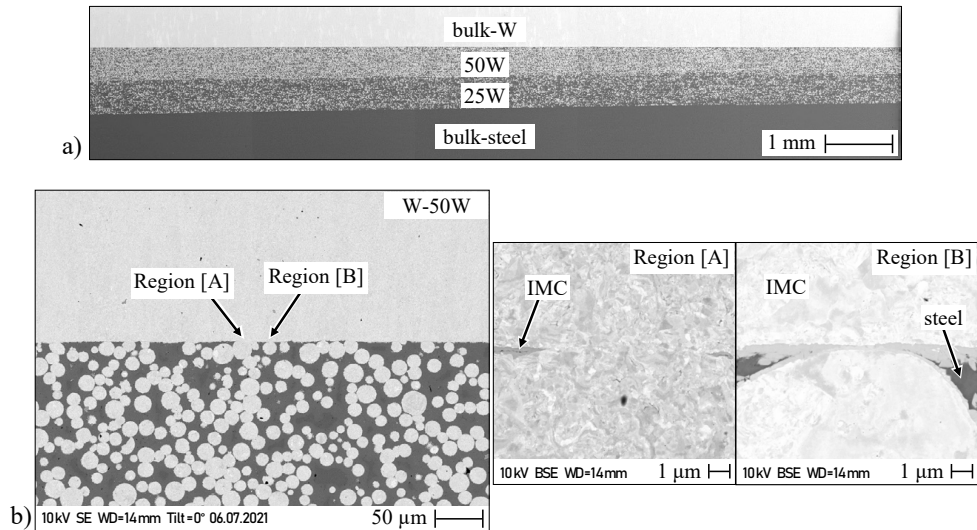


Figure 4.8 a) Cross-section of the W-steel graded joint featuring a 2-layer sintered FGM interlayer; Interface of b) bulk-W and 50W showing two regions of interest

4.2 Joint featuring plasma sprayed graded interlayer

One of the goals of the thesis was to use a hybrid technique involving plasma spraying and current-assisted diffusion bonding (CA-DB) to manufacture a graded joint featuring plasma sprayed FGM. So, individual plasma sprayed composites (25W, 50W, and 75W) were cut out from the steel substrates on which they were sprayed. The objective was to join them together with bulk-W and bulk-steel using CA-DB process, as schematically illustrated in Figure 4.9 a). For simplicity, only two parts are shown. The same SPS setup described in Section 2.3.1 was used, but with a 30 mm diameter graphite tool. The pressure and time profile for the joining procedure is schematically represented in Figure 4.9 b). The bonding pressure was set to 50 MPa and the cooling was done rapidly to form martensite in bulk-steel.

The parts to be joined had a 12 mm × 12 mm geometry. The plasma sprayed composites (25W, 50W, and 75W) were cut into the same geometry with a thickness of ~0.5 mm. The bulk-W and bulk-steel were cut into the same geometry with a thickness of 3 mm. Before joining, the mating surfaces were ground down to P4000 grit size using diamond grinding discs called MD-Piano from Struers GmbH, Germany. This was done to maintain the flatness of the mating surface and avoid any undesirable edge rounding that can result from using SiC grinding papers. Such edge rounding must be avoided, as it can result in unsuccessful bonding. After grinding, the mating surfaces were cleaned in an ultrasonic acetone bath for 20 min.

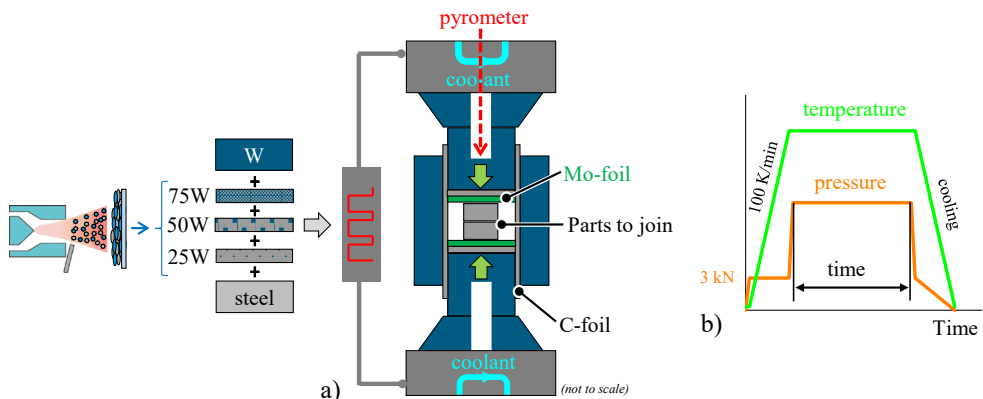


Figure 4.9 Schematic representation of the produce; a) Setup for current-assisted diffusion bonding, b) Temperature, pressure vs time profile for joining

As there are five different materials (bulk-W, 75W, 50W, 25W and bulk-steel) to be joined together, a systematic approach was undertaken, involving three steps:

- First, the joining of 75W and bulk-W.
- Second, the bonding of all three individual layers (25W, 50W and 75W) together.
- Third, the bonding of 25W and bulk-steel.

4.2.1 Joining trials for bonding 75W and bulk-W

The preliminary observations of the feasibility study to join bulk-W and 75W layer are provided in Table 4.1. Two joining times were tested (30 min and 60 min).

Table 4.1 Joining trials for bonding bulk-W with plasma spayed 75W

| Configuration | Joining parameter | | Remarks |
|--------------------|-------------------|-------|---|
| | (°C) | (min) | |
| bulk-W + 75W | 800 | 30 | No signs of bonding, the parts detached just after removing them from the graphite tool after the completion of joining cycle |
| | 900 | 30 | |
| | 1000 | 30 | Only partial metallurgical bonding, most of the regions showed no bonding, as depicted in Figure 4.10 a) and b) |
| | 1000 | 60 | No improvement, and only few locations showed some metallurgical bonding. Long joining time resulted in high amount of IMC |
| | 1100 | 30 | No improvement. Centre of the joint showed sufficient bonding, as seen in Figure 4.11 b) and d). Edge remained unbonded, as seen in Figure 4.11 a) and c). |
| | 1200 | 30 | High amount of detrimental IMC, which drastically increased as the temperature increased to 1200 °C, as can be seen in the rightmost magnified snippet in Figure 4.11 d). |

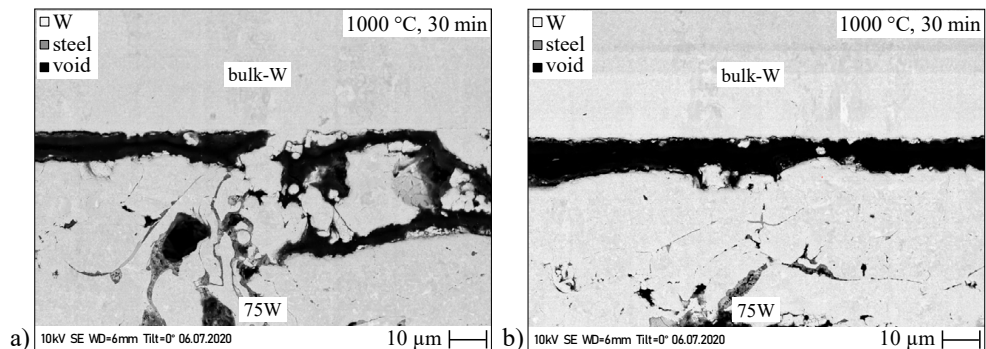


Figure 4.10 Cross-sectional micrographs after joining 75W and bulk-W at 1000 °C, 30 min, showing two random locations with insufficient bonding

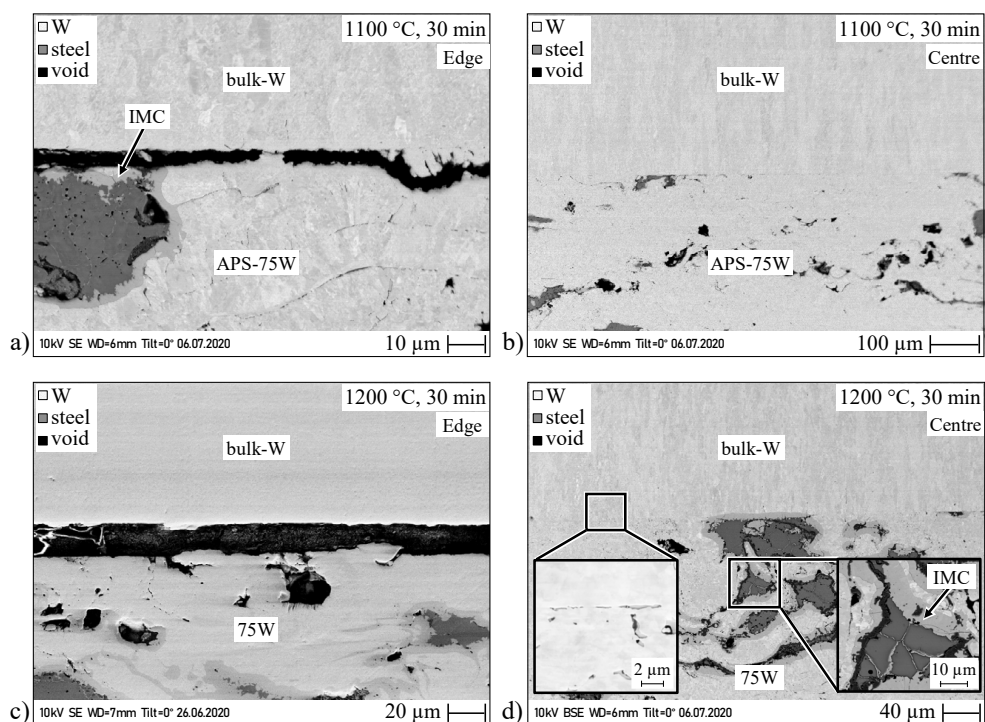


Figure 4.11 Cross-sectional micrographs after joining 75W and bulk-W with the following joining parameters: a), b) 1100 °C, 30 min and c), d) 1200 °C, 30 min

4.2.2 Joining trials for bonding 75W and bulk-W with thin V-foil

According to the feasibility study, the joining of 75W and bulk-W was impossible, indicating the need for a filler material to mediate the joining. W is the major constituent in 75W, signifying that the filler material should be able to form metallurgical bonding with W. As discussed in Section 0, V is one such material that can bond with W. Thus, a 99.9+ % pure V-foil of thickness 0.3 mm was selected for this purpose and purchased from HMW Hauner GmbH & Co. KG, Germany. The V-foil was also cut into the same 12 mm × 12 mm geometry and placed between 75W and bulk-W. The mating surfaces underwent the same preparation steps. This stack was then joined at different joining temperatures, as mentioned in Table 4.2.

Table 4.2 Joining trials for bonding bulk-W and 75W with V-foil and observations

| Configuration | Joining parameter | | Remarks |
|---------------|-------------------|-------|--|
| | (°C) | (min) | |
| bulk-W | 800 | 30 | Satisfactory bonding |
| + | 800 | 60 | |
| V-foil | 900 | 30 | Better diffusion between W and V as compared with that of 800 °C |
| + | 1000 | 30 | |
| 75W | | | |

The introduction of V-filler resulted in better bonding at the centre as well as near the edges. A cross-sectional micrograph of the joint bonded at 900 °C, 30 min is shown in Figure 4.12 a). It is representative of other joints bonded at 800 °C and 1000 °C. The steel-splats of the 75W formed a $\sim 3 \mu\text{m}$ thin reaction layer with V, as can be seen in the magnified snippet in Figure 4.12 b). This reaction layer was found to be vanadium carbide, as suggested by the EDX analysis. Such a vanadium carbide layer was also observed in previous studies of Basuki and Aktaa [36] and Basuki et al. [37]. The W-splats of 75W also formed thorough bonding with the V-foil, as can be seen in Figure 4.12 b).

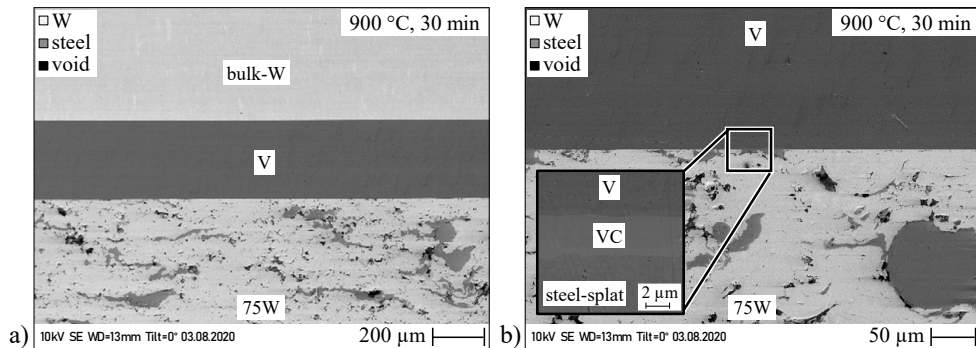


Figure 4.12 a) Cross-sectional micrograph of 75W bonded to bulk-W with a V-filler; joining performed at 900 °C, 30 min, b) Bonding seam between V-filler and 75W showing the formation of vanadium carbide with steel-splat of 75W

Similarly, the bulk-W and V also formed good metallurgical bonding over the entire bonding seam. As can be seen in Figure 4.13, the diffusion of W into V was more predominant at a higher temperature of 900 °C (see Figure 4.13 b)) than at 800 °C (see Figure 4.13 a)). This diffusion is advantageous for the appropriate bonding of bulk-W and V, implying that the preferred bonding temperature must be more than 900 °C.

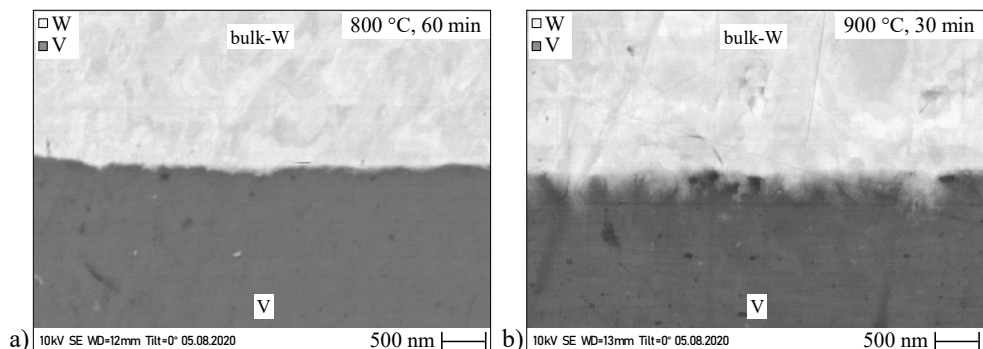


Figure 4.13 Interface of W-V for the joining performed at: a) 800 °C, 60 min and b) 900 °C, 30 min

4.2.3 Joining 75W, 50W, and 25W together

The next step was to study the feasibility of joining 25W, 50W, and 75W layers together. Therefore, the parts to be bonded were placed on top of each other in a graded fashion and joined at different parameters, as mentioned in Table 4.3.

Table 4.3 Joining trials for bonding 75W, 50W and 25W together and their observations

| Configuration | Joining parameter | | Remarks |
|-----------------------------|-------------------|-------|--|
| | (°C) | (min) | |
| 75W + 50W + 25W | 800 | 30 | No substantial metallurgical bond formation; most of the bond interfaces with steel-steel in contact remained unbonded; even the longer bonding time of 60 min did not result in any improvement in bond quality |
| | 800 | 60 | |
| | 900 | 30 | No significant improvement in the bonding |
| | 1000 | 30 | Reasonable metallurgical bonding, but joining time of 60 min resulted in high amount of IMC |
| | 1000 | 60 | |
| | 1100 | 30 | |
| | | | Reasonable bonding High amount of IMC |
| | 1200 | 30 | Severe reduction in the thickness of the layer after the bonding. |

The joining performed at 900 °C did not result in any significant bonding. Figure 4.14 shows the bonding seam between 75W and 50W. Region A shows the interface between the steel-splat of 50W and W-splat of 75W. It was observed that they both formed proper metallurgical bonding, but the steel formed a thin passive oxide layer. This passive oxide layer—possibly chromium oxide—is commonly formed on the surface of stainless steel just after grinding, as stated by Gietzelt et al. [92]. A passive oxide layer is unavoidable because stainless steels always form a passive oxide layer just after surface preparation. It was also mentioned by Gietzelt et al. [92] that a higher joining temperature helps to dissolve these passive layers into the steel, and specific surface preparation techniques can prevent this passive layer like: sputter cleaning with Ar ions using magnetron sputtering, chemical pickling or coating with a thin layer of gold/silver. The interface between the W-splats of 50W and 75W is shown in Region B and C of Figure 4.14. It can be seen that they did not form any metallurgical bonding, suggesting that the bonding temperature was too low to initiate the bond formation between W and W. Likewise, the bonding seam between 50W and 25W for the joining performed at 900 °C is shown in Figure 4.15. Region A and B show the interface between the steel-splats of 50W and 25W. In Region A, a thin passive oxide layer can be seen between them. In Region B, these passive oxides partially dispersed and formed a partial steel-steel metallurgical bonding. Region C shows the interface between W-splats of 50W and 25W. From the interface, it appears that partial metallurgical bonding has taken place.

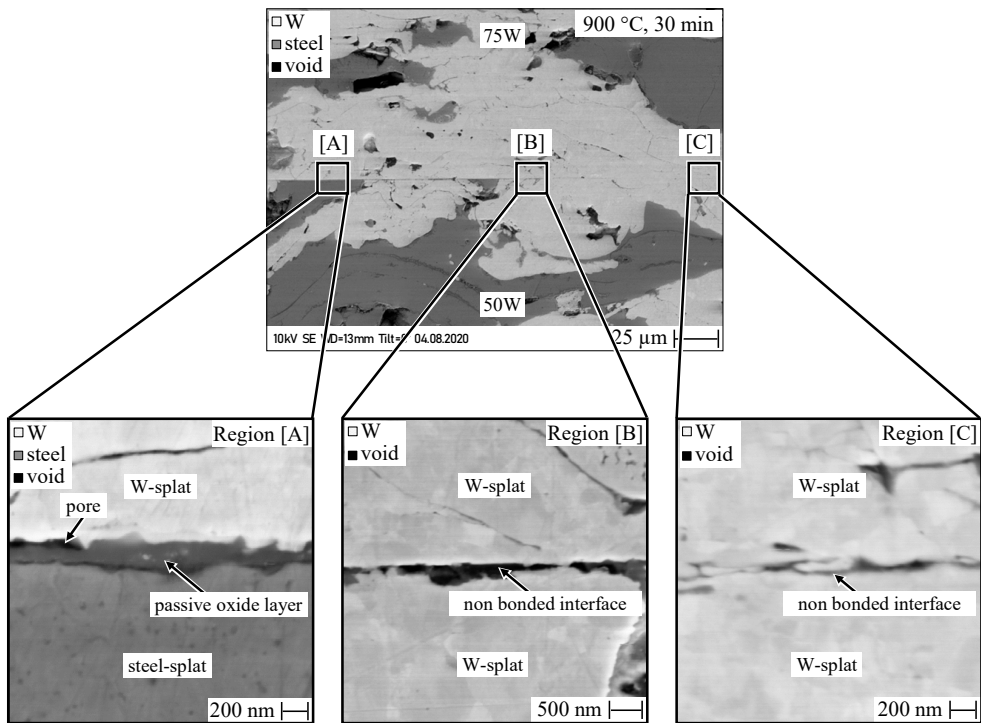


Figure 4.14 Bonding seam between 75W and 50W; joining performed at 900 °C, 30 min

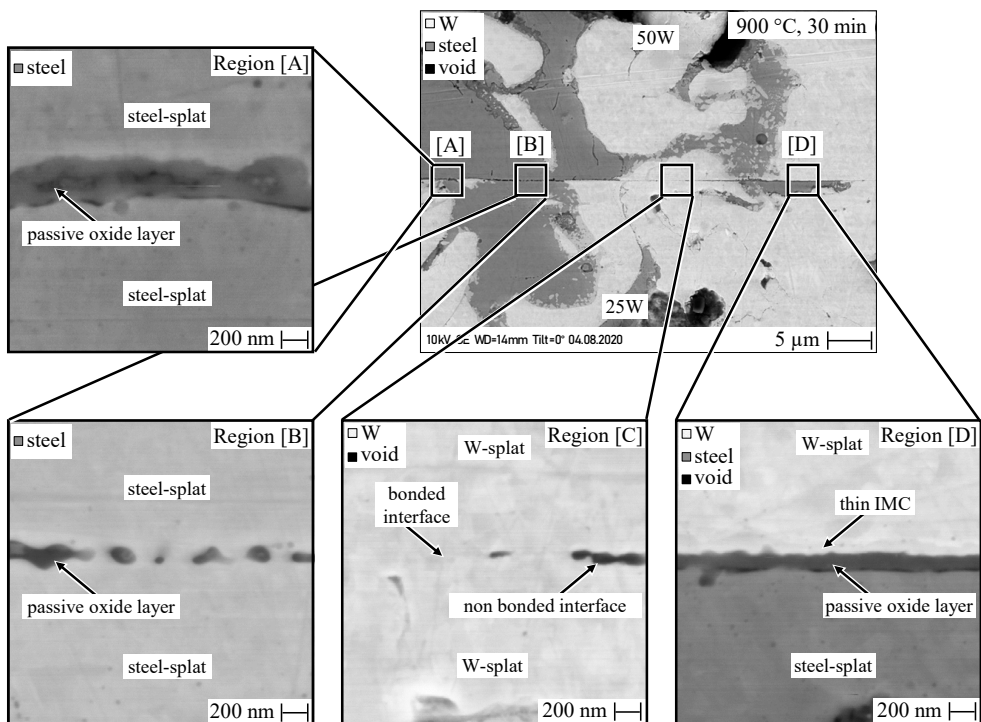


Figure 4.15 Bonding seam between 75W and 50W; joining performed at 900 °C, 30 min

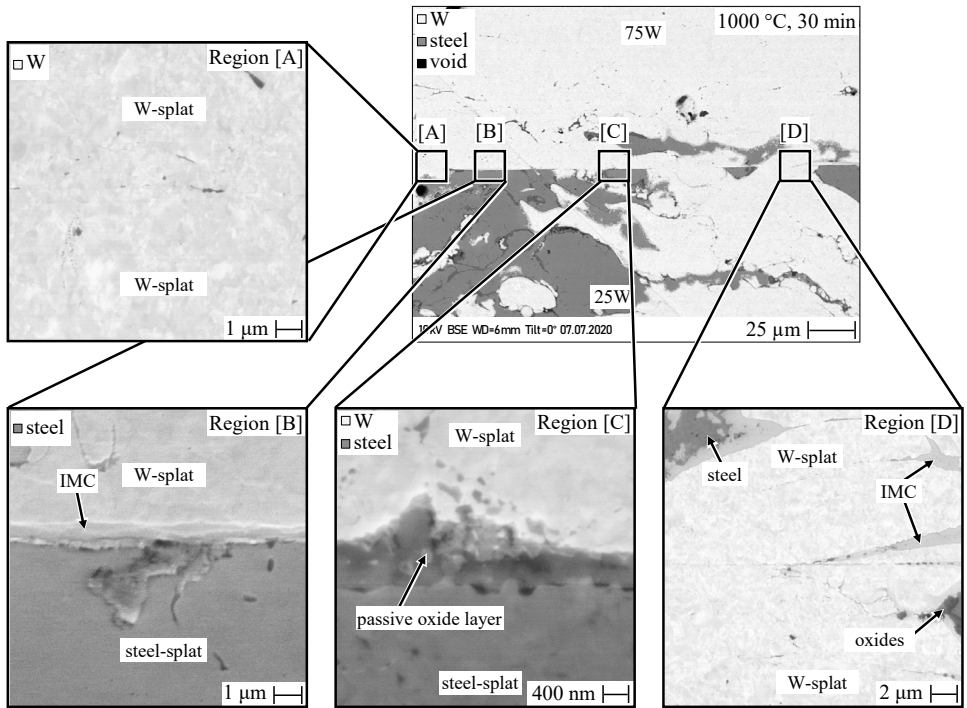


Figure 4.16 Bonding seam between 75W and 50W; joining performed at 1000 °C, 30 min

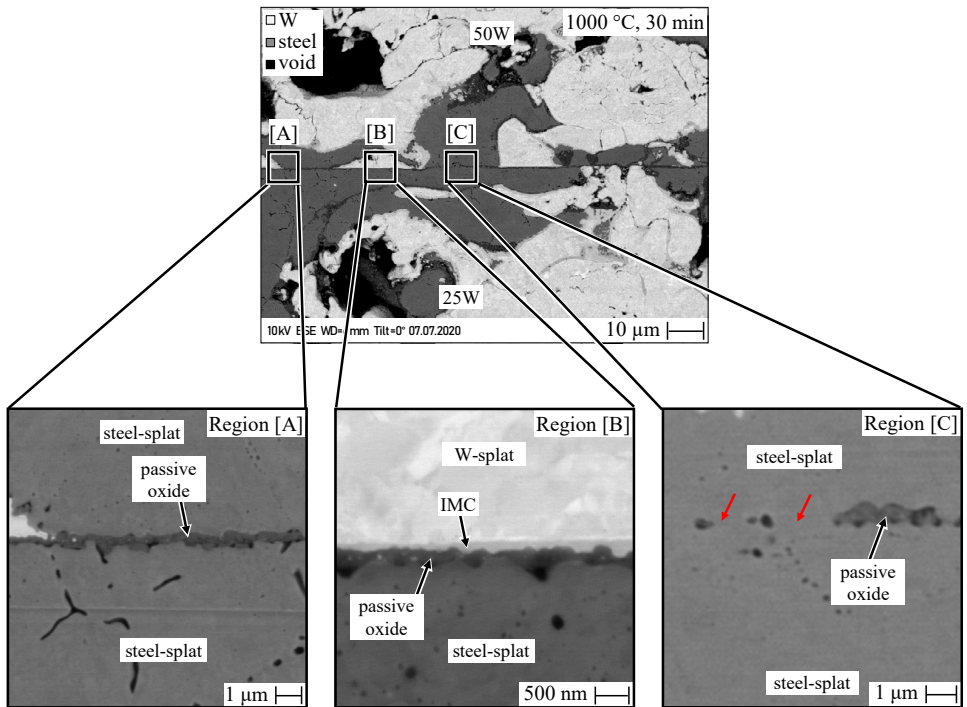


Figure 4.17 Bonding seam between 50W and 25W; joining performed at 1000 °C, 30 min

As mentioned in Table 4.3, increasing the joining temperature to 1000 °C (30 min) improved the bonding reasonably without forming severe amount of IMC. Figure 4.16 shows the corresponding bonding seam between 75W and 50W. Most W-W interfaces at the bonding seam formed somewhat sufficient metallurgical bonding, as can be seen in Region A and D. The joining at higher temperatures (1100 °C and 1200 °C) did not significantly improve the bonding but increased the amount of IMC. After joining at 1100 °C, 30 min, the amount of IMC in 25W, 50W, and 75W composites was around 11 %, 8 %, and 5 %, respectively. This amount increased to around 23 %, 13 % and 10 %, respectively, as the joining temperature increased to 1200 °C. Thus, the feasibility study implied that 1000 °C is the most appropriate joining temperature.

4.2.4 Joining 25W and bulk-steel

The next step was to study the feasibility of joining 25W with bulk-steel. Therefore, these two were bonded at different parameters, as mentioned in Table 4.4.

Table 4.4 Joining trials for bonding 25W and bulk-steel and their observations

| Configuration | Joining parameter | | Remarks |
|------------------------|-------------------|-------|--|
| | (°C) | (min) | |
| 25W + bulk-steel | 800 | 30 | No satisfactory bonding near the edges, as can be seen in Figure 4.18 a) and b). |
| | 800 | 60 | |
| | 900 | 30 | Steel-steel interfaces did not initiate any bonding |
| | 1000 | 30 | Reasonable bonding over the entire bonding surface |
| | 1000 | 60 | Excessive reduction in the thickness of bulk-steel after joining |

Only the joining performed at 1000 °C resulted in appropriate bonding over the entire bonding seam. This can be seen in Figure 4.18 c) and d), which show the bonding seam near the centre and the edge of the joint, respectively. Furthermore, the passive oxide layer somewhat dispersed into the steel resulting in a satisfactory metallurgical bonding, as can be seen in Figure 4.18 d). Thus, this joining parameter (1000 °C, 30 min) is considered optimum.

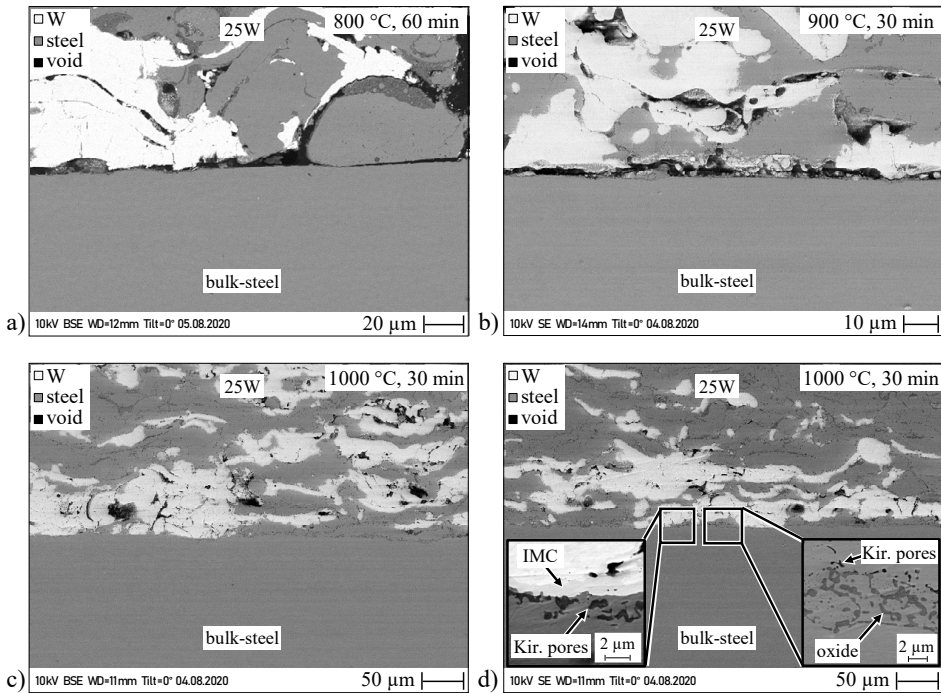


Figure 4.18 Bonding seam between 25W and bulk-steel; a) edge of the joint, performed at 800 °C, 60 min, b) near the edge of a joint, performed at 900 °C, 30 min, c) centre of the joint, performed at 1000 °C, 30 min, d) near the edge of the joint performed at 1000 °C, 30 min

4.2.5 Joining W and steel with 3-layer FGM

The feasibility study indicated that a 0.3 mm thick V-filler is needed to join the bulk-W and 75W layer. Hence, a complete graded joint featuring a 3-layer plasma sprayed FGM was manufactured in a simple one-step manufacturing process by placing all the parts together at 1000 °C, 30 min. This joining parameter was selected because higher temperatures (1100 °C, 1200 °C) lead to excessive IMC formation, and lower temperatures (800 °C, 900 °C) lead to insufficient bonding between 25W, 50W and 75W. Also, as mentioned in Section 4.2.2, the optimal bonding between W and V occurs above 900 °C. The cross-section of the resulting joint is shown in Figure 4.19.

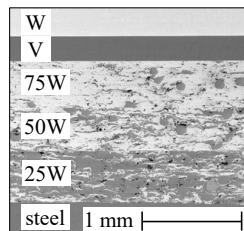


Figure 4.19 Cross-section of the W-steel joint featuring a 3-layer plasma sprayed FGM interlayer

4.2.6 Joining W and steel with 2-layer FGM

For the sintered FGM, a joint featuring 2-layer FGM was manufactured. Thus, a similar joint featuring 2-layer plasma sprayed FGM was manufactured for comparison. The manufacturing procedure was the same as above, but by excluding the 75W and V layers. The whole stack was then joined using the same parameters of 1000 °C, 30 min for simplicity. Although the manufactured joint held together, the topmost bulk-W detached from the 50W layer during the cutting for metallographic investigation, suggesting inadequate bonding between them. Nevertheless, this joint would still be subjected to HHF loading.

4.3 Joining with V interlayer

The W-steel joint featuring a 3-layer plasma sprayed FGM interlayer consists of 0.3 mm thin V-filler material. Additionally, the thickness of the entire interlayer was approximately 1.5 mm. Therefore, it was mandatory to manufacture two joints with only V interlayer of the same thicknesses, one with 0.3 mm and one with 1.5 mm) to assess the influence of this V-filler in the benchmarking HHF test. A similar methodology explained in Section 4.2 was used for the manufacturing. The bulk-W and bulk-steel were cut into a 16 mm × 16 mm × 3 mm geometry. The pure V-foil (0.3 mm thick) and V-sheet (~1.6 mm thick) were purchased from

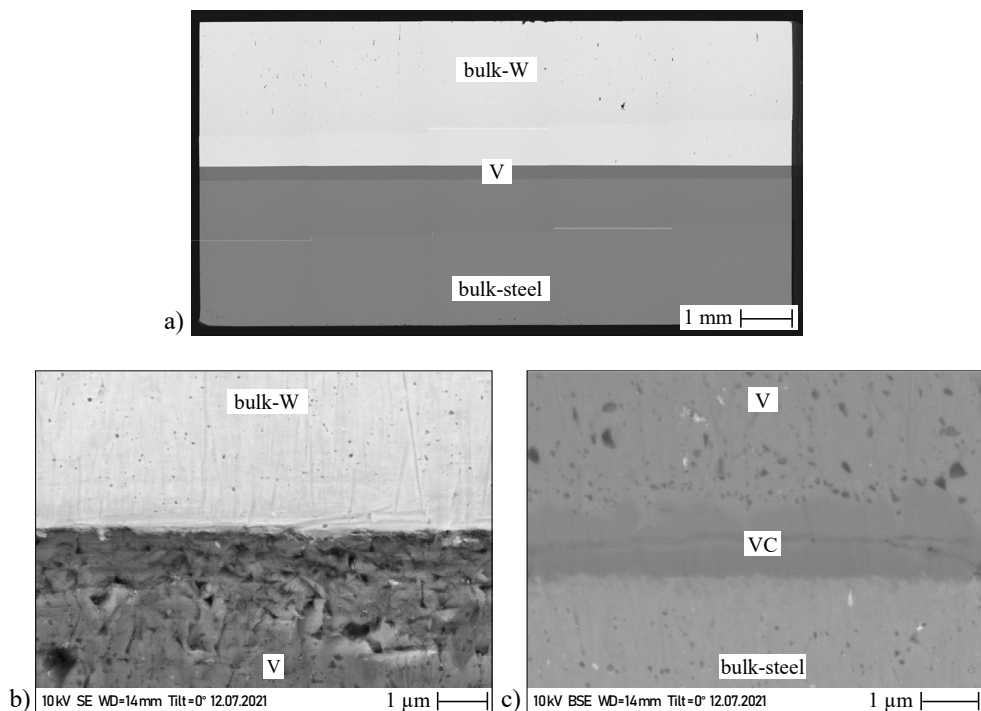


Figure 4.20 a) Cross-section of a W and steel joint with 0.3 mm thick V interlayer, b) W-V bonding interface, c) V-steel bonding seam (*Note: the darker marks on V are not pores/defects, but scratch marks coming from the inappropriate grinding steps used during the metallographic sample preparation*)

HMW Hauner GmbH & Co. KG, Germany, and cut into the same geometry. The mating surfaces were prepared before the joining, as explained in Section 4.2. The V was placed between bulk-W and bulk-steel, and the entire stack was joined using the same joining parameter but with less pressure: 1000 °C, 30 min, 20 MPa. The cross-section of the resulting joint with a 0.3 mm thick V-interlayer is shown in Figure 4.20 a); it is also representative of a joint with a 1.5 mm thick V interlayer. The W-V interface resulted in a defect free bonding over the entire bonding seam. The V-steel interface, similar to what was observed in Section 4.2.2, formed a thin vanadium carbide (VC) reaction layer, as seen in Figure 4.20 c).

4.4 Joining W and steel directly

To manufacture a reference directly bonded joint for the benchmarking HHF test, bulk-W and bulk-steel of similar geometry 16 mm × 16 mm × 3 mm was selected. These were placed inside the SPS setup and joined at 1000 °C, 15 min, 20 MPa. This shorter joining time was selected to inhibit the formation of IMC. The resulting cross-sectional micrograph of the joint is shown in Figure 4.21 a). The joining resulted in the formation of a defect-free bonding seam. The W-steel bonding seam, as shown in Figure 4.21 b) and c), formed three distinct layers:

- First, a thin IMC layer was observed, as can be seen in Figure 4.21 b). In a study by Basuki and Aktaa [28], W and Eurofer 97 were diffusion bonded using a uniaxial press at 1050 °C, 60 min and the IMC layer was found to have a thickness of ~2.5 μm. In another study by Hirose et al. [30], W and Eurofer 97 were bonded using a similar CA-DB process at 960 °C, 30 min. Here as well, an IMC layer of similar thickness (~2.7 μm) was observed. Compared to both these studies, the thickness of the IMC in this was only approximately 1 μm. This shows that keeping a low joining time of 15 min is beneficial in reducing the formation of IMC.
- Second, below this IMC layer, a fully ferritic steel phase (α) was observed with a thickness of roughly 9 μm, as can be seen clearly in Figure 4.21 b) and c). This phase was also observed by the studies of Basuki and Aktaa [28] and Hirose et al. [30]. The elemental composition was found to be: 81.5 wt% Fe, 11.0 wt% W and 7.4 wt% Cr [28]. In the study by Basuki and Aktaa [28], the thickness of this α layer was 13 μm. In the study by Hirose et al. [30], the thickness of this α layer was 53 μm. This further implies that the joining parameter selected in this thesis (1000 °C, 15 min) resulted in lower diffusion of W into steel, resulting in only 9 μm thick ferrite phase. As can be seen in Figure 4.21 b) and c), this ferritic phase also contains pores/voids and a small amount of IMC. These pores/voids are formed due to the Kirkendall diffusion and the increase in the volume, as already discussed in this thesis.

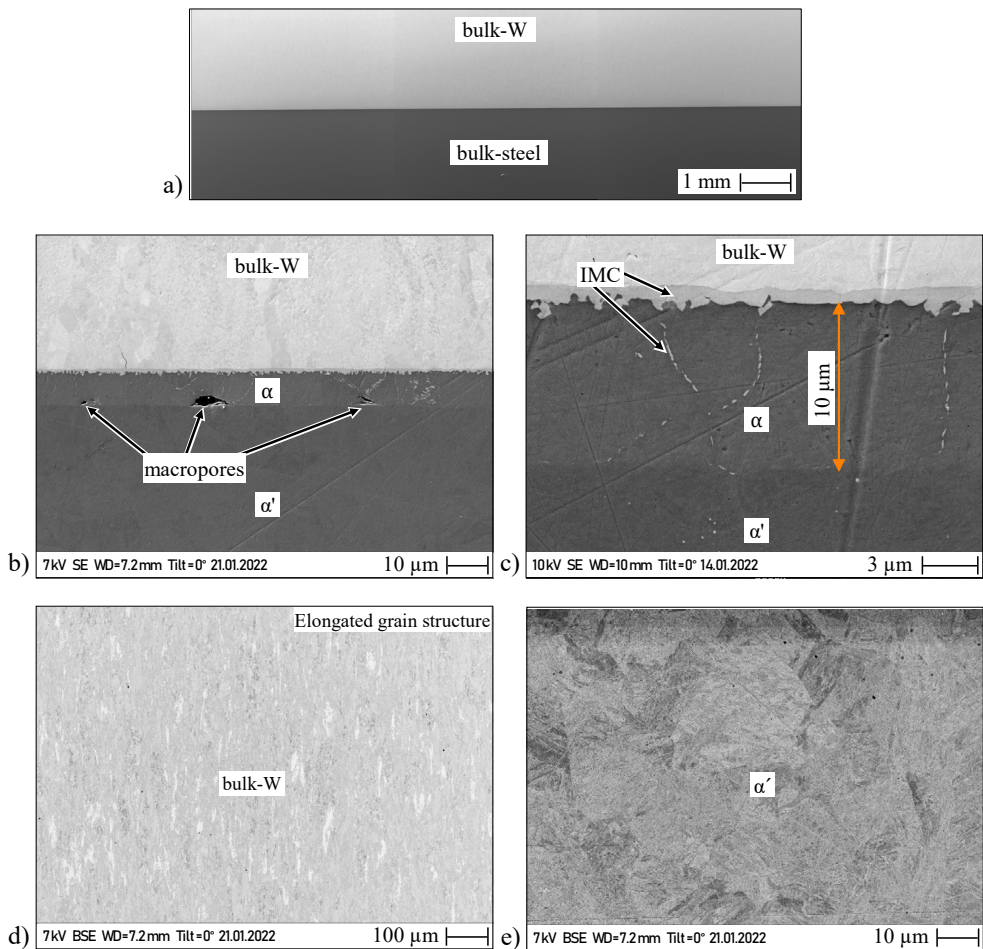


Figure 4.21 a) Cross-sectional micrograph of a directly bonded W-steel joint b) W-steel bonding seam c) W-steel bonding interface showing IMC and a ferrite region d) Grain structure of bulk-W after joining e) Martensitic structure in bulk-steel after joining

- Third, below this ferritic phase, the steel retains its original elemental composition as that of the Eurofer 97 with only 1 wt% W, forming a quenched martensitic phase (α'), as can be seen in Figure 4.10 e). This clearly shows that the cooling rate after the joining process in the SPS is fast enough to form martensite without undergoing any “ferrite+carbide” transformation. Moreover, the bulk-W retained its elongated grain structure without any recrystallization, as can be seen in Figure 4.21 d).

4.5 Summary

This chapter described the manufacturing of six W-steel joints for subsequent testing under HHF loading. Following key highlights and learnings are summarized here:

- W-steel graded joint featuring sintered FGM: The co-sintering of 75W and bulk-W demonstrated that the bonding only occurred with one 75W combination consisting of coarser W powder. Although the bonding was unsatisfactory, a graded joint featuring a 3-layer sintered FGM was manufactured using the sintering parameters 1000 °C, 5 min, 125 MPa. Each layer had a thickness of 0.5 mm, resulting in an overall FGM thickness of 1.5 mm. Furthermore, a decision was made to fabricate an additional joint featuring a two-layer FGM (25W and 50W) by omitting the topmost 75W layer. Therefore, both joints were selected for benchmarking through HHF testing.
- W-steel graded joint featuring plasma sprayed FGM: A hybrid plasma spraying and current-assisted diffusion bonding process was employed to produce a graded joint. It was observed that direct bonding of bulk-W and plasma sprayed 75W was not feasible. Hence a thin 0.3 mm V-filler was inserted between them to establish a good metallurgical bond. After optimizing the joining parameters, a joint comprising 3-layer plasma sprayed FGM was manufactured at 1000 °C, 30 min. Similarly, a 2-layer FGM joint was also fabricated for benchmarking through HHF testing. As the 3-layer FGM joint contained V, two additional W-steel joints featuring pure V interlayers (0.3 mm and 1.5 mm) were also produced for comparison.
- Directly bonded W-steel joint: To compare with the aforementioned graded joints, a reference joint is necessary for benchmarking through HHF testing. Thus, a directly bonded W-steel joint was manufactured at the same joining temperature of 1000 °C but with half the joining time (15 min) to mitigate intermetallic compound (IMC) formation.
- Notably, all the joints discussed above were fabricated at the same temperature of 1000 °C. The bonding times varied, with some featuring short bonding times (5 min for sintered FGM), others with medium bonding times (15 min for directly bonded joint), and some with long bonding times (30 min for plasma-sprayed FGM joint and joint with pure V interlayer). It is crucial to note that the austenitization temperature of steel is also approximately 1000 °C, and all samples were rapidly cooled from this temperature, resulting in a quenched martensite microstructure in the bulk steel. This feature is highly advantageous for comparing the benchmarking through HHF testing.

5 High heat flux testing of W-steel joints

The various W-steel joints manufactured in Chapter 4 were benchmarked under cyclic thermal loading using an electron beam facility JUDITH 2, located at FZJ.

5.1 Methodology of benchmark test

5.1.1 Testing setup

The manufactured joints were cut into a 12 mm × 12 mm geometry using wire-EDM. The cutting surfaces were then ground to eliminate microcracks that occurred from wire-EDM process. The topmost bulk-W, referred to as W-tile henceforth for simplicity, was polished using diamond suspension down to a grit size of 3 μm. This was done to verify the absence of any surface cracks on the W-tile. This is of particular importance as the W-tile may have surface cracks after the joining process due to the brittle nature of W. A broken W-tile may influence the stresses at the joint and, thus, obscure the HHF test results. A thorough investigation using light microscopy revealed no cracks in the W-tiles, except for one of the samples of the joint featuring 3-layer sintered FGM—referred to as Sample D of 3.FG-SPS joint, see Table 5.1 for nomenclature—. Nevertheless, this sample was still included in the HHF testing. The bottom bulk-steel was ground only up to P550 grit size using a diamond grinding disc (MD-Piano from Struers GmbH, Germany) to maintain the flatness of the surface. The thickness of the top W-tile and the bottom bulk-steel after the preparation step was measured using light microscopy. The thickness of both was found to be roughly 3 mm. A macroscopic photograph of the prepared samples is shown in Figure 5.1.

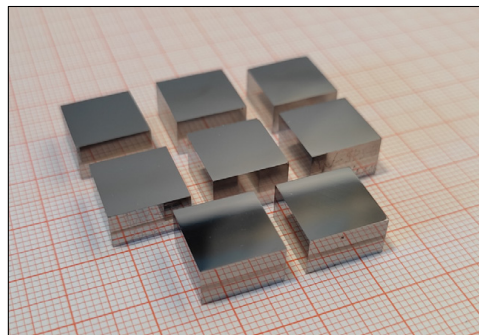


Figure 5.1 Photograph of the prepared samples (joints); top polished surface is W-tile

These joints were then brazed onto copper (Cu) modules consisting of a circular cooling channel of diameter 11 mm, as schematically illustrated in Figure 5.2. A silver-based brazing foil VH780GC (28 wt% Cu, 2 wt% Ge, 0.3 wt% Ni) of thickness 100 μm was used for the

brazing. The brazing was done in a vacuum oven (1.3×10^{-5} mbar) by applying the following sequence: first, heating to 790 °C and holding at this temperature for 15 min; second, continuing the heating up to 845 °C and holding for 15 min; and finally, cooling down to 20 °C. These modules were then mounted inside JUDITH 2, and the cooling circuits were also connected, as schematically illustrated in Figure 5.2. JUDITH 2 consists of an electron beam gun with the following parameters: 200 kW maximum power, 40–60 kV acceleration voltage, 5–12 mm beam diameter. In principle, the samples were thermally loaded through this electron beam; the electron beam hits the top surface of the W-tile while the coolant (water) continuously flows through the Cu module. The coolant conditions were as follows: 20 °C, 25 bar, 3.5 m/s. The facility is also equipped with an infrared (IR) camera to monitor the surface temperature of the W-tiles. Four Cu-modules can be mounted and tested simultaneously. Thus, a total of 24 samples can be tested at once. The benchmarking test was performed in two sets (set-1 and set-2) as the total number of samples was more than 24.

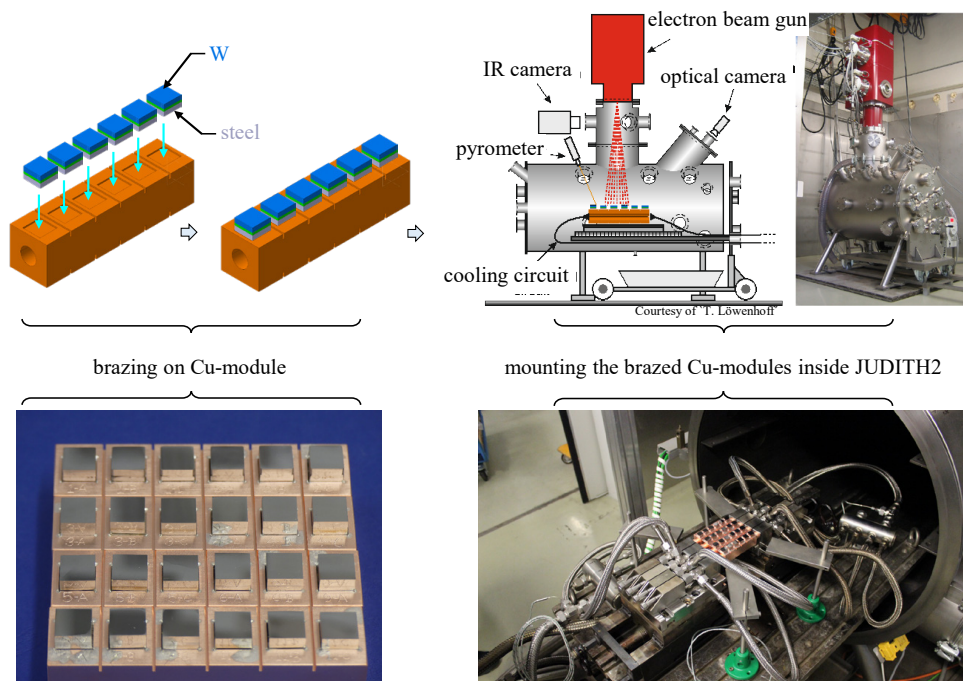


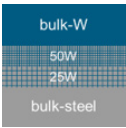
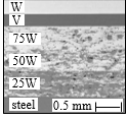
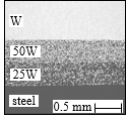
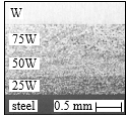
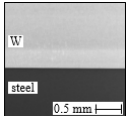
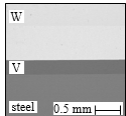
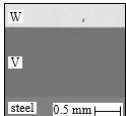
Figure 5.2 Schematic illustration of the testing procedure of HHF benchmark test, along with respective photographs

5.1.2 Overview of joints tested

Table 5.1 provides an overview of the joints that were tested, along with their shortened nomenclature for ease of reading. The two sets of modules mounted are shown in Figure 5.3. The average thickness of the interlayer, measured using light microscopy micrographs, is also listed in Table 5.1. It can be seen that the interlayer thickness of the individual layers of the plasma sprayed FGM was slightly less than the predefined thickness of 0.5 mm. Additionally,

cracks were observed on the surface of W-tile in some of the joints immediately after the brazing step. In the case of the joint consisting of 2-layer sintered FGM, complete debonding of the W-tile from the FGM occurred in 2 samples (G and I). The precise cause of the debonding/cracking of the W-tile is currently unknown. However, one assumption would be due to some inevitable internal residual stress.

Table 5.1 Nomenclature and thickness of various W-steel joints tested

| Configuration | Joint | | Interlayer Thickness (mm) | Number of samples Labelling* | Crack/ debonding* |
|---------------------------|---------------|---|--|---------------------------------|----------------------|
| | Nomenclature* | SEM image | | | |
| W-2layer.FGM(APS)-steel | 2.FG-APS |  | 50W: 0.42 25W: 0.41 | (A to C) 3 | - |
| W-V-3layer.FGM(APS)-steel | V-3.FG-APS |  | V: 0.19 75W: 0.40 50W: 0.39 25W: 0.42 | (A to C) 3 | - |
| W-2layer.FGM(SPS)-steel | 2.FG-SPS |  | 50W: 0.52 25W: 0.45 | (A to I) 9 | G & I debonded |
| W-3layer.FGM(SPS)-steel | 3.FG-SPS |  | 75W: 0.59 50W: 0.50 25W: 0.48 | (A to F) 6 | D crack |
| W-steel (directly bonded) | Direct |  | - | (A to F) 6 | D crack |
| W-V(0.3)-steel | V(0.3) |  | V: 0.30 | (A to C) 3 | A & C crack |
| W-V(1.5)-steel | V(1.5) |  | V: 1.50 | (A to C) 3 | - |

(Note*: A, B, C represents sample labelling. The number below the labelling represents the total number of samples. Cracks represent cracking in W-tile after the brazing process; debonding refers to the delamination of W-tile after brazing; APS and SPS represent FGM manufactured by atmospheric plasma spraying and spark plasma sintering; as discussed in section 4.2.6 the cross-sectional micrograph of 2.FG-APS joint was not possible, and thus, a schematic sketch is made here for ease of understanding)

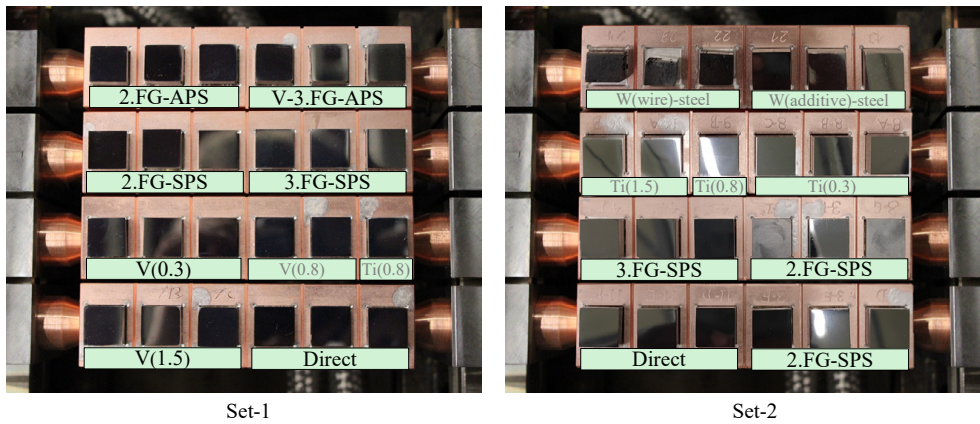


Figure 5.3 Two sets of Cu-modules mounted inside the HHF facility (Note: The experimental campaign also included other W-steel joining concepts which are not relevant to this thesis; V(0.8) joint, Ti(0.3, 0.8, 1.5) was W-Ti-steel joint of different thicknesses of Ti, W(wire)-steel was a conceptual joint consisting of W-wires bonded to steel, W(additive)-steel was an additive manufactured W bonded directly to steel)

5.1.3 Testing protocol

The joints were exposed to cyclic steady-state thermal loads. The electron beam was directed onto the W-tile and nearby Cu module, following a specific pattern designed to load the joints uniformly, as illustrated in Figure 5.4 a). Initially, the joints were exposed to a constant (non-cyclic) heat flux of 1 MW/m^2 , known as screening@1MW in the field of HHF testing. Subsequently, they were exposed to cyclic steady-state thermal loading with a pulse ON/OFF time of 30/30 s, as illustrated in Figure 5.4 b). In each cycle, the electron beam (heat flux) was switched ON for 30 s, reaching a steady-state temperature gradient; caused by the applied heat flux and active cooling of the Cu-module. This steady-state surface temperature of W-tile is termed as T_{surf} . Then, for the next 30 s, the electron beam (heat flux) was switched OFF, causing

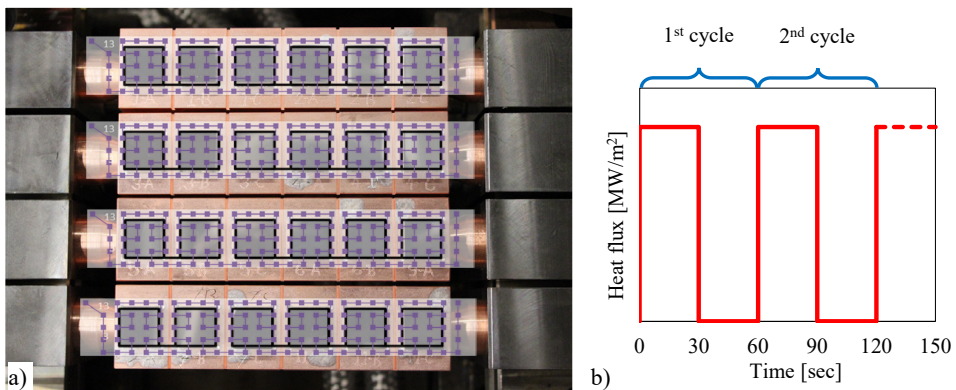


Figure 5.4 a) Schematic of electron beam pattern hitting the actively cooled component, b) Schematic representation of cyclic steady state thermal loading

the entire joint to cool down to 20 °C due to the active cooling. The cyclic testing was performed between the heat fluxes of 1 MW/m² and 4.5 MW/m² in increments of 0.5 MW/m². 200 cycles were performed at each heat flux, as listed in Table 5.2. An exemplary IR temperature field of the samples is shown in Figure 5.5.

Table 5.2 Testing protocol for cyclic steady-state thermal loading

| Power density (MW/m ²) | No. of thermal loading cycles | No. of cumulative cycles |
|---------------------------------------|-------------------------------|--------------------------|
| 1.0 | 200 | 200 |
| 1.5 | 200 | 400 |
| ⋮ | ⋮ | ⋮ |
| 4.5 | 200 | 1600 |

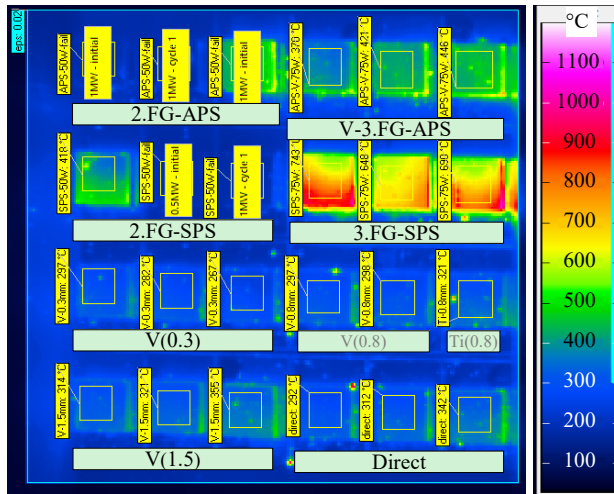


Figure 5.5 An exemplary IR image showing the surface temperature of W-tiles for a screening@1.5MW

5.2 Performance of the joints

The joints were tested up to a heat flux of 4.5 MW/m² until all the samples failed. The macroscopic image of the samples before and after the complete HHF testing is shown in Figure 5.6. The monitored surface temperature of W-tiles (T_{surf}) is shown in Figure 5.7 and Figure 5.8.

- The 2-layer plasma sprayed FGM joint (2.FG-APS) failed during the screening step at 1 MW/m² loading by showing a high surface temperature of around 630 °C—much higher compared to all the other joints (200–300 °C)—, followed by a complete detachment of the W-tile.

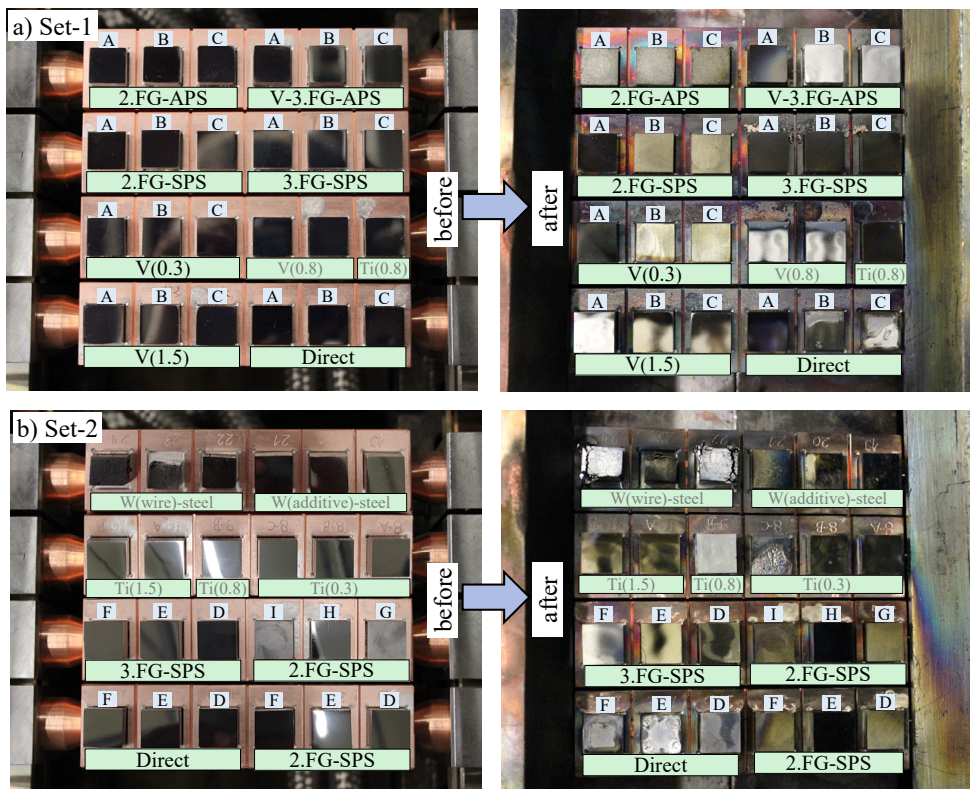


Figure 5.6 Macroscopic image of all the joints before and after the HHF testing (*Note: for the sample labelling please refer to Table 5.1*)

- The 3-layer plasma sprayed FGM joint (V-3.FG-APS) performed relatively better by displaying constant steady-state surface temperature until 2 MW/m^2 loading. However, during the subsequent power densities, samples (B and C) began to show signs of degradation; temperature increased with every cycle, which is evident in Figure 5.7 a). Sample A also showed minor degradation during the 3.0 MW/m^2 loading when its temperature reached around $1000 \text{ }^\circ\text{C}$. During 3.5 MW/m^2 loading, samples B and C experienced a sudden steep increase in the temperature at around 1040th cumulative cycle, which indicates that the bonding seam has debonded/fractured. Similarly, sample A failed with a sudden temperature rise at 1160th cumulative cycle.
- The V(0.3) and V(1.5) joints, included in the test for comparison purposes, displayed no signs of degradation as the temperature remained constant during each power density. The failure occurred when the temperature spontaneously increased, as can be seen in Figure 5.7 b) and c). The V(0.3) joint with a thinner V interlayer failed earlier than the V(1.5) and V-3.FG-APS joints. The V(1.5) joint performed better than the V-3.FG-APS joint, as its temperature was much lower. The high temperature of V-3.FG-APS joint was due to the extremely low thermal conductivity of plasma sprayed FGM ($\sim 20 \text{ W/m}\cdot\text{K}$)

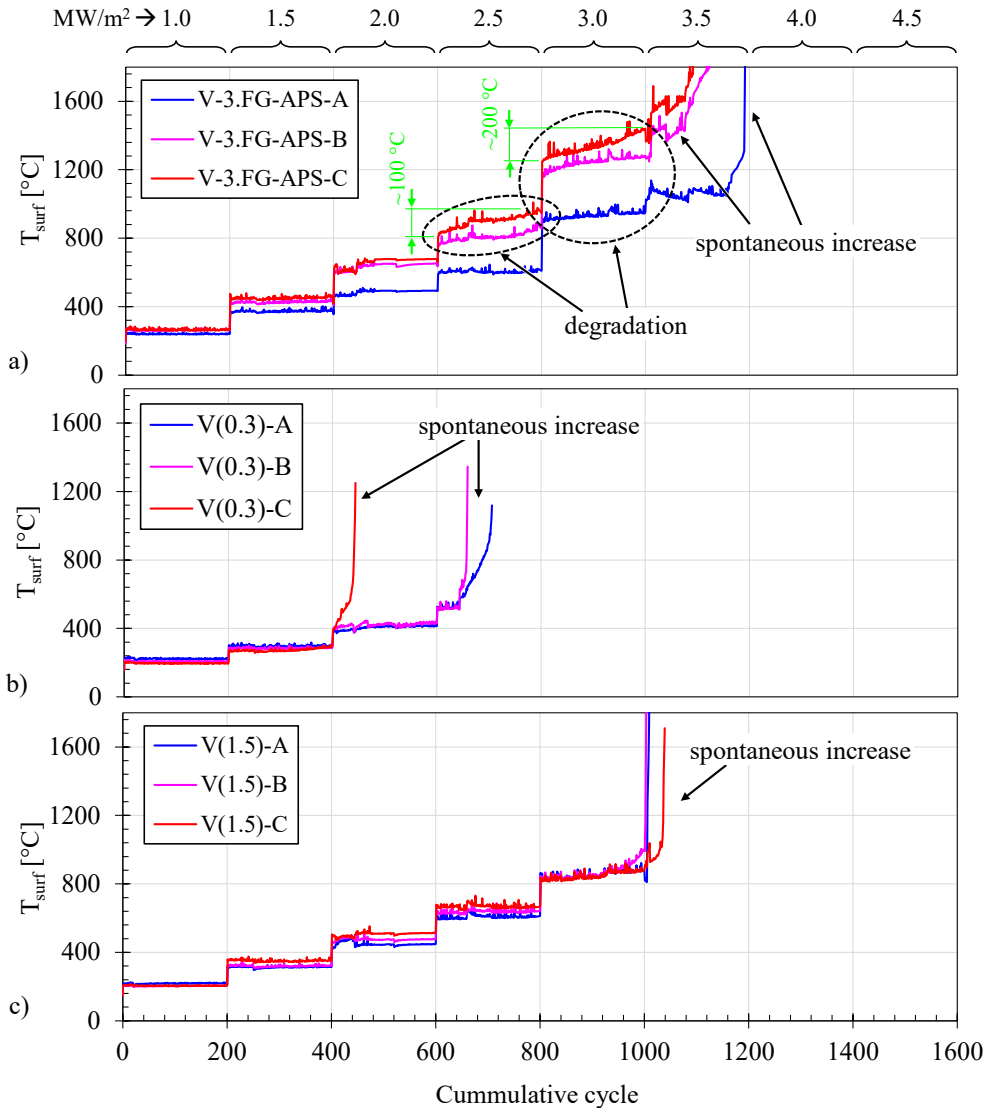


Figure 5.7 Steady-state surface temperature of W-tile over cumulative number of cycles for different samples of a) V-3.FG-APS, b) V(0.3), and c) V(1.5) joints. (Note: A, B, C represents sample label)

compared to V (~ 30 W/m \cdot K). It is worth noting that these joints had the same interlayer thickness of around 1.5 mm.

- In contrast, the joints with sintered FGM exhibited inferior performance despite having better properties than the plasma sprayed FGM. Among the 2.FG-SPS joints, only 3 out of 7 samples tested survived screening step at 1 MW/m 2 , whose steady state W-tile surface temperature profile is provided in Figure 5.8 b). Out of these three samples, only sample A survived till 1.5 MW/m 2 loading, but eventually failed at the beginning of

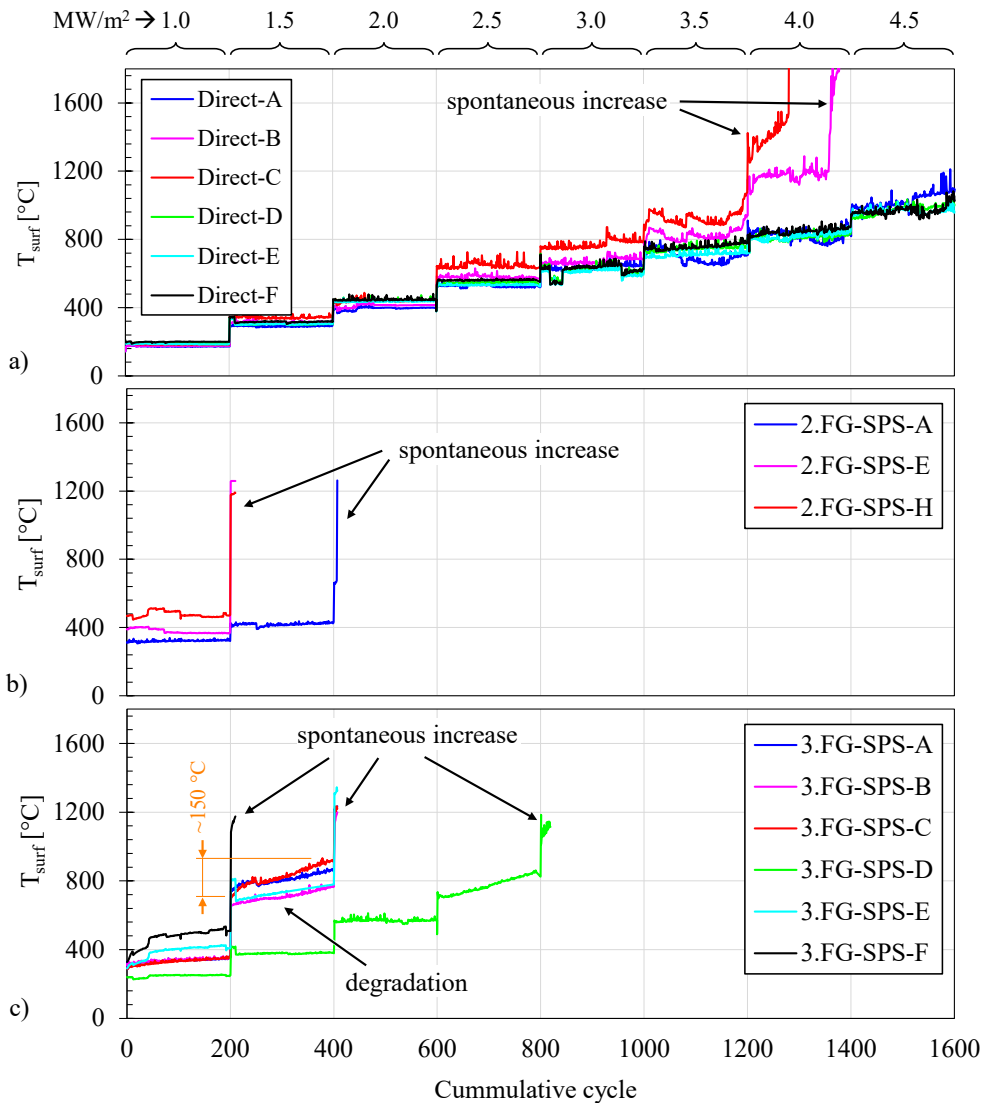


Figure 5.8 Steady state surface temperature of W over cumulative number of cycles for different samples of a) Direct, b) 2.FG-SPS, and c) 3.FG-SPS joints. (Note: A, B, C... represents sample label)

2 MW/m² by showing a spike in the temperature. The 3.FG-SPS joints performed slightly better, with all samples surviving 1 MW/m² loading. However, after this, Sample F failed during the beginning of 1.5 MW/m² by showing a spike in temperature (1200 °C) and severe inhomogeneous temperature over the W-tile surface. For a better understanding of inhomogeneous surface W-tile temperature, see the exemplary IR temperature field in Figure 5.5. During the 1.5 MW/m² loading, all the 3.FG-SPS joints, except Sample D, showed degradation with the increase in the surface temperature for each cycle. At the beginning of 2.0 MW/m² loading, all four samples (A, B, C and E) failed by showing a

spike in temperature (~ 1200 °C). Only Sample D survived 2.0 MW/m^2 loading. However, it is noteworthy that Sample D, which exhibited a lower W-tile surface temperature than other 3.FG-SPS samples, already had cracks in the W-tile before the HHF testing itself (see Section 5.1.1), indicating it had released its residual thermal stresses. Therefore, interpreting results based on this sample alone would be erroneous, and caution should be exercised.

- The directly bonded W-steel reference joint outperformed all other joints. It showed no degradation, as its temperature profile almost remained steady. The joints failed by displaying a steep increase in the surface temperature. The temperature was also the lowest among all the other joints, and all the samples displayed similar surface temperatures. Sample B and C failed during the 4 MW/m^2 loading, while the remaining samples (A, D, E, and F) failed at the end of 4.5 MW/m^2 loading, displaying an inhomogeneous surface temperature of the W-tile.

5.3 Summary and lifetime of the joints

HHF cyclic benchmarking test was performed on diverse W-steel joints consisting of different plasma sprayed and sintered FGM interlayers; a 2-layer FGM and a 3-layer FGM. The test was conducted from a power density of 1 MW/m^2 up to 4.5 MW/m^2 . The overall lifetime of all the joints is depicted in Figure 5.9, and a summary is provided in Table 5.3. In essence, none of the graded joints performed better than a directly bonded W-steel joint.

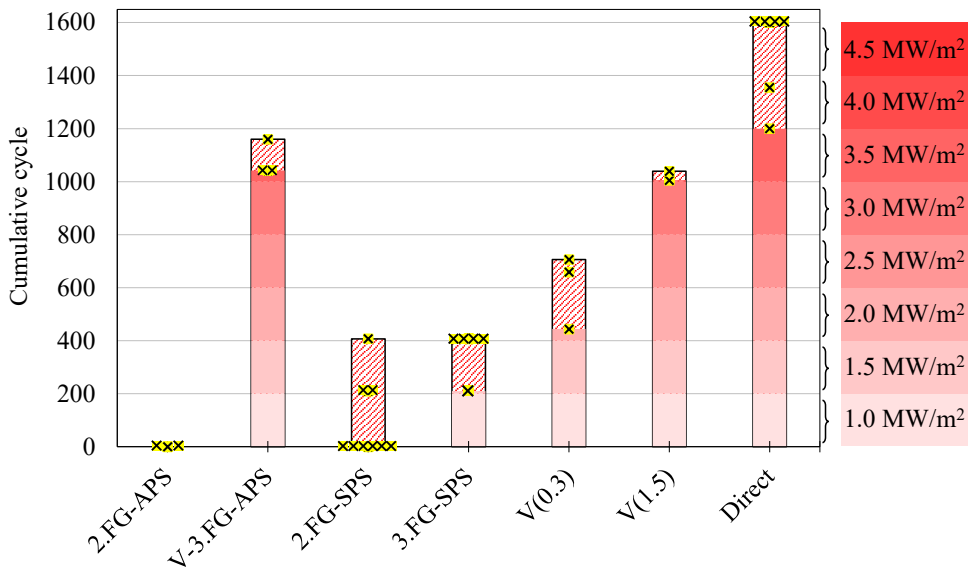


Figure 5.9 Lifetime of various W-steel joints (Note: \times represents the lifetime of each sample and hatched represents the scatter band)

Table 5.3 Summary of the HHF testing of various joints

| Joint type | Observations |
|------------|---|
| 2.FG-SPS | <ul style="list-style-type: none"> - Most joints failed before the cyclic thermal loading by showing complete detachment of the W-tile from the topmost 50W layer. - It is unexpected because the 50W and bulk-W showed good bonding Section 4.1.3. |
| 3.FG-SPS | <ul style="list-style-type: none"> - Unexpectedly, it had a longer lifetime compared to 2.FG-SPS, even though the metallurgical bonding between a 75W and bulk-W is inferior to that of 50W and bulk-W. This indicates that the reduced thermal stress at a 3-layer FGM outperforms the stronger bonding in a 2-layer FGM. - Even though the sintered FGM has better properties than plasma-sprayed FGM, the 3.FG-SPS joint failed much earlier than the V-3.FG-APS joint by showing complete detachment of W-tile. - Lifetime only 16 % as that of the reference directly bonded joint. |
| 2.FG-APS | <ul style="list-style-type: none"> - As expected, it failed before the cyclic heat loading due to poor bonding between the W-tile and the topmost 50W layer of the plasma sprayed FGM. - Unexpectedly, it showed far better lifetime/performance than 3.FG-SPS joint, despite the plasma sprayed FGM's poor mechanical and thermophysical properties. This is due to the attachment of the W-tile and the FGM with the help of a V-filler. So, it can be concluded, at the moment, that the key influencing factor is the bonding between the W-tile and the FGM. |
| V-3.FG-APS | <ul style="list-style-type: none"> - Lifetime approximately 70 % as that of the reference directly bonded joint. - Joints failed predominantly because of the degradation of the FGM. - Despite the poor properties of the plasma sprayed FGM, the joint showed a longer lifetime than the V(0.3) joint, indicating the improvement of combining the two techniques. - Its lifetime was comparable to that of V(1.5) joint. |

6 Post mortem analysis of tested joints

This chapter discusses the post mortem investigation of the following joints tested under HHF loading: V-3.FG-APS, 2.FG-SPS, 3.FG-SPS and Direct joint.

6.1 V-3.FG-APS joint

The visual inspection of failed V-3.FG-APS joints showed that in all three samples (-A, -B and -C), W-tile did not detach, as can be seen in Figure 6.1.

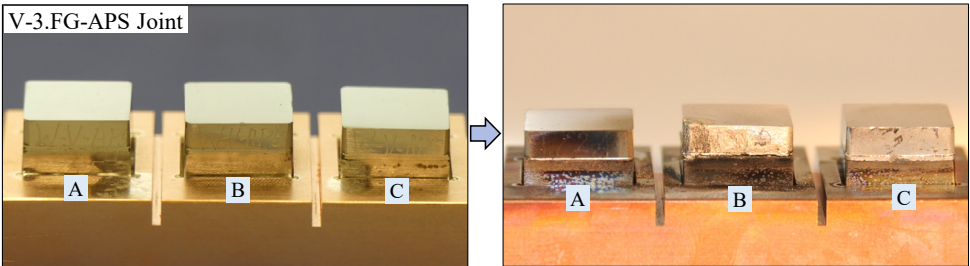


Figure 6.1 Macroscopic examination of V-3.FG-APS joints (before and after HHF testing)

6.1.1 Investigation of the cross-sectional cut

After the visual inspection, cross-sections were made for metallographic investigations. The cross-sectional overview of sample-A is shown in Figure 6.2 with five marked regions (Region-1 to -5), which were investigated closely. The SEM micrograph of Region-1 and Region-2, whose spatial locations are the edge of the joint, is shown in Figure 6.3 a) and b). Cracks were observed inside the V-filler, originating from the edge and propagating at an incline towards

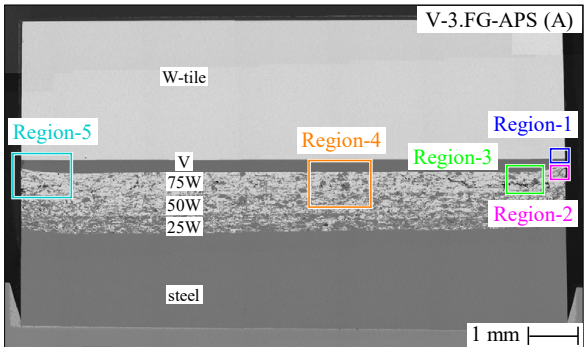


Figure 6.2 Cross-section of the failed V-3.FG-APS joint (sample-A) with five marked regions (Region-1 to -5), which were further analysed (see Figure 6.3 to Figure 6.5)

the W-V bond seam. Similarly, cracks were observed inside the 75W layer; these cracks were found only inside the W constituent and occurred mainly due to the detachment of W-splats, as can be seen in Figure 6.3 b). This was due to the low adhesion strength between the W-splats. In addition, minor delamination of the W-tile and V-filler was also observed, as can be seen in Figure 6.3 c) and d). This delamination can be divided into three modes, as depicted in Figure 6.3 d):

- Debonding of W and V exactly at their interface.
- Fracture inside W material, close to the W-V bond seam.
- Fracture inside V material, close to the W-V bond seam.

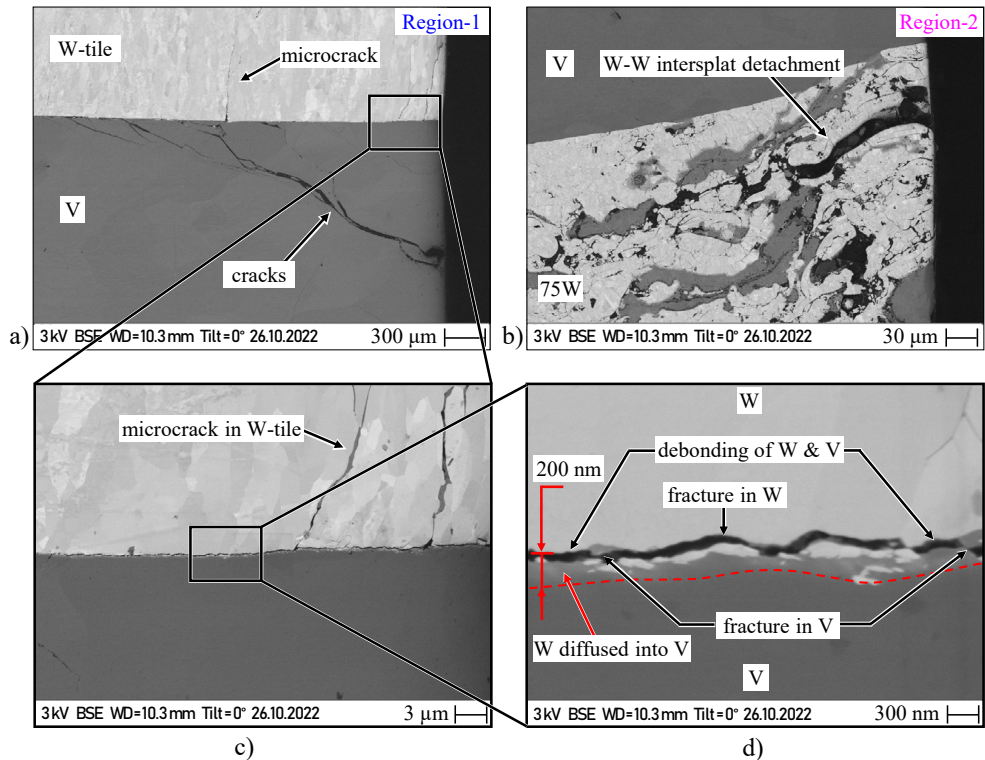


Figure 6.3 a) Micrograph of Region-1, b) Micrograph of Region-2 (their spatial locations are marked in Figure 6.2), c) Close-up of the W-V bond seam, d) Three modes of failure at the W-V bond seam

The cracks inside the 75W layer were also observed in locations close to the edge of the joint, as can be seen in Figure 6.4 a), marked as Region-3. The cracks not only originated from the edge but also appeared to originate near the middle of the joint, as can be seen in Figure 6.4 b), marked as Region-4. It is, however, interesting to note that the bond seam between 75W and 50W layer remained undamaged without showing any debonding. Likewise,

at the left side edge (marked as Region-5 in Figure 6.2) of the joint, similar cracks appeared inside the 75W layer and the V-filler, as can be seen in Figure 6.5 a) and b).

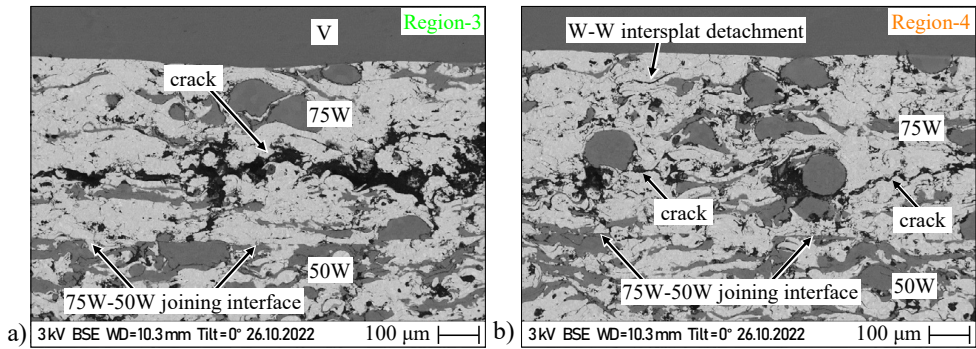


Figure 6.4 a) Micrograph of Region-3, b) Micrograph of Region-4 showing failure inside 75W layer (their spatial locations are marked in Figure 6.2)

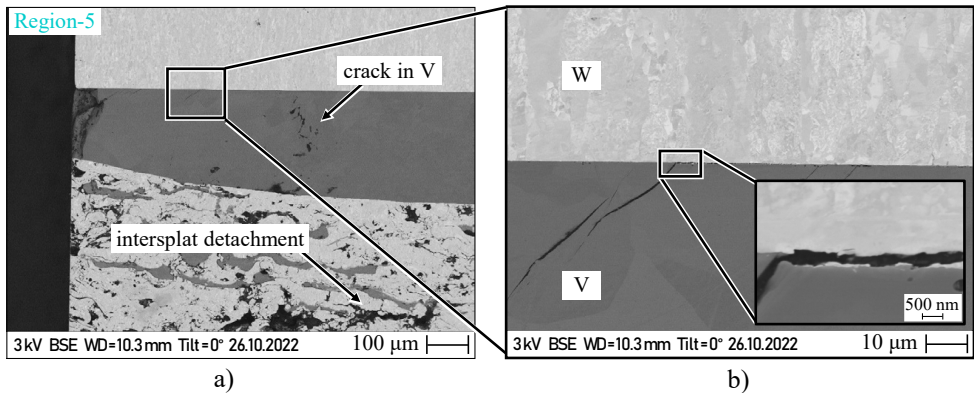


Figure 6.5 a) Micrograph of Region-5 (its spatial location is marked in Figure 6.2), b) Close-up of the W-V bond seam

In another sample (sample-C), as shown in Figure 6.6, a similar failure pattern was observed; cracks inside the 75W layer and V-filler, along with the delamination of W-V bond seam.

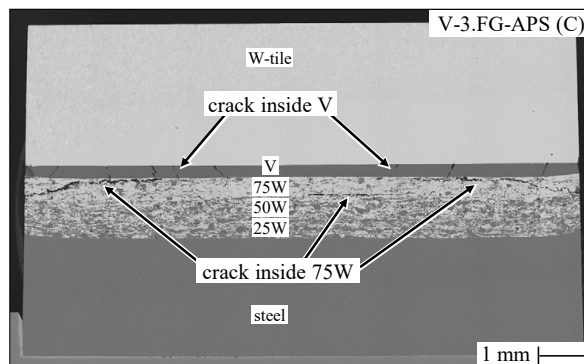


Figure 6.6 Cross-section of the failed V-3.FG-APS joint (sample-C)

The microstructures of the individual APS layers (25W, 50W and 75W) were also examined, as shown in Figure 6.7. The composites showed the formation of IMC, which was not only formed at the W-steel boundaries but also along the grain boundaries of the steel constituents. Interestingly, the amount of IMC was not found to be high. Before the HHF testing, the amount of IMC in 25W, 50W and 75W was approximately 8 %, 6 % and 3 %, respectively. After the HHF testing, the amount of IMC increased to only 10 %, 8 % and 6 %, respectively. No cracks were observed in 25W and 50W, but only inside the W constituents in the 75W layer. Surprisingly the presence of IMC in 75W appeared to have played no role in the initiation or propagation of these cracks, indicating that the formation of IMC was not the major detrimental factor for the failure of the joint.

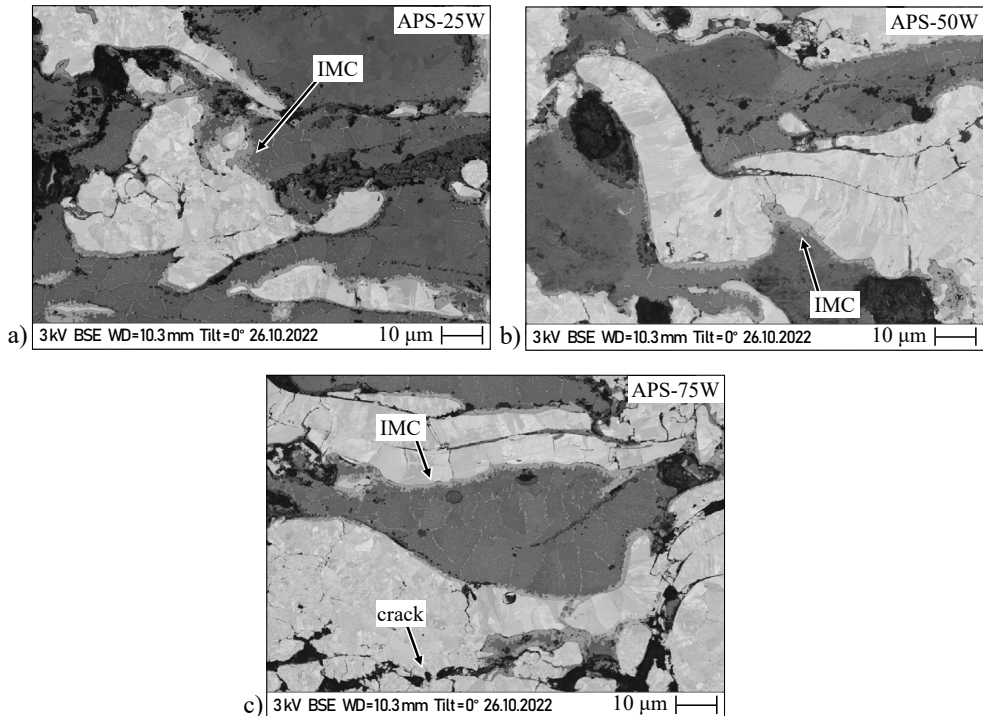


Figure 6.7 Microstructure of individual FGM layers of the failed V-3.FG-APS joint; a) 25W, b) 50W, c) 75W

In another sample (sample-B), the failure was more severe than in sample-A and -C. The entire 75W layer fractured, as shown in Figure 6.8 a). The V-filler showed localized large size voids, as can be seen in Figure 6.8 b) and c). This could be due to the extremely localized heating of the sample, resulting in the localized melting and sublimation of V.

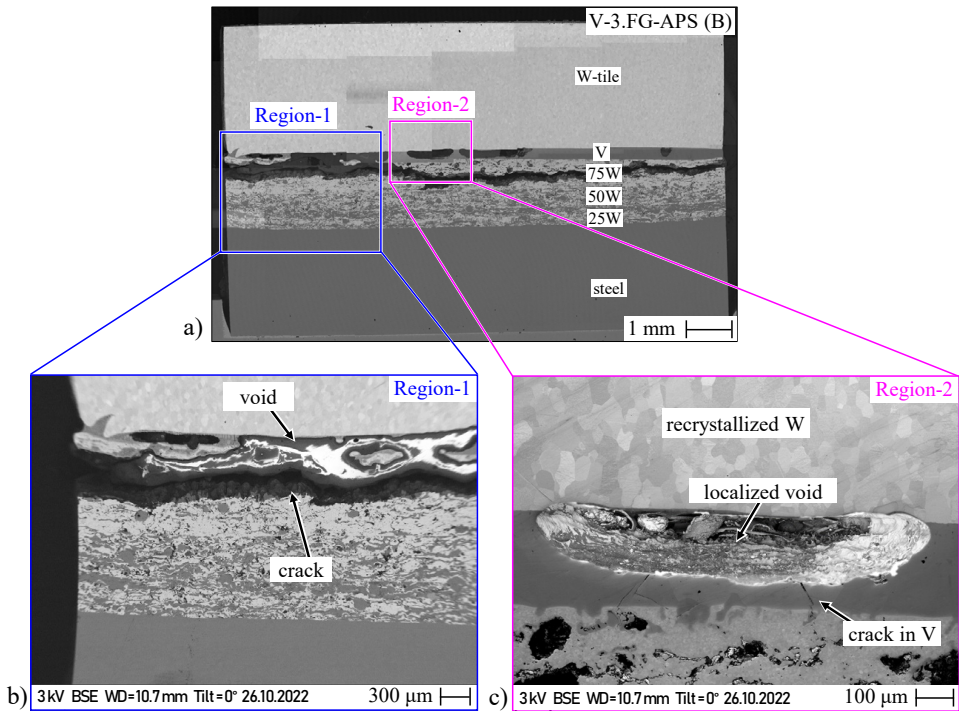


Figure 6.8 a) Cross-section of the failed V-3.FG-APS joint (sample-B) with two marked regions (Region-1 and -2), b) Region-1 showing cracks inside the 75W, c) Region-2 showing macroscale vacancy in V-filler

6.1.2 Summarized failure mechanism

Based on the investigations, the failure pattern of V-3.FG-APS joint can be summarized as follows:

- Crack formation in 75W layer: Horizontal macrocracks were observed predominantly inside the W constituents of 75W layer. There was no preferential location for such cracks; some originated from the corners/edges of the joint and some inside the middle of the joint. The poor adhesion strength between W-splats was the major contributing factor.
- Crack formation in V-filler: Cracks were also observed inside the V-filler along the direction perpendicular as well as inclined to the bonding plane.
- Delamination of the W-V bond seam: Interestingly, most of this delamination was due to the fracture of the parent material (W and V) close to the W-V bond seam. In few areas, the fracture took place exactly at the W-V interface.
- Insignificant influence of IMC: Although IMC was formed in the composites during the HHH testing, the formation of cracks in 75W was not influenced by the formation of IMC.

6.2 2.FG-SPS joint

The visual inspection of the failed 2.FG-SPS joints showed that in most samples, the W-tile detached completely from the topmost 50W layer, as can be seen in Figure 6.9. In other samples (sample-A, -E and -H), the W-tile remained loosely attached to the FGM.

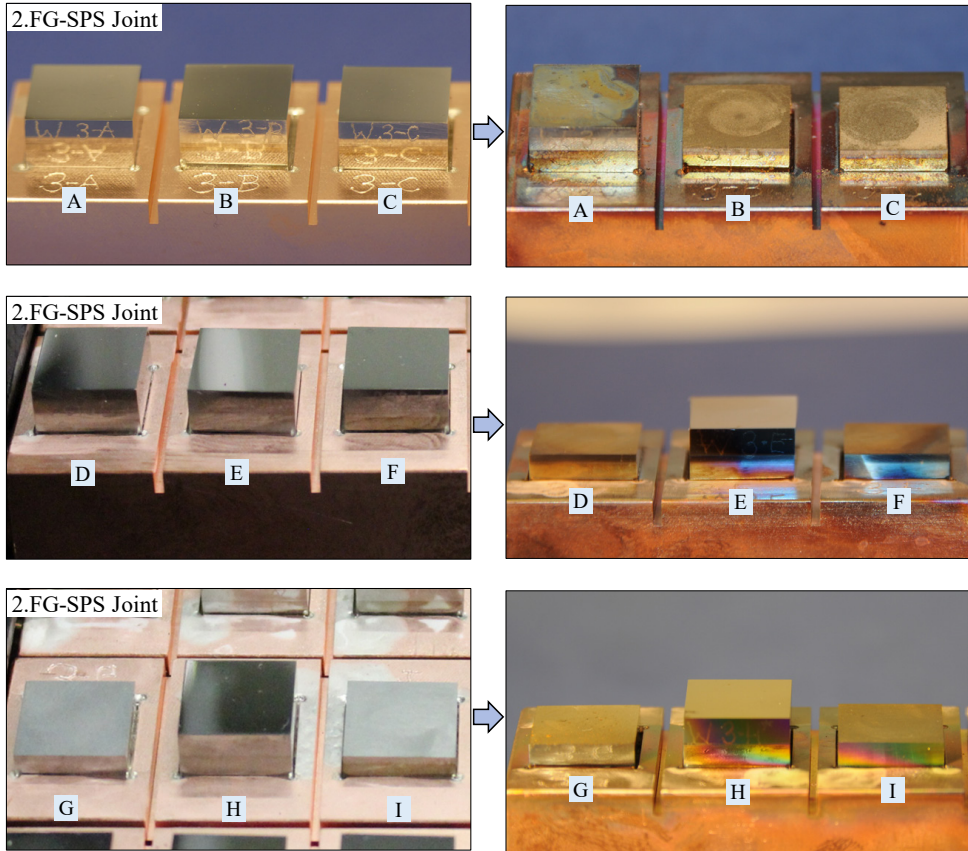


Figure 6.9 Macroscopic examination of 2.FG-SPS joints (before and after the HHF testing)

6.2.1 Investigation of the cross-sectional cut

After the visual inspection, cross-section was made on all three samples (sample-A, -E and -H) for metallographic investigations. However, during the cutting process, the W-tile detached completely except for sample-H, where the W-tile remained partially attached to the 50W layer on only one half of the joint. This partially attached joint was used for further metallographic investigation. Its resulting micrograph is shown in Figure 6.10 with two marked regions (Region-1 and -2) that were examined closely. The W-tile detachment initiated at the edge/corner of the joint (Region-1) and propagated towards the centre (Region-2). The micrograph of the edge of the joint, marked as Region-1, is shown in Figure 6.11 a). The fractured surfaces of the delaminated W-tile (Figure 6.11 b)) and delaminated 50W (Figure 6.11 c)) did not show any cracks or defects.

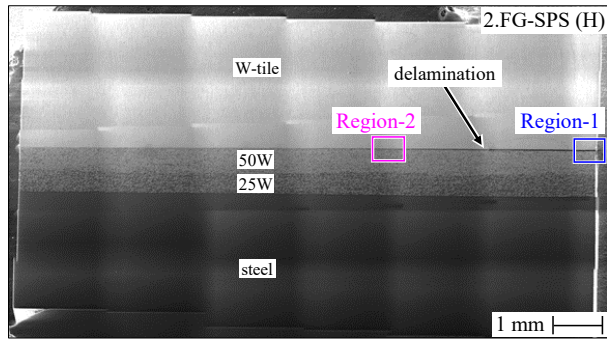


Figure 6.10 Cross-section of the failed 2.FG-SPS joint (sample-H) with two marked regions (Region-1 and -2); these regions were closely analysed as shown in Figure 6.11 and Figure 6.12 (Note: it is a stitched image and thus the stitching lines must be ignored)

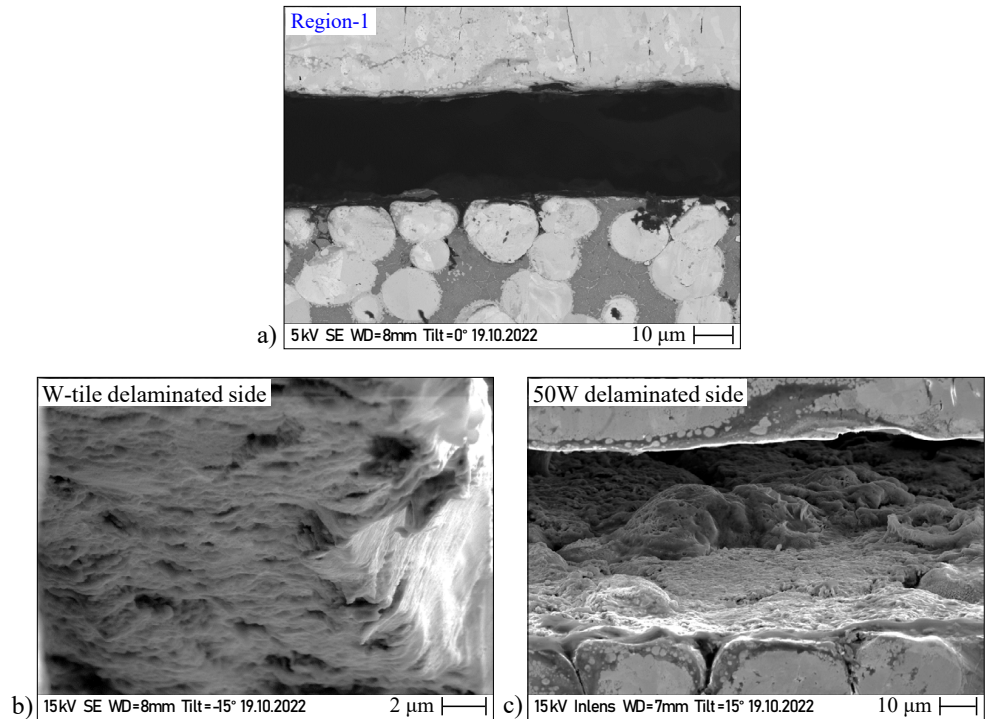


Figure 6.11 a) Micrograph of Region-1 (its spatial location is marked in Figure 6.2); close-up of the fracture surface of: b) delaminated W-tile side, c) delaminated 50W side

The investigation of Region-2 is shown in Figure 6.12 a) with specific marked areas ([A] to [D]) for further analyses. The failure of the joint, because of the delamination of W-tile and 50W, can be divided into five modes, as depicted in Figure 6.12 b) to e):

- Fracture of W-IMC interface: in certain sites (Figure 6.12 b)), fracture occurred precisely at the interface between the W-tile and the IMC, resulting in some IMC fragments sticking onto the delaminated 50W side.

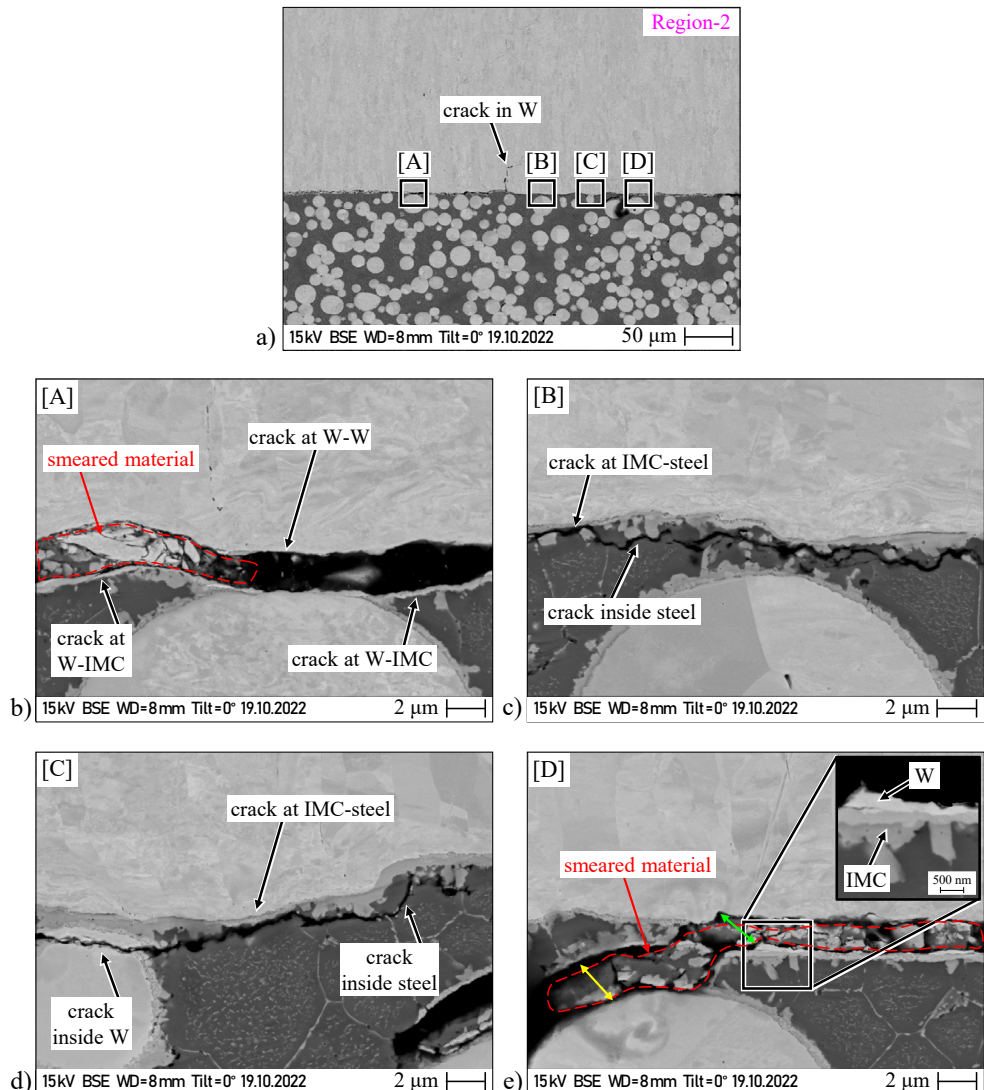


Figure 6.12 a) Micrograph of Region-2 (its spatial location is marked in Figure 6.10); close-up micrograph showing the failure pattern near the W-50W bond line at four sites: b) [A], c) [B], d) [C], e) [D] (Note: during the metallographic preparation (grinding step), some materials might get trapped inside the gaps, termed as smeared material, as can be seen in b) and c). In reality, this gap must be vacant and therefore, these must be ignored)

- Fracture of IMC-steel interface: in certain areas (Figure 6.12 c) and d)), the fracture occurred exactly at the interface between the IMC and the steel phase of 50W layer, resulting in the IMC fragments sticking onto the delaminated W-tile.
- Fracture inside steel phase: in certain areas (Figure 6.12 c) and d)), the fracture was observed to occur within the steel phase located near the W-50W bond seam.
- Debonding of W-W interface: it was observed that fractures also occurred exactly at the interface between the W-particles of the 50W layer and W-tile. This can be seen in Figure 6.12 b). This was due to the weak bonding between the W particles and the W-tile. Interestingly, the bonding between the W particles and W-tile was strong in a few areas, resulting in crack inside the W-particles (see Figure 6.12 d)).
- Minor chipping off of W-tile: in only one specific site (indicated by the green double arrow line in Figure 6.12 e)), the W material from W-tile chipped off along with the IMC.

Therefore, based on this analysis, it can be stated that the failure of the W-50W bond seam occurs through a combination of the above-mentioned failure modes.

6.2.2 Investigation of the delaminated W-tile and 50W surface

Delaminated W-tile surface: To understand the failure pattern further, the delaminated surface of the completely detached W-tile was investigated closely, as can be seen in Figure 6.13 a). EDX analysis was conducted on an area that was scanned (marked as yellow box in Figure 6.13 b)), and elemental compositions were determined at specific points (marked as spectrum-1 to -4). The elemental compositions of these points are provided in Table 6.1. The analysis indicated that the white areas in Figure 6.13 b) were W, while the grey areas were IMC. This suggests that the delaminated W-tile was mostly covered by IMC. This observation supports the earlier finding that the fracture occurring at the interface between the IMC and steel phase of the 50W layer leads to the IMC fragments adhering to the delaminated W-tile.

The surface topography of the delaminated W-tile was also examined by capturing the SEM micrograph while tilting the surface at a 45° angle, as shown in Figure 6.14 a). Microcracks were observed in the delaminated W-tile, indicating that during the delamination, the bonding strength between the W-tile and W-particles of the 50W layer was strong enough to cause some material to chip off, resulting in the formation of these microcracks, as indicated by the red arrow in Figure 6.14 b).

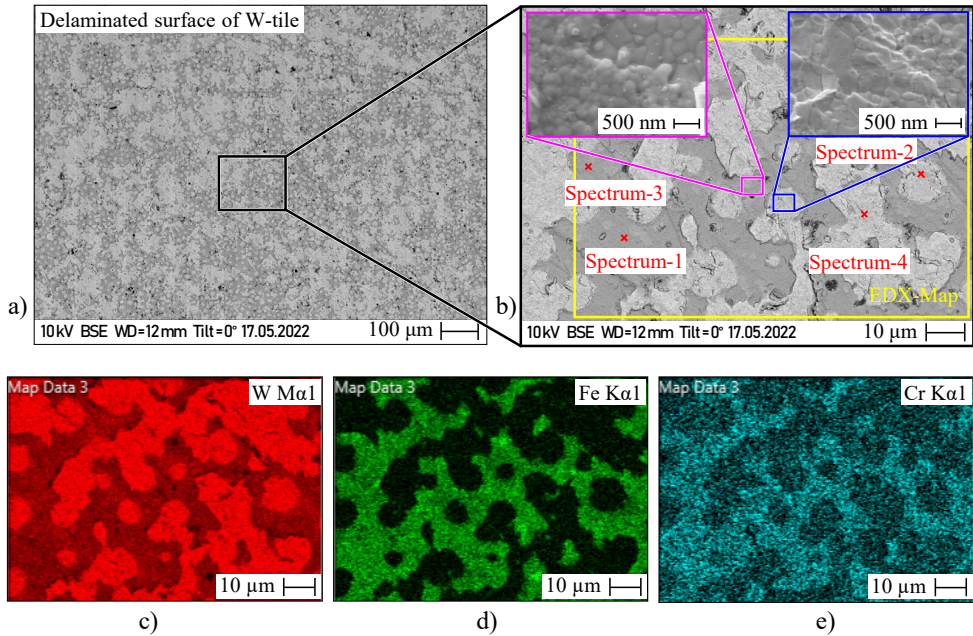


Figure 6.13 a) Delaminated surface of W-tile, b) its close up BSE micrograph showing the topography of W and IMC in purple and pink magnified snippet box; the yellow box is the EDX scan area marked as “EDX-map” along with locations of four EDX point analyses marked as “Spectrum-1 to -4”, c) W spectrum map, d) Fe spectrum map, e) Cr spectrum map

Table 6.1 Element composition at various locations corresponding to Figure 6.13

| EDX-spectrum | Composition | | | Composition | | |
|--------------|-------------|------|-----|-------------|------|-----|
| | (at%) | | | (wt%) | | |
| | Fe | W | Cr | Fe | W | Cr |
| Spectrum-1 | 51.0 | 41.4 | 7.6 | 26.2 | 70.2 | 3.6 |
| Spectrum-2 | 0.8 | 99.1 | 0.1 | 0.2 | 99.7 | 0.1 |
| Spectrum-3 | 48.9 | 43.0 | 8.2 | 24.7 | 71.5 | 3.8 |
| Spectrum-4 | 1.0 | 99.0 | - | 0.3 | 99.7 | - |

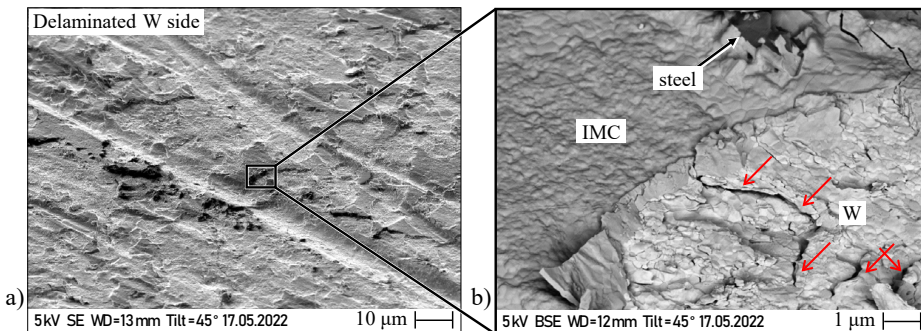


Figure 6.14 a) Micrograph of the delaminated W-tile positioned at 45° tilt, b) its close-up

Delaminated 50W surface: Similarly, the investigation of the delaminated surface of the 50W layer using EDX analysis was performed, as shown in Figure 6.15 and Table 6.2. The point (marked as spectrum-1) indicated the presence of both W and Fe. Its elemental composition suggested that it should be IMC. Therefore, it can be inferred that the delaminated surface was mostly covered by IMC, as can be seen in Figure 6.15 a). In short, the following can be stated: In some areas, the IMC at the W-50W bond seam fractured itself from the W-tile, which is why it was found on the 50W layer. In other areas (marked by enclosed yellow dotted lines in Figure 6.15 a)), IMC was not present; this means that IMC and some steel constituents got fractured out of the 50W and stuck onto the delaminated W-tile. These observations are consistent with the failure mode explained in Section 6.2.1.

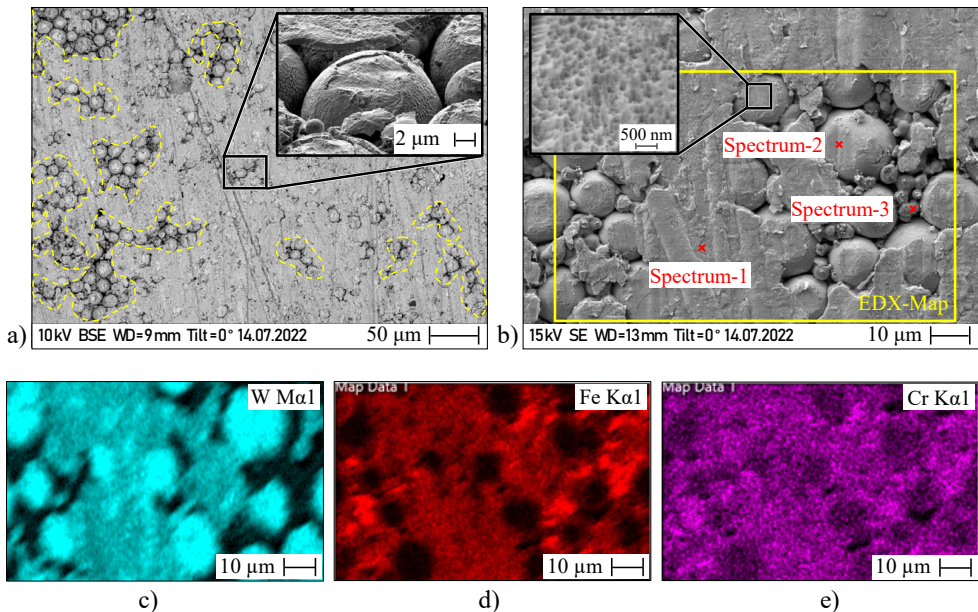


Figure 6.15 a) Micrograph of the delaminated 50W surface, b) The close-up SEM micrograph marked with yellow box showing the EDX scan area marked as “EDX-map” along with the spatial locations of three EDX point analyses marked as “Spectrum-1 to -3”, whose elemental compositions are provided in Table 6.2, c) W spectrum map, d) Fe spectrum map, e) Cr spectrum map

Table 6.2 Element composition at various locations corresponding to Figure 6.15

| EDX-spectrum | Composition | | | Composition | | |
|--------------|-------------|------|-----|-------------|------|-----|
| | (at%) | | | (wt%) | | |
| | Fe | W | Cr | Fe | W | Cr |
| Spectrum-1 | 50.7 | 41.0 | 8.3 | 26.2 | 69.8 | 4.0 |
| Spectrum-2 | 4.5 | 95.5 | - | 1.4 | 98.6 | - |
| Spectrum-3 | 84.8 | 6.1 | 9.1 | 74.8 | 17.8 | 7.5 |

6.2.3 Summarized failure mechanism

Based on the investigations, the failure pattern of 2.FG-SPS joint can be summarized as follows:

- Detachment of W-tile: Macroscopically, the failure occurred at the W-50W bond seam resulting in the complete detachment of W-tile from the topmost FGM layer. Microscopically, the failure occurred near that bond seam by a more complex phenomenon, as explained below.
- The main reason for the failure of the bond seam was the fracture of the two interfaces: W-IMC and IMC-steel. Also, fracture inside the steel phase of the 50W layer, present close to the bond seam, was observed occasionally.
- Major responsible factor: it can be concluded that the main reason for the early failure of the bond seam between the W-tile and 50W layer is the presence of IMC. The FGM layers, i.e., the 25W and 50W layers, did not show any damage.

6.3 3.FG-SPS joint

Similar to 2.FG-SPS joint, the failed 3.FG-SPS joint also exhibited detachment of the W-tile from the topmost 75W layer, as shown in Figure 6.16. In one of the samples (sample-F), the W-tile completely detached; in other samples, it remained loosely attached to the FGM.

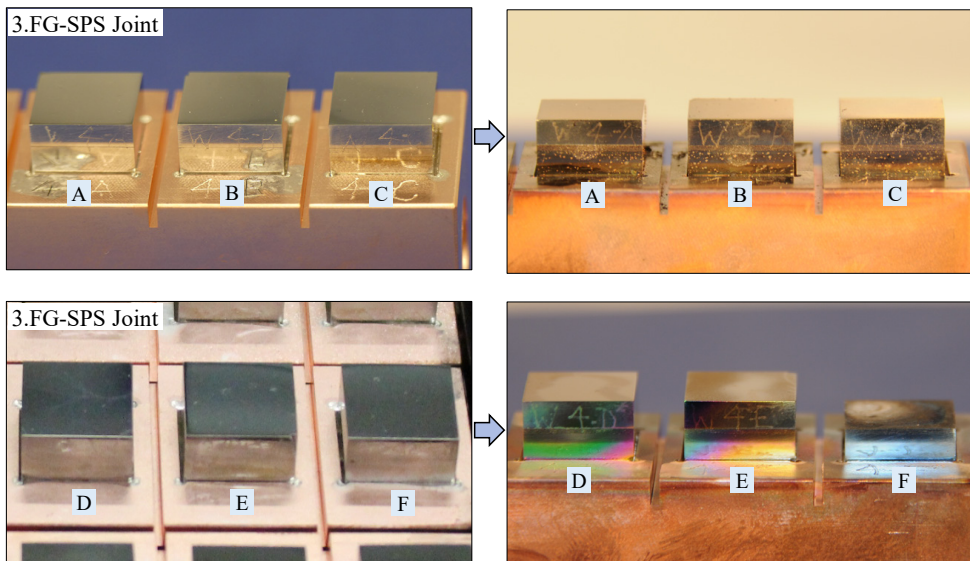


Figure 6.16 Macroscopic examination of 3.FG-SPS joints (before and after the HHF testing)

6.3.1 Investigation of the cross-sectional cut

After the visual inspection, cross-sections were made on all the samples to conduct metallographic investigations. However, during the cutting, the W-tile detached completely in all the samples except for sample-B and -C. One of these samples (sample-C) was selected for metallographic investigation, whose cross-sectional cut is shown in Figure 6.17 with four

marked regions (Region-1 to -4). The delamination of the W-tile was observed to initiate from the corner/edge of the joint and propagate towards the centre of the joint, ultimately resulting in the detachment of the entire W-tile, as can be seen in Region-1 and Region-2 in Figure 6.18 a) and b).

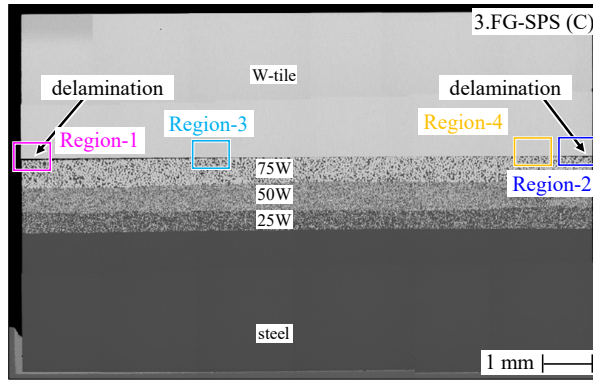


Figure 6.17 Cross-section of the failed 3.FG-SPS joint (sample C) showing four regions of interest (region-1 to region-4) for further examination

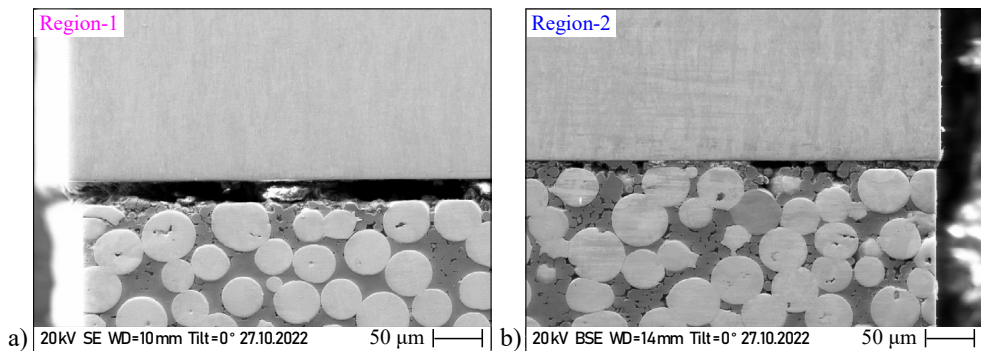


Figure 6.18 Micrograph showing the delamination occurring at the edge of the joint for two regions: a) Region-1 and b) Region-2 (their spatial locations are marked in Figure 6.17).

The SEM micrographs of Region-3 and Region-4, with the corresponding spatial locations marked in Figure 6.17, are shown in Figure 6.19 a) and b). Specific marked areas ([A] to [D]) were investigated further to understand the failure pattern. Similar to 2.FG-SPS joint, the failure that occurred here can be divided into three modes, as depicted in Figure 6.19 c) to f):

- Fracture of W-IMC interface: in some sites (Figure 6.19 f)), the fracture was observed to occur exactly at the interface between W-tile and IMC.
- Fracture of IMC-steel interface: in some sites (Figure 6.19 d) and e)), the fracture occurred exactly at the interface between IMC and steel phase of 75W layer.
- Fracture inside the steel and W-particles: first, in some sites (Figure 6.19 c)), the fracture occurred within the steel phase, which was present close to the W-tile. Second and rarely,

a crack was observed inside the W-particle of the 75W layer. It must be noted that most W-particles do not form strong bonding with the W-tile. Therefore, such cracks inside the W-particles were relatively rare.

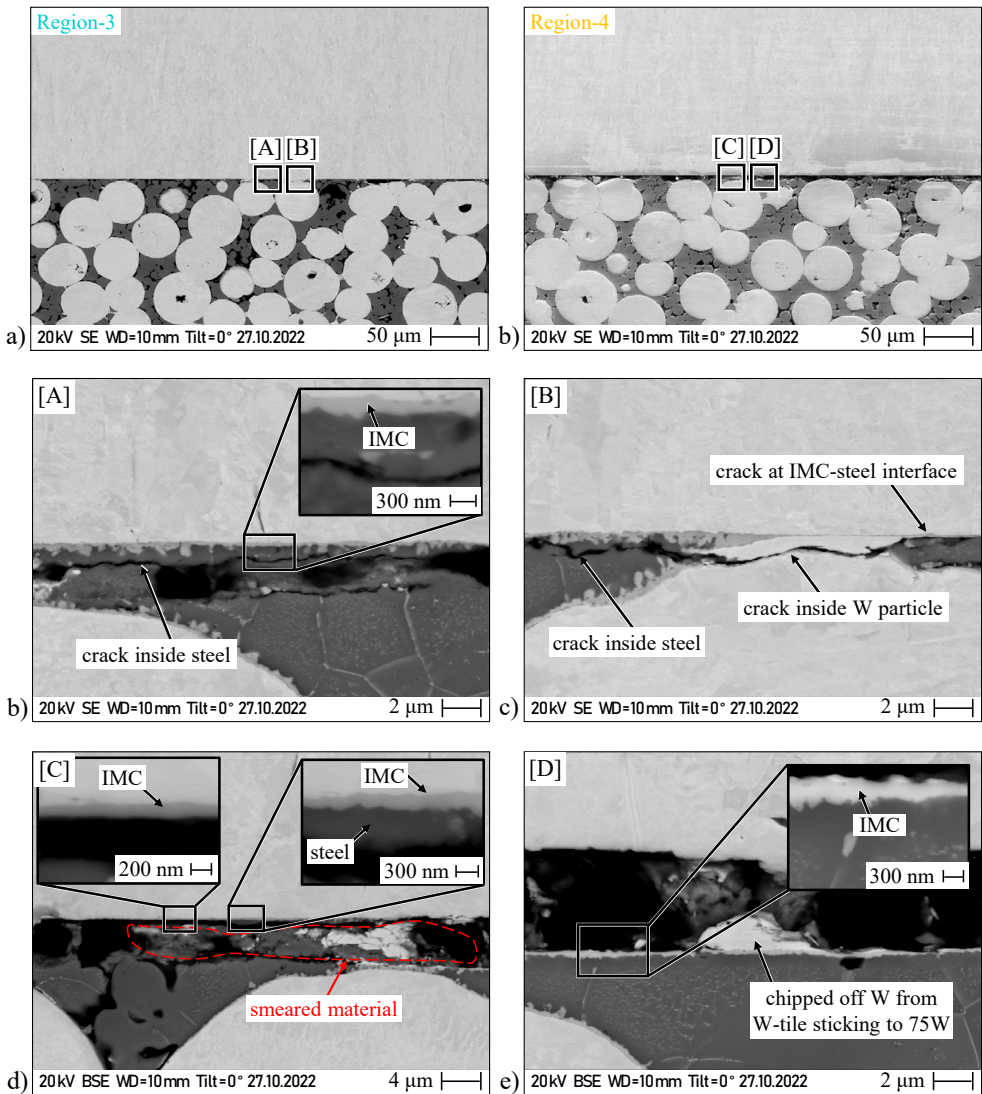


Figure 6.19 a) Micrograph of Region-3, b) SEM micrograph of Region-4 (*their spatial locations are marked in Figure 6.17*); Close-up showing the failure pattern near the W-75W bond line at four sites: b) [A] showing fracture inside steel, c) [B] showing fracture inside steel and W-particle, d) [C] showing fracture at IMC-steel interface, e) [D] showing fracture at W-IMC interface (*Note: as seen in d), some smeared material gets trapped inside the gap and these must be ignored*)

6.3.2 Investigation of the delaminated W-tile and 75W surface

Delaminated W-tile surface: The delaminated W-tile of one of the samples was examined closely, as shown in the SE and BSE micrographs in Figure 6.20. The EDX analysis suggests that the grey, light grey and white areas in the BSE micrographs (Figure 6.20 b) and d)) are steel, IMC and pure W, respectively. The elemental compositions of certain locations were also determined, marked as spectrum-1 to spectrum-5 (see Table 6.3). As previously mentioned in section 6.3.1, the fracture at the W-75W bond seam can occur in any of the three modes: fracture inside steel, fracture at the W-IMC interface or fracture at the IMC-steel interface. Consequently, any of the three constituents, i.e., steel, IMC or W, could be present on the delaminated W-tile surface.

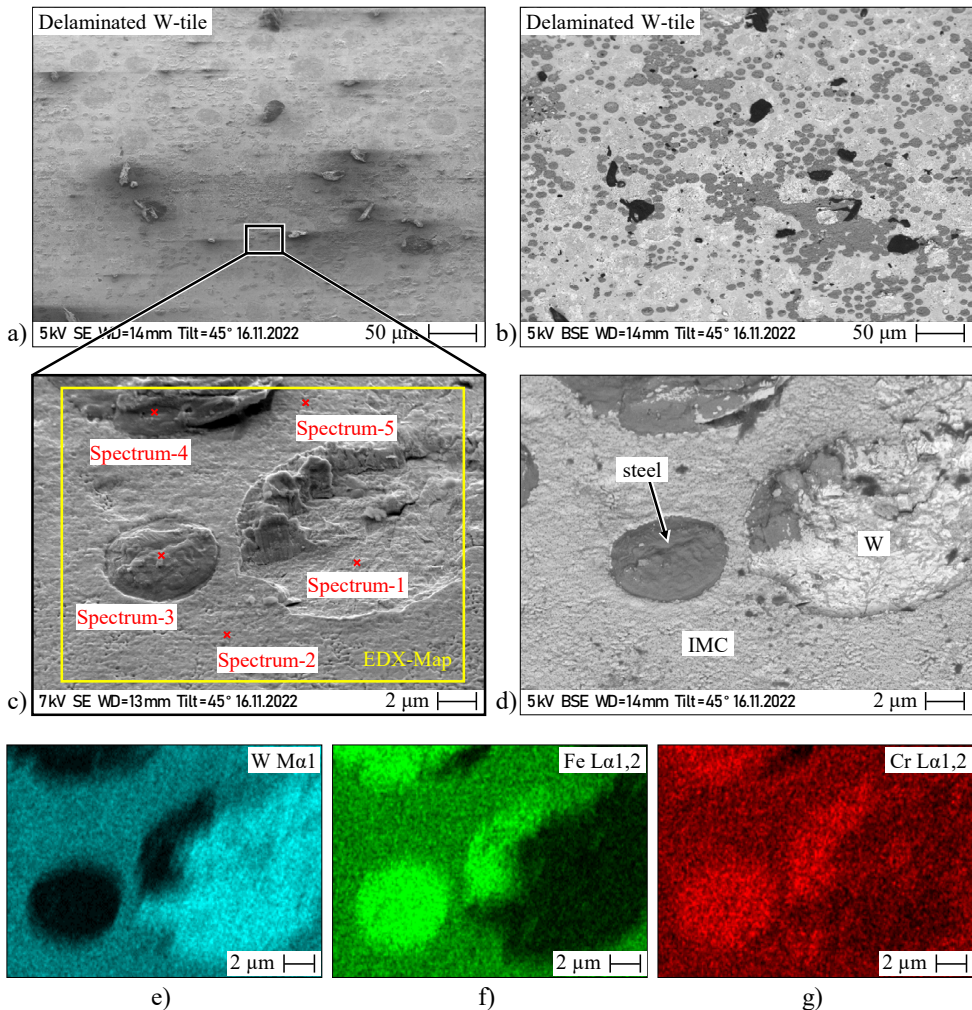
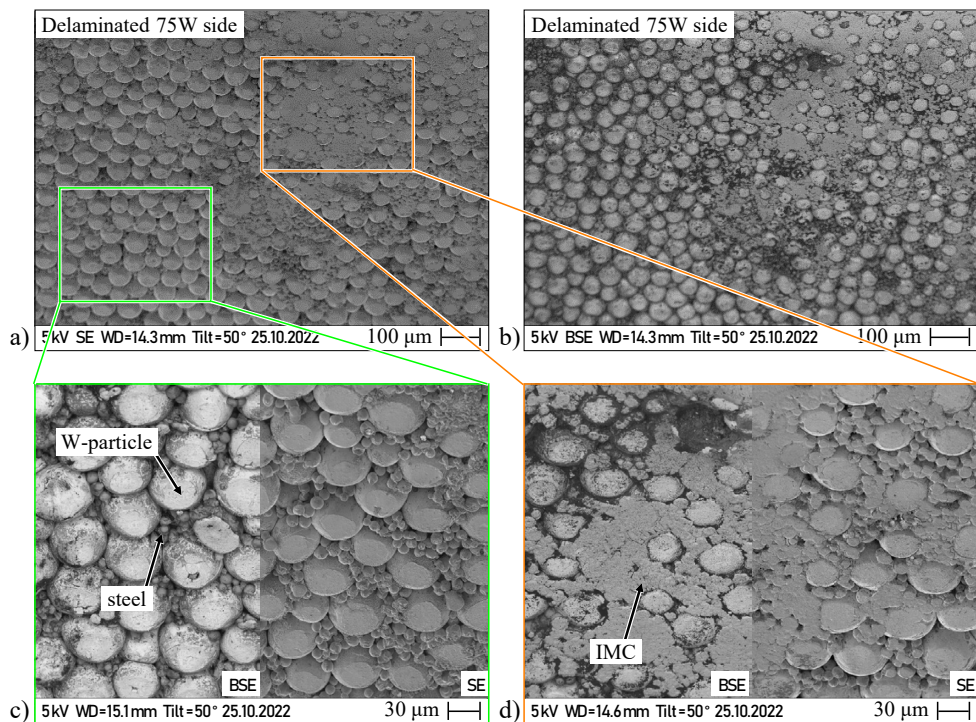


Figure 6.20 a) SE micrograph of the delaminated W-tile, b) BSE micrograph, c) SE micrograph of a location showing EDX-spectrum mapping and marked points for individual elemental composition analyses, d) its BSE micrograph, e) W spectrum map, f) Fe spectrum map, g) Cr spectrum map (*Note: the dark black spots in b) are just dust particles*).

Table 6.3 Element composition at various locations corresponding to Figure 6.20

| EDX-spectrum | Composition (at%) | | | Composition (wt%) | | |
|--------------|----------------------|------|------|----------------------|------|------|
| | Fe | W | Cr | Fe | W | Cr |
| Spectrum-1 | - | 100 | - | - | 100 | - |
| Spectrum-2 | 58.3 | 25.1 | 16.6 | 37.3 | 52.8 | 9.9 |
| Spectrum-3 | 82.8 | 1.2 | 16.0 | 81.5 | 3.9 | 14.6 |
| Spectrum-4 | 86.0 | 1.7 | 12.3 | 87.0 | 4.2 | 8.85 |
| Spectrum-5 | 57.6 | 26.6 | 15.8 | 36.0 | 54.8 | 9.2 |

Delaminated 75W surface: The delaminated surface of the 75W layer was also examined using SE and BSE micrographs, as presented in Figure 6.21 a) and b), respectively. The BSE micrograph was sufficient to identify the individual phases; therefore, additional EDX analysis was not required. The BSE micrograph revealed that in certain areas of the delaminated side, W-particles and steel phases were visible, as shown in Figure 6.21 c), while in other areas, a layer of IMC covered the surface, as observed in Figure 6.21 d).

**Figure 6.21** a) SE micrograph of delaminated 75W side, b) BSE micrograph of the same

6.3.3 Summarized failure mechanism

Based on the investigations, the failure pattern of 3.FG-SPS joint was found to be similar to that of 2.FG-SPS joint. Macroscopically, the failure occurred at the W-75W bond seam resulting in the complete detachment of the W-tile. Microscopically, it was found to be the result of the following fractures:

- Failure of W-75W bond seam: The fracture predominately occurred exactly at the W-IMC interface or IMC-steel interface (steel matrix of 75W). There were also some rare occurrences where the fracture happened inside the steel matrix of the 75W.
- Poor/improper bonding of W-W: Another dominating pattern was the fracture occurring at the interface between the W particle of the 75W and W-tile, which can be attributed to their poor metallurgical bonding.

6.4 W-steel direct joint

The visual inspection indicated the complete detachment of the W-tile (except for sample-A), as shown in Figure 6.22. The detachment originated from the corner/edge and propagated towards the centre.

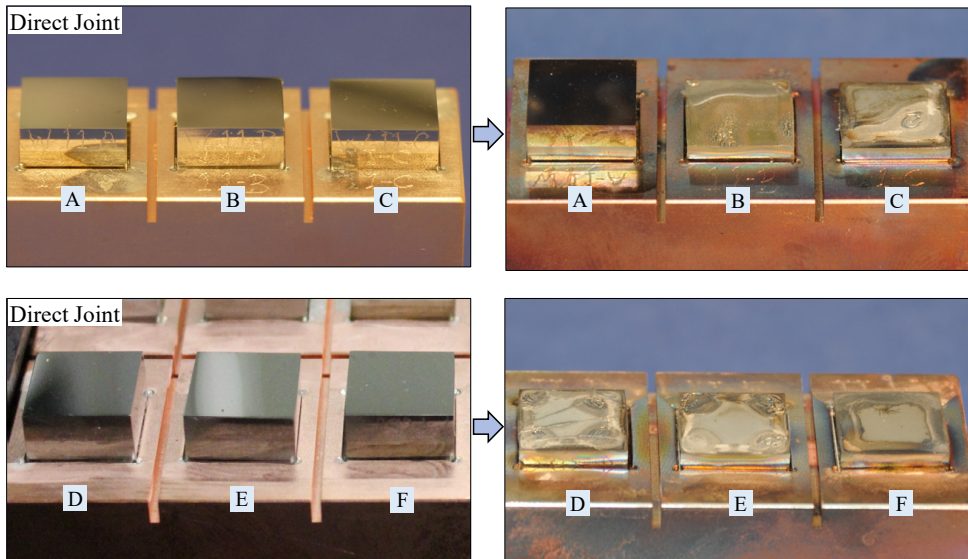


Figure 6.22 Macroscopic examination of Direct joints (before and after the HHF testing)

6.4.1 Investigation of the cross-sectional cut

After the visual inspection, cross-section was made on sample-A for metallographic investigation, as illustrated in Figure 6.24. Four regions, marked as Region-1 to Region-4, were thoroughly investigated. As the detachment of the W-tile originated from the joint's edge, the edge (Region-1) was further examined, as depicted in Figure 6.23 a). As discussed in Section 4.4, directly bonded W-steel joints form thin IMC and reaction layers. This reaction layer

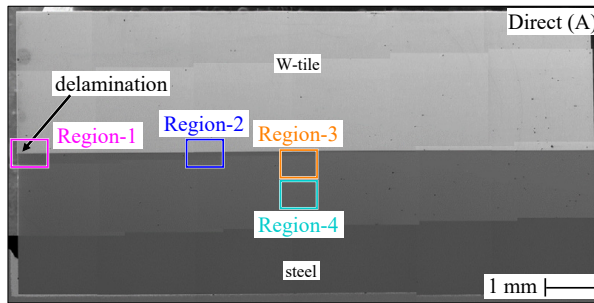


Figure 6.24 Cross-section of the failed direct joint (sample A) with four regions of interest for further analysis

(ferrite+IMC) is present below the IMC on the steel side, as indicated by α +IMC in Figure 6.23 b) and c). The detachment occurred precisely at the interface between W-tile and IMC, which then propagated towards the centre of the joint.

The region close to the joint's centre, marked as Region-2 in Figure 6.24, was also examined. Figure 6.25 illustrates this region, along with the EDX analyses of specific phases, as listed in

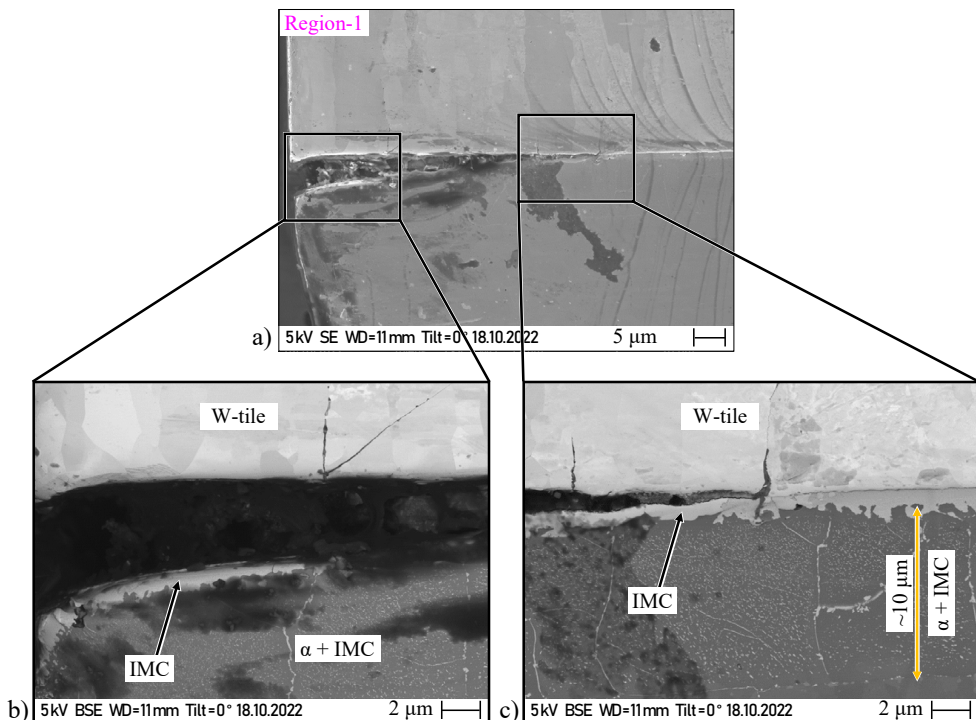


Figure 6.23 a) Region-1 representing the SEM micrograph of location at the edge of the direct joint. b) Delamination of the W-tile at the edge of the joint, c) Close-up of the location showing the delamination pattern (*Note: the dark spots and patches in the SEM micrograph are just external dust and contamination*)

Table 6.4. The W-steel bond seam showed $\sim 1 \mu\text{m}$ thick IMC and $\sim 10 \mu\text{m}$ thick reaction layer (α +IMC), as shown in Figure 6.25 b) and c). Notably, these thicknesses were the same as before the HHF testing, as shown in Figure 4.21 c). However, due to the diffusion of the W from the W-tile, the amount of IMC inside this reaction layer increased significantly to 12 %.

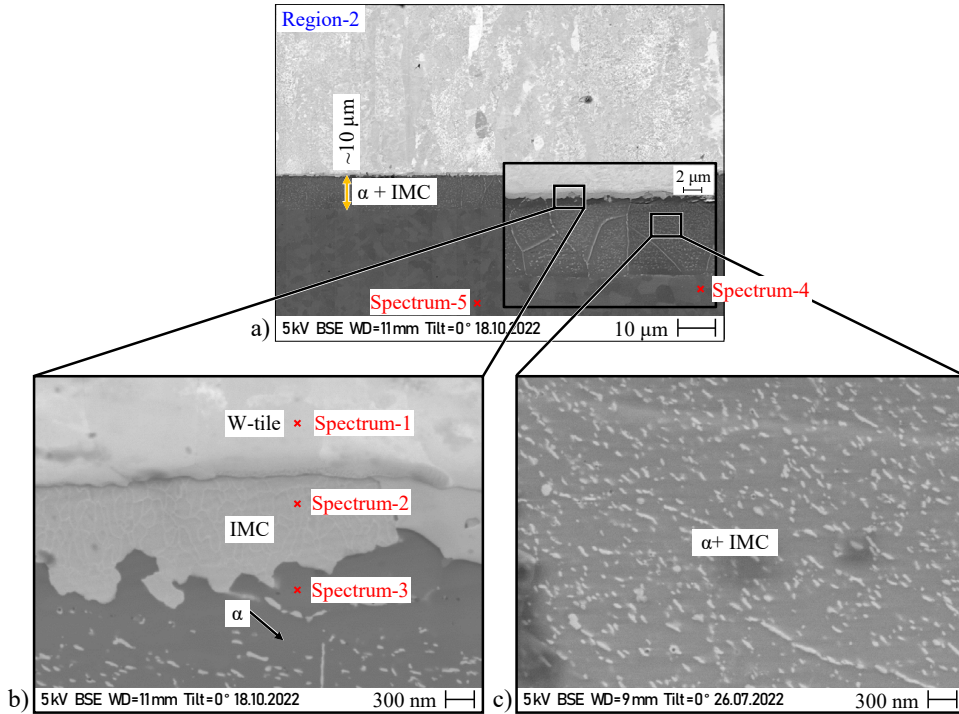


Figure 6.25 a) Region-2 represents the micrograph of a location at the centre of the direct joint. b) Close-up micrograph showing IMC, c) Close-up micrograph of the reaction layer showing a mixture of IMC inside the ferritic phase

Table 6.4 Element composition at various points of interest corresponding to Figure 6.25

| EDX-spectrum | Chemical composition | | | | | | | |
|--------------|----------------------|------|-----|-----|-------|------|------|-----|
| | (wt%) | | | | (at%) | | | |
| | Fe | W | Cr | V | Fe | W | Cr | V |
| Spectrum-1 | 1.6 | 98.3 | 0.2 | - | 5.1 | 94.2 | 0.6 | - |
| Spectrum-2 | 28.3 | 66.5 | 5.2 | - | 52.4 | 37.4 | 10.2 | - |
| Spectrum-3 | 83.9 | 8.6 | 7.5 | - | 88.8 | 2.8 | 8.5 | - |
| Spectrum-4 | 89.4 | 1.1 | 9.2 | 0.2 | 89.5 | 0.3 | 9.9 | 0.2 |
| Spectrum-5 | 89.1 | 1.2 | 9.5 | 0.2 | 89.2 | 0.4 | 10.2 | 0.2 |

The elemental composition of the steel phase just below the reaction layer, marked as spectrum-4 and spectrum-5, have almost the same elemental composition as that of Eurofer 97 with only 1 wt% W. This indicates that the diffusion of W into the steel is only limited to the

first 10 μm and the W does not diffuse deeper into the steel. Despite having the same elemental composition as Eurofer 97, the steel has a ferritic structure, which can be seen in the microstructure in Figure 6.26 a). This is due to the prolonged exposure to high temperature during the HHF testing, resulting in long-term thermal ageing and transforming the martensite to ferrite. The steel farther away from the bonding seam, marked as Region-4 in Figure 6.24, retained its martensitic structure, which can be seen in Figure 6.26 b).

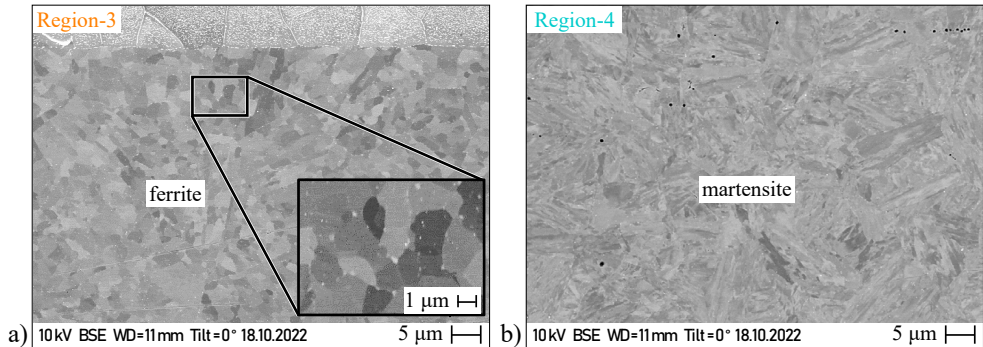


Figure 6.26 a) Region-3 representing the micrograph of location just below the reaction layer showing ferritic phase, b) Region-4 further below showing the martensitic phase

6.4.2 Investigation of delaminated W-tile and steel surfaces

Delaminated W-tile surface: One of the delaminated surfaces of the detached W-tile was examined closely, as shown in Figure 6.27. In contrast to the failure patterns observed in the 2.FG-SPS and 3.FG-SPS joints, the direct joint showed a more complex pattern. Therefore, the delaminated W-tile was studied closely. The delaminated side exhibited a patch of light grey areas. These regions were further analyzed, marked as Region-1 and Region-2 in Figure 6.27.

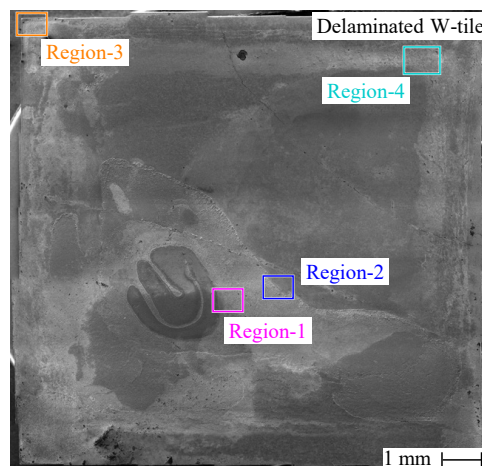


Figure 6.27 Delaminated surface of W-tile with four marked regions (Region-1 to -4) for further investigation

The micrograph of Region-1 indicated a pyramidal pattern on the delaminated W-tile, as shown in Figure 6.28 a) and b). To gain further insight into this pattern, EDX elemental mapping was conducted on the region indicated by the yellow box in Figure 6.28 b). The resulting scans in Figure 6.28 c) and d) suggests that this pyramidal structure should be the IMC, as it emits both the W and Fe signals. Additionally, the surface displayed faint O signals and bright C spots, as depicted in Figure 6.28 f) and g), indicating the presence of some contamination and dust particles.

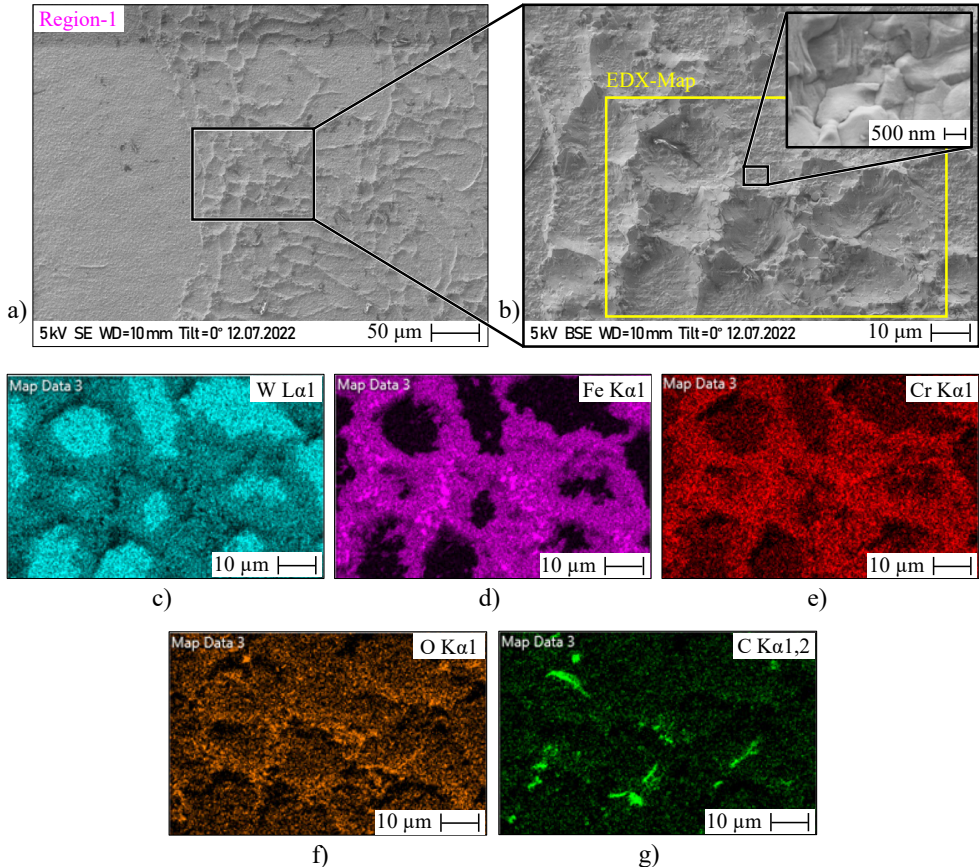


Figure 6.28 a) Micrograph of Region-1 (its location is marked in Figure 6.27), b) Close-up of the pyramidal pattern sticking on to the W-tile and the corresponding EDX spectrum map area, c) W spectrum map, d) Fe spectrum map, e) Cr spectrum map, f) O spectrum map, g) C spectrum map

Similarly, Region-2 was also investigated, as shown in Figure 6.29. The SE and BSE micrographs are shown here for better understanding (Figure 6.29 a) and b)). An area of interest, marked by the yellow box in Figure 6.29 a), was scanned with EDX spectrum mapping. The analysis indicated the presence of IMC (dark grey) and W (white) regions, which was established by the corresponding W and Fe spectrum maps (Figure 6.29 c) and d)).

Both the above investigations indicated that the light grey patch sticking onto the delaminated surface of the W-tile (see Figure 6.27) is IMC.

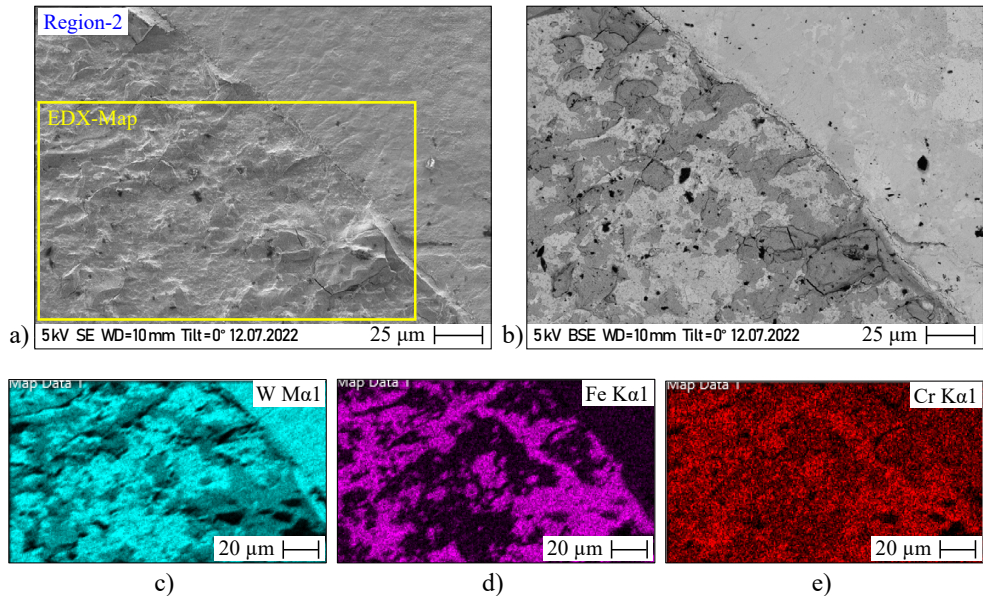


Figure 6.29 a) SE micrograph of Region-2 (its location is marked in Figure 6.30) and the corresponding EDX spectrum map area, b) It's BSE micrograph for better visualization, c) W spectrum map, d) Fe spectrum map, e) Cr spectrum map (*Note: the O and C spectrum maps were not relevant and not shown*)

The SEM micrograph of the corner of the delaminated W-tile, marked as Region-3 in Figure 6.27, is shown in Figure 6.30 a). This region showed some complex contamination patterns. Similarly, Region-4, as depicted in Figure 6.30 b), exhibited a network of microcracks with some visible dust particles. Here again, some dust particles are visible. It is important to

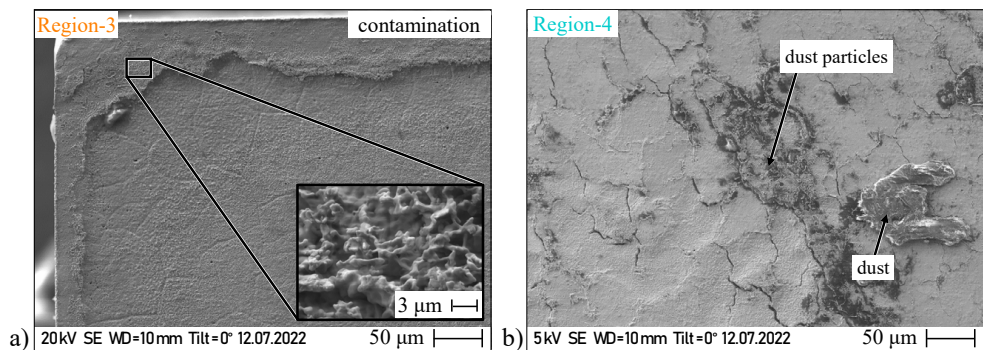


Figure 6.30 a) Micrograph of Region-3 (corner of the delaminated W-tile) showing contamination, b) Micrograph of Region-4 showing microcracks in W-tile (*their locations are marked in Figure 6.27*)

note that these contaminations may have occurred while removing the delaminated W-tiles post-HHF testing. During removal, the W-tiles were still hot and may have caused spontaneous contamination upon exiting the vacuum chamber of the HHF testing setup.

Delaminated steel surface: The delaminated steel surface of the same sample was studied. Its SEM micrograph is shown in Figure 6.31. Notably, the pattern observed in this micrograph is almost a mirror image of the pattern observed in Figure 6.27.

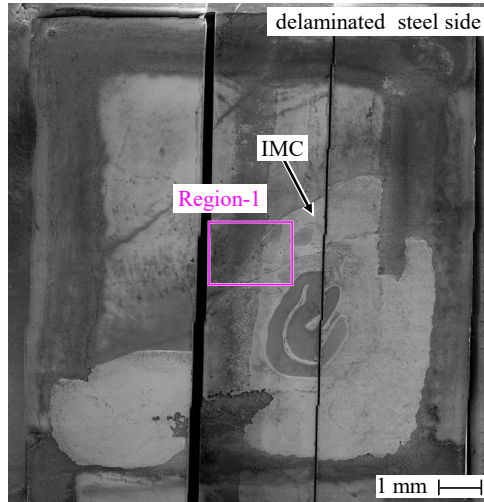


Figure 6.31 Micrograph of the surface of delaminated steel side with a marked Region-1 for further investigation

The SEM micrograph of a further investigated region (Region-1) is shown in Figure 6.32 a). The close-up SEM micrograph of a particular site is displayed in Figure 6.32 b), revealing a thin layer adhering to the steel surface. EDX analysis of this layer suggested that it is IMC, as it produced both W and Fe signals, as shown in Figure 6.32 c) and d). This layer's elemental composition was: 6.3 at% Cr, 52.5 at% Fe, 41.2 at% W. The area on the left side was purely steel, as no W signal was observed except for a faint W signal in the top left corner due to some diffused W. This indicated that the delaminated steel side mainly consisted of steel with a slightly high W concentration and with IMC sticking in few regions. As mentioned above, Figure 6.31 mirrors the pattern observed in Figure 6.27; it can be seen from Figure 6.31 that the IMC is sticking onto a steel surface, and in the corresponding location (mirror image) of Figure 6.27, the IMC is also sticking on the W-tile. This implied that the fracture may have occurred within the IMC in few places.

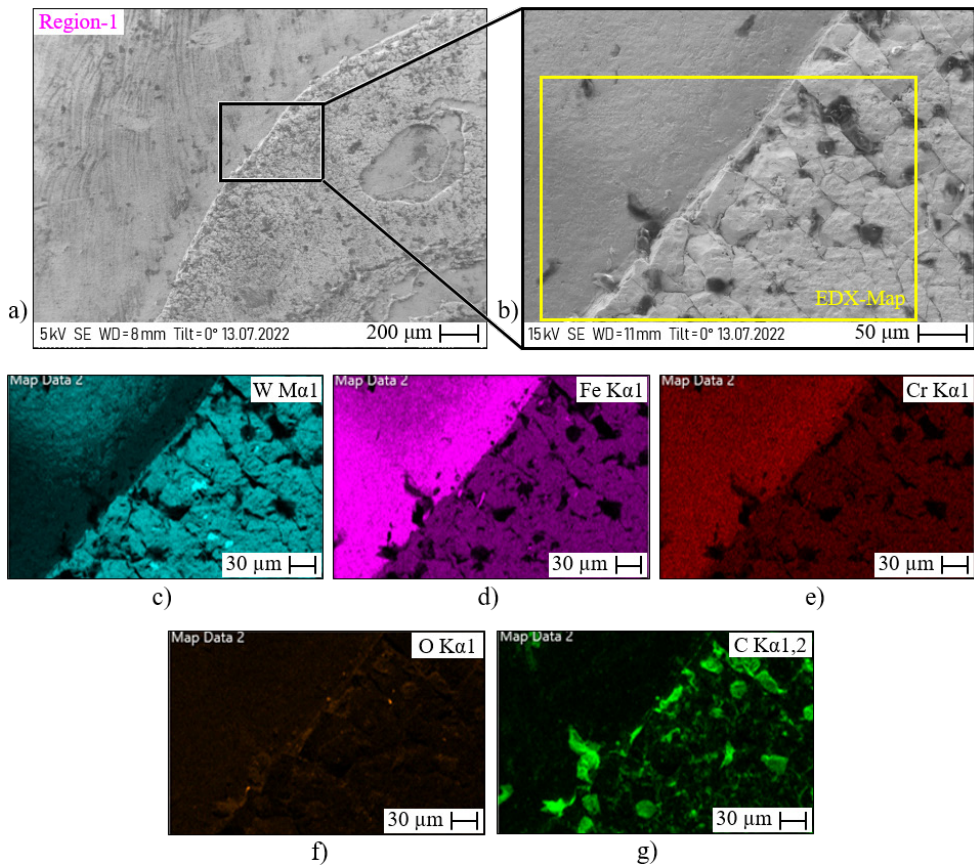


Figure 6.32 a) SE micrograph of Region-1 (its spatial location is marked in Figure 6.31), b) Close-up micrograph of one site and the corresponding EDX spectrum area map marked with yellow box, c) W spectrum map, d) Fe spectrum map, e) Cr spectrum map, f) O spectrum map, g) C spectrum map

6.4.3 Summarized failure mechanism

Based on the comprehensive investigations, the failure pattern of the direct joint can be summarized as follows:

- Macroscopically, the failure occurred at the W-steel bond seam resulting in the complete detachment of the W-tile. Microscopically, the delamination of W-tile and steel occurred by simultaneous fractures, explained below.
- The failure pattern was somewhat different here. Predominantly, the fracture occurred at the W-IMC interface, IMC-steel interface, and also within the IMC.

7 Concluding discussion

7.1 Evaluation of FGM/individual composites

FGM/composites produced in this thesis: A concise assessment of the produced composites is provided in Table 7.1.

Table 7.1 Assessment of FGM/individual sublayers based on important criteria

| Criteria | EDS | APS | SPS |
|-----------------------------|--|---|--|
| Positive aspect | - ultra-fast processing - limited IMC | - industrial process - high material throughput - limited IMC | - shorter processing time - less IMC |
| Individual layers | - 25W: 95 % dense - 50W: 95 % dense - 75W: unable to produce | - 85 % dense (all three compositions) | - 25W, 50W: 99+ % dense - 75W: 96 % dense |
| Ability to form 3-layer FGM | No | Yes | Yes |
| Mechanical properties | – | - brittle - low E_{mod} - low σ_{yield} | - ductile above 300 °C (except 75W) - low E for 75W - low σ_{yield} for 50W, 75W |
| Thermophysical properties | – | - CTE, c_p : as expected - low λ ; even less than that of pure steel | - CTE, c_p : as expected - better λ than that of steel - better λ than that of APS |
| Upscaling | - challenging - questionable | more likely/easier than SPS | possible/feasible |
| Negative aspect | - inhomogeneous sintering - inability to produce 75W | - oxides (up to 6 %) - high porosity - poor intersplat bonding | - insufficient W-W bonding in 50W & 75W - mechanical properties of 50W and 75W lower than expected |

Analyzing the summary (Table 7.1), it can be stated that EDS is most unsuitable for producing FGM and/or individual composites. Although APS can coat large parts, upscaling the setup—used in this thesis—consisting of a shrouding chamber would be challenging and expensive. If the plasma spraying on an actual FW panel for a blanket module is undertaken, then the APS would require a large and complex shrouding chamber. As a result, this process would no longer be cost-effective and straightforward. Thus, it would be meaningful to consider a vacuum plasma spraying (VPS) process.

The composites produced by SPS showed favourable properties, and make this the most suitable process for producing FGM. Even though the SPS is not an as well-known industrial process as plasma spraying (PS), the upscaling of the SPS process is achievable. The total surface area of FW panels in a future fusion reactor is expected to be $\sim 1200 \text{ m}^2$ [7]. Currently, the largest industrial scale SPS equipment can apply 4000 kN pressing force, so a 200 mm disc can be sintered with 125 MPa pressure [93]. Considering a usable square geometry of 140 mm \times 140 mm out of this disc, a basic calculation reveals that one would need 61,300 sintered discs. The use of automated systems could make this achievable. The only disadvantage is the unexpected mechanical properties of sintered 50W and 75W composites; e.g. the elastic modulus (E) of 75W is just 73 % of its theoretical expected value, and 50W and 75W have low yield strength (σ_{yield}) than expected. This is assumed to be the result of insufficient metallurgical bonding between W-W particles, which is discussed below.

W-W metallurgical bonding in SPS sintered composites: As explained in Section 1.4.1, the conventional sintering of pure W is performed at 2000–2500 °C, and even this achieves a relative density of only 92–98 %. The sintering in SPS is performed at a relatively low temperature of 1000 °C—achieving 96 % relative density in 75W—, hence a weak W-W bonding is expected. Nevertheless, it is still vital to examine how worse this bonding is. Therefore, FIB cuts were made at the W-W interfaces; these SEM micrographs are provided in Appendix F, and only the gist of the analysis is summarized here. In 50W, two out of three W-W contact sites examined formed good W-W interfacial metallurgical bonding, while the third one formed a partial bonding. In 75W, a FIB cut is made on the W-W contact site, where the two W particles are sufficiently pressed onto each other. The investigation revealed that these two particles formed partial metallurgical bonding; 45 % of contact showed no metallurgical bonding. This suggests that the bonding between W particles in 75W is still a significant challenge. A possible solution to overcome this is to increase the sintering pressure using high pressure (400 MPa) tools made out of TZM. This might allow the W particles in 75W to deform plastically and come close to each other; thus, allowing them to initiate metallurgical bonding. However, it must be pointed out that increasing the pressure could be challenging for upscaling; currently, the largest SPS equipment can press the tools with a 4000 kN force. Thus instead of \varnothing 200 mm, only \varnothing 55 mm disc could be sintered.

Comparison of SPS and VPS: As mentioned above, if plasma spraying is to be considered, then a VPS should be used instead of the APS. Currently, only one research group has been

developing FGM via VPS for over the past 10–15 years [57,59,60]. However, the thermomechanical and thermophysical properties of individual layers of the FGM have not yet been examined. This research gap makes comparing the FGM produced by the VPS and SPS problematic. Recently, the thermal diffusivity of a 98 % dense 5-layer FGM produced by VPS has been reported [47,57], corresponding to a λ of ~ 24 W/m·K. So, this thermal conductivity can be compared to the 3-layer FGM produced by SPS, which is found to be 44 W/m·K—calculated from the measured conductivities of individual layers (25W, 50W, 75W), see Section 3.4.3—. This incipient comparison suggests that the properties of FGM produced by SPS would be superior to that of VPS. However, a more comprehensive evaluation could not be conducted due to the lack of additional material property.

7.2 Evaluation of graded W-steel joints

3-layer FGM better than 2-layer FGM: The W-steel graded joints consisting of spark plasma sintered FGM did not perform well. As detailed in Section 4.1.3, in a 2.FG-SPS joint, the topmost FGM layer (50W) and W-tile form an excellent metallurgical bonding; even the W particles bond well with W-tile, as can be seen in Figures F.3 and F.4 in Appendix F. In comparison, the 3.FG-SPS joint does not form a suitable bonding between the topmost FGM layer (75W) and the W-tile. However, 3.FG-SPS joint performed better than the 2.FG-SPS joint, which suggests that the 3-layer FGM is better suited to reduce the overall stress.

Necessity for an auxiliary material to join FGM and W-tile: Although APS is not a viable option than VPS, it is still vital to discuss the specific V-3.FG-APS joint. This joint performed noticeably better than 3.FG-SPS joint, despite the worse mechanical, thermal and microstructural properties of the composites prepared by APS than the ones prepared by SPS. In addition to this, the V-3.FG-APS joint has a fundamental flaw, which should have led to a worse performance: a sharp peak in the CTE caused by the V-filler, as can be seen in Figure 7.1. The CTE does not change gradually, which is the basic idea of the FGM conceptual approach. Nevertheless, this joint showed performed relatively well because of the positive characteristics of V-filler, like good ductility and the ability to form a solid solution with W. So, it is essential to note that the lifetime of a joint does not primarily depend only on the gradual

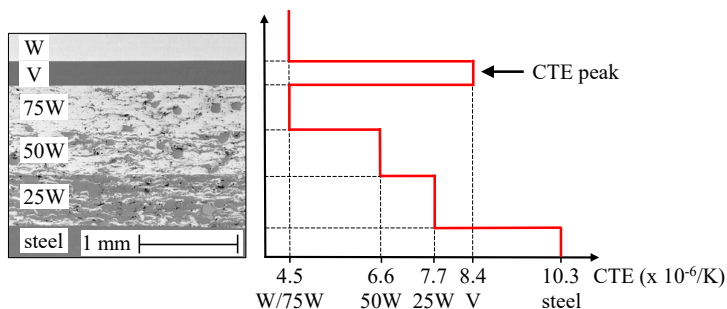


Figure 7.1 CTE distribution for a V-3.FG-APS joint

distribution of the CTE. In summary, the presence of such a ductile auxiliary material, creating good metallurgical bonding with W without forming any detrimental compound, is beneficial.

In the case of 3.FG-SPS joint, macroscopically, the fracture occurs at the W-FGM bond seam and microscopically near/around the bond seam; partially, the failure occurs due to the presence of IMC and partially due to the insufficient W-W bonding. This indicates that the primary stress is generated at the bond seam between W-tile and FGM. Not only in 3.FG-SPS, but also in 2.FG-APS, 2.FG-SPS, and V joints, the failure occurs at the bond seam between W-tile and FGM or V. Also, during the operation of the reactor, the temperature is the highest at the W-tile, and it gradually decreases towards the steel side to the coolant temperature (~300 °C). This means that the temperature at the topmost bond seam is the highest. The higher the temperature, the higher the thermal stress for a given CTE mismatch, so, thermal stresses are also highest at this topmost bond seam. These discussions show that an auxiliary material is required to join FGM and W-tile. This auxiliary material must have the following requirements: ductile, good metallurgical bonding with W, CTE between that of W and 75W, must not form any detrimental compound, and a relatively low melting point to initiate diffusion with W.

At this point, to eliminate any confusion, it is essential to note that an auxiliary material may only be required when using a W-tile as the armour material, as this creates a distinct interface between the W-tile and the underlying FGM. In contrast, when W, along with FGM, is sprayed directly onto the steel using VPS, there is no such discrete interface between the PS-W and the underlying FGM, resulting in a sort of continuous transition.; so such an auxiliary material may not be needed here.

Comparison with existing approaches for producing graded FW:

- Graded joint with sintered FGM (SPS approach): As mentioned above, there is a need for an auxiliary material to join the FGM and W-tile. Considering this, two manufacturing routes can be examined. In the first route, the W-tile, auxiliary material, FGM (in the form of powders) and steel disc can be co-sintered/joined together in the SPS equipment in one step. These produced discs (stack) can then be cut into appropriate geometries (for instance, 50 mm × 50 mm), and the bottom steel side can be joined with the predesigned steel panels, consisting of cooling channels, using HIP-DB. However, this concept may have one major drawback: limited size of the produced discs. The largest SPS equipment can produce Ø 200 mm discs (as mentioned in Section 7.1). However, as the size of the disc increases, the residual stresses at the interfaces also increase. In this thesis, Ø 20 mm disc was produced, and a 10-fold increase in the size would be challenging. This means the residual stresses may result in crack formation in W-tile. In the second route, instead of producing the complete stack with the W-tile, only the FGM and steel disc can be co-sintered in the SPS equipment. Then this stack can be cut into appropriate sizes, joined with W-tiles (with the help of auxiliary material) and predesigned steel panels (at the bottom) using HIP-DB in one step. Furthermore, instead of using the auxiliary material, one could use brazing elements to join the W-tile and FGM. Presently, a few brazing

elements exist to join W, for example, Ti-Fe-Sn, and further developments are ongoing [94]. In the author's opinion, this is the most feasible route if sintered FGM is to be considered for manufacturing full-scale graded FW panels.

- Vacuum plasma spraying of W along with FGM on steel (VPS approach): This is the most researched technique, as mentioned in Section 1.6.1. In the author's opinion, this is the most suitable and realistic approach to manufacture the full-scale graded FW panels: first, plasma spray FGM on the pre-designed steel panels consisting of cooling channels, and then continue to spray pure W on top of it. However, it has one minor technical challenge: relatively inferior properties of the PS-W armour compared to bulk-W. Only future studies will tell whether this is a significant issue or not. Also, to date, only a small-scale FW mock-up manufactured via this approach, featuring 0.2 mm thick PS-W and 1.2 mm thick FGM, has been tested under HHF loading. It survived 1000 cycles at 0.7 MW/m² load with the coolant flowing at 300 °C through steel [66]. However, according to the requirement, a 2 mm thick pure W armour is needed [10].

In both the above-evaluated approaches, the problem of IMC would still need to be addressed, which is discussed in the next section.

Long term effects of IMC on the lifetime of FW: In a future fusion reactor (like EU DEMO), it is expected that the cyclic heat load would be in the form of long plasma pulses with 2 hour duration, and the FW must withstand at least 5 full power years (fpy) [25]. This means the FW would be under heat load for nearly 43,800 hours (ignoring the interpulse duration). In this thesis, for the V-3.FG-APS joint, it is revealed that the failure of the 75W layer is not because of the generation of IMC but because of poor W-W intersplat bonding. For the 3.FG-SPS joint, one part of the reason for the early detachment of the W-tile is the IMC formed at the W-FGM bond seam. The HHF in this thesis is done considering a pulse ON time of 30 s and V-3.FG-APS joint survived approximately 1000 cycles; this equals 8.33 hours under the heat load, which is only 0.02 % of 43,800 hours. Therefore, without a long-term prolonged annealing test, it is beyond the scope of this thesis to state if the IMC is detrimental or not concretely. However, some general theoretical implications/presumptions can be made as follows:

- The IMC is formed not only at the W-steel boundaries but also along the steel grain boundaries.
- The generation of IMC would increase the brittleness of the FGM. It would result in the formation of pores due to the Kirkendall phenomenon and due to volume increase.
- The generation of IMC does not drastically decrease the thermal conductivity. So, the thermal performance of the graded FW would not necessarily degrade.
- It must be considered that the D-T fusion reaction releases neutrons, and materials are damaged due to this high neutron flux (neutron irradiation damage). Usually, the materials lose their ductility and make it brittle. However, the IMC is already brittle, so no speculations can be made.

7.3 Realization of an actual FW for future fusion reactor

Correlation of HHF testing and actual FW loading scenario: In this thesis, various small-scale joints were tested under HHF loading, starting from 1 MW/m^2 up to 4 MW/m^2 ; the joints were brazed on Cu-module (heat sink), and the coolant was flowing at $20 \text{ }^\circ\text{C}$. In comparison, in the actual FW of a future fusion reactor, the coolant will flow at approximately $300 \text{ }^\circ\text{C}$ through steel, not through Cu. Thus, a simple correlation is made on how the various joints would perform if considered as an actual FW in a fusion reactor. A rudimentary steady-state FE thermal simulation is performed using a commercial FE solver (ANSYS). Although the actual design of the FW of a future fusion reactor is not yet finalised, for the simulation, a similar FW geometry is adapted from literature [66], as shown in Figure 7.2. The idea is to compare the maximum surface temperature of the W-tile in this conceptual FW ($T_{\text{surf-FW}}$) and the surface temperature ($T_{\text{surf-HHF}}$) monitored during the HHF testing performed in Chapter 5 (see Figure 5.7 and Figure 5.8). The thermal conductivity required for the FE simulation for the W, V and Eurofer 97 is taken from the literature [16,21,95]. The thermal conductivity for the individual layers (APS layers) is taken from Section 3.4.3. As an example, the temperature distribution, considering an equivalent V-3.FG-APS joint, is shown in Figure 7.2. The obtained surface temperatures for various configurations and their equivalent temperatures obtained in HHF testing are provided in Table 7.2. The 2.FG-SPS, 3.FG-SPS, and V(0.3) joints are not considered here because of their poor performance in the HHF testing, and they failed much earlier than the Direct joint. The comparison in Table 7.2 is not meant to decide which joint configuration would survive in an actual FW loading scenario. In fact, an actual FW must withstand 5 fpy, meaning 21,900 cycles. Thus, this comparison is meant to provide a simple first-hand indication.

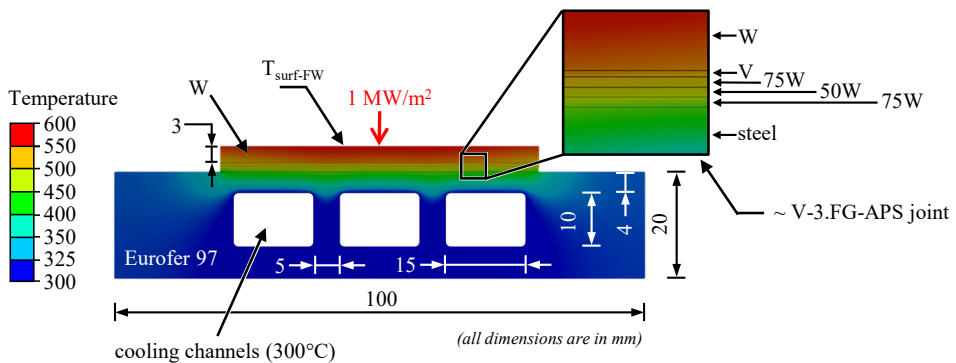


Figure 7.2 Geometry and temperature distribution of a conceptual FW panel considering a V-3.FG-APS joint with a 3 mm thick W-tile and coolant flowing at $300 \text{ }^\circ\text{C}$ through steel

As seen in Table 7.2, the temperature obtained for a conceptual FW is comparable to roughly 2 MW/m^2 loading during the HHF testing. The V-3.FG-APS joint would survive the first 200 cycles with the $T_{\text{surf-FW}}$ being $557 \text{ }^\circ\text{C}$. In the HHF testing, this joint start to degrade when the surface temperature of W reaches $770 \text{ }^\circ\text{C}$; hence, it is difficult to predict whether it will

show any degradation after 200 cycles. The Direct and the V(1.5) joints would also survive the first complete 200 cycles. In the HHF testing (see Figure 5.7 to 5.9), the heat flux was increased step-wise and not kept constant at 2 MW/m². The higher the heat flux, the higher the W-tile surface temperature and the higher the thermal stress. Thus, it is difficult to predict how many cycles these two joints would have survived in the actual fusion reactor, but in total, V(1.5) survived 600 cycles, and the direct joint survived 800 cycles for a varying heat load starting from 2 MW/m² (see Figure 5.9). Therefore, it can be said that both V(1.5) and the direct joint conceptual FW would survive a minimum of 600 and 800 cycles, respectively, in an actual fusion reactor. This means these two joint configurations could be important.

Table 7.2 Correlation of HHF testing (see Figure 5.7 to 5.9) and conceptual FW loaded with 1 MW/m², representing the maximum expected heat load scenario for a future fusion reactor ($T_{\text{surf-HHF}}$ is the average surface temperature of all samples in the HHF testing)

| FW concept | $T_{\text{surf-FW}}$ | $T_{\text{surf-HHF}}$ | Remarks* | Theoretical FW life |
|------------------|----------------------|------------------------------|---------------------|--|
| Direct joint | 465 °C | 430 °C @ 2 MW/m ² | survived 200 cycles | would assuredly survive the first 800 cycles, probably even more |
| V-3.FG-APS joint | 557 °C | 594 °C @ 2 MW/m ² | survived 200 cycles | would assuredly survive the first 600 cycles |
| V(1.5) joint | 507 °C | 477 °C @ 2 MW/m ² | survived 200 cycles | would assuredly survive the first 600 cycles, probably even more |

(*: corresponds to the results of the HHF testing in this thesis)

Solid interlayer (V or Ti) as a potential approach: This approach is not favoured in some studies because of the two presumed drawbacks (see Section 0). First, V produces brittle compound (V₂C and σ phase) at the steel side, and Ti produces brittle compound (FeTi, Fe₂Ti) at the steel side. These brittle compounds are presumed to be drawbacks, although they are not experimentally proven. Second, the HHF testing performed in this thesis (see Chapter 5) revealed that the failure occurs at the W-V bond seam and not at the V-steel bond seam, even though a brittle V₂C is present at the V-steel bond seam. This shows that the presumed drawback is false. In fact, using such interlayers is the most straightforward and simplistic method for joining dissimilar materials. Therefore, it is recommended to emphasise this approach more in future studies.

Is there really a problem with joining W and steel directly? Many studies have suggested the necessity of either a solid or a graded interlayer (FGM), assuming that the direct joining of W and steel, because of their different CTE, would result in early failure. However, to date, no experimental investigation has quantitatively evaluated the thermal fatigue life of a directly bonded joint. Therefore, the term "early failure" lacks quantitative significance. Based on this presumption, only three studies have been carried to date.

- Is PBHT an actual cause? In one of the studies, after the successful bonding of W and steel, of geometry \varnothing 18 mm, using diffusion bonding (DB) with the help of a uniaxial hot press, a PBHT was performed. After the PBHT, W and steel fell apart [28]. In another study, W and steel, of geometry 50 mm \times 50 mm, were joined successfully using DB with the help of HIP, and after this, PBHT was performed. Here they do not fall apart, but cracks were observed in W-tile [29]. The reason mentioned was the presence of thermal stress at the interface. In the third study, W and steel, of geometry 5 mm \times 10 mm, were joined using CA-DB. The PBHT was also performed, and the joint remained intact, but no further information was provided [30]. This raises the question that perhaps PBHT is why the W and steel cannot be successfully bonded. Therefore, in order to understand this anomaly, a directly bonded W and steel joint of size 16 mm \times 16 mm with 3 mm thick W-tile was manufactured using the same process (CA-DB), and then a PBHT was also performed; the joint was heated in a vacuum oven for 760 °C\90 min. After the PBHT, the W and steel tile did not debond. So, at this moment, it is difficult to state if the PBHT is the cause.
- Could the size of the W-tile have an influence? Another reason for this discrepancy might be W-tile size (bonding area). In the above-mentioned studies, the geometry of the W-tile was different. The thermal stresses are expected to be higher for larger sizes of the W-tile. Unfortunately, the available lab scale SPS equipment cannot produce larger joints, so this anomaly could not be examined. Although, one might argue that a 12 mm \times 12 mm tile size for the FW might be suitable as they performed well. However, the downside of this is the increase in the manufacturing effort. For instance, to cover a FW area of 1200 m², around 8.34 million W-tiles are required. If the geometry is increased to 35 mm \times 35 mm, one requires significantly fewer (0.98 million) tiles.

The above discussion was put in this thesis to emphasise that, in the future, equal importance should be given to first fully understand the discrepancies related to the direct joining of W and steel before proceeding to develop complex FGM.

7.4 Closure

As a closing remark, all the suitable approaches are evaluated as provided in Table 7.3. The numbering scale mentioned, for instance, "complexity" on a scale of 1 to 5, is meant to provide an informal qualitative comparison.

Table 7.3 Closing remark considering all available existing approaches

| Aspect | SPS approach | VPS approach | Solid interlayer | Direct joint |
|--------------------------------|--|--|--|--|
| Problems to tackle | <ul style="list-style-type: none"> - Development of filler material to join W and FGM - Improvement of W-W particle bonding - Long term effect of IMC | <ul style="list-style-type: none"> - Characterization of individual layers and PS-W - Is PS-W suitable armour? - Long term effect of IMC - Investigation of W-W intersplat bonding even in VPS process | <ul style="list-style-type: none"> - More emphasis and experiments - Additional HHF testing | <ul style="list-style-type: none"> - Long term effect of IMC at W-steel bond seam - More emphasis and experiments - Manufacturing larger scale joints - Additional HHF testing |
| Neutron irradiation | <ul style="list-style-type: none"> - Behaviour of IMC & FGM | <ul style="list-style-type: none"> - Behaviour of PS-W, IMC & FGM | <ul style="list-style-type: none"> - Behavior of solid interlayers (V/Ti) and other brittle compounds like V₂C, FeTi, Fe₂Ti and other phases | <ul style="list-style-type: none"> - Behaviour of IMC present at the W-steel bond seam |
| Reactor relevant HHF loading | <ul style="list-style-type: none"> - Poor performance | <ul style="list-style-type: none"> - 1000 cycles at 0.7 MW/m² [66] - Further development is required to survive 1 MW/m² | <ul style="list-style-type: none"> - 600 cycles at 1 MW/m² (based on the results of V(1.5) joint in this thesis) | <ul style="list-style-type: none"> - 800 cycles at 1 MW/m² (based on the results of Direct joint in this thesis) |
| Industry readiness (scale 1-5) | <p style="text-align: center;">(0)</p> <ul style="list-style-type: none"> - Still in the preliminary stage of proof of concept - Need a lot of development | <p style="text-align: center;">(4)</p> <ul style="list-style-type: none"> - Recently a medium size mockup has been manufactured with the help of an industrial partner | <p style="text-align: center;">(2)</p> <ul style="list-style-type: none"> - HIP-DB is industrially well-known process, once the proof of concept is proved - Industrial production is possible | <p style="text-align: center;">(2)</p> <ul style="list-style-type: none"> - HIP-DB is industrially well-known process, once the proof of concept is proved - Industrial production is possible |
| Complexity (scale 1-5) | (4) | (3) | (2) | (1) |

The author would like to present the closing remark with the following thought-provoking questions, which would help set up future goals:

Considering the graded joining concepts—whether it is SPS or VPS approach—: is it practical/sensible to put much effort into developing these concepts and simultaneously solve numerous challenges to achieve a slightly better lifetime, even though, as per the current requirement, the FW must only be able to withstand a maximum heat loading of just 1 MW/m²?

Shouldn't the aim be to develop a joining concept for the FW using the simplest and mature technology that can be qualified successfully in the near future, keeping in mind the fact that a fusion power plant is still a “nuclear installation” and needs nuclear licensing/qualification, which is a time-consuming task?

Considering the joining concept featuring a solid interlayer: ITER's FW panels would soon be in the industrial series production stage, where the beryllium tiles would diffusion bonded to CuCrZr using HIP. So, shouldn't it be more feasible/practical to follow the same technology to bond W to steel with V or Ti layer using HIP?

8 Summary and outlook

8.1 Summary

This thesis aimed to investigate joining technologies for manufacturing graded joints for the first wall (FW) of a future fusion reactor. At first, the individual layers (W/steel-composites) of the FGM were investigated using three manufacturing processes: electro-discharge sintering (EDS), spark plasma sintering (SPS), and modified atmospheric plasma spraying (APS). Composites of three concentrations of W were considered: 25, 50, and 75 vol% W. Next, the produced optimized composites were characterized for their microstructural, mechanical and thermophysical properties. Subsequently, the graded joints featuring 2-layer and 3-layer FGM were manufactured. Finally, the joints were then benchmarked by HHF testing and compared with a directly bonded W-steel reference joint.

A thorough analysis of the produced individual composites results in the following conclusions:

- EDS is not a suitable process due to its inability to produce a 75W composite, as well as its inability to produce a homogenous composite.
- APS is also not a suitable process, as the produced composites have poor properties: low thermal conductivity ($\sim 20 \text{ W/m}\cdot\text{K}$), low elastic modulus (150–250 GPa), brittle nature, and low relative density ($\sim 85 \%$). Their properties are even worse than that of pure steel.
- SPS is the most suitable process to produce these composites, as the produced composites have relatively superior properties than APS: high thermal conductivity (30–90 $\text{W/m}\cdot\text{K}$), appropriate ductile behaviour, and high relative density (96–100 %).

Highlight from the production of graded W-steel joints are:

- Manufactured graded joints featured a 2-layer FGM (25W, 50W) and a 3-layer FGM (25W, 50W, 75W).
- The joint featuring plasma sprayed FGM was manufactured using a thin V-filler to bond the topmost layer of the 3-layer FGM and W.
- Apart from the graded joints, joints featuring a solid V interlayer of two thicknesses were also manufactured.
- It was shown that it is possible to join W and steel directly, which was presumed to be complicated/impractical in several studies.

Through the benchmarking by HHF testing, the following inferences were made:

- It was observed that the most important feature that influences the lifetime of the joint is the bonding between the W and the topmost FGM layer. The properties of the FGM—more precisely, the mechanical and thermophysical properties of the individual layers of the FGM—have no significant influence on the lifetime of the FW. Despite the inferior properties of the plasma sprayed FGM compared to the sintered FGM, the joint featuring plasma sprayed FGM performed much better in the HHF test. It is because the plasma sprayed FGM was bonded to W with the help of a ductile V-filler. The comprehensive post mortem analysis also revealed that the failure occurred at the bond seam between the FGM and W, indicating that the thermal stresses are predominant at this bond seam. This is also in accordance with the FE numerical simulation by Heuer et al. [44] that the dominant stresses perpendicular to the bond seam are present at the corners of the joint at the W-FGM interface. Thus, the critical element in successfully realising a graded joint requires a ductile filler or brazing material to bond the 75W and W.
- It was observed that none of the FGM variants improved the lifetime of the joint.
- It was observed that a 3-layer FGM performs better than a 2-layer FGM.
- A direct joint and a joint featuring a V interlayer performed relatively better. The results show that these two approaches should be considered before developing the graded joint.

8.2 Outlook

The future work should tackle the following challenges in the given order of priority:

- HHF testing of directly bonded W and steel medium-scale mockup
Manufacturing a medium-scale mockup with W-tiles bonded directly to a steel structure (heat sink)—of geometry 100 mm × 150 mm—with cooling channels inside the steel. Two industrial scale SPS setups readily available at FZJ can be used: Dr. Fritsch DSP 515 or FCT Systeme H-HP D25. The joining can be performed using the parameters optimized in this thesis, followed by PBHT. W tiles' geometrical size influence on thermal stress should also be studied. For this, W-tiles of different sizes can be joined, for example, 12 mm × 12 mm, 16 mm × 16 mm, and 36 mm × 36 mm.
- HHF testing of medium-scale mockup featuring either V or Ti interlayer
Similar to a directly bonded mockup, a medium-scale mockup featuring either V or Ti interlayer of suitable thickness should be investigated.
- Development of a brazing technology for bonding sintered 75W and W-tile
Brazing is also a promising technology that could be explored soon. Here, the priority should be to develop a technology towards joining the sintered 75W layer and the W-tile to prove the viability of the graded joint featuring sintered FGM.

- Tensile properties of sintered composites

As of now, the FE numerical simulations supporting the concept of FGM interlayer have modelled the yield stress of the composites assuming a simple linear interpolation based formula (Equation (3.4)) [44,45,75]. This linear interpolation overestimates the yield stress of the composites. As already mentioned by Heuer [11], this underestimates the actual stresses inside the FGM. This thesis also proved this. Therefore, in the future, the properties must be determined through proper experimental tests to model the FGM carefully. In the scope of this thesis, a miniature-scale high-temperature tensile testing was planned but not completed. Thus, future work should focus on performing these tensile tests to investigate the composites' tensile behaviour.

- Coarser W powder instead of finer W powder for the 50W composition

Future work on the 50W sintered composite could consider using coarser W powder of PSF 30–60 μm , instead of the finer W powder (10–30 μm) used in this thesis. This may result in improved toughness and possibly higher yield strength of the 50W composite, as it would have relatively 25 times fewer W particles—fewer W particles leads to fewer W-W interfaces—.

- Pure Fe instead of reduced activation ferritic/martensitic steel (Eurofer 97) in FGM

The steel adjacent to the W-particles in the sintered FGM was observed to transform into ferrite. After the heat treatment, majority of steel exhibited a ferrite structure; furthermore, during the operation of the reactor, the entirety of steel inside the FGM would eventually become ferrite, as the W would diffuse into steel. So, using martensitic steel, like Eurofer 97, as a starting powder to make the FGM is unnecessary. Thus, instead, a simple W/Fe FGM system could be considered. Pure Fe is a better choice compared to steel due to its several advantages: higher thermal conductivity (80 W/m·K), better ductility, suitable ductility even after neutron irradiation, commercial availability, and more straightforward scientific understanding of the composite as it contains only two elements (Fe, W).

9 References

- [1] EUROfusion, European research roadmap to the realisation of fusion energy, Garching / Munich, Germany, 2018.
- [2] Ember, Global electricity review 2022, London, 2022.
- [3] R. Pravalie, G. Bandoc, Nuclear energy: Between global electricity demand, worldwide decarbonisation imperativeness, and planetary environmental implications, *J. Environ. Manage.* 209 (2018) 81–92. <https://doi.org/10.1016/j.jenvman.2017.12.043>.
- [4] C.M. Braams, P.E. Stott, Nuclear fusion: Half a century of magnetic confinement fusion research, Institute of Physics Publishing, Bristol, 2002.
- [5] S. Li, H. Jiang, Z. Ren, C. Xu, Optimal Tracking for a Divergent-Type Parabolic PDE System in Current Profile Control, *Abstract and Applied Analysis* 2014 (2014) 1–8. <https://doi.org/10.1155/2014/940965>.
- [6] P. Magaud, G. Marbach, I. Cook, Nuclear Fusion Reactors, in: C.J. Cleveland, R.U. Ayres (Eds.), *Encyclopedia of energy*, Elsevier Academic Press, Amsterdam, Boston, 2004, pp. 365–381.
- [7] S. Heuer, J.W. Coenen, G. Pintsuk, J. Matejcek, M. Vilemova, C. Linsmeier, Overview of challenges and developments in joining tungsten and steel for future fusion reactors, *Physica Scripta T171* (2020) 14028. <https://doi.org/10.1088/1402-4896/ab47a4>.
- [8] G. Federici, L.V. Boccaccini, F. Cismondi, M. Gasparotto, Y. Poitevin, I. Ricipito, An overview of the EU breeding blanket design strategy as an integral part of the DEMO design effort, *Fusion Eng. Des.* 141 (2019) 30–42. <https://doi.org/10.1016/j.fusengdes.2019.01.141>.
- [9] F. Maviglia, C. Bachmann, G. Federici, T. Franke, M. Siccino, R. Albanese, R. Ambrosino, W. Arter, R. Bonifetto, G. Calabrò, R. de Luca, L.E. Di Grazia, E. Fable, P. Fanelli, A. Fanni, M. Firdaouss, J. Gerardin, R. Lombroni, M. Mattei, M. Moscheni, W. Morris, G. Pautasso, S. Pestchanyi, G. Ramogida, M.L. Richiusa, G. Sias, F. Subba, F. Villone, J.-H. You, Z. Vizvary, Integrated design strategy for EU-DEMO first wall protection from plasma transients *Fusion Engineering and Design* 177 (2022) 113067, *Fusion Eng. Des.* 178 (2022) 113125. <https://doi.org/10.1016/j.fusengdes.2022.113125>.
- [10] T.R. Barrett, G. Ellwood, G. Pérez, M. Kovari, M. Fursdon, F. Domp tail, S. Kirk, S.C. McIntosh, S. Roberts, S. Zheng, L.V. Boccaccini, J.-H. You, C. Bachmann, J. Reiser, M. Rieth, E. Visca, G. Mazzone, F. Arbeiter, P.K. Domalapally, Progress in the engineering design and assessment of the European DEMO first wall and divertor plasma facing components, *Fusion Eng. Des.* 109-111 (2016) 917–924. <https://doi.org/10.1016/j.fusengdes.2016.01.052>.

- [11] S. Heuer, Charakterisierung gradiert Eisen/Wolfram-Schichten für die erste Wand von Fusionsreaktoren. PhD dissertation, Bochum, Germany, 2017.
- [12] H. Tanigawa, K. Shiba, A. Möslang, R.E. Stoller, R. Lindau, M.A. Sokolov, G.R. Odette, R.J. Kurtz, S. Jitsukawa, Status and key issues of reduced activation ferritic/martensitic steels as the structural material for a DEMO blanket, *J. Nucl. Mater.* 417 (2011) 9–15. <https://doi.org/10.1016/j.jnucmat.2011.05.023>.
- [13] E. Lassner, W.-D. Schubert, Tungsten: Properties, chemistry, technology of the elements, alloys and chemical compounds, Kluwer Academic, New York, London, 1999.
- [14] Plansee AG, Austria, Tungsten: Material properties and applications. <https://www.plansee.com/>.
- [15] M. Wirtz, J.W. Coenen, T. Lownhoff, G. Pintsuk, B. Unterberg, Interaction of heat loads and seeding impurities with tungsten using different experimental methods, in: 32nd Symposium on Fusion Technology, Dubrovnik, Croatia, 2022.
- [16] ITER, Materials Properties Handbook (MPH): ITER Doc. G74 MA 16 04-05-07 R0.1., 2017.
- [17] M. Kaufmann, R. Neu, Tungsten as first wall material in fusion devices, *Fusion Eng. Des.* 82 (2007) 521–527. <https://doi.org/10.1016/j.fusengdes.2007.03.045>.
- [18] N.D. Bega, A.V. Babak, E.I. Uskov, Recrystallization and embrittlement of sintered tungsten, *Soviet Powder Metallurgy and Metal Ceramics* 21 (1982) 408–411. <https://doi.org/10.1007/BF00802116>.
- [19] R.L. Klueh, D.R. Harries, High-chromium ferritic and martensitic steels for nuclear applications, ASTM International; ASTM, 100 Barr Harbor Drive, PO Box C700, West Conshohocken, PA 19428-2959, 2001.
- [20] M. Rieth, M. Schirra, A. Falkenstein, P. Graf, S. Heger, H. Kempe, R. Lindau, H. Zimmermann, EUROFER 97: Tensile, charpy, creep and structural tests. Wissenschaftliche Berichte, FZKA-6911, Karlsruhe Institut für Technologie, Karlsruhe, 2003.
- [21] EUROfusion, DEMO Material Property Handbook (MPH): EUROFER 97.
- [22] K.D. Zilnyk, V.B. Oliveira, H.R.Z. Sandim, A. Möslang, D. Raabe, Martensitic transformation in Eurofer-97 and ODS-Eurofer steels: A comparative study, *J. Nucl. Mater.* 462 (2015) 360–367. <https://doi.org/10.1016/j.jnucmat.2014.12.112>.
- [23] T. Weber, Entwicklung und Optimierung von gradierten Wolfram/EUROFER97-Verbindungen für Divertorkomponenten. PhD dissertation, KIT Scientific Publishing, Karlsruhe, Germany, 2013.
- [24] A. Bhattacharya, X. Chen, K.D. Linton, Y. Yamamoto, M.A. Sokolov, L.N. Clowers, Y. Katoh, Mechanical properties and microstructure characterization of unirradiated Eurofer-97 steel variants for the EUROfusion project, 2018.
- [25] K. Hesch, L.V. Boccaccini, R. Stieglitz, Blankets – key element of a fusion reactor – functions, design and present state of development, *Kerntechnik* 83 (2018) 241–250. <https://doi.org/10.3139/124.110923>.

- [26] O.K. von Goldbeck, Fe—W Iron—Tungsten, in: O.K. von Goldbeck (Ed.), *Iron-Binary Phase Diagrams*, Springer, Berlin, Heidelberg, 1982, pp. 164–167.
- [27] A. Antoni-Zdziobek, T. Commeau, J.M. Joubert, Partial Redetermination of the Fe-W Phase Diagram, *MTA* 44 (2013) 2996–3003. <https://doi.org/10.1007/s11661-013-1658-2>.
- [28] W.W. Basuki, J. Aktaa, Investigation on the diffusion bonding of tungsten and EUROFER97, *J. Nucl. Mater.* 417 (2011) 524–527. <https://doi.org/10.1016/j.jnucmat.2010.12.121>.
- [29] Y.-I. Jung, J.-Y. Park, B.-K. Choi, D.-W. Lee, S. Cho, Fabrication of W/FMS joint mock-ups using a hot isostatic pressing, *Fusion Eng. Des.* 89 (2014) 1029–1032. <https://doi.org/10.1016/j.fusengdes.2014.02.063>.
- [30] T. Hirose, K. Shiba, M. Ando, M. Enoda, M. Akiba, Joining technologies of reduced activation ferritic/martensitic steel for blanket fabrication, *Fusion Eng. Des.* 81 (2006) 645–651. <https://doi.org/10.1016/j.fusengdes.2005.07.015>.
- [31] D. Mori, R. Kasada, S. Konishi, Y. Morizono, K. Hokamoto, Underwater explosive welding of tungsten to reduced-activation ferritic steel F82H, *Fusion Eng. Des.* 89 (2014) 1086–1090. <https://doi.org/10.1016/j.fusengdes.2013.12.038>.
- [32] S. Noh, R. Kasada, N. Oono, T. Nagasaka, A. Kimura, Joining of ODS steels and tungsten for fusion applications, *MSF* 654-656 (2010) 2891–2894. <https://doi.org/10.4028/www.scientific.net/MSF.654-656.2891>.
- [33] Y.I. Jung, H.-G. Kim, D.W. Lee, Y.-S. Lim, B.K. Choi, HIP Joining of tungsten armor to ferritic-martensitic steel with a zirconium interlayer, *Fusion Science and Technology* (2017) 1–7. <https://doi.org/10.1080/15361055.2017.1330610>.
- [34] Y.S. Touloukian, R.K. Kirby, R.E. Taylor, P.D. Desai, *Thermophysical properties of matter - the TPRC data series: Volume 12. Thermal expansion-metallic elements and alloys*, Springer US, Boston, MA, 1975.
- [35] W.W. Basuki, J. Aktaa, Diffusion bonding between W and EUROFER97 using V interlayer, *J. Nucl. Mater.* 429 (2012) 335–340. <https://doi.org/10.1016/j.jnucmat.2012.05.049>.
- [36] W.W. Basuki, J. Aktaa, Process optimization for diffusion bonding of tungsten with EUROFER97 using a vanadium interlayer, *J. Nucl. Mater.* 459 (2015) 217–224. <https://doi.org/10.1016/j.jnucmat.2015.01.033>.
- [37] W.W. Basuki, R. Dahm, J. Aktaa, Thermomechanical analysis of diffusion-bonded tungsten/EUROFER97 with a vanadium interlayer, *J. Nucl. Mater.* 455 (2014) 635–639. <https://doi.org/10.1016/j.jnucmat.2014.09.007>.
- [38] Z. Zhong, T. Hinoki, A. Kohyama, Diffusion bonding of tungsten to reduced activation ferritic/martensitic steel F82H using a titanium interlayer, in: T. Yao (Ed.), *Zero-carbon energy Kyoto 2009: Proceedings of the first International Symposium of Global COE Program "Energy Science in the Age of Global Warming--Toward CO₂ s Zero-Emission Energy System"*, Springer, Tokyo, New York, 2010, pp. 266–273.

- [39] J. Wang, W. Wang, Z. Sun, X. Wang, R. Wei, C. Xie, Q. Li, G. Luo, Microstructure and mechanical analysis of W/P91 steel HIP-joint with Ti interlayer, *Fusion Eng. Des.* 112 (2016) 67–73. <https://doi.org/10.1016/j.fusengdes.2016.07.012>.
- [40] Y.I. Jung, J.Y. Park, B.K. Choi, D.W. Lee, S. Cho, Interfacial microstructures of HIP joined W and ferritic–martensitic steel with Ti interlayers, *Fusion Eng. Des.* 88 (2013) 2457–2460. <https://doi.org/10.1016/j.fusengdes.2013.02.049>.
- [41] J. Wang, W. Wang, R. Wei, X. Wang, Z. Sun, C. Xie, Q. Li, G. Luo, Effect of Ti interlayer on the bonding quality of W and steel HIP joint, *J. Nucl. Mater.* 485 (2017) 8–14. <https://doi.org/10.1016/j.jnucmat.2016.12.024>.
- [42] W. Kong, X. Li, B. Chen, C. Wang, H. Chu, Y. Chen, P. Hua, W. Zhou, Microstructure and mechanical properties of diffusion bonded W/MA956 steel joints with a titanium interlayer by SPS, *J. Adhes. Sci. Technol.* 33 (2019) 1847–1857. <https://doi.org/10.1080/01694243.2019.1615723>.
- [43] H. Chen, L. Luo, G. Luo, Y. Wu, X. Zan, J. Zhang, X. Zhu, Investigation on W/Fe diffusion bonding using Ti foil and Ti powder interlayer by SPS, *J. Nucl. Mater.* 467 (2015) 566–571. <https://doi.org/10.1016/j.jnucmat.2015.10.045>.
- [44] S. Heuer, T. Weber, G. Pintsuk, J.W. Coenen, J. Matejcek, C. Linsmeier, Aiming at understanding thermo-mechanical loads in the first wall of DEMO: Stress-strain evolution in a Eurofer-tungsten test component featuring a functionally graded interlayer, *Fusion Eng. Des.* 135 (2018) 141–153. <https://doi.org/10.1016/j.fusengdes.2018.07.011>.
- [45] T. Weber, J. Aktaa, Numerical assessment of functionally graded tungsten/steel joints for divertor applications, *Fusion Eng. Des.* 86 (2011) 220–226. <https://doi.org/10.1016/j.fusengdes.2010.12.084>.
- [46] J. Matejcek, H. Boldyryeva, Processing and temperature-dependent properties of plasma-sprayed tungsten–stainless steel composites, *Phys. Scr.* T138 (2009) 14041. <https://doi.org/10.1088/0031-8949/2009/T138/014041>.
- [47] D. Qu, Development of functionally graded tungsten/EUROFER coating systems. PhD dissertation, Karlsruhe, Karlsruhe, Germany, 2016.
- [48] H. Greuner, H.H. Bolt, B. Böswirth, S. Lindig, W. Kühnlein, T. Huber, K. Sato, S. Suzuki, Vacuum plasma-sprayed tungsten on EUROFER and 316L: Results of characterisation and thermal loading tests, *Fusion Eng. Des.* 75-79 (2005) 333–338. <https://doi.org/10.1016/j.fusengdes.2005.06.240>.
- [49] J. Matejcek, T. Kavka, R. Musalek, P. Ctibor, J. Medricky, M. Vilemova, B. Nevrla, S. Degot, A. Denoirjean, Tungsten-steel composites and FGMs prepared by argon-shrouded plasma spraying, *Surf. Coating Tech.* 406 (2021) 126746. <https://doi.org/10.1016/j.surfcoat.2020.126746>.
- [50] S. Heuer, J. Matejcek, M. Vilemova, M. Koller, K. Illkova, J. Veverka, T. Weber, G. Pintsuk, J.W. Coenen, C. Linsmeier, Atmospheric plasma spraying of functionally graded steel/tungsten layers for the first wall of future fusion reactors, *Surf. Coating Tech.* 366 (2019) 170–178. <https://doi.org/10.1016/j.surfcoat.2019.03.017>.

- [51] T.J. Gareth, Advanced materials for plasma facing components in fusion devices. PhD dissertation, Oxford, United Kingdom, 2009.
- [52] T. Nagasaka, R. Kasada, A. Kimura, Y. Ueda, T. Muroga, Thermophysical properties and microstructure of plasma-sprayed tungsten coating on low activation materials, *Fusion Science and Technology* 56 (2009) 1053–1057. <https://doi.org/10.13182/FST56-1053>.
- [53] Y. Yahiro, M. Mitsuhashi, K. Tokunaga, N. Yoshida, T. Hirai, K. Ezato, S. Suzuki, M. Akiba, H. Nakashima, Characterization of thick plasma spray tungsten coating on ferritic/martensitic steel F82H for high heat flux armor, *J. Nucl. Mater.* 386-388 (2009) 784–788. <https://doi.org/10.1016/j.jnucmat.2008.12.219>.
- [54] T. Tokunaga, H. Watanabe, N. Yoshida, T. Nagasaka, R. Kasada, Y.-J. Lee, A. Kimura, M. Tokitani, M. Mitsuhashi, T. Hinoki, H. Nakashima, S. Masuzaki, T. Takabatake, N. Kuroki, K. Ezato, S. Suzuki, M. Akiba, Development of high-grade VPS-tungsten coatings on F82H reduced activation steel, *J. Nucl. Mater.* 442 (2013) S287-S291. <https://doi.org/10.1016/j.jnucmat.2012.11.004>.
- [55] K. Tokunaga, T. Hotta, K. Araki, A. Kurumada, M. Tokitani, S. Masuzaki, K. Ezato, S. Suzuki, M. Enoda, M. Akiba, M. Hasegawa, K. Nakamura, Heat loading behavior and thermomechanical analyses on plasma spray tungsten coated reduced-activation ferritic/martensitic steel, *Fusion Eng. Des.* 136 (2018) 1624–1628. <https://doi.org/10.1016/j.fusengdes.2018.05.073>.
- [56] K. Tokunaga, T. Hotta, K. Araki, Y. Miyamoto, T. Fujiwara, M. Hasegawa, K. Nakamura, K. Ezato, S. Suzuki, M. Enoda, M. Akiba, T. Nagasaka, R. Kasada, A. Kimura, High heat loading properties of vacuum plasma spray tungsten coatings on reduced activation ferritic/martensitic steel, *J. Nucl. Mater.* 438 (2013) S905-S908. <https://doi.org/10.1016/j.jnucmat.2013.01.196>.
- [57] T. Emmerich, D. Qu, B.-E. Ghidersa, M. Lux, J. Rey, R. Vaßen, J. Aktaa, Development progress of coating first wall components with functionally graded W/EUROFER layers on laboratory scale, *Nucl. Fusion* 60 (2020) 126004. <https://doi.org/10.1088/1741-4326/aba336>.
- [58] T. Emmerich, R. Vaßen, J. Aktaa, Thermal fatigue behavior of functionally graded W/EUROFER-layer systems using a new test apparatus, *Fusion Eng. Des.* 154 (2020) 111550. <https://doi.org/10.1016/j.fusengdes.2020.111550>.
- [59] T. Grammes, T. Emmerich, J. Aktaa, W/EUROFER functionally graded coatings for plasma facing components: technology transfer to industry and upscaling, *Fusion Eng. Des.* 173 (2021) 112940. <https://doi.org/10.1016/j.fusengdes.2021.112940>.
- [60] T. Weber, M. Stüber, S. Ulrich, R. Vaßen, W.W. Basuki, J. Lohmiller, W. Sittel, J. Aktaa, Functionally graded vacuum plasma sprayed and magnetron sputtered tungsten/EUROFER97 interlayers for joints in helium-cooled divertor components, *J. Nucl. Mater.* 436 (2013) 29–39. <https://doi.org/10.1016/j.jnucmat.2013.01.286>.

- [61] J. Matejcek, M. Vilemova, D. Moskal, R. Musalek, J. Krofta, M. Janata, Z. Kutilek, J. Klecka, S. Heuer, J. Martan, E. Nardozza, S. Houdkova, D. Dorow-Gerspach, The role of laser texturing in improving the adhesion of plasma sprayed tungsten coatings, *J. Therm. Spray Technol.* 28 (2019) 1346–1362. <https://doi.org/10.1007/s11666-019-00924-7>.
- [62] C. Tan, G. Wang, L. Ji, Y. Tong, X.-M. Duan, Investigation on 316L/W functionally graded materials fabricated by mechanical alloying and spark plasma sintering, *J. Nucl. Mater.* 469 (2016) 32–38. <https://doi.org/10.1016/j.jnucmat.2015.11.024>.
- [63] M. Koller, A. Kruisova, R. Musalek, J. Matejcek, H. Seiner, M. Landa, On the relation between microstructure and elastic constants of tungsten/steel composites fabricated by spark plasma sintering, *Fusion Eng. Des.* 133 (2018) 51–58. <https://doi.org/10.1016/j.fusengdes.2018.05.056>.
- [64] S. Heuer, T. Lienig, A. Mohr, T. Weber, G. Pintsuk, J.W. Coenen, F. Gormann, W. Theisen, C. Linsmeier, Ultra-fast sintered functionally graded Fe/W composites for the first wall of future fusion reactors, *Compos. B. Eng.* 164 (2019) 205–214. <https://doi.org/10.1016/j.compositesb.2018.11.078>.
- [65] O.K. von Goldbeck (Ed.), *Iron-Binary Phase Diagrams*, Springer, Berlin, Heidelberg, 1982.
- [66] B.-E. Ghidersa, A. Abou Sena, M. Rieth, T. Emmerich, M. Lux, J. Aktaa, Experimental investigation of EU-DEMO breeding blanket first wall mock-ups in support of the manufacturing and material development programmes, *Energies* 14 (2021) 7580. <https://doi.org/10.3390/en14227580>.
- [67] S.-K. Kim, C.W. Shin, D.J. Kim, S.D. Park, H.G. Jin, E.H. Lee, J.-S. Yoon, D.W. Lee, Bonding techniques and performance qualification of plasma facing components for Korean fusion research, *Fusion Eng. Des.* 136 (2018) 1510–1513. <https://doi.org/10.1016/j.fusengdes.2018.05.044>.
- [68] Institute of Plasma Physics and ProjectSoft HK, Hybrid water-stabilized plasma torch WSP®-H 500. <https://www.wsp-h.com/>.
- [69] J. Matejcek, M. Vilemova, B. Nevrla, L. Kocmanova, J. Veverka, M. Halasova, H. Hadraba, The influence of substrate temperature and spraying distance on the properties of plasma sprayed tungsten and steel coatings deposited in a shrouding chamber, *Surf. Coating Tech.* 318 (2017) 217–223. <https://doi.org/10.1016/j.surfcoat.2016.10.055>.
- [70] J. Matejcek, B. Nevrla, M. Vilemova, H. Boldyryeva, Overview of processing technologies for tungsten-steel composites and FGMs for fusion applications, *Nukleonika* 60 (2015) 267–273. <https://doi.org/10.1515/nuka-2015-0049>.
- [71] P. Schütte, *Aufbau einer Kurzzeitsinteranlage zur Herstellung verschleißbeständiger Verbundwerkstoffe*. PhD dissertation, Bochum, Germany, 2013.
- [72] L. Leich, A. Röttger, R. Kuchenbecker, W. Theisen, Electro-discharge sintering of nanocrystalline NdFeB magnets: process parameters, microstructure, and the resulting magnetic properties, *J Mater Sci: Mater Electron* 31 (2020) 20431–20443. <https://doi.org/10.1007/s10854-020-04562-6>.

- [73] N. Kwak, G. Min, Y. Oh, D.-W. Suh, H.C. Kim, S. Kang, H.N. Han, Tantalum and molybdenum barriers to prevent carbon diffusion in spark plasma sintered tungsten, *Scr. Mater.* 196 (2021) 113759. <https://doi.org/10.1016/j.scriptamat.2021.113759>.
- [74] C. Yin, D. Terentyev, T. Pardoen, R. Petrov, Z. Tong, Ductile to brittle transition in ITER specification tungsten assessed by combined fracture toughness and bending tests analysis, *Mater. Sci. Eng. A* 750 (2019) 20–30. <https://doi.org/10.1016/j.msea.2019.02.028>.
- [75] D. Qu, W.W. Basuki, J. Aktaa, Numerical assessment of functionally graded tungsten/EUROFER coating system for first wall applications, *Fusion Eng. Des.* 98-99 (2015) 1389–1393. <https://doi.org/10.1016/j.fusengdes.2015.06.120>.
- [76] K. Volenik, F. Hanousek, P.J. Chraska, J. Ilavsky, K. Neufuss, In-flight oxidation of high-alloy steels during plasma spraying, *Mater. Sci. Eng. A* 272 (1999) 199–206. [https://doi.org/10.1016/S0921-5093\(99\)00478-5](https://doi.org/10.1016/S0921-5093(99)00478-5).
- [77] C. Tan, S. Wang, Y. Chen, G. Wang, L. Ji, Y. Tong, X.-M. Duan, Microstructure and wear properties of spark plasma sintered 316L-30W composites, *Materials Science and Technology* 34 (2018) 513–518. <https://doi.org/10.1080/02670836.2017.1374523>.
- [78] P. Gustafson, An experimental study and a thermodynamic evaluation of the Cr-Fe-W system, *MTA* 19 (1988) 2531–2546. <https://doi.org/10.1007/BF02645481>.
- [79] R. Lindau, M. Schirra, First results on the characterisation of the reduced-activation-ferritic-martensitic steel EUROFER, *Fusion Eng. Des.* 58-59 (2001) 781–785. [https://doi.org/10.1016/S0920-3796\(01\)00562-2](https://doi.org/10.1016/S0920-3796(01)00562-2).
- [80] R.G. Leisure, F.A. Willis, Resonant ultrasound spectroscopy, *J. Phys.: Condens. Matter* 9 (1997) 6001–6029. <https://doi.org/10.1088/0953-8984/9/28/002>.
- [81] ASTM Standard D30, D30 Committee, Standard test method for flexural properties of polymer matrix composite materials: Designation: D7264/D7264M-07, ASTM International, West Conshohocken, PA.
- [82] S. Timoshenko, *Strength of materials: Part 1 Elementary theory and problems*, thirdrd edition. reprint twentieth0second, CBS Publishers, New Delhi, 2002.
- [83] J. Matejicek, B. Kolman, J. Dubsy, K. Neufuss, N. Hopkins, J. Zwick, Alternative methods for determination of composition and porosity in abradable materials, *Materials Characterization* 57 (2006) 17–29. <https://doi.org/10.1016/j.matchar.2005.12.004>.
- [84] S. Elomari, M.D. Skibo, A. Sundarajan, H. Richards, Thermal expansion behavior of particulate metal-matrix composites, *Composites Science and Technology* 58 (1998) 369–376. [https://doi.org/10.1016/S0266-3538\(97\)00124-3](https://doi.org/10.1016/S0266-3538(97)00124-3).
- [85] A.A.F. Tavassoli, A. Alamo, L. Bedel, L. Forest, J.M. Gentzittel, J.W. Rensman, E. Diegele, R. Lindau, M. Schirra, R. Schmitt, H.C. Schneider, C.G. Petersen, A.M. Lancha, P. Fernandez, G. Filacchioni, M.F. Maday, K. Mergia, N.K. Boukos, Baluc, P. Spätig, E. Alves, E. Lucon, Materials design data for reduced activation martensitic steel type EUROFER, *J. Nucl. Mater.* 329-333 (2004) 257–262. <https://doi.org/10.1016/j.jnucmat.2004.04.020>.

- [86] ASM International, ASM handbook: Volume 4: Heat treating, ASM International, Materials Park, Ohio, 1991.
- [87] J. Molgaard, W.W. Smeltzer, Thermal conductivity of magnetite and hematite, *J. Appl. Phys.* 42 (1971) 3644–3647. <https://doi.org/10.1063/1.1660785>.
- [88] M. den van Burg, J. de Hosson, Microstructure of Cr₂O₃ coatings on steel and the effect of silicon, *J. Mater. Res.* 9 (1994) 142–150. <https://doi.org/10.1557/JMR.1994.0142>.
- [89] V. Ganesh, D. Dorow-Gerspach, S. Heuer, J. Matejicek, M. Vilemova, M. Bram, J.W. Coenen, M. Wirtz, G. Pintsuk, W. Theisen, C. Linsmeier, Manufacturing of W-steel joint using plasma sprayed graded W/steel-interlayer with current assisted diffusion bonding, *Fusion Eng. Des.* 172 (2021) 112896. <https://doi.org/10.1016/j.fusengdes.2021.112896>.
- [90] J. Matejicek, B. Nevrla, J. Cech, M. Vilemova, V. Klevarova, P. Hausild, Mechanical and thermal properties of individual phases formed in sintered tungsten-steel composites, *Acta Phys. Pol. A* 128 (2015) 718–721. <https://doi.org/10.12693/APhysPolA.128.718>.
- [91] M. Wirtz, J. Linke, T. Loewenhoff, G. Pintsuk, I. Uytendhouwen, Thermal shock tests to qualify different tungsten grades as plasma facing material, *Physica Scripta T167* (2016) 14015. <https://doi.org/10.1088/0031-8949/T167/1/014015>.
- [92] T. Gietzelt, V. Toth, A. Huell, Diffusion bonding: influence of process parameters and material microstructure, in: M. Ishak (Ed.), *Joining Technologies*, InTech, 2016.
- [93] H.U. Kessel, J. Hennicke, R. Kirchner, T. Kessel, *Kurzzeitsinterng neuer Materialien mittels FAST/SPS vom Labor zum Kosteneffizienten Produktionsverfahren*, 2010.
- [94] D. Bachurina, V. Vorkel, A. Suchkov, J. Gurova, A. Ivannikov, M. Penyaz, I. Fedotov, O. Sevryukov, B. Kalin, Overview of the mechanical properties of tungsten/steel brazed joints for the DEMO fusion reactor, *Metals* 11 (2021) 209. <https://doi.org/10.3390/met11020209>.
- [95] Y.S. Touloukian, R.W. Powell, C.Y. Ho, P.G. Klemens, *Thermophysical properties of matter - the TPRC data series: Volume 1. Thermal conductivity-metallic elements and alloys*, Springer US, Boston, MA, 1970.

Appendix A: Metallographic preparation

For microstructural investigations, the sample to be examined is cut with the help of a fine cutting machine with water cooling. The exemplary macroscopic photographs of the produced composites are shown in Figure A.1. For better understanding; the cutting planes are shown in Figure A.2. The sample is then cold mounted in epoxy resin. The embedded sample is then ground using SiC paper from grit size P120 to P4000 in successive steps. It is then successively polished using diamond suspensions, for 5 min each, with particles of size 6 μm , 3 μm , and 1 μm . Finally, it is polished using an oxide polishing suspension with particles of size 0.05 μm for 3 min with water. It is then cleaned with distilled water and under an ultrasonic acetone bath for 20 min.

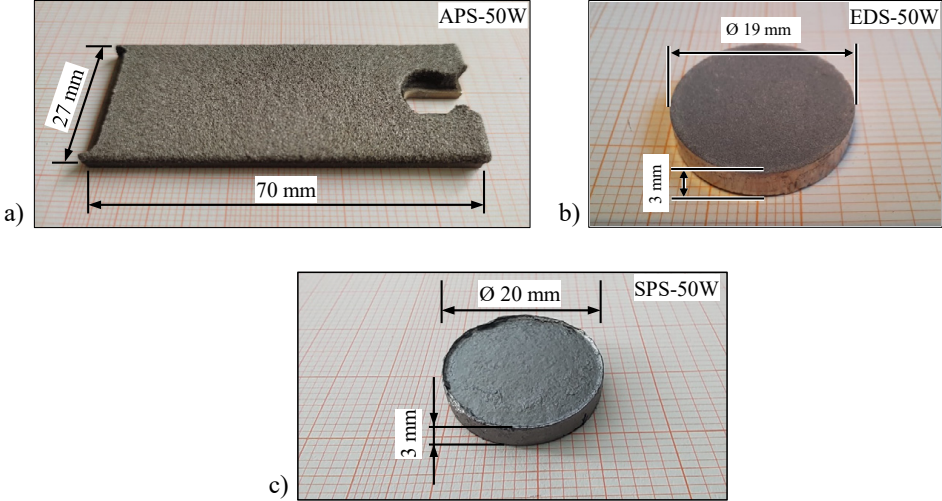


Figure A.1 Exemplary macroscopic image of produced composites via: a) APS, b) EDS, c) SPS

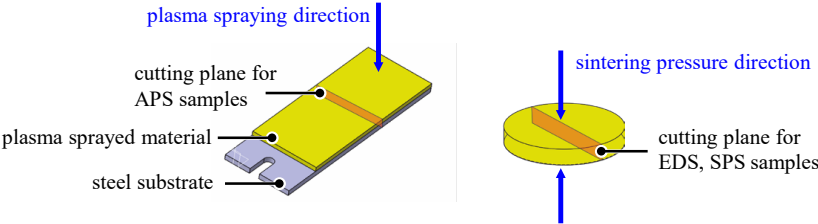


Figure A.2 Cutting plane for metallographic preparation

Appendix B: SEM micrographs of starting powders

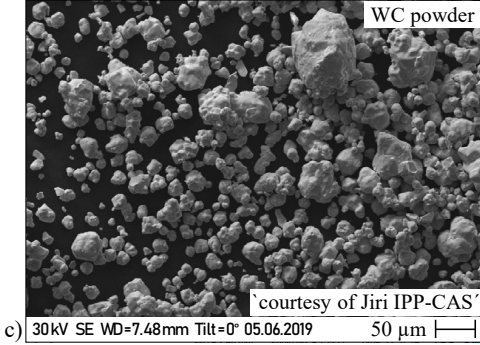
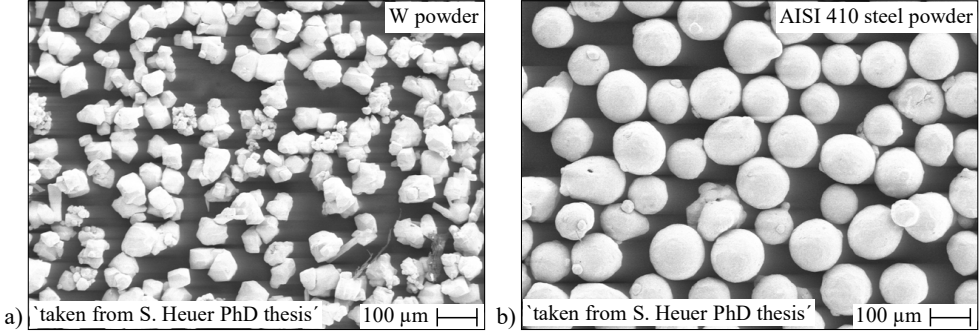


Figure B.1 Micrographs of feedstock powders used for APS; a) W powder of PSF 63–80 μm, b) WC powder of PSF 40–80 μm, c) AISI 410 powder of PSF 90–140 μm (refer to Table 2.1)

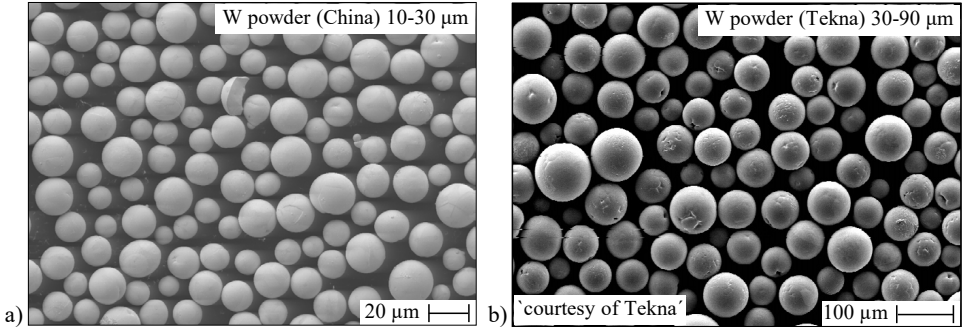


Figure B.2 Micrographs of W powders for EDS and SPS; a) W powder from China of PSF 10–30 μm, b) W powder from Tekna of PSF 30–90 μm (please refer to Table 2.4 and Table 2.9)

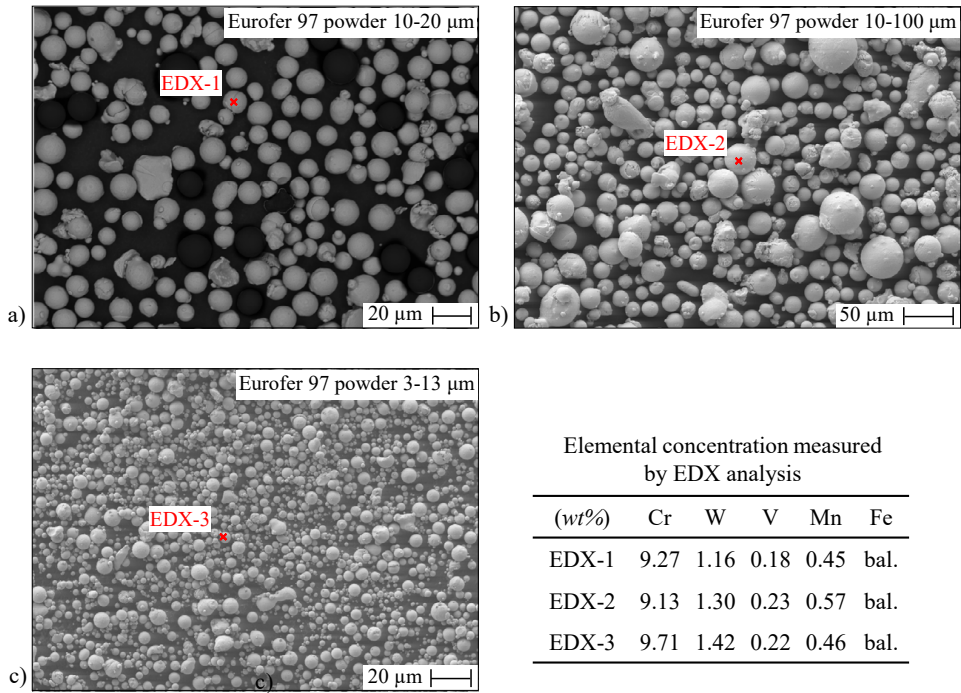


Figure B.3 Micrographs of Eurofer 97 powders for EDS and SPS of different PSF: a) 10–20 μm , b) 10–100 μm , c) 3–13 μm ; along with the elemental concentration detected by EDX (please refer to Table 2.4 and Table 2.9)

Appendix C: Shrouding chamber and process control of APS

Effectiveness of shrouding chamber in limiting oxidation: To demonstrate the shrouding chamber's effectiveness, a 50W composite was sprayed on the substrate with and without the presence of the inert gas Ar + 7 % H₂ inside the shrouding chamber. Figure C.1 a) shows the micrograph of this 50W composite sprayed without this inert gas; the composite is full of Fe based oxides. The amount of oxide (Fe_xCr_yO), determined by image analysis, was approximately 15 %. For comparison, a 50W composite sprayed under inert gas inside the shrouding chamber is shown in Figure C.1 b). Here, the oxide was only 3 %.

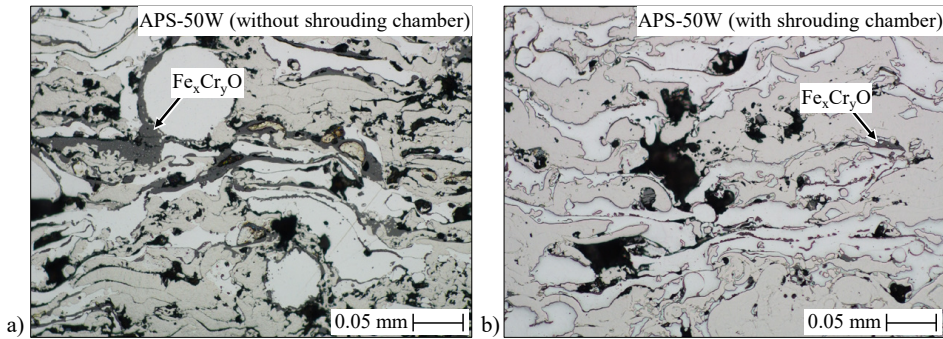


Figure C.1 Effect of the shrouding chamber on limiting the oxidation; SEM micrograph of 50W plasma sprayed composite: a) without the shrouding chamber, b) with shrouding chamber

Temperature monitoring/control during plasma spraying: The real-time monitored/controlled temperature of the substrate during the plasma spraying, for instance of 25W, is shown in Figure C.2. The substrate is, at first, preheated to ~ 500 °C with the help of induction coils of the shrouding chamber, then plasma spraying passes are performed. A single spraying pass here corresponds to 10 vertical reciprocating motions of the plasma gun/torch (attached to the robotic manipulator). During each spraying pass, the substrate's temperature increases, so intermittent pauses are necessary to keep its temperature below 500 °C. Once the substrate cools down to ~ 450 °C, the next spraying pass is performed. After roughly 5 to 6 spraying passes, the slit of the shrouding chamber through which the composite is sprayed gets clogged, as shown in Figure C.3. This reduces the spraying efficiency and needs to be manually removed. Therefore a long pause had to be included. During this pause, the substrate is maintained at ~ 450 °C, and the material clogging the slit is manually removed. After this, the spraying passes are continued. A total of 15–17 such spraying passes were performed for each composition, as seen in Figure C.2, resulting in a coating thickness of around 2 mm.

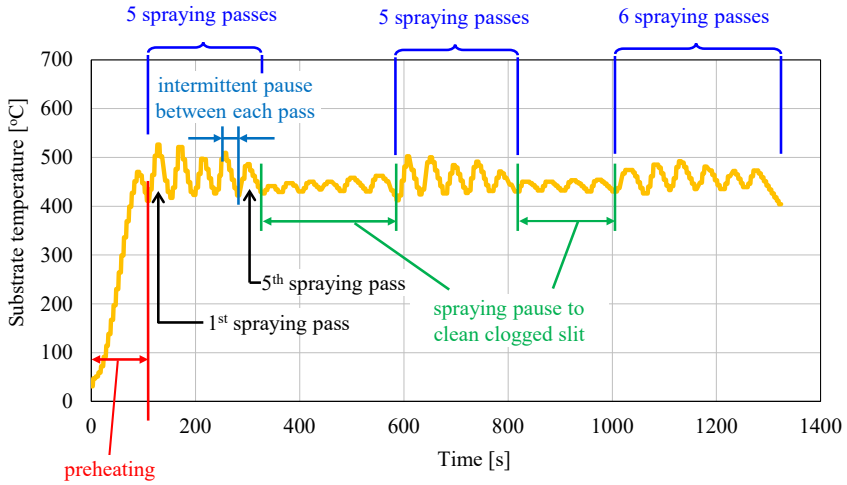


Figure C.2 Temperature of the substrate during the plasma spraying of 25W



Figure C.3 Clogging of the slit at the shrouding chamber, which needs to be manually removed

Appendix D: Resistance and efficiency of EDS sintering trials

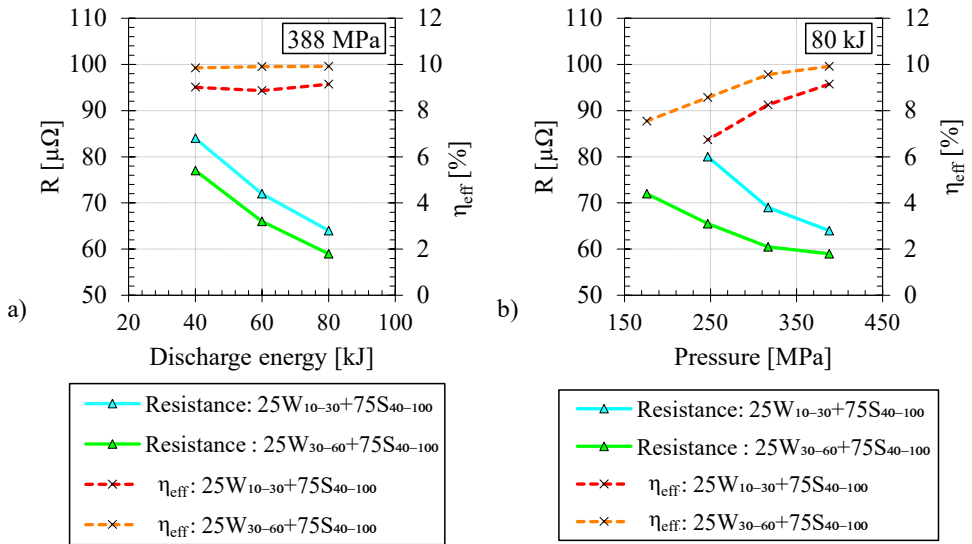


Figure D.1 a) Effect of discharge energy (sintered at 388 MPa), b) Effect of sintering pressure (sintered at 80 kJ) on the resistance and efficiencies for two 25W compositions

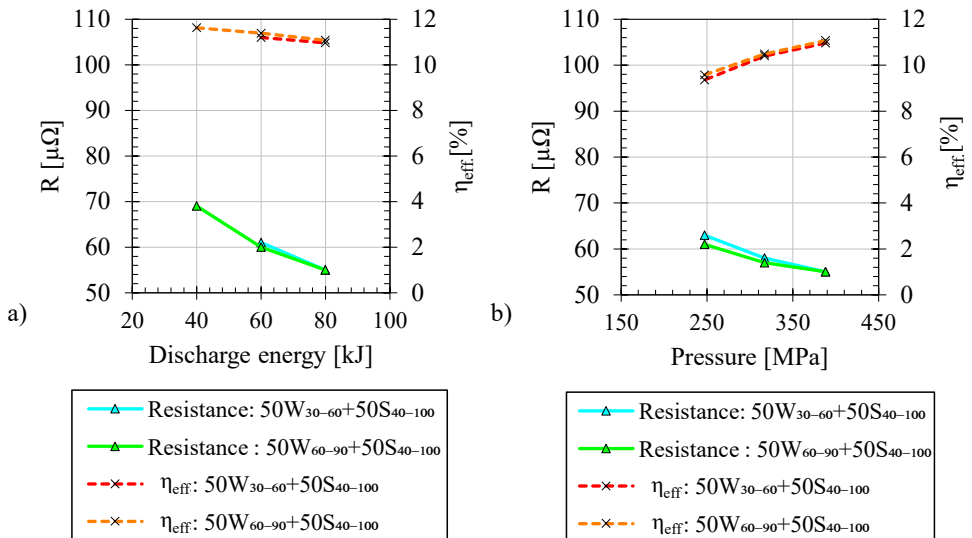


Figure D.2 a) Effect of discharge energy (sintered at 388 MPa), b) Effect of sintering pressure (sintered at 80 kJ) on the resistance and efficiencies for two 50W compositions

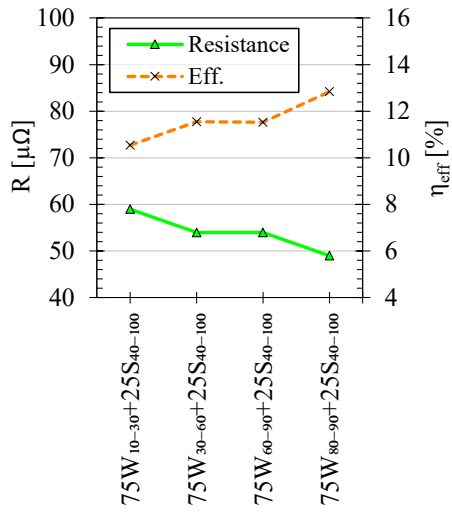


Figure D.3 Effect of various combinations of PSF for 75W composite on the resistance and efficiency

Appendix E: Instruments for measuring thermophysical properties

Dilatometer: Dilatometer is a measurement device to measure the thermally induced changes in length. The calibration is done using Al_2O_3 samples used as reference. The working principle of such a device is schematically shown in Figure E.1. Two samples can be placed vertically on Al_2O_3 rod at the same time. The samples are present inside a furnace under inert atmosphere surrounded by heating element. Upon heating, the sample's length changes, which is recorded by the displacement transducer sensor connected via pushrod.

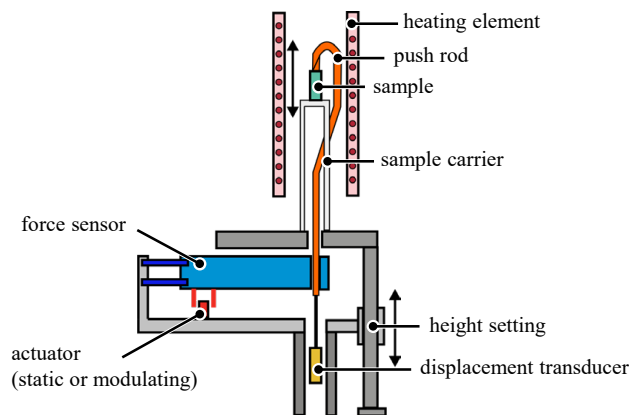


Figure E.1 Schematic representation of vertical dilatometer (adapted from Netzsch-Gerätebau GmbH, Germany)

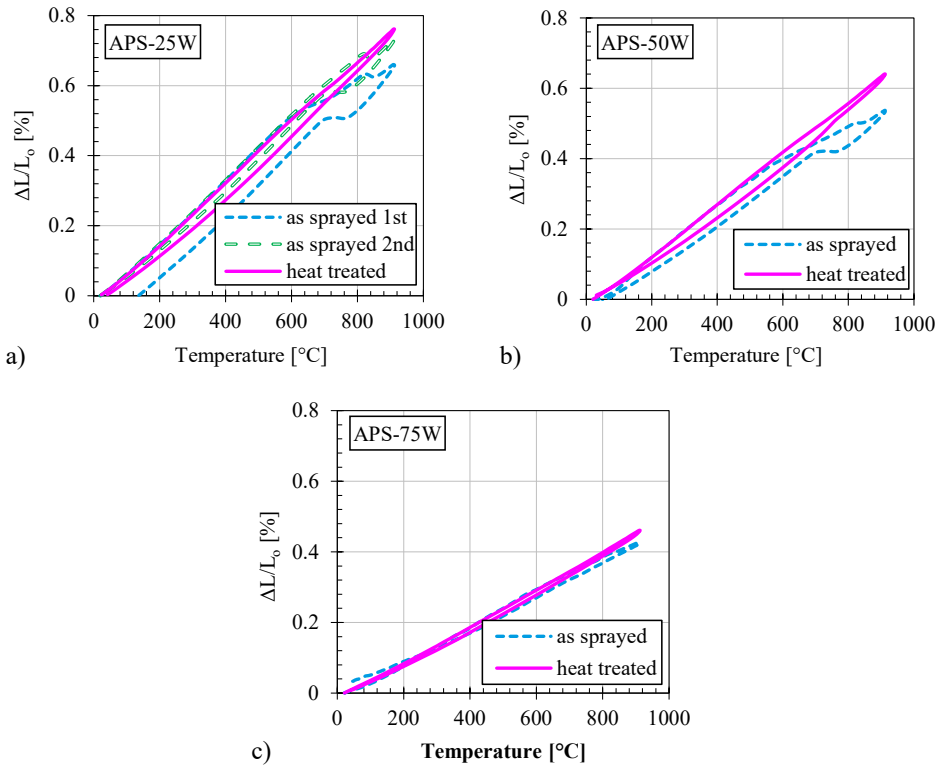


Figure E.2 Relative change in length for the as-sprayed as well as heat treated plasma sprayed composites a) 25W, b) 50W, c) 75W

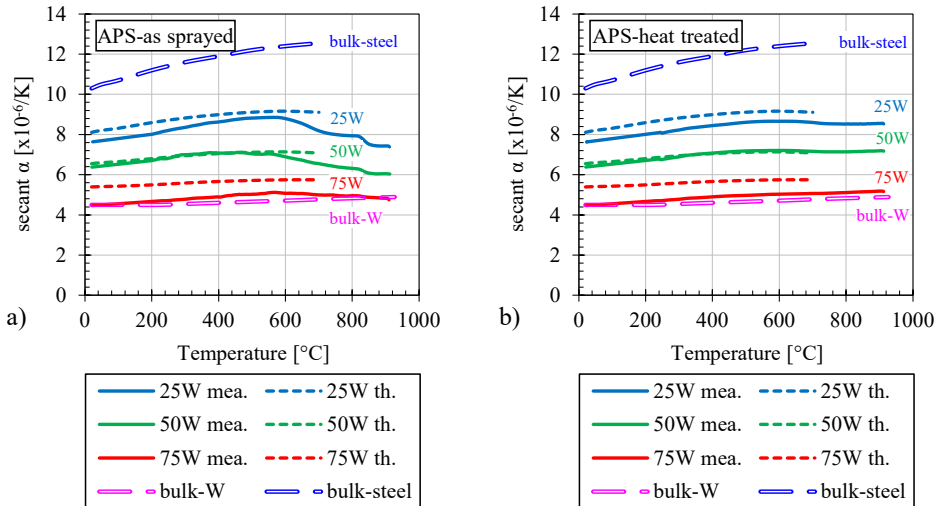


Figure E.3 Secant CTE of plasma sprayed composites in their a) as-sprayed state and b) heat treated state, along with the theoretical expected values

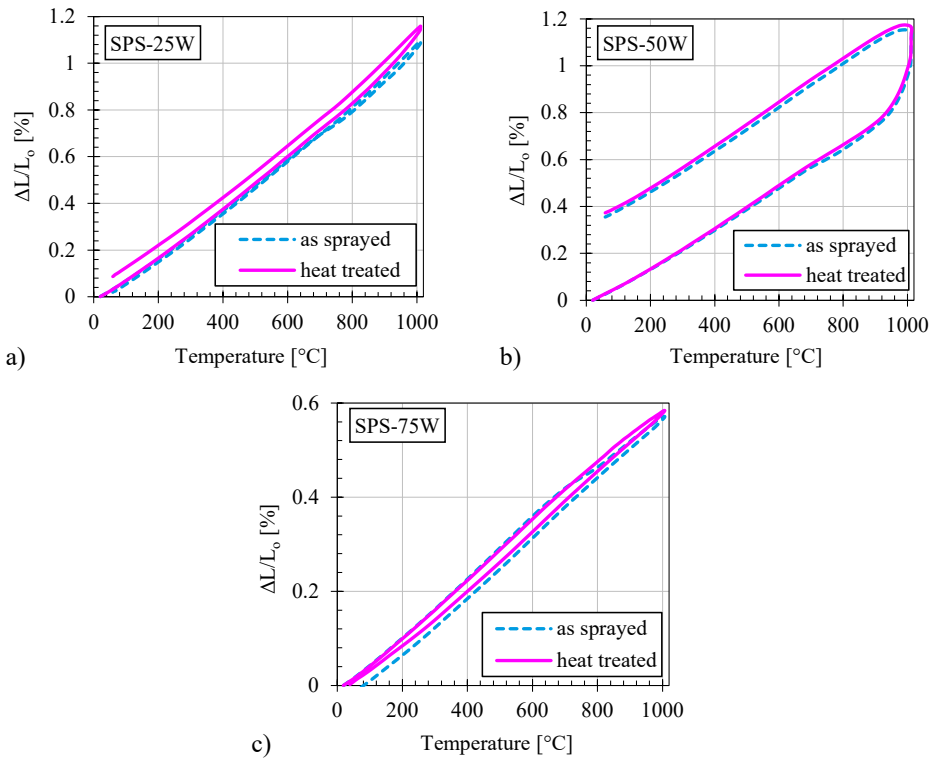


Figure E.4 Relative change in length for the as-sprayed as well as heat treated sintered composites a) 25W, b) 50W, c) 75W

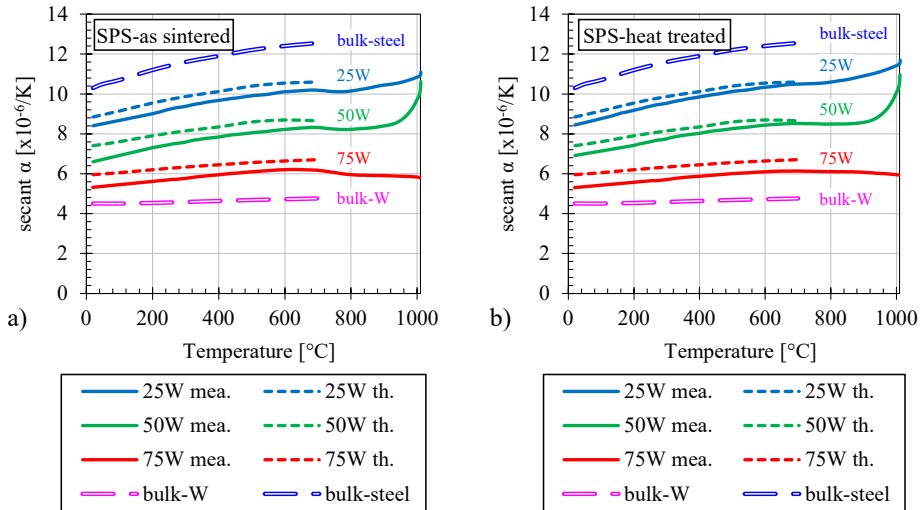


Figure E.5 Secant CTE of plasma sprayed composites in their a) as-sprayed state and b) heat treated state, along with the theoretical expected values

Differential scanning calorimetry (DSC): DSC is an analytical method to determine the temperature dependent specific heat capacity of a material. The DSC used in this work is DSC 404 F3 from Netzsch-Gerätebau GmbH, Germany. The brief working principle of such a device is schematically shown in Figure E.6. The method comprises two platinum crucibles placed next to each other inside a furnace under an inert atmosphere. The furnace is closed of heating elements to heat the crucibles to the required temperature. The crucibles are connected to two highly sensitive thermocouples/sensors to measure the temperature dependent electrical potential. The reference crucible is kept empty, and the sample is placed in the second crucible. The electrical potentials corresponding to both crucibles are recorded as the temperature increases. The sample to be examined either emits or absorbs the heat energy during heating. As a result, the crucible containing the sample's temperature differs from that of the empty crucible. For better understanding, the electrical potential response of the reference crucible and the sample is represented by the green dotted line and orange line in Figure E.6. The resulting difference over the whole time can be plotted, and the corresponding area is equivalent to the heat of transformation; which is the specific heat capacity of the sample.

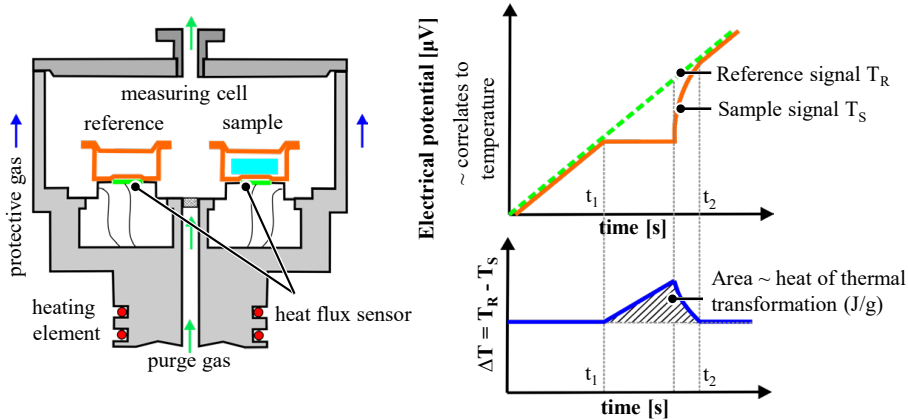


Figure E.6 Schematic representation of DSC instrument (adapted from Netzsch-Gerätebau GmbH, Germany)

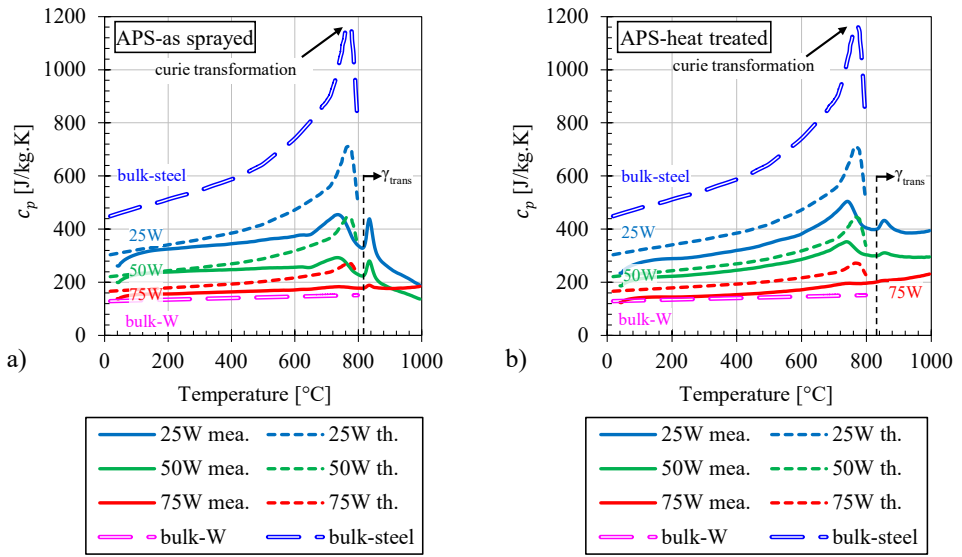


Figure E.7 Specific heat capacity of plasma sprayed composites in their a) as-sprayed state and b) heat-treated state, along with the theoretical expected values

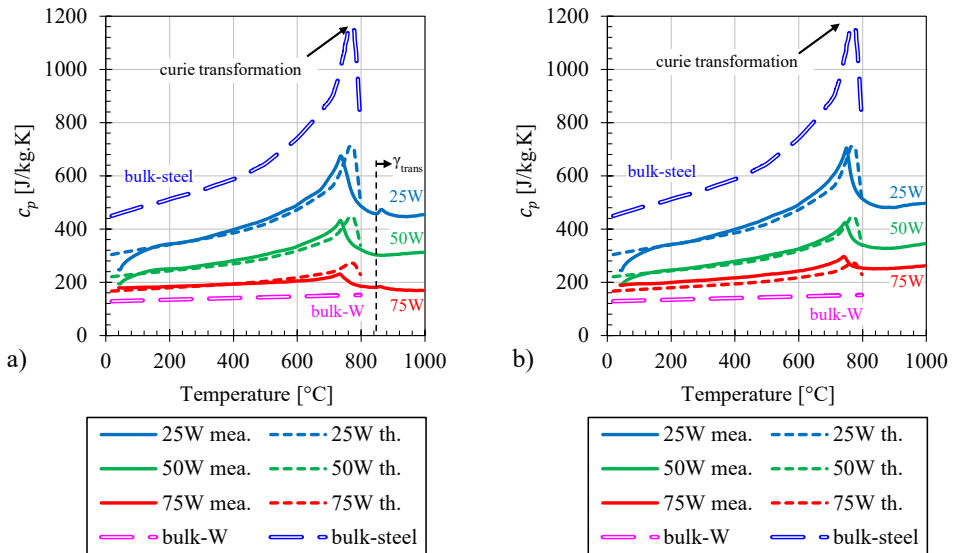


Figure E.8 Specific heat capacity of sintered composites in their a) as sintered state and b) heat treated state, along with the theoretical expected values

Laser flash analysis (LFA): LFA is an analytical method to determine directly the temperature dependent thermal diffusivity (a) of a material. The LFA used in this work is LFA 427 from Netzsch-Gerätebau GmbH, Germany and its working principle is briefly explained in a schematic representation in Figure E.9. The sample to be examined is placed inside a furnace under an inert atmosphere and heated to the measurement temperature with the help of heating elements. The underside of the sample is then fired with a short laser pulse of specified energy. This induced energy flows through the sample and results in a slight increase in the temperature at the top side of the sample. This rise in the temperature (ΔT) as a function of time (t) is recorded by the infrared (IR) detector, pointed at the top side of the sample. The maximum rise in the temperature (ΔT_{\max}) is inversely proportional to the mass of the sample (m) and the specific heat capacity of the sample (c_p). The time required to reach half of ΔT_{\max} is $t_{1/2}$. The a could be then determined with the help of a simple empirical equation, proposed by Parker^a, from $t_{1/2}$ and the thickness of the sample: $a = 0.1388 \frac{d^2}{t_{1/2}}$. This relation is, however, only valid for one dimensional sample. The LFA system used in this work uses a much more complex Cape-Lehmann^b model to determine the thermal diffusivity by considering the three dimensional heat flow and other secondary effects. After a is known, the thermal conductivity (λ) is calculated by multiplying a , c_p and density (ρ is measured using Archimedes' principle).

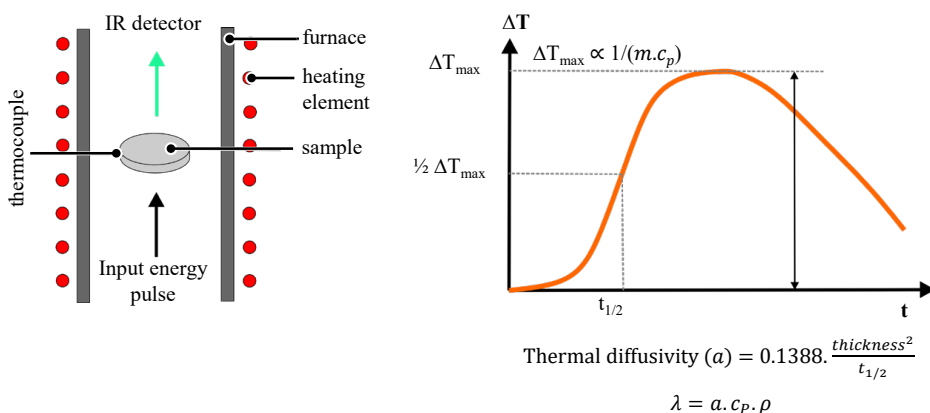


Figure E.9 Schematic representation of LFA instrument (adapted from Netzsch-Gerätebau GmbH, Germany)

^a W.J. Parker, R.J. Jenkins, C.P. Butler, G.L. Abbott, Flash method of determining thermal diffusivity, heat capacity, and thermal conductivity, *Journal of Applied Physics* 32 (1961) 1679–1684. <https://doi.org/10.1063/1.1728417>

^b J.A. Cape, G.W. Lehman, Temperature and Finite Pulse-Time Effects in the Flash Method for Measuring Thermal Diffusivity, *Journal of Applied Physics* 34 (1963) 1909–1913. <https://doi.org/10.1063/1.1729711>

Appendix F: Metallurgical bonding of W-W interface

A site is selected, each in SPS-50W and SPS-75W, where two W-particles appear to form some metallurgical bonding. Then FIB cuts are made at these sites for further investigation, as shown in Figure F.1 (SPS-50W) and Figure F.2 (SPS-75W), respectively.

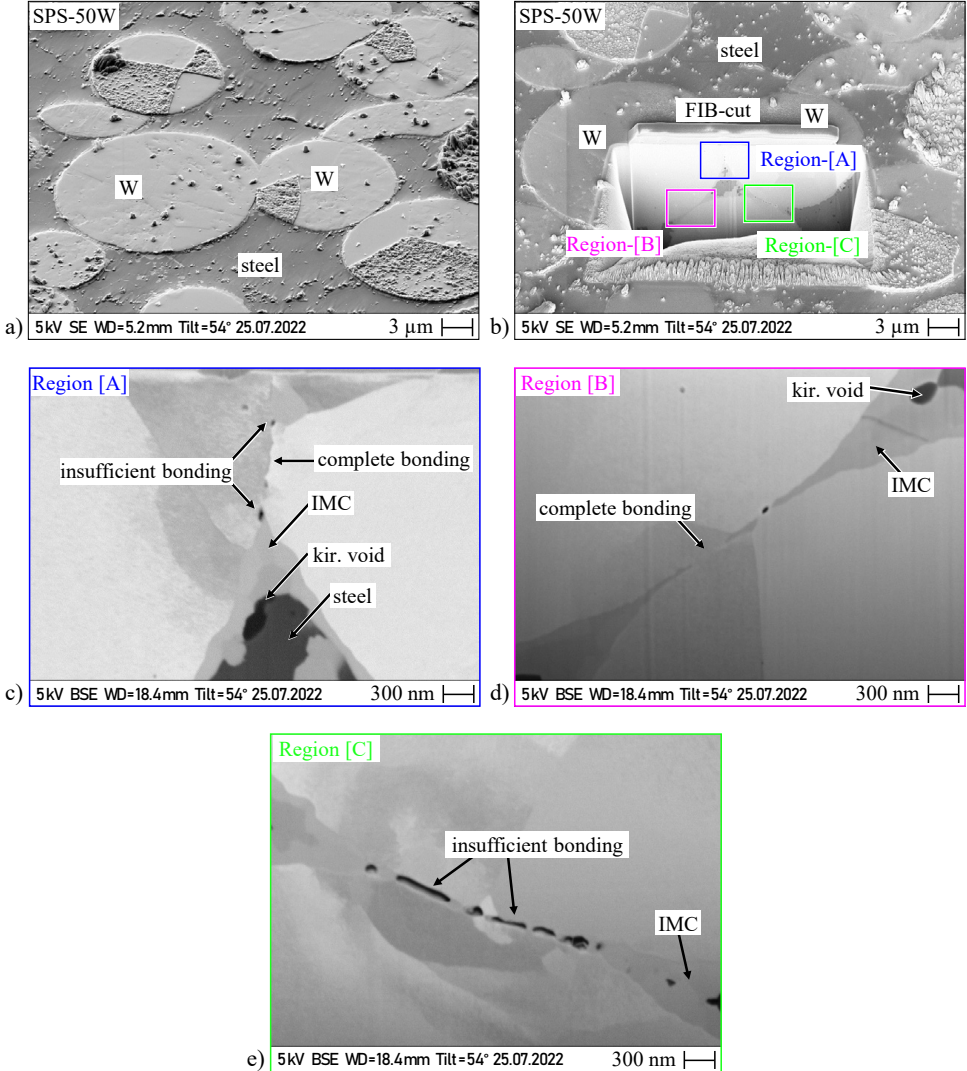


Figure F.1 a) A site in SPS-50W where two W particles appear to form metallurgical bonding, b) FIB cut at this site, c), d) and e) showing W-W interface

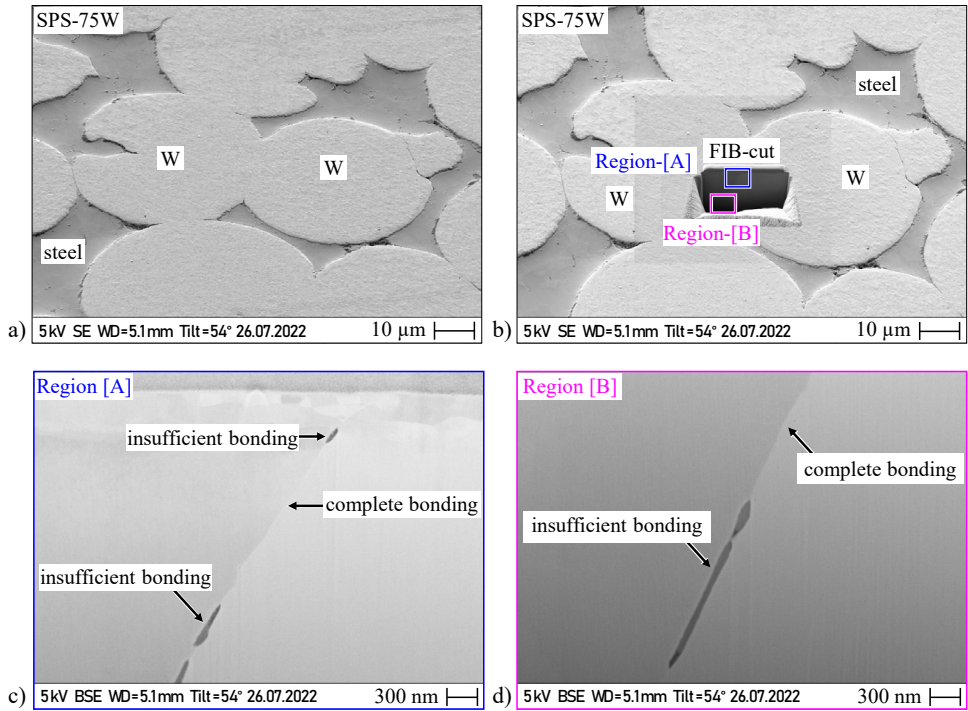


Figure F.2 a) A site in SPS-75W where two W particles appear to form metallurgical bonding, b) FIB cut at this site, c) and d) showing W-W interface

W and steel were joined with a 3-layer sintered FGM and a 2-layer sintered FGM. It was observed that few W particles appear to form proper metallurgical bonding with bulk-W. However, it was unclear how good this bonding was. Thus, it was essential to investigate the degree of metallurgical bonding of the W particles of the topmost sintered 50W or 75W layer and the bulk-W (W-tile). This investigation is also necessary since both these joints failed at this joining interface (as mentioned in Chapter 6). For this, two sites were selected at each of these joints, where the W-particles and bulk-W (W-tile) appear to form metallurgical bonding. These investigations are shown in the following figures: Figure F.3, Figure F.4 at the bond seam of SPS-50W and W-tile, and Figure F.5, Figure F.6 at the bond seam of SPS-75W and W-tile.

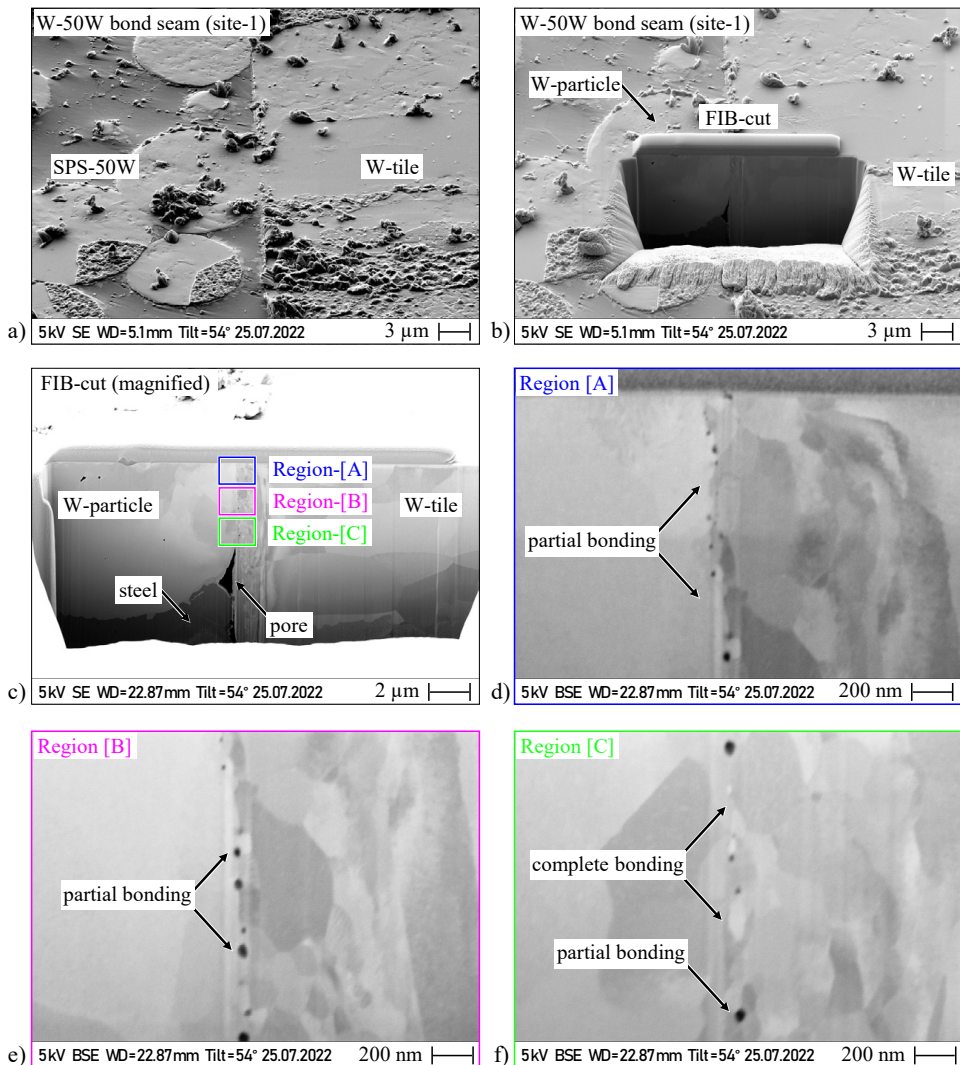


Figure F.3 a) Site-1 at the bond seam between SPS-50W and W-tile, b) FIB cut made at the interface between W-particle of SPS-50W and W-tile, c) Magnified SEM micrograph of the FIB cut, d), e), and f) showing W-W interface

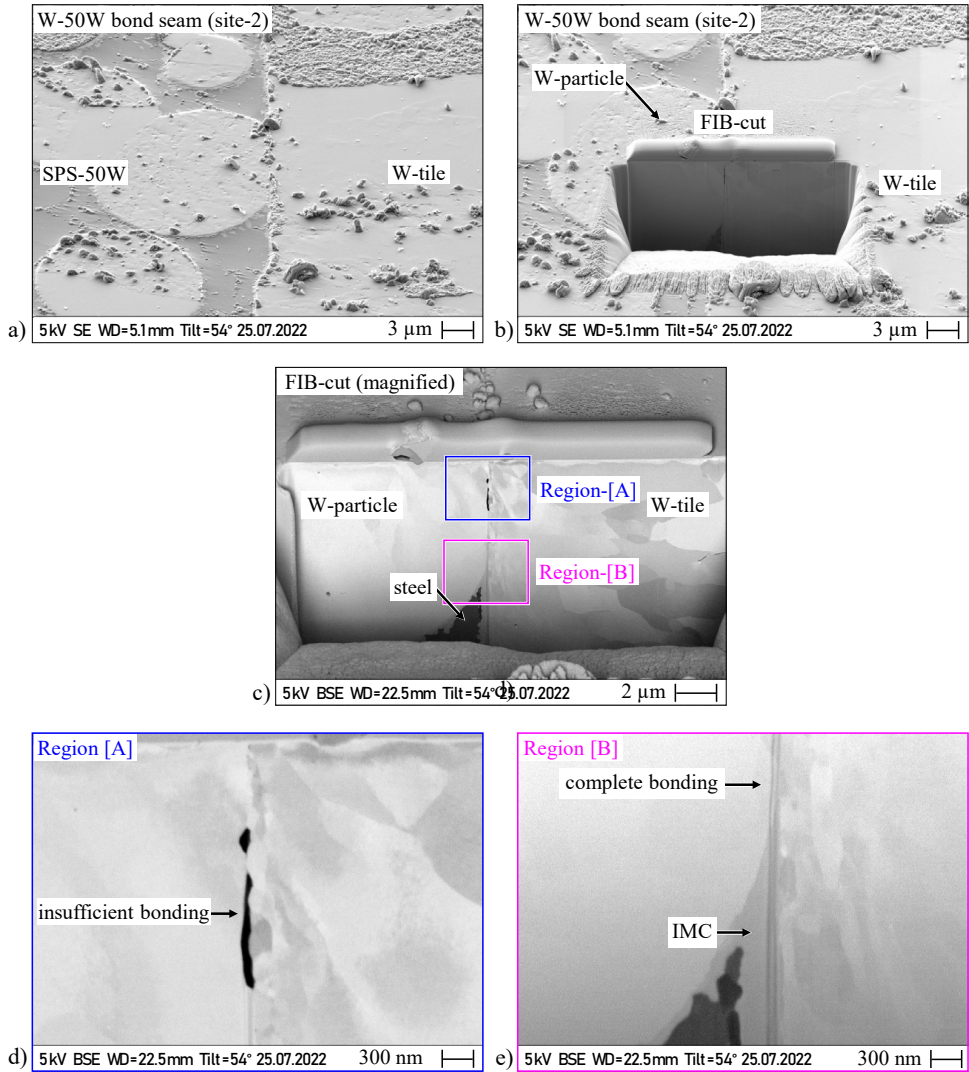


Figure F.4 a) Site-2 at the bond seam between SPS-50W and W-tile, b) FIB cut made at the interface between W-particle of SPS-50W and W-tile, c) Magnified SEM micrograph of the FIB cut, d) and e) showing W-W interface

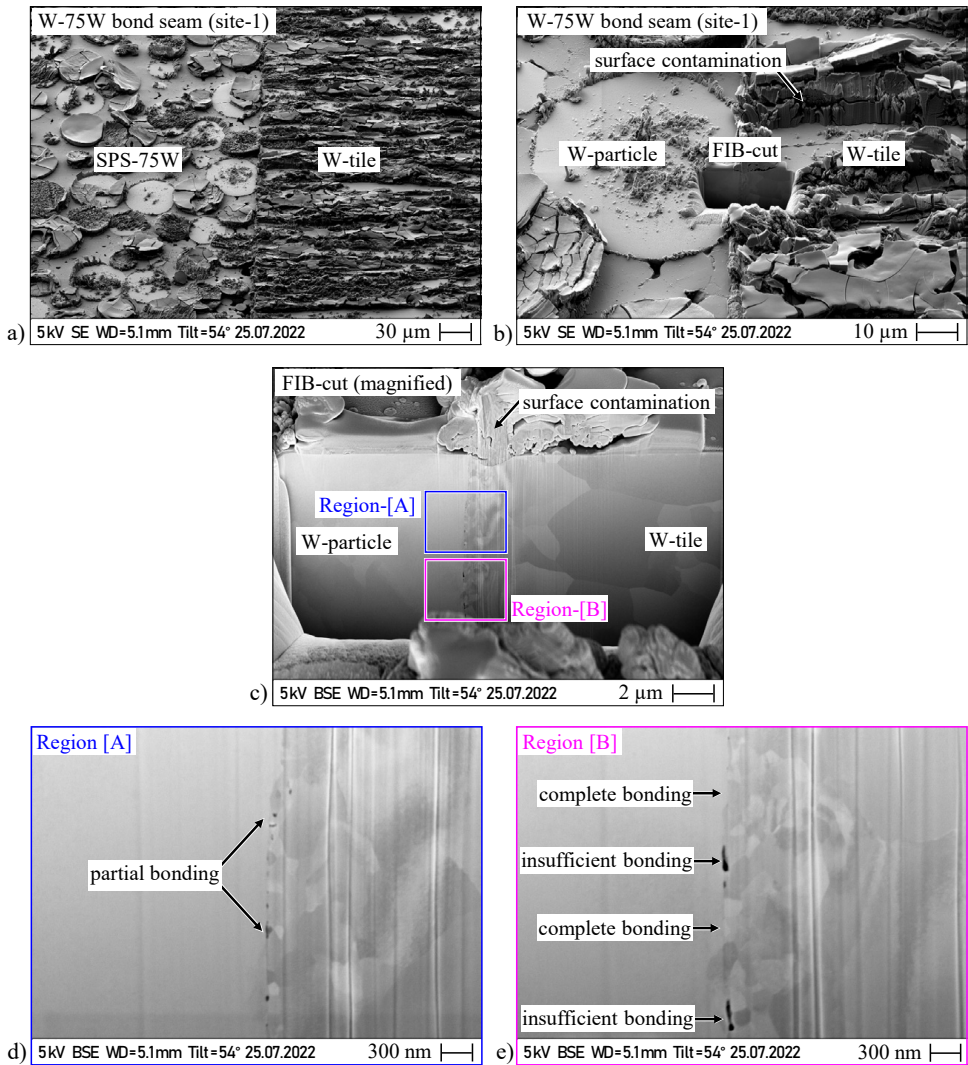


Figure F.5 a) Site-1 at the bond seam between SPS-75W and W-tile, b) FIB cut made at the interface between W-particle of SPS-75W and W-tile, c) Magnified SEM micrograph of the FIB cut, d) and e) showing W-W interface (*Note: this particular specimen got exposed to air accidentally and the platinum coating on the specimen – necessary for SEM analysis – oxidized and showed surface contamination. This is just surface contamination and does not affect the investigation*)

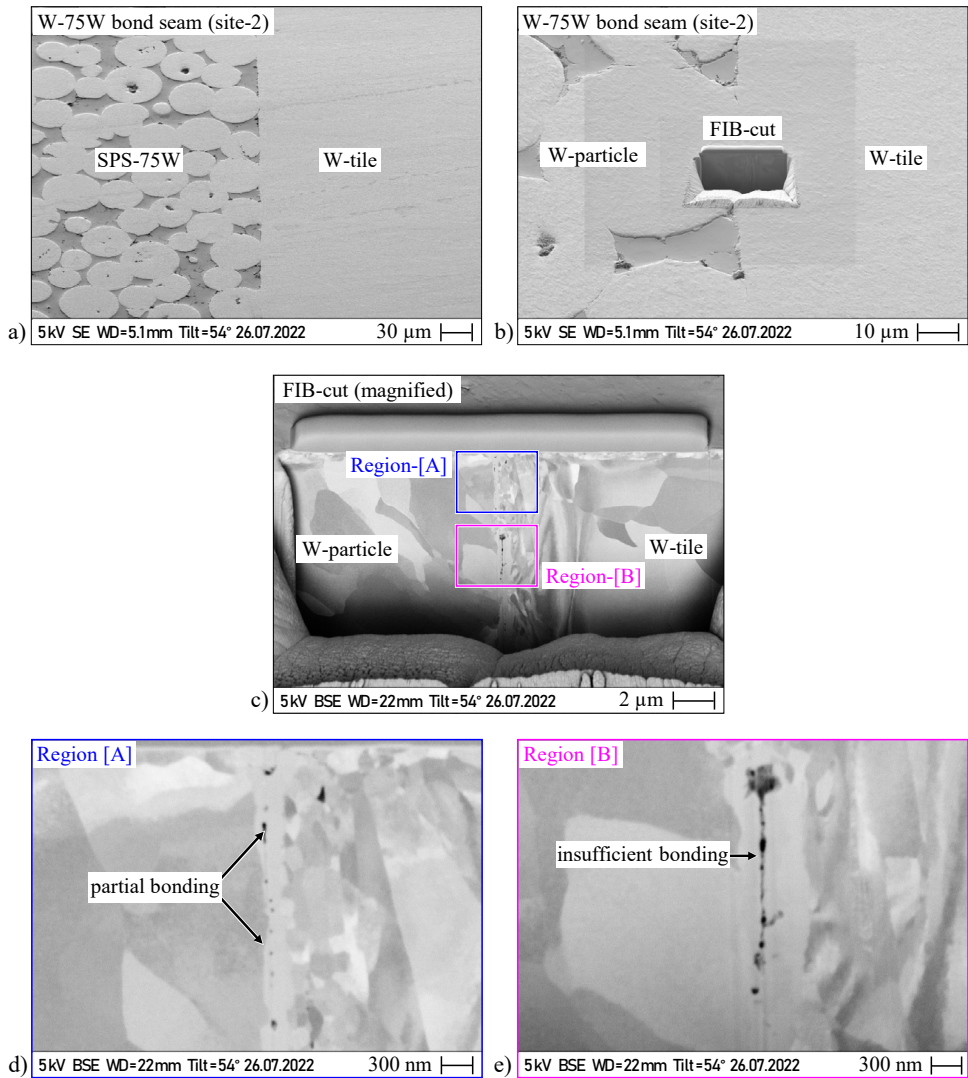


Figure F.6 a) Site-2 at the bond seam between SPS-75W and W-tile, b) FIB cut made at the interface between W-particle of SPS-75W and W-tile, c) Magnified SEM micrograph of the FIB cut, d) and e) showing W-W interface

Lebenslauf

Persönliche Daten

Name: Vishnu Ganesh
Geburtsdatum: 12.01.1992
Geburtsort: Shillong, Indien

Bildungsweg

06.2010–07.2014 Bachelorstudium im Maschinenbau,
Indian Institute of Technology, Indien (Note: 1,7)

10.2014–05.2018 Masterstudium im Manufacturing Technology
Technische Universität Dortmund (Note: 1,2)

05.2016–12.2016 Freiwilliges Praktikum
Bharat Forge CDP GmbH, Ennepetal

05.2017–06.2018 Wissenschaftliche Hilfskraft
Institut für Umformtechnik und Leichtbau, Dortmund

04.2019– Promotionsstudent im Fakultät Maschinenbau
Lehrstuhl Werkstofftechnik, Ruhr-Universität Bochum

04.2019–03.2023 Doktorand am Forschungszentrum Jülich GmbH,
Institut für Energie- und Klimaforschung – Plasmaphysik, Jülich

Sprachkenntnisse

Deutsch: Niveaustufe B2
Englisch: Verhandlungssicher
Tamil, Hindi Muttersprache

Conferences

- 18th International Conference on Plasma-Facing Materials and Components for Fusion Applications, Jülich Germany, 2021
Poster: First results on the manufacturing of W/steel composites using plasma spraying under inert atmosphere
- 9th Forum on New Materials, Perugia Italy, 2022
Poster: W/steel composites as a potential interlayer for the joining of W and steel for the first wall of a fusion reactor
- 32nd Symposium on Fusion Technology, Dubrovnik Croatia, 2022
Poster: High heat flux testing results of various W-FGM-steel joints

Acknowledgement

I am grateful for the support and guidance of the following individuals:

My Doktorvater, Prof. Werner Theisen, for his guidance and support during my PhD journey. He was always open to discussions and provided invaluable help. He kindly allowed me to use the EDS setup at LWT, RUB.

My second academic supervisor, Prof. Christian Linsmeier, for giving me this interesting topic to work on. He was always open to many discussions and offered his support. I thank him for giving the freedom to explore creative approaches, attending conferences, and supporting my research stay at IPP-CAS, Prague.

My daily supervisor at FZJ, Dr. Daniel Dorow-Gerspach, for his unwavering support and guidance throughout my PhD journey. He was always kind, helpful and kept an open mind for fruitful discussions. We had many fair shares of scientific arguments and debates over research ideas and methods, which is one of the key pillars for scientific progress. However, he always welcomed my criticism, doubts and concerns in a very supportive and sportive manner and encouraged me to achieve my results. He corrected and proofread many of my articles, and through his corrections, I significantly improved my scientific writing skills. He has always responded to my problems in a quick and timely manner. Without his supervision and help, this PhD work would not have been possible.

Dr Simon Heuer, my second daily supervisor at FZJ, for supervising me during the first year of my PhD, alongside. His expertise and guidance established the basis of my work on FGM.

Many thanks to Prof. Bram for allowing me to use the FAST/SPS equipment, which was the central part of the experimental work for the manufacturing purpose. He was always open for discussions and offered valuable advice.

Dr. Jiri Matejicek, my external mentor at IPP-CAS, for his assistance with plasma spraying and for his regular and fruitful discussions. He has always answered my never-ending-countless E-Mails and provided immense help. He has corrected many of my posters and articles and always offered sound advice. I also thank him for making my stay at IPP-CAS enjoyable.

Dr. Monika Vilemova, IPP-CAS, for her assistance with the plasma spraying and for her help during my stay at IPP-CAS.

Marek Janata and Zdenek Kutilek, of IPP-CAS, for their help with the plasma spraying.

Dr. Jan Cizek and Jakub Kleka of IPP-CAS for their help with RF-plasma spraying and for helping me during my stay at IPP-CAS

Dr. Jan Willem Coenen and Dr. Marius Wirtz, the project leaders and internal mentor at IEK-4, were always available for discussion, suggestions and helpful guidance.

Dr. Gerald Pintsuk, for answering my many thought-provoking questions.

Lennart Leich of LWT, RUB, with whom I performed the experiments at the EDS setup.

Beatrix Göths, for her help in the metallography lab.

Ruth Hanke and Martina Mangels, of our purchase department at IEK-4, for processing countless paperwork related to order; placing orders at ZEA-1, arranging lab keys, and many more miscellaneous things. (*Paperwork is an eternal part of FZJ* :)

Angelika Hallmanns for taking care of monthly time sheets and things related to “Strahlenschutz”.

Judith Schönbrenner, for taking care of arranging appointments with Prof. Linsmeier and many countless bureaucratic things.

Rudi Casper for his help with the cutting of samples

Thomas Koppitz of ZEA-1 for his assistance with dilatometry and brazing.

Philipp Lied and Siegfried Baumgärtner of KIT for their assistance in the bending test.

Friedel Gormann for taking care of the things related to “Strahlenschutz” at HML and his assistance with DSC and LFA measurements.

Thanks to our mechanical workshop at IEK-4, especially Tim Rüttgers, Rene Dohmen and Noah Richter, for machining copper electrodes for EDS, machining of tensile testing setup from Inconel and various parts for my PhD.

Ralf Steinert was always open for help when something went wrong with the SPS.

Volker Bader from IEK-1 for his help with the heat treatment of the samples

Karsten Dominiczak and Thorsten Tietz, for their help with the testing at JUDITH 2

Jörg Bartsch and Volker Gutzeit, for their help in the metallography lab of IEK-2, FZJ.

Thanks to my PhD fellow mates at IEK-4, especially my office colleague Dr. Rahul Rayaprolu for making the working environment enjoyable.

Dr. Marcin Rasinski for teaching me how to use the SEM systems and always providing helpful tips to get satisfactory images. Also, thanks to him for helping with the FIB cutting.

Prof. Sebastijan Brezinsek and Prof. Andrey Litnovsky for signing several purchase orders.

Stefan Kirtz for IT-related things, and Thorsten Gürth as well.

Thanks to my family, parents and sister for showing unconditional love, patience and support. Thanks to my motorcycle, with whom I enjoyed several sunny weekends around Eifel, which helped me to freshen up my mind. Thanks to my friends for making some weekends enjoyable, like playing Cricket in Dortmund and many more outdoor activities.

Band / Volume 601

**High-resolution imaging of transport processes
with GPR full-waveform inversion**

P. Haruzi (2022), iv, 173 pp

ISBN: 978-3-95806-678-6

Band / Volume 602

**Synthesis of optimized cathode materials
for all-solid-state lithium batteries**

C. Roitzheim (2022), xv, 221 pp

ISBN: 978-3-95806-679-3

Band / Volume 603

**Development of components based on Ti₂AlC/fiber composites
for aggressive environmental conditions**

S. Badie (2023), x, 161 pp

ISBN: 978-3-95806-680-9

Band / Volume 604

Multiregionales Energiesystemmodell mit Fokus auf Infrastrukturen

T. M. Groß (2023), xx, 235 pp

ISBN: 978-3-95806-681-6

Band / Volume 605

Temporal Aggregation Methods for Energy System Modeling

M. A. C. Hoffmann (2023), XXVI, 341 pp

ISBN: 978-3-95806-683-0

Band / Volume 606

**Examining transport in the Upper Troposphere –
Lower Stratosphere with the infrared limb imager GLORIA**

L. Krasauskas (2023), v, 107 pp

ISBN: 978-3-95806-691-5

Band / Volume 607

**Sustainable Fabrication of Ceramic Solid Electrolytes
for Solid-State Lithium Batteries**

R. Ye (2023), vi, 119 pp

ISBN: 978-3-95806-694-6

Band / Volume 608

**Improving Nitrogen Retention in Soils Treated with Pig and Cattle Slurry
Through the Use of Organic Soil Amendments**

X. Cao (2023), XVI, 119 pp

ISBN: 978-3-95806-696-0

Band / Volume 609

Mechanisches Verhalten von Polymer-Elektrolyt-Membran-Elektrolysezellen und -Stacks

S. Holtwerth (2023), x, 251 pp

ISBN: 978-3-95806-697-7

Band / Volume 610

Membrane Reactor Concepts for Power-to-Fuel Processes

H. Huang (2023), VI, 197 pp

ISBN: 978-3-95806-703-5

Band / Volume 611

Deployment of Fuel Cell Vehicles in Road Transport and the Expansion of the Hydrogen Refueling Station Network: 2023 Update

R. C. Samsun, M. Rex (2023), i, 39 pp

ISBN: 978-3-95806-704-2

Band / Volume 612

Behavior/performance of tungsten as a wall material for fusion reactors

M. Gago (2023), X, 120 pp

ISBN: 978-3-95806-707-3

Band / Volume 613

Strategieentwicklung zur Umsetzung der Klimaschutzziele im Verkehrssektor mit dem Fokus Kraftstoffe

M. Decker (2023), ix, 243 pp

ISBN: 978-3-95806-714-1

Band / Volume 614

Joining of tungsten and steel for the first wall of a future fusion reactor

V. Ganesh (2023), xxx, 142, a-v pp

ISBN: 978-3-95806-715-8

Weitere *Schriften des Verlags im Forschungszentrum Jülich* unter
<http://www.zbw1.fz-juelich.de/verlagextern1/index.asp>

Energie & Umwelt / Energy & Environment
Band / Volume 614
ISBN 978-3-95806-715-8